Doctoral Dissertation
Doctoral Program in Chemical Engineering (33th Cycle)

Novel crystallization platforms for drugs and biomolecules: self-assembled surface functionalization and gels

Fiora Artusio
* * * * * *

Supervisor
Prof. R. Pisano

Doctoral Examination Committee:
Prof. A. Barresi, Politecnico di Torino
Dr. P. Colpo, Joint Research Centre – European Commission
Dr. J. Gomez Morales, University of Granada
Prof. F. Pattarino, University of Piemonte Orientale
Dr. E. Simone, University of Leeds

Politecnico di Torino
March 30th, 2021

This thesis is licensed under a Creative Commons License, Attribution - Noncommercial - NoDerivative Works 4.0 International: see www.creativecommons.org. The text may be reproduced for non-commercial purposes, provided that credit is given to the original author.

I hereby declare that, the contents and organisation of this dissertation constitute my own original work and does not compromise in any way the rights of third parties, including those relating to the security of personal data.

…….....

Fiora Artusio

Turin, March 30th, 2021

Summary

The production of crystalline materials represents a key point in the pharmaceutical field. The majority of drug manufacturing processes take advantage of crystallization to isolate or purify an active ingredient. Moreover, crystals of complex macromolecules, such as proteins, are vital for the determination of their molecular structure. In this scenario, crystallization can be carried out with the help of heteronucleants, minimizing the required amounts of drug. The present thesis investigates the design and the application of bidimensional, i.e., flat surfaces, and tridimensional systems, i.e., gels, to the crystallization of target molecules, ranging from small molecule drugs to biomacromolecules.

As a first step, the functionalization of glass with different chemical groups was investigated. Self-assembled monolayers immobilized on glass were selected since they provided an ideal platform for studying the heterogeneous nucleation of small-molecule drugs and deconvoluting the action of heteronucleant chemistry from topography. Trimethoxysilanes were selected as functionalizing agents thanks to their high reactivity toward hydroxylated glass. A general and adaptive protocol for the synthesis of self-assembled monolayers was identified thanks to the thorough physico-chemical characterization of surface attributes. The presence of specific chemical groups, the thickness and the uniformity of the functionalized layer, the absence of defects, the surface wettability, the zeta potential, and the topography were evaluated according to different sets of synthesis conditions and guided the identification of the optimal surface activation method, as well as the optimal reaction medium, time, and silane concentration. As a result, a portfolio of surfaces carrying thiol, amino, glycidyloxy, and methacrylate groups, which were able to offer different kinds of interaction with a target molecule in solution, along with sub-nm roughness, was obtained.

Self-assembled monolayers were employed as supports for inducing the heterogeneous nucleation of a model small-molecule drug, namely aspirin, from morphologically equivalent, but chemically different surfaces. The mere action of heteronucleant chemistry strongly boosted or inhibited the nucleation kinetics of aspirin batch crystallization from solution. To identify the dominant mechanism of interaction, the investigation then focused on the interface between monolayers and aspirin. Thin films of crystallized drug were prepared with the help of spin coating techniques and analyzed by X-rays diffraction. The confinement of crystallization within a limited volume revealed the ability of surface chemistries to promote the oriented growth of crystals, and a matching between the acid surface tension component of monolayers and the preferential nucleation of certain crystal facets was identified.

Monolayers also modified the nucleation step of much more complex molecules, like proteins, by altering the time needed to observe the first crystals in solution. A finer tuning of the nucleation time was obtained for proteins with wider metastability zones. Also, the effect of pH on the protein crystallization was studied, and both the crystal habit and the

nucleation time were successfully tuned by establishing pH gradients. As a step further, a tridimensional system was employed as a nucleant for proteins. The crystallization of proteinase K, insulin, and lysozyme was studied inside agarose gels. The agarose concentration was identified as the key parameter for the tuning of the crystal size and the nucleation density. Interestingly, the action of agarose gels resulted to be independent both of the protein nature and of the average crystal size, denoting the predominant physical interaction with the gel fibers. Agarose was employed to study protein crystallization in batch and in counter-diffusion environments to demonstrate its applicability to a wide range of proteins, precipitants, and crystallization techniques.

In conclusion, the crystallization pathway of small-molecule drugs and complex biomacromolecules was successfully modified thanks to the fine-tuning of chemical and physical interactions between the heteronucleants and the target molecules. By carefully matching the heteronucleant and the solute features, the nucleation time was significantly shortened, the crystallization success was enhanced, or, conversely, the crystallization phenomena were strongly delayed or inhibited. Self-assembled surface functionalization and gels served as an effective tool to guide crystallization and increase its reproducibility.

Acknowledgment

I would like to express sincere gratitude to my supervisor, prof. Roberto Pisano, for believing in me from the beginning and for encouraging me in constantly exploring new research horizons and thinking out-of-the-box. His insightful comments and suggestions guided and enlighted me. His lungimirant mindset has always been inspiring and motivational throughout the Ph.D. research journey.

This work would not have been possible without the contribution of some outstanding scientists. It was a honor and pleasure to work with all of you, and I feel lucky now to address you as friends. I warmly thank Dr. Giacomo Ceccone and Dr. Francesco Fumagalli of Joint Research Centre (JRC) – European Commission as, during the months spent as a Visiting Scientist in Ispra, I learnt so much about surface analysis techniques, as well as good food and music. I am deeply grateful to Dr. Josè Gavira "Gavi" of Laboratorio de Estudios Cristalográficos (LEC) in Granada for introducing me to the fancy world of protein crystallization and for teaching me Spanish. I had the most wonderful time in Granada and will always remember our great scientific talks in front of many cups of coffees. I would also like to thank Dr. Andrea Valsesia (JRC), Dr. Jorge Bañuls-Ciscar (JRC), and Dr. Albert Castellví (ALBA synchrotron) for our great collaboration.

A special mention goes to all the students I worked with during these years: Francesca, Valeria, Dario, Yuri, Margherita, and Monia. I wish you the best in life.

I would like to extend my sincere thanks to all my office mates: Daniele, Jagadish, Molla, Francesca, and Claudia at Poli, Giacomino at JRC, Raquel and Joaquim at LEC. I had so much fun with all of you! We shared so many moments together, and we were always there for each other in good and bad times. Just to mention a few: the nights spent at Poli for collecting data, the "tisana" moments in the late afternoon, and the deep philosophical talks.

Even if Ph.D. can sometimes be very harsh and immersive, the years spent at Poli also gave me the privilege to meet true friends and enjoy many breaks together. Thank you Marco Sangermano, Luigi, Andrea, Luisa, Cata, and all the "sushi group" for sharing with me the adventure at Poli. The Japanese cuisine has no secrets for us anymore, and I am confident that many other dinners will have to come.

My deepest gratitude goes to my best friends Alice, Jessica, Melodj, Elisa, and Alejandro for their unwavering support and believing in me. We all have such different lives, but friendship is stronger than distance, age, or schedules.

Eventually, family. Thank you Alessandro for being my best (boy)friend and for the craziest year ever. Thanks to “zio” Piotr, for your wise advice and for being a guide for me. Thanks to my Mum, for the unique connection we have. Thanks to my Dad, I know you are proud of me up there.

I made your motto mine: “*Per aspera ad astra*”.

Contents

List of Tables

List of Figures

Chapter 1

Introduction to surface-induced crystallization of pharmaceuticals

1.1 Overview on pharmaceutical crystallization

The pharmaceutical industry strongly relies on crystallization processes for the manufacturing of active pharmaceutical ingredients (APIs). Its widespread occurrence in the field is justified by its application as a separation and purification step for the isolation of target intermediates or stereoisomers and as a final step for the industrial production of pharmaceuticals. The process represents one of the most ancient unit operations in chemical engineering and is largely employed as a liquid-solid separation technique. The avoidance of high temperatures and the high efficiency represent two of the most outstanding hallmarks of crystallization (Chen et al., 2011; Myerson, 2002), which make it suitable for the production of chemicals from the small to the massive scale. Moreover, this process has been applied to a variety of products ranging from low molecular weight compounds, such as small molecule drugs and organics, to more complex constructs, such as proteins or viruses.

From the early reports on the extraction of crystal salts from seawater and brines found in Egyptian and Latin texts (Schoen et al., 1956) to the most recent technological advancements in pharmaceutics, photonics, catalysis, etc., the intimate nature of crystallization still remains unknown. Countless studies have contributed in looking beyond the Maya's veil wrapping crystallization, but a comprehensive and mechanistic understanding of the rules governing the appearance of crystals is still missing.

Despite being a robust and reliable process, crystallization has to be carefully designed from lab-scale to industrial manufacturing since it is extremely sensitive to process conditions. Minimal variations in temperature, pH, level of supersaturation, stirring, and unexpected contamination or vibrations may influence the process and compromise the quality of the end product (Myerson, 2002). The issue becomes particularly relevant in the pharmaceutical field, where drug purity and particle size distribution must meet stringent requirements imposed by regulatory agencies before they can be commercialized. In addition, different quality attributes of the crystallized product would in turn affect downstream procedures, including filtration, milling and drying (Chen et al., 2011). In this

scenario, among the main concerns of the pharmaceutical industry, one can find the formation of fines, the appearance of uncontrolled crystal morphologies, and the instability of the obtained crystalline form. To solve such issues, the rigorous control of the crystallization process is vital and can be achieved by implementing two simultaneous strategies. From the production point of view, technologies for *in situ* real-time monitoring of solution concentration and crystal features coupled to automatic control systems guarantee the precise tuning of crystal form and size distribution of crystalline slurries (Bakar et al., 2009; Fujiwara et al., 2005; Nagy & Braatz, 2012). From the R&D point of view, advanced methodologies have to be designed in order to impose specific crystallization pathways, perform screening of polymorphism, and optimize the process. The employment of engineered heteronucleants with *ad hoc* designed surface properties represents one of the most promising and studied techniques to achieve such a goal (Artusio & Pisano, 2018). Crystallization may be forced towards new routes by simply tuning the surface attributes of heteronucleants without altering process conditions.

1.2 Fundamentals of crystallization

Crystallization is defined as the phase change from the disordered state typical of a solution, liquid or gas to a crystalline state. The product displays a long-range ordered structure which builds up a lattice thanks to the regular repetition of a fundamental structure, i.e., the unit cell, over a tridimensional (3D) space.

Every crystallization process first enters the nucleation stage, followed by crystal growth, thanks to the establishment of an external driving force. For example, when the process is carried out in solution, supersaturation is required to create a non-equilibrium condition that evolves to lower the supersaturation and reach equilibrium by producing crystalline material. In a liquid environment, despite an overall constant solute concentration, local fluctuations may occur and promote the aggregation of molecules into clusters. Such clusters can either dissolve or grow up to reach a critical size and become nuclei. Then, the crystal growth occurs. Growth is a complex phenomenon, especially for biological molecules, as it involves the diffusion of molecules within the solution and their incorporation into the crystal lattice thanks to superficial diffusion and interaction with steps or kinks on the growing cluster. At this stage, nucleation and crystal growth compete for solute molecules, and the ratio between their rates determines the final dimensional distribution of crystals (Myerson, 2002; Rodríguez-Hornedo & Murphy, 1999).

In the following subsections, the peculiarities of homogeneous and heterogeneous nucleation and the establishment of supersaturation conditions will be discussed.

1.2.1 Homogeneous vs. heterogeneous nucleation

A nucleus represents the minimal quantity of a new phase which is able to exist stably. According to the mechanism leading to the formation of nuclei, homogeneous or heterogeneous nucleation can be distinguished. The former occurs when Brownian motion leads to molecular clustering and ordering in the bulk of a system. The latter requires a foreign surface that lowers the energetical penalty of forming nuclei.

Nucleation is an intrinsically probabilistic phenomenon and has been modelled as a one-step process according to the classical nucleation theory (CNT). According to CNT, unstable molecular clusters are continuously formed and dissolved thanks to thermal fluctuations as a random process. An energetic barrier is associated to nucleation, and the interplay between volume and surface contributions determines the free energy required for forming a nucleus, ΔG:

$$\Delta G = \Delta G_v + \Delta G_s = v\Delta g_v + s\Delta g_s \quad (1)$$

where ΔG_v is the negative and favorable volume contribution associated to the formation of bulk material and ΔG_s is the positive and adverse surface term linked to the creation of the new solid-liquid interface. v and s represent the volume and the superficial area of the cluster, respectively. If an aggregate crosses a threshold size after subsequent molecular additions, the demand for free energy due to the creation of a new interface is compensated by the energy gain of creating new bulk material. Nuclei are formed and can undergo growth.

More recently, the idea of nucleation being a two-step process has gained increasing interest. The modelling of homogeneous nucleation of globular proteins pointed out that, around a critical temperature, critical nuclei were formed not from a crystalline embryo but rather came from the structural re-arrangement of liquid-like droplets (Ten Wolde & Frenkel, 1997). Thus, two-step nucleation foresees the preliminary formation of a dense, disordered, solute-rich liquid phase thanks to density fluctuations. Then, the molecular re-orientation of metastable clusters is achieved by structure fluctuations (Myerson & Trout, 2013; Vorontsova et al., 2015; Wallace et al., 2013), as highlighted in Fig. 1. According to this theory, two energy barriers have to be crossed to get a crystalline nucleus (Erdemir et al., 2009; Vekilov, 2010).

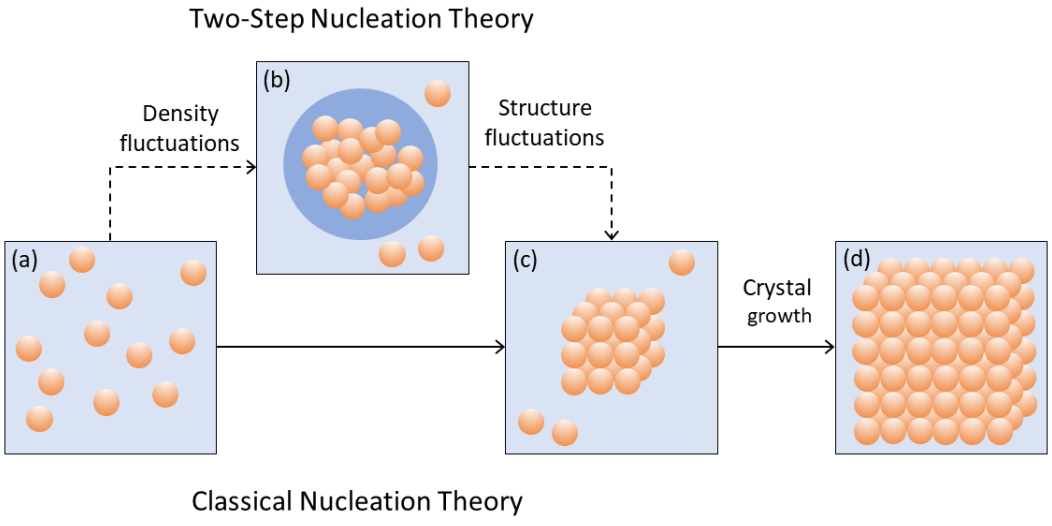

Figure 1 Comparison between one-step CNT and two-step nucleation theories. The picture was taken from (Artusio & Pisano, 2018) with modification.

Conversely, heterogeneous nucleation occurs on a foreign surface that can be intentionally added to the system, as engineered heteronucleants or seeds, or can be adventitiously present in solution, as impurities and particles, or even be part of the

crystallization equipment, such as baffles, stirrers, and the vessel walls. Phase boundaries lower the energetical demand for nucleation thanks to their beneficial action on the surface term of Eq. 1. Nuclei can thus be formed at lower supersaturation compared to homogeneous nucleation, as less driving force is required. In addition, heterogeneous nucleation foresees a narrower metastable zone compared to homogeneous nucleation, so the same nucleation rate can be achieved with lower supersaturation values. Lower supersaturations, in turn, promote the formation of larger and higher quality crystals since the excessive formation of nuclei and rapid growth are both hindered.

A final distinction has to be made between primary and secondary nucleation, the former developing without pre-existing crystals and the latter being promoted by the detachment of seed particles from previous crystals. In the present thesis, primary nucleation will only be addressed.

1.2.2 Supersaturation conditions

Supersaturation represents the driving force of crystallization in solution and governs the kinetics of the process. Higher supersaturation promotes faster nucleation as the logarithm of supersaturation is inversely proportional to the number of solute molecules needed to form a critical nucleus, as stated by CNT.

Change in temperature or pH, addition of solute antisolvent, solvent removal by evaporation or freezing, addition of indifferent salts or dissolution of metastable solid phases are some examples of different methods for achieving supersaturation (Rodríguez-Hornedo & Murphy, 1999). They all rely on the modification of solution activity and hence solute concentration, in the case of ideal solutions. Since equilibrium is lost, a driving force is obtained.

Supersaturation conditions have to be carefully established when investigating heterogeneous nucleation. Homogeneous nucleation must be hindered but the whole process has to be fast enough to allow the formation of crystals in a decent amount of time (López-Mejías et al., 2013). Various methods for creating supersaturation in presence of heteronucleants have been used in the literature. The choice of the method is generally dictated by the shape of the solubility curves (Reutzel-Edens, 2006). Crystallization by cooling is the most common method to trigger the crystallization of APIs. Supersaturation is achieved by quench cooling ramps followed by isothermal crystallization in static conditions. Surfaces may be vertically inserted or placed at the bottom of the glass vials, or can even cover the vial internal walls as polymeric layers (Curcio et al., 2014; Di Profio et al., 2012). Supersaturation may also be achieved by means of progressive solvent evaporation at room temperature or in heated systems completed with heteronucleants (Price et al., 2005). A similar approach based on slow equilibration thanks to solvent removal is also commonly used to crystallize proteins (Chayen & Saridakis, 2008). Less common techniques to study surface-induced crystallization involve vapor phase deposition. The API is sublimated from its powder and deposited on the heteronucleants inside a sealed chamber directly from the vapor (Lopez-Mejías, 2011).

1.3 Surface-induced crystallization

Nucleation is a stochastic phenomenon, and its aleatory nature complicates the gain of a mechanistic understanding of the process. Indeed, nucleation represents the key step of crystallization from many points of view. Nucleation is considered as the rate-limiting step of the whole process since the formation of nuclei is much slower than growth (Oxtoby, 1998). Then, it determines the properties of the final crystals, such as their form and size. Therefore, trying to control the nucleation step is fundamental to the outcome of crystallization in terms of product quality attributes (Vekilov, 2010a). The presence of nucleation sites on surfaces makes them active towards nucleation, thanks to the lowering of the energetical barrier and the shortening of the time required to form nuclei. Heterogeneous nucleation can be exploited as a tool to manipulate the crystallization process, provided that surfaces with precise and controlled characteristics are synthesized. This strategy has been reported for many research fields, including the synthesis of polymeric materials with defined properties (Li & Yan, 2011), the study of mineralization of calcium carbonate (Naka & Chujo, 2001), the controlled crystallization from vapors (Campbell et al., 2017; Holbrough et al., 2012), and the crystallization of pharmaceuticals (Artusio & Pisano, 2018), which is the aim of the present thesis. In the following sections, the main advantages and disadvantages of the technique, and the investigated aspects of crystallization will be discussed.

1.3.1 Advantages and drawbacks

The hallmark of surface-induced crystallization, and its main advantage, is the possibility to force crystallization towards various crystal sizes, shapes and forms, and to tune nucleation kinetics without altering the process conditions. The mere modification of surface features is enough for modifying the conventional crystallization pathway. In this way, different crystallization outcomes can be studied under exactly the same operating conditions, thus excluding secondary effects. In addition, as many studies focused on boosting the nucleation step, the crystallization time can be significantly shortened. As nucleation is the most time-consuming step of the process, advantages in terms of time-optimization and development of new finished pharmaceutical products (FPPs) can be obtained. Moreover, surface-induced crystallization supports the screening, isolation and discovery of new polymorphs. Another advantage is its ability in inducing nucleation at low supersaturation, making the technique interesting for highly expensive solutes, such as biological macromolecules.

Nevertheless, the technique presents some limitations in terms of implementation of experiments. The design of high quality heteronucleants, both as regards their synthesis and final properties, is vital and can be a long, expensive, and tedious process. In addition, the number of trials necessary to build robust statistics and identify the optimal surface-solute matching is noteworthy because of the stochastic nature of nucleation.

Overall, surface-induced crystallization has the potential to be applied at industrial scale for processes involving both small molecules and biopharmaceuticals. The technique can accelerate kinetics and guarantee the selection of a target crystal form, ensuring precise control of physico-chemical properties of the crystalline product. As far as biopharmaceutical manufacturing is considered, this technology might be regarded as an alternative to expensive chromatographic separation and purification processes. If properly

implemented, purification, stabilization, and concentration of a target protein could be achieved with a single unit operation, reducing the number of required downstream corrective actions. However, nowadays amorphous nucleation-active surfaces have not been applied to industrial processes yet. Much effort is still required to overcome a series of technological obstacles, such as the difficult inhibition of homogeneous and secondary nucleation. A critical point is represented by the scale up of surfaces and how they can be coupled to the manufacturing process. Nevertheless, small-scale studies using polymeric particles acting as heteronucleants and as excipients performed inside mixed-suspension mixed-product removal (MSMPR) crystallizers are promising. Recently, the crystallization of acetaminophen on porous poly(vinyl alcohol) (PVA) particles was successfully applied as a process intensification technology (PIT) in the framework of integrated continuous manufacturing (ICM) process, starting from the synthesis of APIs and leading to a stream of dried composite API-polymer particles that can easily be tableted (Testa et al., 2021). Surface-induced crystallization can also be potentially extended to other research fields, such as environmental and energetic applications, prevention of scaling, and water softening (Shah et al., 2015).

1.3.2 Interactions between surface and solute

Nucleation can be influenced by the chemical and morphological features of heteronucleants, which generally act in a synergistic way (Shah et al., 2015). Their deconvolution is rather difficult and typically one out of the two contributions is considered as dominant. As an alternative approach, their combination has also been studied to achieve optimized performances. An overview of the most common heteronucleants, as well as the model APIs and proteins investigated on the corresponding surface, is given in Tab. 1.

As far as surface chemistry is concerned, advantageous molecular interactions between the superficial groups and the solute functional groups can increase the local solute concentration next to the heteronucleant. Molecular recognition events may also promote the ordered arrangement of molecules. In both cases, non-specific adsorption, hydrogen or π-π bonds facilitate nucleation (Diao et al., 2011a; Lopez-Mejías et al., 2011; Weissbuch et al., 1991). Non-specific adsorption simply contributes to the decrease in surface free energy penalty, whereas more specific interactions such as hydrogen bonding can also induce oriented growth (Stojaković et al., 2017). Also, when charged surfaces are employed, electrostatic interactions can attract or repulse charged species. Even local charges can affect the nucleation pathway, especially for complex macromolecules (Fermani et al., 2001). A recent effort in synthesizing polymeric surfaces with tunable chemistry, but unmodified surface area and morphology, to isolate the role of functional groups from topographic effects has been reported. Substitution of chloromethyl groups of Merrifield Resin with several functionalized phenols enabled the synthesis of a set of substrates with identical microstructure but different surface chemistry (Frank & Matzger, 2017).

As far as morphological features are concerned, nano-featured surfaces have been proposed as heteronucleants as they are able to act on nucleation because of the coherency in length-scale between surface irregularities and molecular clustering. Surface topography and geometry play a key role since confinement effects and angular matching between surface features and growing lattice facilitate nucleation (Diao et al., 2011a; Sear, 2011). Also, the shape of the pores influences nucleation, since faster nucleation rate was obtained

Table 1 Overview of the heteronucleant systems, model APIs, and model proteins employed to study the surface-induced crystallization.

Heteronucleant	API	Reference	Protein	Reference
Functionalized glass	Carbamazepine	Parambil et al., 2014	Ferritin Thaumatin	Liu et al., 2007 Tsekova et al., 1999
Langmuir-Blodgett films	-	-	Human protein kinase CK2α Cytochrome P450scc	Pechkova and Nicolini, 2002
Laser-etched glass	Aspirin	Nordquist et al., 2017	Thaumatin Trypsin	Nordquist et al., 2017
Mica	-	-	Concanavalin A Lysozyme Thaumatin	Falini et al., 2002
Minerals	-	-	Canavalin Catalase Lysozyme	McPherson & Shlichta, 1988
Nanoporous glass	Acetaminophen	Beiner et al, 2007 Rengarajan et al., 2007 Sonnenberger et al., 2016	Catalase Concanavalin A Ferritin HSA Lysozyme Trypsin	Chayen et al., 2006 Falini et al., 2002 Shah et al., 2012a,b
Patterned films, Microgels Molecularly imprinted polymers (MIPs)	Acetaminophen Aspirin Carbamazepine Indomethacin Mefenamic acid ROY	Diao et al., 2011a, b Diao et al., 2012b Ha et al., 2004 López-Mejías et al., 2013 Stojaković et al., 2017 Tan et al.., 2015	Lysozyme Trypsin Catalase Haemoglobin	Saridakis et al., 2011
Polymer films	Acetaminophen Aspirin Carbamazepine Flufenamic acid Glycine Phenobarbital ROY Sulfamethoxazole Tolfenamic acid	Curcio et al., 2014 Diao et al., 2011c Diao et al., 2012a Di Profio et al., 2012 Lang et al., 2002 López-Mejías et al., 2009 López-Mejías et al., 2012 Price et al., 2005 Roy et al., 2016	Catalase Concanavalin A Glucose isomerase Lysozyme Xylanase	Ghatak and Ghatak, 2013
Self-assembled monolayers (SAMs)	Glycine	Kim et al., 2009 Lee et al., 2005	Catalase Haemoglobin Lysozyme Thaumatin	Ji et al., 2000 Pham et al., 2004 Tsekova et al., 2012
Silica nanoparticles on glass	Acetaminophen	Delmas et al., 2013	-	-

by simulating Lennard-Jones molecules in wedged grooves compared to flat surfaces (Page & Sear, 2009). Moreover, if the wedge angle matched an intrinsic angle of the crystal lattice, strain-free growth of nuclei is obtained thanks to the interactions between the groove walls and the cluster. Smaller angles led to incomplete crystallization because additional free energy is required to compensate for the irregular packing. Surface roughness also affects nucleation, mainly because of the change in the surface wetting behavior. Increasing the roughness of hydrophobic polymer films led to reduced nucleation activity towards acetaminophen, aspirin, and glycine. On the other side, hydrophilic polymers with increased roughness enhanced the APIs nucleation because of the reduction in solution contact angle, in agreement with CNT (Di Profio et al., 2012). Also, other alterations of surface morphology have been explored. Nano-wrinkles have been proposed to act as local throughs for concentrating solute molecules (Ghatak & Ghatak, 2013). Lastly, nano-islands with defined chemical composition (Kim et al., 2009) and regular arrays or motifs have been applied to selectively induce nucleation (Nordquist et al., 2017). An overview of the heteronucleants with modified morphology is given in Fig. 2.

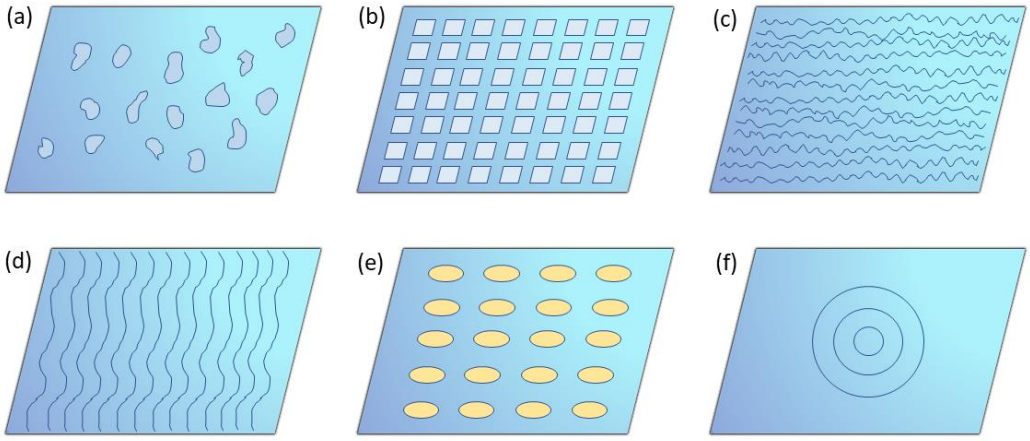

Figure 2 Examples of surface morphologies of heteronucleants: (a) irregular pores, (b) periodic pore array, (c) superficial rugosity, (d) nano-wrinkles, (e) nano-islands, (f) regular geometric pattern. The picture was taken from (Artusio & Pisano, 2018) with modification.

Moreover, the role of solvent in crystallization experiments with heteronucleants has not to be neglected. The ability of a surface in promoting nucleation is not an intrinsic and absolute property but is related to the composition of the liquor. The competitive binding of API and solvent molecules to the surface affects the rate of nucleation. Thus, solute molecules must display a greater affinity toward the surface compared to solvent molecules. For example, it has been demonstrated that competitive solvent binding determines the polymer nucleation activity towards acetaminophen (Frank & Matzger, 2017).

1.4 Investigated crystallization aspects

Several aspects concerning crystallization have to be evaluated to determine the success of a batch for the production of pharmaceuticals and biopharmaceuticals. Polymorphism,

nucleation rate, crystal size and habit are the most studied parameters as regards surface-induced crystallization, as outlined in Fig. 3.

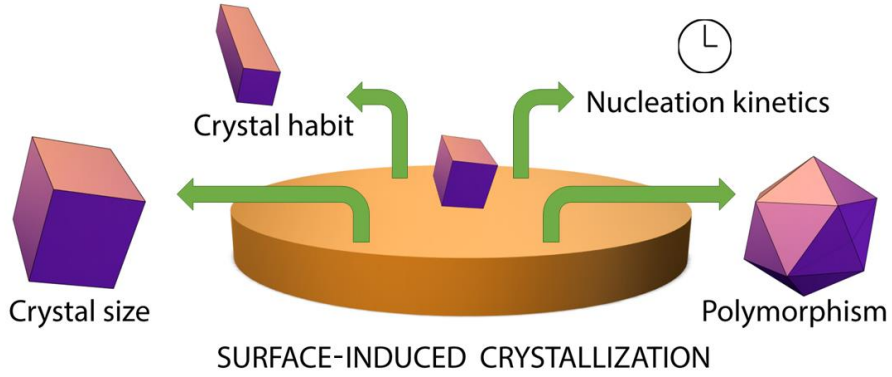

Figure 3 Surface-induced crystallization is a versatile platform for studying many crystallization aspects. The picture was taken from (Artusio & Pisano, 2018) with modification.

1.4.1 Polymorphism

The organization of molecules within a lattice can follow diverse packing arrangements, molecular conformations, and synthon diversities. Polymorphism is responsible for significant changes in the physico-chemical properties of the crystals, such as density, dissolution rate, melting point, color, chemical and physical stability. In the pharmaceutical field, also the amorphous form and the hydrated forms of the same API are commonly referred to as polymorphs.

Solubility and dissolution rates are correlated to the specific crystal form of APIs. The two properties determine the bioavailability of the final dosage form and the drug absorption, and this is why polymorphism is one of the most outstanding concerns of pharmaceutical industry. In addition, different polymorphs display different flowability and compressibility, which affect the tableting process, the drug activity and stability. Generally, the production of the most stable form is demanded, which is also the least soluble one. However, specific cases may require the production of metastable or amorphous forms so as to improve the dissolution of poorly soluble drugs.

The appearance of specific polymorphs is related to their energetic profiles, which in turns dictates their thermodynamic stability. More traditionally, polymorph selection has been achieved by means of seed crystals or soluble additives as salts that can inhibit the growth of undesired phases (Lee et al., 2008; Llinàs & Goodman, 2008). Also, reaction byproducts and impurities (Beckmann et al., 2001; Blagden et al., 1998), excipients (Aaltonen et al., 2009), or different solvents can promote target crystal motifs by specific interactions (Nicholas Blagden & Davey, 2003). However, the use of additives is highly specific and related to a particular solute.

Polymorph screening can be supported by surface-based techniques thanks to their action on nucleation. The crystallization of metastable forms, the selection of a target crystal form, the discovery of new polymorphs, and the shift in thermotropic relationships can be achieved by designing the chemical and topological features of surfaces (Hamilton et al., 2012).

1.4.2 Nucleation rate

The nucleation induction time is defined as the time elapsed from the achievement of the desired supersaturation conditions to the formation of the first stable nuclei in solution. It is a function of the supersaturation level and the temperature of the system. Since the direct detection of crystals is unfeasible in most experimental set-ups, nucleation induction time can be considered as the detectable induction time, which is the time elapsed from the achievement of supersaturation to the appearance of detectable crystals (Kashchiev, 2000). Nucleation rate is a key parameter since it affects the final crystalline product and dictates process time.

1.4.3 Crystal size

The dissolution kinetics of drugs is strongly affected by crystal size. Increased surface/volume ratios enhance the bioavailability of poorly soluble drug crystals and modify powder flowability. Several techniques have been proposed to control crystal size involving supercritical fluids, solvent displacements, and ultrasounds (Bund & Pandit, 2007; Llinàs & Goodman, 2008). Also, post-crystallization processing may be implemented to adjust crystals dimensional distribution, such as micronization or milling, but they can promote modifications in crystal features and contamination (Shekunov & York, 2000). Surface-induced crystallization promotes a control over crystal growth by means of confinement strategies. Macro, micro, or nanoscale crystals can be obtained by controlling the nucleation density and the nucleation kinetics.

1.5 2D heteronucleants

Bidimensional systems have been widely applied to induce nucleation, including amorphous and crystalline surfaces. As regards the latter, ordered molecular interfaces such as minerals, Langmuir monolayers and Langmuir-Blodgett films have been employed to promote heterogeneous nucleation by epitaxy. However, crystalline surfaces display intrinsic limits as regards the adjustment of superficial characteristics. Conversely, amorphous surfaces are being increasingly studied since they can more easily be modified.

1.5.1 Crystalline surfaces

Epitaxy is a commonly used technique to grow crystals based on the deposition of material on surfaces displaying structural periodicity. The ordered array of functional groups of the substrate promotes the ordered organization of solute molecules. The growing lattice can perfectly match the underlying crystal structure, i.e., commensurism, or display some mismatch, i.e., incommensurism.

Early studies on protein crystallization performed on crystalline surfaces are dated 1988. Mineral surfaces were able to induce crystallization at lower supersaturation and in a shorter time thanks to heterogeneous nucleation and epitaxial growth (McPherson & Shlichta, 1988). Epitaxy was also exploited to grow streptavidin crystals from

bidimensional crystals (Hemming et al., 1995) or to template the growth of crystals from Langmuir-Blodgett films composed of the same protein to be crystallized (Pechkova & Nicolini, 2002). The nucleation of glucose isomerase on mica sheets revealed that molecules aligned in an ordered array (Sleutel et al., 2014), and silane-functionalized mica substrates induced lysozyme and concanavalin A crystallization at low protein concentration by adjusting the density of ionizable groups (Falini et al., 2002). Such groups modified the superficial charge density and the extent of electrostatic interactions. Attractive forces promoted high molecular concentration on the surface and nuclei stabilization, whereas repulsive forces might result in the localization of protein molecules into a thin layer above the surface (Tosi et al., 2008).

Epitaxial mechanisms were also exploited to organize molecular films (Hooks et al., 2001), discover new drug polymorphs (Mitchell et al., 2001) or promote the growth of specific crystal forms (Lee et al., 2010; Rodríguez-Hornedo et al., 1992). The nucleation of acetaminophen on α-lactose monohydrate and D-mannitol crystals highlighted the importance of hydrogen bonding in determining nucleation kinetics (Chadwick et al., 2012). However, in the perspective of gaining mechanistic insight in the nucleation phenomena, epitaxial growth would complicate the study of the interrelationship between solute and heteronucleants since an additional mechanism has to be considered. Since it has been demonstrated that functionality, rather than lattice matching, was most effective towards nucleation (Chadwick et al., 2012), amorphous substrates were selected in the present thesis.

1.5.2 Amorphous surfaces

From the pioneering work of Lang et al. (2002) reporting the ability of polymers to selectively induce the nucleation of various crystal forms of acetaminophen and carbamazepine, many technological solutions have been implemented to study the role of surfaces in crystallization. A mandatory requirement for the application of surfaces as heteronucleants regards their insolubility in the crystallization medium. Therefore, to guarantee surface stability, amorphous substrates are generally prepared by polymerization of monomers or are built from pre-formed polymers. Nano-structuration and functionalization of silicon-based materials have also been applied.

1.5.2.1 Polymeric films

Cross-linked polymer films can direct the polymorph pathway of drugs, such as sulfamethoxazole and carbamazepine, keeping solvent and temperature constant (Price et al., 2005). The use of polymers as polymorph selectors is effective not only for cooling crystallization but also for crystallization from melts, as demonstrated by the stabilization of α or δ forms of supercooled indomethacin by acrylates (McKellar et al., 2012). The polymorph selectivity of polymeric films was attributed to the possibility of playing with the hydrogen bonding interactions between surface groups and solutes, as demonstrated by sum frequency generation vibrational spectroscopy (McClelland et al., 2011). Moreover, copolymer films were demonstrated to be a valuable tool for the discovery of new polymorphs of drugs such as tolfenamic acid (López-Mejías et al., 2009), flufenamic acid (López-Mejías et al., 2012), and phenobarbital (Liu & Miao, 2018).

UV-photosensitive monomers were polymerized to obtain films carrying functional groups and pores, which had an impact on the aspirin crystal face nucleating first (Diao et al., 2011c). Also, poly(ethylene glycol) diacrylate (PEGDA) films promoted the alignment of drug molecules along preferred orientations thanks to a chemical templating effect (Diao et al., 2012b). Poly(4-acryloylmorpholine) films led to threefold enhancements of nucleation kinetics of aspirin thanks to favorable hydrogen bonding, which increased up to 78-fold faster kinetics compared to bulk crystallization when 50 nm pores disturbed the superficial morphology of the film. The increased performance of the porous structure was attributed to the higher interfacial area available for nucleus formation (Diao et al., 2011c).

The ability of some soluble additives to selectively interact with crystal faces for inhibiting their growth has been recently exploited to obtain an opposite outcome. Additives were incorporated into insoluble polymeric matrixes to induce nucleation thanks to the strong interaction between additive and solute. N-hydroxyphenyl methacrylamide and p-acetamidostyrene additives, which mimic the chemical structure of acetaminophen, were able to promote the appearance of the API monoclinic form within about 2 hours instead of several days (Pfund et al., 2015).

Polymer films were also directly prepared on the internal walls of crystallizers by evaporating pre-formed polymeric solutions. Crystallization of the weak acid acetaminophen was favored by films with strong Lewis acid-base character as ethylene/acrylic acid copolymers and polyimide (Curcio et al., 2014). Polymeric films were also employed to accelerate the nucleation step of proteins (Fermani et al., 2001; Grzesiak & Matzger, 2008) and to elucidate the role of the solvent in API crystallization. Thin Nylon films prepared by spin-coating revealed that protic solvents promoted the growth of orthorhombic form of acetaminophen, whereas aprotic solvents nucleated the monoclinic form (Lopez-Mejías et al., 2011).

1.5.2.2 Nano-structured surfaces

Surfaces carrying monodisperse and reproducible topographic features were also tested as heteronucleants. Morphologically controlled surfaces carrying cylindrical pores were prepared by selectively etching one block of aligned copolymers (Olson et al., 2008; Rzayev & Hillmyer, 2005; Zalusky et al., 2002). Patterned polyacrylic acid films prepared by nanoparticle imprint lithography ensured the precise repetition of regular arrays of shaped pores between 15 and 300 nm. Aspirin nucleation kinetics was inhibited by spherical pores, whereas hexagonal and square pores induced nucleation at their corners (Diao et al., 2011a). A similar approach was used to prepare mesh-like structures made of hydroxylpropylmethyl cellulose, 2-hydroxyethyl cellulose and PVA by solution casting over silicon masters. Overall, shaped pores were found to have an impact both on nucleation kinetics and polymorphism. The former was accelerated to the greatest extent when wedged pores matching the angles between major crystal faces were used. The latter was studied considering that different polymorphs have different intrinsic angles. The crystalline angles and the API chemistry were employed for the rational design of pores and chemistry of heteronucleants, respectively (López-Mejías et al., 2013; Stojaković et al., 2017; Tan et al., 2015). A similar approach has been also reported for nucleating proteins as lysozyme, which indeed showed a preferential growth from the corners (Salazar-Kuri et al., 2015).

1.5.2.3 Functionalized Si-based materials

The physico-chemical properties of glass can be modified by silanes and acrylates to stabilize metastable forms of drugs (Liu et al., 2007; Parambil et al., 2014). The selective functionalization of a silicon substrate with 3-aminopropyltriethoxysilane and octadecyltrichlorosilane led to hydrophilic islands surrounded by hydrophobic regions (Kim et al., 2009). The islands were active in inducing the nucleation of nano-sized organic crystals. Self-assembled monolayers (SAMs) immobilized on glass also promoted the growth of large protein crystals by inhibiting nucleation in favor of growth (Ji et al., 2000; Pham et al., 2004). Chemically modified glasses have been applied to the crystallization of various proteins for controlling crystal size and density, but direct correlation with surface properties remained obscure (Tsekova et al., 2012).

Different site arrays were also patterned on soda-lime glass thanks to lasers to create nucleation active sites. Alternatively, microlitography helped in the preparation of p- and n-doping on silicon wafers with tunable charge for the heterogeneous nucleation of proteins (Sanjoh, 2001). Glass coverslips have also been functionalized with silica nanoparticles to couple surface topography and chemistry effects at low supersaturations. Acetaminophen polymorphs were selected by functional groups and nanoconfinement synergies, which could stabilize high energy phases (Delmas et al., 2013).

Wrinkled polydimethylsiloxane (PDMS) films promoted the crystallization of proteins having radius of gyration comparable to the wrinkle curvature (Ghatak & Ghatak, 2013). Monte Carlo simulations of sinusoidal surfaces pointed out that nucleation enhancement was attributable to the increased protein concentration at the troughs, whereas low curvature radii hindered nuclei formation (Bommineni & Punnathanam, 2016). Furthermore, PDMS substrates with controlled topography and charge allowed for precipitant-free protein crystallization thanks to surface potential gradients (Ghatak & Ghatak, 2017). Lastly, the physical modification by laser etching of glass surfaces has been recently proposed to speed up the nucleation kinetics of aspirin (Nordquist et al., 2017).

1.6 3D heteronucleants

In addition to bidimensional systems, also tridimensional heteronucleants have been proposed to study the crystallization behavior of pharmaceuticals and biopharmaceuticals. Polymeric beads or mesoporous silica monoliths can be dispersed in the crystallization medium. Alternatively, the crystallization medium can be gelled to establish diffusive conditions for the growth of crystals, as detailed in Chap. 10.

1.6.1 Porous polymeric materials and gels

Polymeric beads carrying nm-scale pores were employed for studying nucleation and polymorph selectivity thanks to their ability to locally confine clusters and promote molecular aggregation. For example, porous poly(cyclohexylethylene) monoliths stabilized different API polymorphs (Ha et al., 2004). It was found that if the pore size matched a critical nucleus size, the confinement of API molecules to the nanoscopic chambers could favor the corresponding polymorph (Hamilton et al., 2012).

Gels were also studied as supports for crystallization thanks to the possibilities offered by a softer confinement, compared to hard mesoporous matrices. PEGDA cube-like microgels induced the formation of less stable form II of carbamazepine. Mesh size, nucleation kinetics, and polymorphism were found to be strongly correlated. An optimal mesh size of 15 Å was selected by varying the molecular weight of the monomers, guaranteeing 10-fold reduction in induction nucleation time. Smaller mesh sizes, i.e., 7 Å, inhibited the formation of sufficiently large clusters because of solute reduced mobility and excessive interaction with the polymer. Larger sizes, i.e., 20 Å, could not effectively promote nucleation because of insufficient interactions. The tuning of mesh size and exposed chemistry provide an ideal environment for the soft confinement of crystallization (Diao et al., 2011b; Diao et al., 2012a).

Hydrogels were also employed as nucleating substrates for proteins using the imprinting technique to produce molecularly imprinted polymers (MIPs). The presence of bovine hemoglobin during the polymerization of acrylamide hydrogels templated the formation of cavities by physical entrapment and successive removal of the protein. The memory effect resulted in complementary shape, size, and charge of the grooves (Hawkins et al., 2005; Hawkins et al., 2006). A similar approach was used to grow large diffraction-quality crystals with the help of MIPs. The experiments evidenced a broad applicability of MIPs: substrates imprinted with lysozyme were found to induce crystallization of other proteins having similar molecular weights (Saridakis et al., 2011).

1.6.2 Porous Si-based materials

Silicon with pore size ranging 5-10 nm was obtained via electrochemical routes and served for the immobilization of solutes. The growth of lysozyme, trypsin, catalase, and thaumatin within the metastable zone was promoted by porous silicon thanks to the creation of a local higher supersaturation, which has also been confirmed by modeling of the phenomena on fractal substrates (Chayen et al., 2001; Stolyarova et al., 2006).

The effect of sponge-like nanostructures on crystallization was also studied by employing the commercially available controlled porous glass (CPG) with pore size < 100 nm. Nanoporous glasses stabilized crystal forms and promoted longer life-time of amorphous acetaminophen, which could not be obtained by bulk crystallization (Rengarajan et al., 2007, 2008). The polymorph selectivity of nanoporous glass was attributed to the crystallization conditions, rather than to direct matching between pore and nucleus size (Beiner et al., 2007). In addition, the presence of a thin nanometric layer of amorphous drug between the CPG walls and crystals was evidenced by spectroscopy studies (Sonnenberger et al., 2016). In a similar fashion, mesoporous bioactive gel-glass (CaO-P_2O_5-SiO_2, "bio-glass", pore size 2-10 nm) was proposed as a universal nucleant for proteins thanks to its pore size heterogeneity (Chayen et al., 2006; Saridakis & Chayen, 2009). The optimal matching between pore and macromolecule diameters could be achieved by dimensional screening and induced the nucleation of proteins with very different molecular weights. In the perspective of identifying a universal nucleant for proteins, also carbon nanotubes dispersed in gelatin were proposed (Asanithi et al., 2009).

As a step further, mesoporous glasses were functionalized with specific groups to elucidate the effect of porosity and chemistry on protein crystallization (Shah et al, 2012a,b). Crystals of target proteins were successfully obtained at very low protein concentrations thanks to tailored attractive electrostatic interactions and pore size matching

the protein radius of gyration, as sketched in Fig. 4. The existing correlation between the pore and the protein diameter was confirmed by increasing the protein radius of gyration and studying the crystallization outcome. Increasing amounts of PEG 4000 were added to lysozyme solutions to increase the protein's hydrodynamic diameter. Protein solutions with 1% and 10% (w/v) PEG preferentially crystallized on nanotemplates having an average pore size of 3.5 and 11 nm, respectively (Shah et al., 2017). Coarse-grained models and molecular dynamics simulations also confirmed the increased protein thermodynamic stability and folding in confined nano-spaces (Zhang & Cheung, 2007).

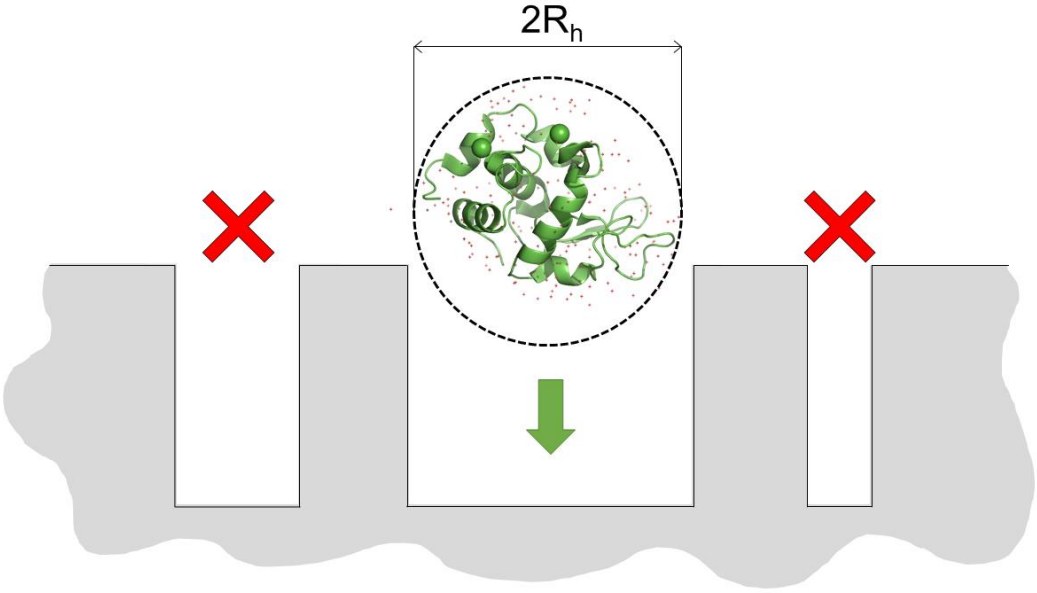

Figure 4 Schematic mechanism of the relationship between protein radius of gyration (R_h) and pore diameter: dimensional matching favors nucleation because of confinement effects. The picture was taken from (Artusio & Pisano, 2018) with modification.

1.7 Motivation of the thesis

The present thesis is devoted to the elucidation of the role of engineered supports in guiding the nucleation step of target molecules. The design of the research work was conceived so as to answer to a series of questions thanks to the collection of experimental evidence. Different research goals were set according to the type of solute to be crystallized, which in turn dictated specific choices in terms of surface design of heteronucleants. Starting from the literature analysis, the following points were identified:

- *Is it possible to physically isolate the effect of surface chemistry from surface morphology when performing heterogeneous nucleation?* Many heteronucleants are characterized by intrinsic roughness or nano-structuration, or scarce attention has been paid to the investigation of surface topography and morphology. The lowering of the energetic penalty required for nucleation results from the competition between surface chemistry and morphology, and the isolation of the two components would help the fundamental understanding of the phenomenon.

- *Are smooth surfaces sufficiently nucleation-active?* The restriction of surface activity towards nucleation to the mere chemistry may result in long nucleation time due to the exclusion of favorable energetic contributions due to surface roughness. If the slowing down of nucleation phenomena is too pronounced, the resulting testing times will not be compatible to empirical studies.

- *What is the main mechanism of interaction governing surface-induced nucleation? How can it be identified?* The action of heteronucleants may be rather chemical, thus involving specific secondary interactions, or physical. The dominant mechanism of interaction has to be identified by selecting specific strategies according to the nature of the target molecule to be crystallized, being it a small molecule or a macromolecule. The understanding of the interactions between surface and solute would clarify their role in governing crystallization.

- *How do surfaces affect small molecule drug and protein crystallization?* The crystallization of small molecule drugs and the crystallization of proteins differ for many aspects. Compared to the former, the latter is affected by the complex nature of the biomacromolecules; protein crystals can be obtained only when additional chemical species, like salts and/or polymers, are added to the system. Thus, it is reasonable to expect that surfaces will perform differently on nucleation in these two cases.

- *Is the action of networks on protein crystallization mainly physical or chemical?* Protein crystallization can be confined inside gelled networks to tailor nucleation phenomena, but the nature of the inducing ability of specific gels is still unclear. Knowledge on the mechanism of nucleation promotion would support rational design of crystallization experiments in gels.

- *Is it possible to fine-tune nucleation to get reproducible and defined crystal populations?* A detailed study on the possibility to control nucleation kinetics and several crystal features, such as size, habit, and form, thanks to the fine-tuning of nucleation step with engineered systems would clarify the potentiality of such a technique.

To try to answer these questions, the research work is divided into three parts: Part I is devoted to the synthesis and characterization of self-assembled monolayers exposing different functional groups, Part II presents the application of monolayers to the batch and thin-film crystallization of a model pharmaceutical compound, Part III extends the application of monolayers to protein crystallization and investigates the use of gels as nucleation promoters for a set of selected proteins.

References

Aaltonen, J., Allesø, M., Mirza, S., Koradia, V., Gordon, K. C., & Rantanen, J. (2009). Solid form screening - A review. *European Journal of Pharmaceutics and Biopharmaceutics*, **71**(1), 23–37.

Ahmad, M., Jones, J. R., & Hench, L. L. (2007). Fabricating sol-gel glass monoliths with controlled nanoporosity. *Biomedical Materials*, **2**(1), 6–10.

Artusio, F., & Pisano, R. (2018). Surface-induced crystallization of pharmaceuticals and biopharmaceuticals: A review. *International Journal of Pharmaceutics*, **547**(1–2), 190–208.

Asanithi, P., Saridakis, E., Govada, L., Jurewicz, I., Brunner, E. W., Ponnusamy, R., Cleaver, J. A. S., Dalton, A. B., Chayen, N. E. & Sear, R. P. (2009). Carbon-nanotube based materials for protein crystallisation. *ACS Applied Materials and Interfaces*, **1**(6), 1203–1210.

Bakar, M. R. A., Nagy, Z. K., Saleemi, A. N., & Rielly, C. D. (2009). The impact of direct nucleation control on crystal size distribution in pharmaceutical crystallization processes. *Crystal Growth and Design*, **9**(3), 1378–1384.

Beckmann, W., Otto, W., & Budde, U. (2001). Crystallisation of the stable polymorph of hydroxytriendione: Seeding process and effects of purity. *Organic Process Research and Development*, **5**(4), 387–392.

Beiner, M., Rengarajan, G. T., Pankaj, S., Enke, D., & Steinhart, M. (2007). Manipulating the crystalline state of pharmaceuticals by nanoconfinement. *Nano Letters*, **7**(5), 1381–1385.

Blagden, N., Davey, R. J., Rowe, R., & Roberts, R. (1998). Disappearing polymorphs and the role of reaction by-products: The case of sulphathiazole. *International Journal of Pharmaceutics*, **172**(1–2), 169–177.

Blagden, Nicholas, & Davey, R. J. (2003). Polymorph Selection: Challenges for the Future? *Crystal Growth and Design*, **3**(6), 873–885.

Bommineni, P. K., & Punnathanam, S. N. (2016). Enhancement of nucleation of protein crystals on nano-wrinkled surfaces. *Faraday Discussions*, **186**(1), 187–197.

Bund, R. K., & Pandit, A. B. (2007). Sonocrystallization: Effect on lactose recovery and crystal habit. *Ultrasonics Sonochemistry*, **14**(2), 143–152.

Campbell, J. M., Meldrum, F. C., & Christenson, H. K. (2017). Observing the formation of ice and organic crystals in active sites. *Proceedings of the National Academy of Sciences of the United States of America*, **114**(5), 810–815.

Chadwick, K., Chen, J., Myerson, A. S., & Trout, B. L. (2012). Toward the rational design of crystalline surfaces for heteroepitaxy: Role of molecular functionality. *Crystal Growth and Design*, **12**(3), 1159–1166.

Chayen, N. E., Saridakis, E., El-Bahar, R., & Nemirovsky, Y. (2001). Porous silicon: An effective nucleation-inducing material for protein crystallization. *Journal of Molecular Biology*, **312**(4), 591–595.

Chayen, Naomi E., & Saridakis, E. (2008). Protein crystallization: From purified protein to diffraction-quality crystal. *Nature Methods*, **5**(2), 147–153.

Chayen, Naomi E., Saridakis, E., & Sear, R. P. (2006). Experiment and theory for heterogeneous nucleation of protein crystals in a porous medium. *Proceedings of the National Academy of Sciences of the United States of America*, **103**(3), 597–601.

Chen, J., Sarma, B., Evans, J. M. B., & Myerson, A. S. (2011). Pharmaceutical crystallization. *Crystal Growth and Design*, **11**(4), 887–895.

Curcio, E., López-Mejías, V., Di Profio, G., Fontananova, E., Drioli, E., Trout, B. L., & Myerson, A. S. (2014). Regulating nucleation kinetics through molecular interactions at the polymer-solute interface. *Crystal Growth and Design*, **14**(2), 678–686.

Damman, P., Dosière, M., Smith, P., & Wittmann, J. C. (1995). Orientation of p-nitrophenol molecules induced by epitaxial crystallization on friction-transferred poly(tetrafluoroethylene) substrates. *Journal of the American Chemical Society*,

117(3), 1117–1120.

Delmas, T., Shah, U. V., Roberts, M. M., Williams, D. R., & Heng, J. Y. Y. (2013). Crystallisation of the orthorhombic form of acetaminophen: Combined effect of surface topography and chemistry. *Powder Technology*, **236**(February), 24–29.

Di Profio, G., Fontananova, E., Curcio, E., & Drioli, E. (2012). From tailored supports to controlled nucleation: Exploring material chemistry, surface nanostructure, and wetting regime effects in heterogeneous nucleation of organic molecules. *Crystal Growth and Design*, **12**(7), 3749–3757.

Diao, Y., Harada, T., Myerson, A. S., Alan Hatton, T., & Trout, B. L. (2011a). The role of nanopore shape in surface-induced crystallization. *Nature Materials*, **10**(11), 867–871.

Diao, Y., Helgeson, M. E., Myerson, A. S., Hatton, T. A., Doyle, P. S., & Trout, B. L. (2011b). Controlled nucleation from solution using polymer microgels. *Journal of the American Chemical Society*, **133**(11), 3756–3759.

Diao, Y., Helgeson, M. E., Siam, Z. A., Doyle, P. S., Myerson, A. S., Hatton, T. A., & Trout, B. L. (2012a). Nucleation under soft confinement: Role of polymer-solute interactions. *Crystal Growth and Design*, **12**(1), 508–517.

Diao, Y., Myerson, A. S., Hatton, T. A., & Trout, B. L. (2011c). Surface design for controlled crystallization: The role of surface chemistry and nanoscale pores in heterogeneous nucleation. *Langmuir*, **27**(9), 5324–5334.

Diao, Y., Whaley, K. E., Helgeson, M. E., Woldeyes, M. A., Doyle, P. S., Myerson, A. S., Hatton, T. A., Trout, B. L. (2012b). Gel-induced selective crystallization of polymorphs. *Journal of the American Chemical Society*, **134**(1), 673–684.

Erdemir, D., Lee, A. Y., & Myerson, A. S. (2009). Nucleation of crystals from solution: Classical and two-step models. *Accounts of Chemical Research*, **42**(5), 621–629.

Falini, G., Fermani, S., Conforti, G., & Ripamonti, A. (2002). Protein crystallisation on chemically modified mica surfaces. *Acta Crystallographica Section D: Biological Crystallography*, **58**(10 II), 1649–1652.

Fermani, S., Falini, G., Minnucci, M., & Ripamonti, A. (2001). Protein crystallization on polymeric film surfaces. *Journal of Crystal Growth*, **224**(3–4), 327–334.

Frank, D. S., & Matzger, A. J. (2017). Influence of chemical functionality on the rate of polymer-induced heteronucleation. *Crystal Growth and Design*, **17**(8), 4056–4059.

Fujiwara, M., Nagy, Z. K., Chew, J. W., & Braatz, R. D. (2005). First-principles and direct design approaches for the control of pharmaceutical crystallization. *Journal of Process Control*, **15**(5), 493–504.

Ghatak, A. S., Rawal, G., & Ghatak, A. (2017). Precipitant-free crystallization of protein molecules induced by incision on substrate. *Crystals*, **7**(8), 245.

Grzesiak, A. L., & Matzger, A. J. (2008). Selection of protein crystal forms facilitated by polymer-induced heteronucleation. *Crystal Growth and Design*, **8**(1), 347–350.

Ha, J. M., Wolf, J. H., Hillmyer, M. A., & Ward, M. D. (2004). Polymorph selectivity under nanoscopic confinement. *Journal of the American Chemical Society*, **126**(11), 3382–3383.

Hamilton, B. D., Ha, J. M., Hillmyer, M. A., & Ward, M. D. (2012). Manipulating crystal growth and polymorphism by confinement in nanoscale crystallization chambers. *Accounts of Chemical Research*, **45**(3), 414–423.

Hawkins, D. M., Stevenson, D., & Reddy, S. M. (2005). Investigation of protein imprinting in hydrogel-based molecularly imprinted polymers (HydroMIPs). *Analytica Chimica Acta*, ***542***(1), 61–65.

Hawkins, D. M., Trache, A., Ellis, E. A., Stevenson, D., Holzenburg, A., Meininger, G. A., & Reddy, S. M. (2006). Quantification and confocal imaging of protein specific molecularly imprinted polymers. *Biomacromolecules*, **7**(9), 2560–2564.

Hemming, S. A., Bochkarev, A., Darst, S. A., Kornberg, R. D., Ala, P., Yang, D. S. C., & Edwards, A. M. (1995). The mechanism of protein crystal growth from lipid layers. *Journal of Molecular Biology*, **246**(2), 308–316.

Holbrough, J. L., Campbell, J. M., Meldrum, F. C., & Christenson, H. K. (2012).

Topographical control of crystal nucleation. *Crystal Growth and Design*, **12**(2), 750–755.

Hooks, B. D. E., Fritz, T., & Ward, M. D. (2001). Epitaxy and molecular organization on solid substrates. *Advanced Materials*, **13**(4), 227–241.

Ilevbare, G. A., Liu, H., Edgar, K. J., & Taylor, L. S. (2012). Understanding polymer properties important for crystal growth inhibition-impact of chemically diverse polymers on solution crystal growth of ritonavir. *Crystal Growth and Design*, **12**(6), 3133–3143.

Ji, D., Arnold, C. M., Graupe, M., Beadle, E., Dunn, R. V., Phan, M. N., Villazana, Ramon J., Benson, R., Colorado, R., Randall Lee, T., & Friedman, J. M. (2000). Improved protein crystallization by vapor diffusion from drops in contact with transparent, self-assembled monolayers on gold-coated glass coverslips. *Journal of Crystal Growth*, **218**(2), 390–398.

Kashchiev, D. (2000). Nucleation: Basic Theory with Applications. Oxford, Boston: Butterworth-Heinemann.

Kim, K., Lee, I. S., Centrone, A., Hatton, T. A., & Myerson, A. S. (2009). Formation of nanosized organic molecular crystals on engineered surfaces. *Journal of the American Chemical Society*, **131**(51), 18212–18213.

Lang, M., Grzesiak, A. L., & Matzger, A. J. (2002). The use of polymer heteronuclei for crystalline polymorph selection. *Journal of the American Chemical Society*, **124**(50), 14834–14835.

Lee, E. H., Boerrigter, S. X. M., Rumondor, A. C. F., Chamarthy, S. P., & Byrn, S. R. (2008). Formation and solid-state characterization of a salt-induced metastable polymorph of flufenamic acid. *Crystal Growth and Design*, **8**(1), 91–97.

Lee, E. H., Boerrigter, S. X. M., & Byrn, S. R. (2010). Epitaxy of a structurally related compound on the (100) faces of flufenamic acid form i and iii single crystals. *Crystal Growth and Design*, **10**(2), 518–527.

Li, H., & Yan, S. (2011). Surface-induced polymer crystallization and the resultant structures and morphologies. *Macromolecules*, **44**(3), 417–428.

Liu, D., & Miao, Q. (2018). Recent progress in interface engineering of organic thin film transistors with self-assembled monolayers. *Materials Chemistry Frontiers*, **2**(1), 11–21.

Liu, Y. X., Wang, X. J., Lu, J., & Ching, C. B. (2007). Influence of the roughness, topography, and physicochemical properties of chemically modified surfaces on the heterogeneous nucleation of protein crystals. *Journal of Physical Chemistry B*, **111**(50), 13971–13978.

Llinàs, A., & Goodman, J. M. (2008). Polymorph control: past, present and future. *Drug Discovery Today*, **13**(5–6), 198–210.

López-Mejías, V., Kampf, J. W., & Matzger, A. J. (2009). Polymer-induced heteronucleation of tolfenamic acid: Structural investigation of a pentamorph. *Journal of the American Chemical Society*, **131**(13), 4554–4555.

Lopez-Mejías, V., Knight, J. L., Brooks, C. L., & Matzger, A. J. (2011). On the mechanism of crystalline polymorph selection by polymer heteronuclei. *Langmuir*, **27**(12), 7575–7579.

López-Mejías, V., Kampf, J. W., & Matzger, A. J. (2012). Nonamorphism in flufenamic acid and a new record for a polymorphic compound with solved structures. *Journal of the American Chemical Society*, **134**(24), 9872–9875.

López-Mejías, V., Myerson, A. S., & Trout, B. L. (2013). Geometric design of heterogeneous nucleation sites on biocompatible surfaces. *Crystal Growth and Design*, **13**(8), 3835–3841.

McClelland, A. A., López-Mejías, V., Matzger, A. J., & Chen, Z. (2011). Peering at a buried polymer-crystal interface: Probing heterogeneous nucleation by sum frequency generation vibrational spectroscopy. *Langmuir*, **27**(6), 2162–2165.

McKellar, S. C., Urquhart, A. J., Lamprou, D. A., & Florence, A. J. (2012). Polymer templating of supercooled indomethacin for polymorph selection. *ACS*

Combinatorial Science, **14**(3), 155–159.
McPherson, A., & Shlichta, P. (1988). The use of heterogeneous and epitaxial nucleants to promote the growth of protein crystals. *Journal of Crystal Growth*, **90**(1–3), 47–50.
Mitchell, C. A., Yu, L., & Ward, M. D. (2001). Selective nucleation and discovery of organic polymorphs through epitaxy with single crystal substrates. *Journal of the American Chemical Society*, **123**(44), 10830–10839.
Myerson, A. S. (2002). Handbook of Industrial Crystallization (2nd ed.). Woburn: Butterworth-Heinemann.
Myerson, A. S., & Trout, B. L. (2013). Nucleation from solution. *Science*, **341**(6148), 855–856.
Nagy, Z. K., & Braatz, R. D. (2012). Advances and new directions in crystallization control. *Annual Review of Chemical and Biomolecular Engineering*, **3**(1), 55–75.
Naka, K., & Chujo, Y. (2001). Control of crystal nucleation and growth of calcium carbonate by synthetic substrates. *Chemistry of Materials*, **13**(10), 3245–3259.
Nordquist, K. A., Schaab, K. M., Sha, J., & Bond, A. H. (2017). Crystal nucleation using surface-energy-modified glass substrates. *Crystal Growth and Design*, **17**(8), 4049–4055.
Olson, D. A., Chen, L., & Hillmyer, M. A. (2008). Templating nanoporous polymers with ordered block copolymers. *Chemistry of Materials*, **20**(3), 869–890.
Oxtoby, D. W. (1998). Nucleation of first-order phase transitions. *Accounts of Chemical Research*, **31**(2), 91–97.
Page, A. J., & Sear, R. P. (2009). Crystallization controlled by the geometry of a surface. *Journal of the American Chemical Society*, **131**(48), 17550–17551.
Parambil, J. V., Poornachary, S. K., Tan, R. B. H., & Heng, J. Y. Y. (2014). Template−induced polymorphic selectivity: The effects of surface chemistry and solute concentration on carbamazepine crystallisation. *CrystEngComm*, **26** (1), 4927–4930.
Pechkova, E., & Nicolini, C. (2002). Protein nucleation and crystallization by homologous protein thin film template. *Journal of Cellular Biochemistry*, **85**(2), 243–251.
Pfund, L. Y., Price, C. P., Frick, J. J., & Matzger, A. J. (2015). Controlling pharmaceutical crystallization with designed polymeric heteronuclei. *Journal of the American Chemical Society*, **137**(2), 871–875.
Pham, T., Lai, D., Ji, D., Tuntiwechapikul, W., Friedman, J. M., & Lee, T. R. (2004). Well-ordered self-assembled monolayer surfaces can be used to enhance the growth of protein crystals. *Colloids and Surfaces B: Biointerfaces*, **34**(3), 191–196.
Price, C. P., Grzesiak, A. L., & Matzger, A. J. (2005). Crystalline polymorph selection and discovery with polymer heteronuclei. *Journal of American Chemical Society*, **127**(1), 5512–5517.
Rengarajan, Gopalakrishnan T., Enke, D., & Beiner, M. (2007). Crystallization behavior of acetaminophen in nanopores. *The Open Physical Chemistry Journal*, **1**(1), 18–24.
Rengarajan, G. T., Enke, D., Steinhart, M., & Beiner, M. (2008). Stabilization of the amorphous state of pharmaceuticals in nanopores. *Journal of Materials Chemistry*, **18**(22), 2537–2539.
Reutzel-Edens, S. M. (2006). Achieving polymorph selectivity in the crystallization of pharmaceutical solids: Basic considerations and recent advances. *Current Opinion in Drug Discovery and Development*, **9**(6), 806–815.
Rodríguez-Hornedo, N., Lechuga-Ballesteros, D., & Hsiu-Jean Wu. (1992). Phase transition and heterogeneous/epitaxial nucleation of hydrated and anhydrous theophylline crystals. *International Journal of Pharmaceutics*, **85**(1–3), 149–162.
Rodríguez-Hornedo, N., & Murphy, D. (1999). Significance of controlling crystallization mechanisms and kinetics in pharmaceutical systems. *Journal of Pharmaceutical Sciences*, **88**(7), 651–660.
Rzayev, J., & Hillmyer, M. A. (2005). Nanoporous polystyrene containing hydrophilic pores from an ABC triblock copolymer precursor. *Macromolecules*, **38**(1), 3–5.
Salazar-Kuri, U., Estevez, J. O., Antunez, E. E., Martinez-Aguila, B. S., Warren, J. B.,

Andi, B., Cerniglia, M. L., Stojanoff, V., & Agarwal, V. (2015). Nucleation of sub-micrometer protein crystals in square-shaped macroporous silicon structures. *Crystal Growth and Design*, **15**(6), 2801–2808.

Sanjoh, A., Tsukihara, T., & Gorti, S. (2001). Surface-potential controlled Si-microarray devices for heterogeneous protein crystallization screening. *Journal of Crystal Growth*, **232**(1–4), 618–628.

Saridakis, Emmanuel, & Chayen, N. E. (2009). Towards a "universal" nucleant for protein crystallization. *Trends in Biotechnology*, **27**(2), 99–106.

Saridakis, E., Khurshid, S., Govada, L., Phan, Q., Hawkins, D., Crichlow, G. V, Lolis, E. R., Subrayal M., & Chayen, N. E. (2011). Protein crystallization facilitated by molecularly imprinted polymers. *Proceedings of the National Academy of Sciences*, **108**(27), 11081–11086.

Schoen, H. M., Grove, C. S., & Palermo, J. A. (1956). The early history of crystallization. *Journal of Chemical Education*, **33**(8), 373–375.

Sear, R. P. (2011). Crystal nucleation: In a tight corner. *Nature Materials*, **10**(11), 809–810.

Sengupta Ghatak, A., & Ghatak, A. (2013). Disordered nanowrinkle substrates for inducing crystallization over a wide range of concentration of protein and precipitant. *Langmuir*, **29**(13), 4373–4380.

Shah, U. V., Allenby, M. C., Williams, D. R., & Heng, J. Y. Y. (2012a). Crystallization of proteins at ultralow supersaturations using novel three-dimensional nanotemplates. *Crystal Growth and Design*, **12**(4), 1772–1777.

Shah, U. V., Williams, D. R., & Heng, J. Y. Y. (2012b). Selective crystallization of proteins using engineered nanonucleants. *Crystal Growth and Design*, **12**(3), 1362–1369.

Shah, U. V., Amberg, C., Diao, Y., Yang, Z., & Heng, J. Y. Y. (2015). Heterogeneous nucleants for crystallogenesis and bioseparation. *Current Opinion in Chemical Engineering*, **8**(1), 69–75.

Shah, U. V., Jahn, N. H., Huang, S., Yang, Z., Williams, D. R., & Heng, J. Y. Y. (2017). Crystallisation via novel 3D nanotemplates as a tool for protein purification and bio-separation. *Journal of Crystal Growth*, **469**(1), 42–47.

Shekunov, B. Y., & York, P. (2000). Crystallization process in pharmaceutical technology and drug delivery design. *Journal of Crystal Growth*, **211**(1), 122–136.

Sleutel, M., Lutsko, J., Van Driessche, A. E. S., Durán-Olivencia, M. A., & Maes, D. (2014). Observing classical nucleation theory at work by monitoring phase transitions with molecular precision. *Nature Communications*, **5**(1), 5598.

Sonnenberger, N., Anders, N., Golitsyn, Y., Steinhart, M., Enke, D., Saalwächter, K., & Beiner, M. (2016). Pharmaceutical nanocrystals confined in porous host systems-interfacial effects and amorphous interphases. *Chemical Communications*, **52**(24), 4466–4469.

Stojaković, J., Baftizadeh, F., Bellucci, M. A., Myerson, A. S., & Trout, B. L. (2017). Angle-directed nucleation of paracetamol on biocompatible nanoimprinted polymers. *Crystal Growth and Design*, **17**(6), 2955–2963.

Stolyarova, S., Saridakis, E., Chayen, N. E., & Nemirovsky, Y. (2006). A model for enhanced nucleation of protein crystals on a fractal porous substrate. *Biophysical Journal*, **91**(10), 3857–3863.

Tan, L., Davis, R. M., Myerson, A. S., & Trout, B. L. (2015). Control of heterogeneous nucleation via rationally designed biocompatible polymer surfaces with nanoscale features. *Crystal Growth and Design*, **15**(5), 2176–2186.

Ten Wolde, P. R., & Frenkel, D. (1997). Enhancement of protein crystal nucleation by critical density fluctuations. *Science*, **277**(5334), 1975–1978.

Testa, C. J., Shvedova, K., Hu, C., Wu, W., Born, S. C., Takizawa, B., & Mascia, S. (2021). Heterogeneous crystallization as a process intensification technology in an integrated continuous manufacturing process for pharmaceuticals. *Organic Process Research & Development*, **25**(2), 225–238.

Tosi, G., Fermani, S., Falini, G., Gavira Gallardo, J. A., & García Ruiz, J. M. (2008).

Crystallization of proteins on functionalized surfaces. *Acta Crystallographica Section D: Biological Crystallography*, **64**(10), 1054–1061.

Trasi, N. S., & Taylor, L. S. (2012). Effect of polymers on nucleation and crystal growth of amorphous acetaminophen. *CrystEngComm*, **14**(16), 5188–5197.

Tsekova, D. S., Williams, D. R., & Heng, J. Y. Y. (2012). Effect of surface chemistry of novel templates on crystallization of proteins. *Chemical Engineering Science*, **77**(1), 201–206.

Vekilov, P. G. (2010a). Nucleation. *Crystal Growth and Design*, **10**(12), 5007–5019.

Vekilov, P. G. (2010b). The two-step mechanism of nucleation of crystals in solution. *Nanoscale*, **2**(11), 2346–2357.

Vorontsova, M. A., Maes, D., & Vekilov, P. G. (2015). Recent advances in the understanding of two-step nucleation of protein crystals. *Faraday Discussions*, **179**(2), 27–40.

Wallace, A. F., Hedges, L. O., Fernandez-Martinez, A., Raiteri, P., Gale, J. D., Waychunas, G. A., Whitelam, S., Banfield, J. F., & De Yoreo, J. J. (2013). Microscopic evidence for liquid-liquid separation in supersaturated $CaCO_3$ solutions. *Science*, **341**(6148), 885–889.

Weissbuch, I., Addadi, L., Lahav, M., & Leiserowitz, L. (1991). Molecular recognition at crystal interfaces. *Science*, **253**(5020), 637–645.

Zalusky, A. S., Olayo-Valles, R., Wolf, J. H., & Hillmyer, M. A. (2002). Ordered nanoporous polymers from polystyrene-polylactide block copolymers. *Journal of the American Chemical Society*, **124**(43), 12761–12773.

Zhang, S. Q., & Cheung, M. S. (2007). Manipulating biopolymer dynamics by anisotropic nanoconfinement. *Nano Letters*, **7**(11), 3438–3442.

Zhao, D., Feng, J., Huo, Q., Melosh, N., Fredrickson, G. H., Chmelka, B. F., & Stucky, G. D. (1998). Triblock copolymer syntheses of mesoporous silica with periodic 50 to 300 angstrom pores. *Science*, **279**(5350), 548–552.

PART I:

The synthesis and characterization of self-assembled monolayers (SAMs)

Chapter 2

Formulation design of self-assembled monolayer (SAM) synthesis

2.1 Fundamentals of self-assembly

The process of self-assembly requires that the components of a system autonomously organize in an ordered manner at a given scale. Such a phenomenon can be considered as the fundamental growth step of hierarchical structures from the nano to the macroscale (Passoni et al., 2014; Scales et al., 2018). A monomolecular film surfactant is spontaneously assembled on a surface thanks to the lowering of the interfacial tension between two phases. The functionalized layer is immobilized on a specific substrate thanks to chemisorption or physisorption of the surfactant molecules. Molecules forming SAMs include a head group, which is capable of specific interaction with a solid substrate, a backbone, and an end group, which dictates the new surface properties.

From the pioneering studies of Zisman dated 1946 on the adsorption of a monomolecular layer of surfactant onto a metal surface (Bigelow et al., 1946), self-assembled monolayers (SAMs) have experienced tremendous interest in the literature and boast countless applications in disparate fields, such as corrosion (Chechik et al., 2000), adhesion (Senaratne et al., 2005), biosensors (Spampinato et al., 2016; Wink et al., 1997), field-effect transistors (Liu & Miao, 2018; Yan et al., 2011), and organic thin films (Marmont et al., 2008). The design of smart surfaces (Osicka et al., 2016), the improvement of the tribological behavior of microelectromechanical systems (Jian, 2008), the anchoring of biomolecules onto surfaces (Samanta & Sarkar, 2011), and the functionalization of nanostructured semiconductors (Rodriguez et al., 2019), nanoparticles and fibers (Ruckenstein & Li, 2005) are just few examples of the practical importance of SAMs.

Given the proximity of molecules in SAMs, intra-film reactions are also possible, such as condensation between unsaturated monomers, photopolymerization in presence of an immobilized photoinitiator within the SAM, or formation of inter-chain anhydrides from mercaptohexanoic acid monolayers (Chechik et al., 2000). In addition, SAMs can be used

---

The results presented in this chapter have been partially published in (Artusio et al., 2020a).

for successive reactions involving their end groups so as to dock additional layers to a surface.

SAMs exhibit a series of physico-chemical properties which are not allowed for inorganic materials, including optical, mechanical, electrical, and chemical features. An outstanding feature of SAMs is represented by the exposure of the monomer end group to the environment, even in solvent-free conditions. As they are easy to access to reagents, SAMs are particularly appealing for many technological applications (Chechik et al., 2000).

2.1.1 Preparation of SAMs

SAMs have been prepared on many different substrates, including gold, silicon, copper, silver, mica, and minerals, thanks to the robustness of the surface chemical modification. However, the selection of synthesis conditions for limiting the surface functionalization to a single layer of monomer is still under debate (Casalini et al., 2017; Haensch et al., 2010; Oberleitner et al., 2013; Samanta & Sarkar, 2011; Taglietti et al., 2019). For many applications, ranging from biochemistry to materials science, it is indeed crucial to control parameters such as the thickness, density, or reproducibility of the functionalized layer. At the same time, achieving an accurate control over the synthesis outcome can be rather difficult.

Among the most popular methods for SAM synthesis, one can find reactions between trialkoxy- or trichlorosilanes and hydroxylated silicon, or between reactants carrying disulfide or thiol groups and gold substrates (Athanasopoulou et al., 2018). The pair formed by the monomer head group and the substrate typically defines the system. The monomer can be either located in the vapor or in the liquid phase. In the former case, SAMs are obtained through vapor deposition as the increase in monomer partial pressure in the vapor triggers chemisorption (Finocchio et al., 2007; Pavlovic et al., 2002). In the latter case, SAMs can be obtained via wet-chemistry by immersing a substrate in the functionalizing solution (Glass et al., 2011; Pallavicini et al., 2009), drop-casting the solution on a surface (Yang et al., 2008), or heating pristine monomers deposited over a surface (Husseini et al., 2003).

The literature accounts for a wide variety of synthesis protocols of SAMs starting from alkoxysilanes. Nevertheless, the majority of such studies is limited to the analysis of just one or two functionalizing agents, thus limiting the general applicability of the approach (Allen et al., 2005; Buscher et al., 1996; Dietrich et al., 2015; Kessel & Granick, 1991; Kuo et al., 2011; Wang et al., 2005). Also, the growth mechanism of SAMs is still controversial, as it may proceed by thickening of a homogeneous layer, or in island-mode, where close-packed areas are formed along the surface and then laterally grow. SAM growth is a very complex process as its kinetics depends on the adsorption energy, the substrate corrugation and the energetical differences among the adsorption sites, the chain-chain interactions, the conformational energy of the chains, the interactions among end groups, and the admolecule energetics (Schreiber, 2000).

The SAM-functionalization density and reproducibility are affected by the synthesis environment, the solvent, the chemistry of monomers, and the cleaning of the substrate (Hu et al., 2001; La Spina et al., 2017). The amount of water in the system influences the assembly into monolayers and the resulting structure, both for shortage or excess conditions (Bunker et al., 2000; Tan et al., 2008; Ulman, 1996). The degree of order of the layer can

vary from disordered liquid-like structures to quasi-crystalline and highly oriented conformations. Order is dictated by the chemical composition, the chain length, and the intermolecular forces of the surfactant, but it can also be affected by the morphology of the substrate (Chew & Van Lehn, 2018; Fick et al., 2004). Long-range order and precise tilt direction were observed for thiols on Au (111), whereas silanes on hydroxylated surfaces lacked defined periodicity (Schreiber, 2000).

2.2 Aim of the synthesis of SAMs

In this thesis, SAMs were selected as supports for tackling the nucleation of pharmaceuticals and proteins. As outlined in Chapter 1, surface characteristics must be precisely controlled before the setting up of surface-induced crystallization. As a first step, both formulation and process conditions of SAM synthesis were carefully designed and optimized. The aim was the identification of a general route for the preparation of SAMs, which could potentially be applied to any alkoxysilane chemistry. In the framework of process standardization and reproducibility, four different trimethoxysilanes were selected as SAM building blocks to identify a unique synthesis protocol which could be fully compatible with silanes' chemistry by simply varying one process parameter. In addition, surface heterogeneities deriving from different synthesis methods could be avoided. Such a rational was dictated by the final application of SAMs to crystallization. In this way, the rigorousness of the nucleation study from the point of view of the substrate was ensured.

Many reasons related to SAM properties supported their application as heteronucleants. More specifically, the goals of the synthesis optimization were manifold, and the main features that were evaluated encompassed:

- reproducibility: the developed synthesis protocol must ensure precise and reproducible functionalization of surfaces. Thus, the uniformity of surface functionalization will be carefully studied by carrying surface characterization on multiple spots per sample and on samples prepared from different batches to test intra batch repeatability;
- functionalization stability: the new chemical groups introduced on the surface must be covalently bonded to the substrate. The adlayer must be stable to avoid the risk of contamination of the solution during crystallization. Moreover, the generation of particles from the surface coating or other physical alterations must be avoided during the crystallization trials;
- surface roughness: functionalized surfaces must be as smooth as possible. Surface roughness is known to play a major role during the nucleation step. The general goal of the crystallization study was to deconvolute, as much as physically possible, the chemical and the topographical effects of heteronucleants;
- absence of defects: surfaces must display a continuous and uniform functionalization. The presence of local defects has to be avoided as they may act as preferential nucleation sites and compromise the results;
- density of functionalization: surfaces must display a large number of chemical groups available for the direct interaction with solute molecules. Such a feature is extremely important in order to maximize the role of heteronucleant chemistry and counteract the kinetic bottleneck rising from surface smoothness;
- surface tension: the functionalized surfaces must display comparable surface tension to exclude wettability effects on the alteration of nucleation. Moreover, for

protein crystallization, similar surface tension is essential for maintaining a constant surface/volume ratio of drops of protein solution;
- optical transparency: functionalized surfaces will be used for kinetic studies. The periodical inspection and data acquisition is performed by means of an optical microscope operating with transmitted light. The presence of shadow areas or thick supports would disturb or even hinder the crystallization study.

As will be discussed in Chapter 2, the identification of a robust route for the preparation of SAMs started with the study of glass hydroxylation with piranha treatments. Then, the formulation used for SAM synthesis was designed in terms of solvent and silane concentration. 3-mercaptopropyltrimethoxysilane was selected as the reference silane for this part of the study. When studying the effect of silane concentration, a comparison with the synthesis outcome employing 3-aminopropyltrimethoxysilane was also performed. Contact angle analyses and spectroscopic methods such as Fourier transform infrared spectroscopy (FTIR) and X-ray photoelectron spectroscopy (XPS) were used to investigate the surface chemistry, whereas surface topography was studied by means of atomic force microscopy (AFM). Process parameters such as reaction time and temperature were optimized in a second step (Chapter 3). As a third step, the optimized protocol was validated by applying it to two additional trimethoxysilanes and comparing the resulting surface features (Chapter 4).

2.3 Materials & Methods

2.3.1 Materials

Hydrogen peroxide (30 wt% aqueous solution, ACS reagent), sulfuric acid (95.0 – 98.9%, ACS reagent), acetone (99.5%, ACS reagent), ethanol (≥ 99.8%, puriss. p.a., absolute), toluene (≥ 99.5%, ACS reagent), anhydrous toluene (99.8%, water < 0.001%), and silanes were purchased from Sigma-Aldrich (Cesano Maderno, MI, Italy). The silanes used in this part of the study were 3-mercaptopropyltrimethoxysilane (THIOL, 95%) and 3-aminopropyltrimethoxysilane (AMINO, 97%). The chemical structure of the silanes is reported in Fig. 5. The solvent bottles were purchased specifically for the study and freshly opened before the start of synthesis.

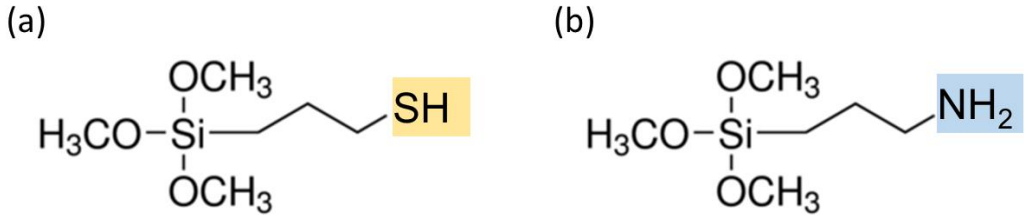

Figure 5 The chemical structure of THIOL and AMINO silanes. The silane end group is highlighted.

2.3.2 Synthesis of SAMs

All the operations devoted to the synthesis of SAMs and the manipulation of solvents were carried out in a fume-hood at room temperature (20 °C). Glass coverslips (D263M,

diameter = 14 mm, Neuvitro, Vancouver, WA, USA) were preliminarily sonicated twice in ethanol for 10 min (Bandelin, Sonorex, Germany). The coarse cleaning step contributed to the removal of particles and soluble impurities adsorbed on the glass surface. Coverslips were carefully dried with nitrogen and transferred to the piranha treatment step for surface activation. Piranha solutions were prepared with extreme care because of their high oxidizing power. If not properly manipulated, hazardous explosions and severe injuries may occur. Piranha solutions were freshly prepared by mixing H_2SO_4 and H_2O_2 in different proportions, namely 3:1 or 5:1. The incubation time ranged from 30 min to 2 h. After the activation, coverslips were thoroughly rinsed with deionized water to remove all the residues of the oxidizing solution. The pH of the rinsing water was monitored until neutral values were obtained. Coverslips were blown dry with nitrogen and immediately transferred to the silanization step. The formulation was designed in terms of solvent and silane concentration. Each coverslip was individually inserted into tubes containing 10 mL of silane solution. Silane concentration ranged from 0.014 to 0.135 M. The tested reaction media were ethanol, acetone, and anhydrous toluene. A slight nitrogen overpressure was ensured while withdrawing anhydrous toluene from its container to minimize the risk of solvent hydration. The silanization reaction was carried out at room temperature for 15 h. The synthesis conditions and the sample codes are detailed in Tab. 2. After silanization, coverslips were withdrawn and thoroughly rinsed with toluene, toluene/ethanol (1:1), and ethanol to remove reaction residues and solvents. Finally, the functionalized coverslips were dried with nitrogen and characterized. Each synthesis condition was replicated three times to assess reproducibility.

Table 2 The detail of silanization conditions studied during the optimization of formulation design.

Sample code	Silane	Silane concentration, M	Solvent	Reaction time, h
T1	THIOL	0.054	Ethanol	15
T2	THIOL	0.054	Acetone	15
T3	THIOL	0.054	Anhydrous toluene	15
T4	THIOL	0.027	Anhydrous toluene	15
T5	THIOL	0.135	Anhydrous toluene	15
A1	AMINO	0.054	Anhydrous toluene	15
A2	AMINO	0.027	Anhydrous toluene	15
A3	AMINO	0.014	Anhydrous toluene	15

2.3.3 Physico-chemical characterization

2.3.3.1 Contact angle

The effectiveness of surface activation and functionalization steps were first tested with contact angle analyses (MSE DigiDrop, GBX, France). 3 μL drops were produced and deposited on the samples thanks to a manual dispensing apparatus. The probing liquid was HPLC water. Static contact angle was measured by fitting the drop contour line. The contact angle was measured on four different spots of triplicate samples. Thus, the average contact angle value resulted from the average of 12 measurements.

2.3.3.2 Infrared spectroscopy

FTIR in attenuated total reflectance (ATR) mode (Nicolet iS50, Thermo Scientific, Waltham, MA, USA) was adopted to investigate the surface activation. The IR spectra of untreated and piranha-treated glass coverslips were acquired between 600 and 4000 cm^{-1}. Resolution was 4 cm^{-1} and a smart ITX diamond was used. Each final spectrum was obtained by running 64 scans per sample. Analyses were carried out on triplicates.

2.3.3.3 X-ray photoelectron spectroscopy (XPS)

The surface chemistry was extensively investigated by XPS (AXIS ULTRA, DLD Kratos Analytical, UK). The instrument was equipped with a monochromatic Al Kα source ($h\nu$ = 1486.6 eV) which was operated at 150 W. Survey spectra were collected by recording wide scans of binding energy from 1100 to 0 eV. Hybrid mode, "slot" aperture (corresponding to 400 x 700 μm^2 as analysis area) and pass energy = 160 eV were selected. Core-level spectra, instead, were recorded using pass energy of 20 eV. The operating pressure was 6×10^{-7} Pa. Low energy (~5 eV) electrons were used to compensate surface charging. The instrument's charge balance plate was also used for adjusting surface charging. The take-off angle (ToA) was set at 0° for both survey and high-resolution (HR) spectra. ToA was defined as the angle between the normal to the surface sample and the analyzer, as schematized in Fig. 6.

Three different spots were analyzed per sample. XPS data were processed with CasaXPS (ver. 2.3.20). The spectra calibration was performed by setting the hydrocarbon C1s at 285.0 eV. A U-3 Tougaard background (Tougaard, 1998; Tougaard & Yubero, 2004) was fitted and subtracted from the survey spectra. Then, surface atomic composition was calculated using the relative sensitivity factors (RSF) provided by the manufacturer (library: Kratos-C1.lbb). The peak fitting was carried out without performing preliminary smoothing. As regards HR-XPS spectra, the line shape of the fitting components was approximated with Gaussian-Lorentzian (70% Gaussian, 30% Lorentzian) product functions.

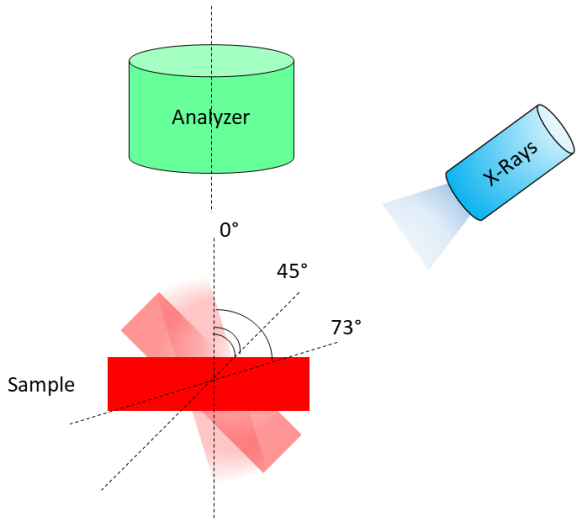

Figure 6 Scheme of the AR-XPS operative configuration. ToA was defined as the angle between the normal to the surface and the analyzer.

2.3.3.4 Atomic force microscopy (AFM)

The surface topography of untreated glass and SAMs was studied by AFM (Solver NANO, NT-MDT Spectrum Instruments, Russia). The instrument was operated in tapping mode. The scanned area was 1 x 1 μm^2, and 256 lines were acquired per scan. Tips made of Si_3N_4 were selected, and the cantilever frequency was set at 0.8 Hz. Data were processed with Gwyddion software (ver. 2.51, Czech Metrology Institute). The average surface roughness, R_q, and the selected area difference (SAD) were calculated. 5^{th} order polynomials were used to fit the data and get the surface topography. Three measurements were carried out on different areas of the same sample, and the analyses were repeated on triplicate samples.

2.4 Surface activation

The first step of the surface functionalization process with SAMs involved the cleaning and activation of glass surface. Such a step is pivotal for the quality of functionalization as it provides the anchoring sites for the silane molecules. Surface hydroxylation allows condensation reactions to occur, as superficial -OH groups are reacting with the methoxy head groups of silanes. Thus, methanol is produced after the condensation reaction. The process is schematized in Fig. 7 for a generic trimethoxysilane.

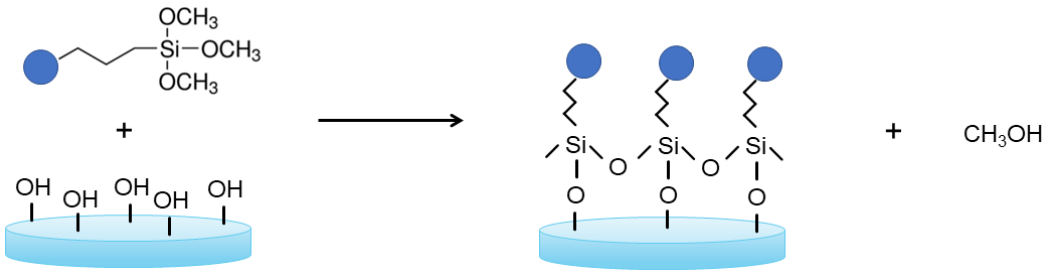

Figure 7 Schematic representation of the condensation reaction occurring between the superficial -OH groups of glass and the methoxy head groups of silanes. Blue circles stand for the silane end group.

Many surface activation strategies are reported in literature, including UV irradiation, oxygen plasma, and incubation in oxidizing solution (Glass et al., 2011). In the present study, piranha solutions were selected because of their high efficiency in surface hydroxylation. Moreover, a wet surface activation route could also be effective in achieving deeper surface cleaning and avoiding the risk of depositing undesired species on the surface, compared to plasma treatments.

2.4.1 Surface hydrophilicity measurements

Piranha solutions are extremely oxidizing as their constituents are H_2SO_4 and H_2O_2. 3:1 and 5:1 ratios between the two species and incubation time ranging 30 min – 2 h were tested. As reported in Tab. 3, the outcome of surface activation was first evaluated by means of contact angle. The average contact angle of the untreated glass surface was 62.9 (± 5.4)°. The activation conditions strongly influenced the hydrophilicity of the glass surface. 3:1 ratio resulted to be more effective in increasing surface hydrophilicity after 30 min, compared to 5:1 samples. However, 30 min were not enough for the complete removal of surface contaminants. After 1 h of incubation, 5:1 ratios led to super-hydrophilic surfaces, having contact angle below 2°. Conversely, the glass hydrophilicity stabilized around 7° for samples prepared with 3:1 piranha solution.

Water contact angles provided a rough but effective estimation of the degree of hydroxylation of glass after the piranha treatment. 5:1 ratio and 1 h as the incubation time were selected as the optimal combination to achieve the maximum hydrophilicity increase in minimal time.

Table 3 Water contact angle (± SD) of glass surface activated with different H_2SO_4:H_2O_2 ratios and incubation times.

H_2SO_4 : H_2O_2	Incubation time	Contact angle, °
3:1	30 min	9.6 (± 1.8)
3:1	1 h	6.1 (± 3.3)
3:1	2 h	7.2 (± 1.7)
5:1	30 min	17.1 (± 6.7)
5:1	1 h	< 2
5:1	2 h	< 2

2.4.2 FT – IR of activated glass

The effective presence of hydroxyl groups on the activated glass surface was demonstrated by means of IR analyses. Samples referring to untreated glass and activated glass (5:1 piranha, incubation time = 1 h) were compared, as reported in Fig. 8.

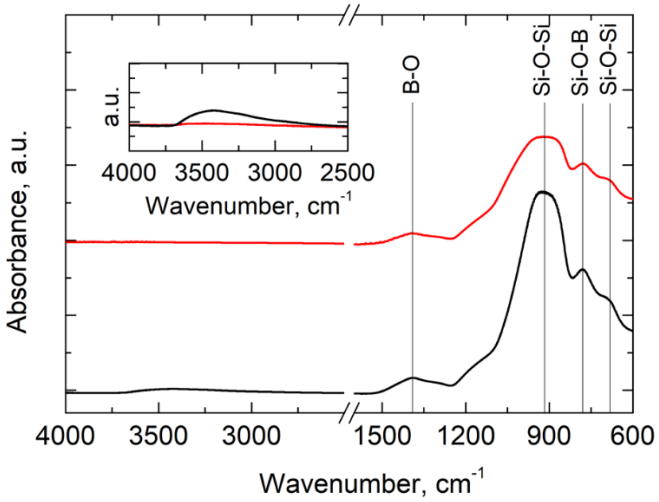

Figure 8 FT-IR ATR spectra of untreated glass (red curve) and glass activated by 1 h incubation in 5:1 piranha solution (black curve). The main peaks have been attributed to the respective bond roto-vibrational modes. Embedded in the panel is the region of interest between 3600 and 3200 cm^{-1}, displaying the -OH shoulder of activated glass.

The untreated and activated glass displayed the typical Si-O-Si stretching at 910 cm^{-1} and Si-O-Si bending at 684 cm^{-1}. The presence of boron was also detected and related to B-O at 1390 cm^{-1} and Si-O-B at 781 cm^{-1}. As expected, the IR spectra of the two surfaces could be overlapped, except for the region between 3600 and 3200 cm^{-1}, highlighted in the embedded panel. The activated glass displayed a broad shoulder in this region, which was attributed to the superficial -OH groups. It has to be noticed that the detection of -OH groups by IR is commonly quite tricky. As a matter of fact, the formation of a layer of absorbed water from the atmosphere over the sample surface is not unusual and may lead to misinterpretation of the effectiveness of activation treatments. However, the total absence of IR absorbance in the 3600 - 3200 cm^{-1} region of untreated glass excluded such an inconvenient and confirmed the successful hydroxylation step.

2.4.3 Quantification of the reduction in carbon contamination by XPS

The last investigated aspect of the activation step was the superficial contamination of glass by carbon. Hydrocarbons coming from the atmosphere can easily adsorb on the surfaces and compromise the quality of surface functionalization. XPS survey scans of the untreated and the activated glass were performed to verify the reduction of contamination provided by the piranha treatment, and spectra are reported in Fig. 9.

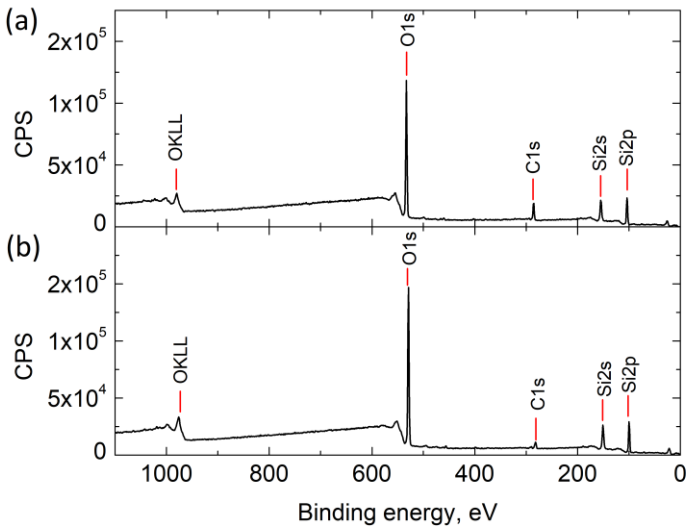

Figure 9 XPS survey scans of (a) untreated and (b) activated glass. Major elements of the samples are highlighted. Spectra were collected at ToA = 0°. The picture was taken from (Artusio et al., 2020a) with modification.

Typical elements of borosilicate glass were detected by XPS, such as silicon (Si2s and Si2p peaks) and oxygen (O1s and OKLL peaks). Also, some metals were detected as they were present as oxide impurities in the glass. Zinc, aluminum, sodium, potassium, and titanium were identified as minor elements. However, the sum of their atomic compositions resulted to be lower than 3 at%. With regard to carbon, an intense C1s peak was recorded for untreated glass, corresponding to 19 at%. The surface activation treatment led to more than 50% reduction in carbon contamination, and the total carbon decreased to 8 at%.

XPS analyses also confirmed that the bulk chemistry of glass was not altered by the piranha treatments, as confirmed by the elemental ratios reported in Tab. 4. C/Si ratio was strongly reduced by the activation treatment, whereas O/Si was constant. O/Si ratio refers to elements of bulk glass, proving that piranha solutions only attacked the superficial layers of contamination on glass, without altering the chemical composition of glass.

Table 4 Elemental ratios of glass before and after the surface activation treatments as evaluated from XPS survey scans at ToA = 0°.

Sample	C/Si	O/Si
Untreated glass	0.87	2.54
Activated glass	0.32	2.57

In order to better understand the nature of carbon contamination and the action of surface activation treatments, HR-XPS of C1s regions was performed. Fig. 10 (a) reports a representative spectrum obtained for untreated glass. An intense C1s peak was detected and fitted with three components. The most intense one was centered at 285.0 eV and referred to C-C. Components referring to C-O and COO were also detected at 286.5 and 289.0 eV, respectively. Two minor peaks were detected next to C1s peak and identified as $K2p_{3/2}$ and $K2p_{1/2}$ components. The comparison to the activated glass spectrum, in Fig. 10 (b), revealed significant differences. The relative component quantification reported in Tab. 5 highlighted a strong decrease of C-C. Conversely, C-O and COO increased. In absolute

terms, the overall intensity of C1s peak was strongly reduced by the piranha treatment. In relative terms, piranha resulted to be more aggressive toward hydrocarbon contamination.

Interesting considerations could also be made starting from K2p data. Thanks to the removal of superficial contamination, K2p signal was 3-fold higher in the activated glass. Potassium represents a bulk element that is present in borosilicate glass as an oxide impurity. K2p strong increase after activation denoted the XPS higher sensitivity toward bulk elements. Such a reference will serve as an indicator of the thickness of functionalization in the following part of the study.

In conclusion, the optimal surface activation involved 5:1 as piranha solution ratio and 1 h as incubation time. The effectiveness of the treatment in hydroxylating the glass surface was proven by FT-IR. The reduction in superficial carbon contamination was demonstrated by XPS, as well as the unmodified bulk chemistry of glass.

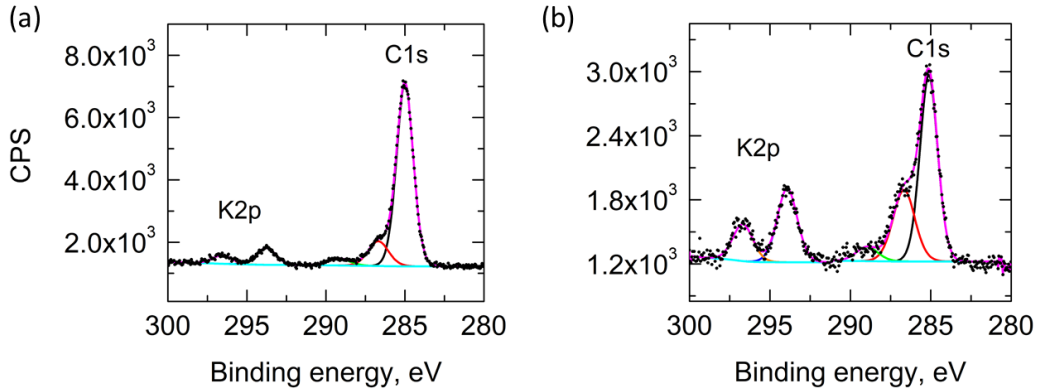

Figure 10 HR-XPS of C1s region of (a) untreated and (b) activated glass. C1s and K2p peaks were fitted with GL30 curves to identify components. After the activation step, the intensity of K2p peaks significantly increased. Spectra were recorded at ToA = 0°.

Table 5 Detail of carbon and potassium components and respective at% identified in the C1s HR-XPS spectra of untreated and activated glass of Fig. 10.

Sample	C-C% (285.0 eV)	C-O% (286.5 eV)	COO% (289.0 eV)	$K2p_{3/2}$% (293.2 eV)	$K2p_{1/2}$% (296.0 eV)
Untreated glass	80.29	13.32	3.97	1.61	0.81
Activated glass	58.97	27.96	5.52	5.03	2.52

2.5 The selection of solvent for SAM synthesis

After the assessment and optimization of the surface activation treatment, surface functionalization with SAMs was studied. The design of the optimal formulation began with the selection of the most appropriate solvent to carry out the silanization process.

Literature reports a wide variety of solvents commonly employed to perform self-assembly on a surface (Dannenberger et al., 1999; Pallavicini et al., 2009). In the present study, ethanol (T1), acetone (T2), and anhydrous toluene (T3) were selected. 3-

mercaptopropyltrimethoxysilane (THIOL silane) was selected as the model functionalizing agent and its concentration was fixed at 1% v/v, i.e., 0.054 M. The reaction time was 15 h. The outcome of silanization was investigated with water contact angle, XPS, and AFM.

2.5.1 Contact angle

Contact angle is a macro-characterization technique that allows for a rapid and easy evaluation of the alteration of superficial properties. After the silanization step, surfaces are expected to undergo a marked increase in their hydrophobicity. The introduction of functionalizing agents having a hydrocarbon skeleton is responsible for the loss of the super-hydrophilicity features of the activated glass. As summarized in Tab. 6, the highest value of contact angle, i.e., 65.7°, was obtained for samples prepared in anhydrous toluene. Ethanol and acetone, instead, led to approx. halved contact angle values, suggesting a lower extent of functionalization. With regard to ethanol, the functionalization turned out to be scarcely reproducible, as highlighted by the high value of SD. Such a behavior was attributed to the interaction between the silane and the solvent molecules, as further discussed in § 2.5.2 and 2.5.3. It has to be noted that contact angle only provided a rough estimation of the effectiveness of surface functionalization. Complementary surface analysis techniques such as XPS and AFM are essential for understanding the impact of synthesis conditions on surface functionalization.

Table 6 Water contact angle (± SD) of glass coverslips functionalized with THIOL silane in different solvents.

Sample	Solvent	Contact angle, °
T1	Ethanol	38.9 (± 4.9)
T2	Acetone	33.4 (± 2.2)
T3	Anh. toluene	65.7 (± 1.7)

2.5.2 Elemental quantification by XPS

A more detailed investigation of the role of the solvent during the functionalization process was performed by XPS. Survey scans of T1, T2, and T3 samples were initially collected at ToA = 0°, and their atomic composition is detailed in Tab. A1 (Appendix A). A representative XPS survey spectrum of T3 sample is displayed in Fig. 11.

The presence of characteristic elements of THIOL silane molecules anchored on glass, i.e., carbon and sulfur, was confirmed. The comparison between T3 and activated glass spectra highlighted the presence sulfur-related peaks, S2s (~230 eV) and S2p (~164 eV). However, S2p signal overlapped with the Si2s descending shoulder, making its detection rather difficult. Therefore, S2s peak was considered for elemental quantification. The concentration of carbon C1s increased compared to the activated glass. All the evidence confirmed the addition of propylic chains on the glass surface.

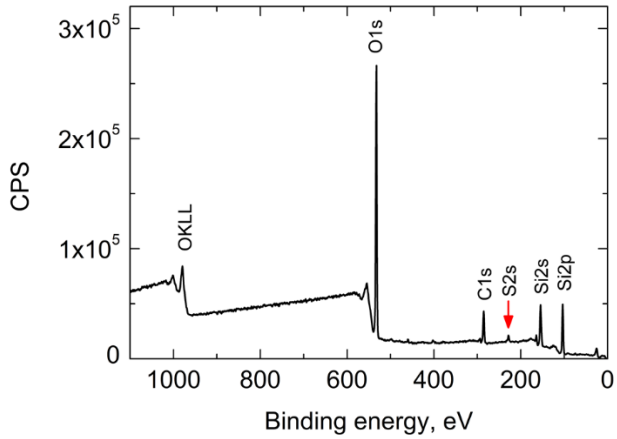

Figure 11 XPS survey scans of T3 sample collected at ToA = 0°. The most intense peaks were attributed to the respective elements. The presence of S2s peak denoted the presence of THIOL silane molecules on the glass surface.

Sulfur peaks were also detected in T1 and T2 samples, but major differences in the overall atomic composition were identified. In order to facilitate the interpretation of data, the ratio between elements belonging to the functionalized adlayer and bulk elements, such as S/Si and C/Si, were calculated. Also, ratios between bulk elements, like O/Si, and adlayer elements, like S/C, are reported in Tab. 7. Nevertheless, a remark has to be done on the distinction between bulk and adlayer elements. Among all the elements considered, only sulfur can rigorously be considered as an adlayer-exclusive element. Silicon and oxygen are mostly bulk elements of glass, but they may also come from unreacted methoxy groups of silanes. The presence of carbon is mainly due to the SAM propylic chain, but the sample surface can also display a certain degree of hydrocarbons adsorbed from the atmosphere. Therefore, all these factors may affect the actual values of the element ratios.

As reported in Tab. 7, the highest S/Si, C/Si, and S/C ratios were obtained for T3 sample. Therefore, T3 displayed the maximum surface concentration of carbon and sulfur. Such a finding confirmed that anhydrous toluene was the most suitable solvent for carrying out the silanization process, in agreement with the contact angle results. Moreover, the S/C ratio of T3 was the closest one to the ideal value of 0.33, calculated considering that every THIOL silane molecule carries three carbon atoms and one sulfur atom.

Table 7 S/Si, C/Si, O/Si, and S/C ratio of T1, T2, and T3 samples evaluated from XPS survey scans.

Sample	S/Si	C/Si	O/Si	S/C
T1	0.03	0.59	2.72	0.04
T2	0.06	0.58	2.80	0.10
T3	0.14	0.82	2.60	0.17

The silanization process resulted to be compromised by the employment of polar solvents as reaction medium. The results suggested the presence of significant amounts of water in such solvents, which could favor the silane self-polymerization in suspension at the expense of high yields in surface anchoring. When a polar protic solvent as ethanol was employed, such a tendency was even more marked. The number of -OH groups of ethanol by far exceeded that of glass surface, thus minimizing the surface contribution to the condensation reaction.

2.5.3 Evaluation of surface topography

In order to confirm the hypothesized mechanism of interaction with solvents, the surface topography was evaluated before and after the silanization step. Fig. 12 (a) displays the surface topography of untreated glass. The average surface roughness R_q was 130 (± 5) pm, and the average height of surface features was 0.76 nm. The selected area difference (SAD) was 0.10%. The untreated glass was therefore extremely smooth, confirming the suitability of the support material as regards the roughness constraints introduced in § 2.2.

T1 and T2 samples displayed an altered topography, as illustrated in Fig. 12 (b) and (c). The presence of local deposits of polymerized material was clearly identified. The poor surface functionalization highlighted by contact angle and XPS was confirmed by AFM investigation, pointing out inhomogeneous and localized islands of organic matter on glass surface. The maximum height of the deposits reached 4.1 and 6.6 nm in T1 and T2 samples, respectively. In addition, the discontinuous layer of functionalization could explain the lower reproducibility pointed out by the contact angle and XPS analyses, which significantly depended on the measured spot of the sample.

Conversely, the topography of T3 sample strongly resembled that of untreated glass, as highlighted in Fig. 12 (d). The silanization process in anhydrous toluene led to extremely smooth surfaces, with R_q = 128 (± 9) pm. The absence of local silane clusters was demonstrated, as well as the achievement of a continuous and uniform functionalized layer.

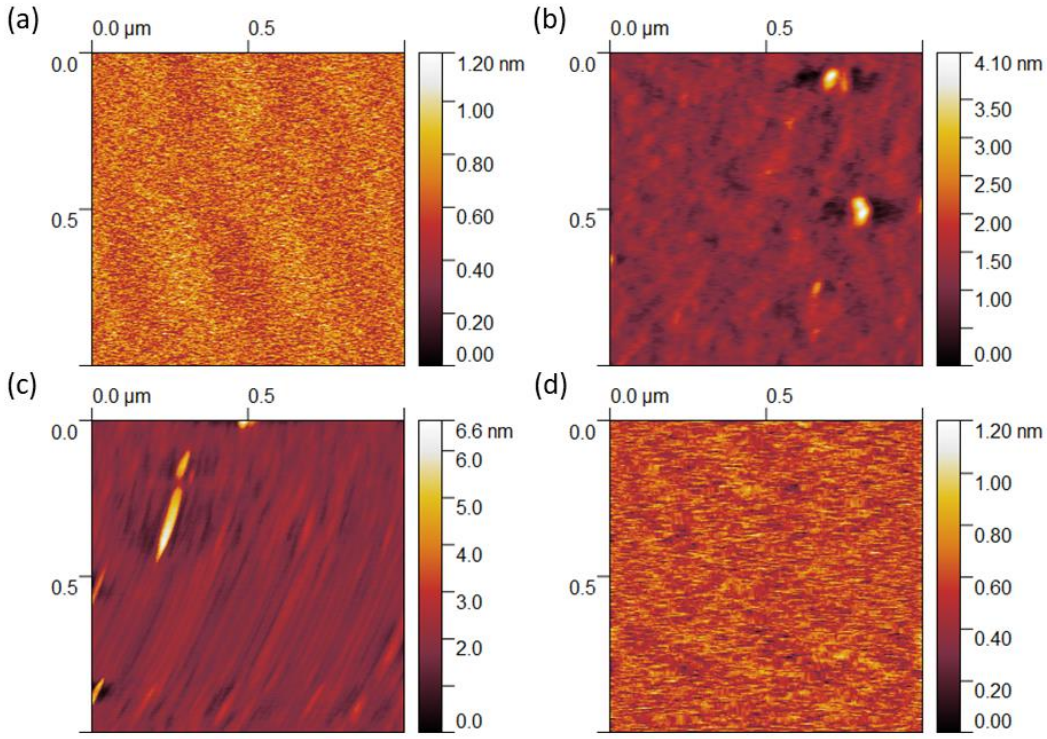

Figure 12 Surface topographies of (a) untreated glass, (b) T1, (c) T2, and (d) T3 samples as measured with AFM.

In conclusion, the silanization in anhydrous toluene led to extremely flat surfaces and to the highest extent of functionalization and reproducibility. It was demonstrated that polar solvents strongly reduced the yield of silane anchoring onto the glass surface and did not guarantee smooth and defect-free topographies.

2.6 The selection of silane concentration

After the solvent selection, formulation design focused on the optimal silane concentration to be set. The silane concentration represents an important parameter since, if not properly selected, poor surface functionalization may occur. THIOL and AMINO silanes were employed as model molecules in this part of the study. The reaction medium was anhydrous toluene, and the reaction time was 15 h. Water contact angle, XPS, and AFM analyses were performed to evaluate the impact of synthesis conditions on surface functionalization.

2.6.1 Contact angle

The effect of silane concentration was first evaluated by water contact angle. Silane concentration was expressed as molarity to easily compare samples prepared with different silanes. Results are summarized in Tab. 8. With regard to THIOL silane, halving the silane concentration (T4) had a marginal impact on the hydrophobicity of the surface, and contact angle values similar to the reference sample (T3) were obtained. Conversely, a much higher silane concentration (T5) led to increased hydrophobicity. With regard to AMINO silane, samples prepared with the same conditions used for THIOL silane led to higher contact angles, as reported for A1 and A2. Further reduction in silane concentration was not beneficial for getting surface hydrophobicity comparable to samples prepared with THIOL silane. Water contact angles above 80° were always obtained, suggesting the over-functionalization of glass with AMINO silanes. XPS and AFM analyses were carried out to confirm such an hypothesis.

Table 8 Water contact angle (± SD) of glass coverslips functionalized with different concentrations of THIOL and AMINO silanes.

THIOL		
Sample	**Silane concentration, M**	**Contact angle, °**
T3	0.054	65.7 (± 1.7)
T4	0.027	63.2 (± 1.5)
T5	0.135	70.5 (± 2.1)
AMINO		
Sample	**Silane concentration, M**	**Contact angle, °**
A1	0.054	82.4 (± 0.9)
A2	0.027	82.8 (± 3.2)
A3	0.014	85.2 (± 0.6)

2.6.2 Elemental quantification by XPS

Survey scans of samples prepared for the study on silane concentration were collected by XPS. A representative spectrum of A1 sample is reported in Fig. 13 (a). Characteristic

elements of the adlayer were detected, namely carbon and nitrogen. An intense signal was attributed to N1s at ~400 eV. Compared to T3 sample, the at% of carbon increased from 18% to 54%. The content of the characteristic adlayer element was 3% for T3, whereas it reached 12% for A1. The approx. 4-fold higher values of such elements pointed out an uncontrolled functionalization with AMINO silanes, leading to multiple layers of organic material on the glass surface, as highlighted by the sample topography reported in Fig. 13 (b). Such a phenomenon was also confirmed by the physical appearance of the samples. Coverslips functionalized with THIOL silane were optically transparent, whereas those functionalized with AMINO silane were opaque.

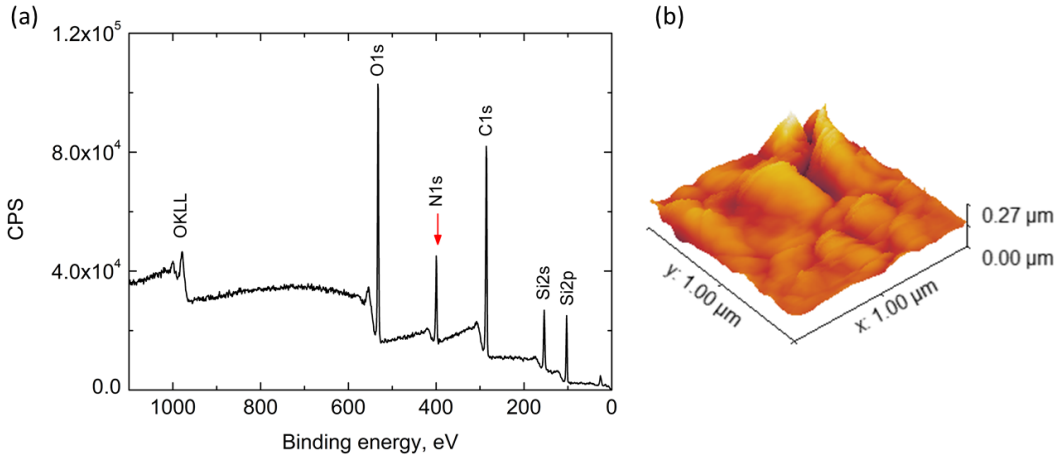

Figure 13 (a) XPS survey scans of sample A1 collected at ToA = 0°. Major elements of the sample are highlighted. (b) Surface topography of sample A1 as measured by AFM.

Characteristic element ratios were calculated and collected in Tab. 9. The element ratios concerning THIOL silane confirmed the trend reported for the contact angle analyses. On the one hand, T4 sample highlighted the marginal impact of halving silane concentration in solution on the surface chemistry. On the other hand, increased silane concentrations led to significantly higher C/Si and S/Si ratios. Such results confirmed that the at% of carbon was higher in T5 samples and that the functionalization was less controlled. It was likely that islands of polymerized silanes had populated the surface because of the excess of functionalizing agent in solution.

The optimal THIOL silane concentration was set at 0.054 M. As highlighted by the atomic compositions reported in Appendix A, T3 sample featured the lowest standard deviation. Such conditions ensured more uniform surface composition not only among different spots on the same sample but also among different replicas. A slight excess of silane molecules in solution resulted to be beneficial for the process. The molecules reservoir guarantees the interaction with the surface and ensures bonding before the decay of the labile surface activation. With regard to AMINO silane, a more complex picture was obtained. The progressive reduction of the silane concentration did not lead to controlled surface functionalization. High N/Si and C/Si ratios denoted excessive deposition of organic material on the surface. The silane self-polymerization could not be limited, and the tuning of other synthesis parameters was necessary.

Table 9 Characteristic element ratios of glass functionalized with THIOL and AMINO silanes as evaluated from XPS survey scans collected at ToA = 0°.

THIOL					
Sample	**Silane concentration, M**	**S/Si**	**C/Si**	**O/Si**	**S/C**
T3	0.054	0.14	0.82	2.60	0.17
T4	0.027	0.15	1.47	2.37	0.10
T5	0.135	0.34	2.18	2.20	0.16
AMINO					
Sample	**Silane concentration, M**	**N/Si**	**C/Si**	**O/Si**	**N/C**
A1	0.054	1.09	4.91	2.12	0.22
A2	0.027	1.12	5.22	2.30	0.21
A3	0.014	0.74	3.45	1.88	0.21

2.7 Final remarks

Glass surface activation and SAM formulation design were optimized. The effective surface hydroxylation and cleaning by means of piranha solutions was demonstrated by means of IR and XPS analyses. Functionalized glass was thoroughly investigated by means of a variety of macro- and micro-characterization techniques to get an accurate picture of its physico-chemical properties. Anhydrous toluene was selected as the best performing reaction medium. The absence of water resulted in higher density of THIOL silane molecules anchored to glass. Syntheses carried out under moderate excess of silane (0.054 M) ensured a good interaction between the functionalizing agent and the superficial -OH groups. Conversely, AMINO silane led to uncontrolled functionalization, as demonstrated by characteristic element ratios calculated from XPS data and surface topography. Therefore, the tuning of other synthesis parameters, such as reaction time and temperature, will be studied in order to identify a general synthesis protocol that guarantees controlled functionalization with both THIOL and AMINO silanes.

References

Allen, G. C., Sorbello, F., Altavilla, C., Castorina, A., & Ciliberto, E. (2005). Macro-, micro- and nano-investigations on 3-aminopropyltrimethoxysilane self-assembly-monolayers. *Thin Solid Films*, **483**(1–2), 306–311.

Artusio, F., Fumagalli, F., Bañuls-Ciscar, J., Ceccone, G., & Pisano, R. (2020a). General and adaptive synthesis protocol for monolayers as tunable surface chemistry platforms for biochemical applications. *Biointerphases*, **15**(4), 041005.

Athanasopoulou, E. N., Nianias, N., Ong, Q. K., & Stellacci, F. (2018). Bimodal atomic force microscopy for the characterization of thiolated self-assembled monolayers. *Nanoscale*, **10**(48), 23027–23036.

Bigelow, W. C., Pickett, D. L., & Zisman, W. A. (1946). Oleophobic Monolayers. I. Films Adsorbed from Solution in Non-polar Liquids. *Journal of Colloid and Interface Science*, **1**, 513–538.

Bunker, B. C., Carpick, R. W., Assink, R. A., Thomas, M. L., Hankins, M. G., Voigt, J. A., Sipola, D., De Boer, M., P., & Gulley, G. L. (2000). Impact of solution agglomeration on the deposition of self-assembled monolayers. *Langmuir*, **16**(20), 7742–7751.

Buscher, C. T., McBranch, D., & Li, D. Q. (1996). Understanding the relationship between surface coverage and molecular orientation in polar self-assembled monolayers. *Journal of the American Chemical Society*, **118**(12), 2950–2953.

Casalini, S., Bortolotti, C. A., Leonardi, F., & Biscarini, F. (2017). Self-assembled monolayers in organic electronics. *Chemical Society Reviews*, **46**(1), 40–71.

Chechik, V., Crooks, R. M., & Stirling, C. J. M. (2000). Reactions and reactivity in self-assembled monolayers. *Advanced Materials*, **12**(16), 1161–1171.

Chew, A. K., & Van Lehn, R. C. (2018). Effect of Core Morphology on the Structural Asymmetry of Alkanethiol Monolayer-Protected Gold Nanoparticles. *Journal of Physical Chemistry C*, **122**(45), 26288–26297. research-article.

Dannenberger, O., Buck, M., & Grunze, M. (1999). Self-assembly of n-alkanethiols: A kinetic study by second harmonic generation, *Journal of Physical Chemistry B*, **103**(12), 2202–2213.

Dietrich, P. M., Streeck, C., Glamsch, S., Ehlert, C., Lippitz, A., Nutsch, A., Kulak, N., Beckhoff, B., & Unger, W. E. S. (2015). Quantification of silane molecules on oxidized silicon: are there options for a traceable and absolute determination? *Analytical Chemistry*, **87**(19), 10117–10124.

Fick, J., Steitz, R., Leiner, V., Tokumitsu, S., Himmelhaus, M., & Grunze, M. (2004). Swelling behavior of self-assembled monolayers of alkanethiol-terminated poly(ethylene glycol): A neutron reflectometry study. *Langmuir*, **20**(10), 3848–3853.

Finocchio, E., Macis, E., Raiteri, R., & Busca, G. (2007). Adsorption of trimethoxysilane and of 3-mercaptopropyltrimethoxysilane on silica and on silicon wafers from vapor phase: An IR study. *Langmuir*, **23**(5), 2505–2509.

Glass, N. R., Tjeung, R., Chan, P., Yeo, L. Y., & Friend, J. R. (2011). Organosilane deposition for microfluidic applications. *Biomicrofluidics*, **5**(3), 1–7.

Haensch, C., Hoeppener, S., & Schubert, U. S. (2010). Chemical modification of self-assembled silane based monolayers by surface reactions. *Chemical Society Reviews*, **39**(6), 2323–2334.

Hu, M., Noda, S., Okubo, T., Yamaguchi, Y., & Komiyama, H. (2001). Structure and morphology of self-assembled 3-mercaptopropyltrimethoxysilane layers on silicon oxide. *Applied Surface Science*, **181**(3–4), 307–316.

Husseini, G. A., Peacock, J., Sathyapalan, A., Zilch, L. W., Asplund, M. C., Sevy, E. T., & Linford, M. R. (2003). Alkyl monolayers on silica surfaces prepared using neat, heated dimethylmonochlorosilanes with low vapor pressures. *Langmuir*, **19**(12), 5169–5171.

Jian, L. (2008). Preparation and tribological characteristics of sulfonated self-assembled monolayer of 3-mercaptopropyl trimethoxysilane TiO_2 films. *Journal of Experimental Nanoscience*, **3**(4), 307–317.

Kessel, C. R., & Granick, S. (1991). Formation and characterization of a highly ordered and well-anchored alkylsilane monolayer on mica by self-assembly. *Langmuir*, **7**(3), 532–538.

Kuo, C. H., Chang, H. Y., Liu, C. P., Lee, S. H., You, Y. W., & Shyue, J. J. (2011). Effect of surface chemical composition on the surface potential and iso-electric point of silicon substrates modified with self-assembled monolayers. *Physical Chemistry Chemical Physics*, **13**(9), 3649–3653.

La Spina, R., Spampinato, V., Gilliland, D., Ojea-Jimenez, I., & Ceccone, G. (2017). Influence of different cleaning processes on the surface chemistry of gold nanoparticles. *Biointerphases*, **12**(3), 031003.

Liu, D., & Miao, Q. (2018). Recent progress in interface engineering of organic thin film

transistors with self-assembled monolayers. *Materials Chemistry Frontiers*, **2**(1), 11–21.

Marmont, P., Battaglini, N., Lang, P., Horowitz, G., Hwang, J., Kahn, A., Amato, C., & Calas, P. (2008). Improving charge injection in organic thin-film transistors with thiol-based self-assembled monolayers. *Organic Electronics*, **9**(4), 419–424.

Oberleitner, B., Dellinger, A., Castanet, A. S., Galtayries, A., & Semetey, V. (2013). A facile and versatile approach to design self-assembled monolayers on glass using thiol–ene chemistry. *Chemical Communications*, **49**(16), 1615–1617.

Osicka, J., Ilčiková, M., Popelka, A., Filip, J., Bertok, T., Tkac, J., & Kasak, P. (2016). Simple, reversible, and fast modulation in superwettability, gradient, and adsorption by counterion exchange on self-assembled monolayer. *Langmuir*, **32**(22), 5491–5499.

Pallavicini, P., Dacarro, G., Galli, M., & Patrini, M. (2009). Spectroscopic evaluation of surface functionalization efficiency in the preparation of mercaptopropyltrimethoxysilane self-assembled monolayers on glass. *Journal of Colloid and Interface Science*, **332**(2), 432–438.

Passoni, L., Criante, L., Fumagalli, F., Scotognella, F., Lanzani, G., & Di Fonzo, F. (2014). Self-Assembled hierarchical nanostructures for high-efficiency porous photonic crystals. *ACS Nano*, **8**(12), 12167–12174.

Pavlovic, E., Quist, A. P., Gelius, U., & Oscarsson, S. (2002). Surface functionalization of silicon oxide at room temperature and atmospheric pressure. *Journal of Colloid and Interface Science*, **254**(1), 200–203.

Rodriguez, C., Noval, A. M., Torres-Costa, V., Ceccone, G., & Silván, M. M. (2019). Visible light assisted organosilane assembly on mesoporous silicon films and particles. *Materials*, **12**(1), 1–14.

Ruckenstein, E., & Li, Z. F. (2005). Surface modification and functionalization through the self-assembled monolayer and graft polymerization. *Advances in Colloid and Interface Science*, **113**(1), 43–63.

Samanta, D., & Sarkar, A. (2011). Immobilization of bio-macromolecules on self-assembled monolayers: Methods and sensor applications. *Chemical Society Reviews*, **40**(5), 2567–2592.

Scales, S. A., Whitesides, G. M., Grzybowski, B., Griffin, C., Zumer, S., Whitesides, G. M., & Grzybowski, B. (2018). Self-assembly at all scales, **295**(5564), 2418–2421.

Schreiber, F. (2000). Structure and growth of self-assembling monolayers. *Progress in Surface Science*, **65**(5–8), 151–257.

Senaratne, W., Andruzzi, L., & Ober, C. K. (2005). Self-assembled monolayers and polymer brushes in biotechnology: Current applications and future perspectives. *Biomacromolecules*, **6**(5), 2427–2448.

Spampinato, V., Parracino, M. A., La Spina, R., Rossi, F., & Ceccone, G. (2016). Surface analysis of gold nanoparticles functionalized with thiol-modified glucose SAMs for biosensor applications. *Frontiers in Chemistry*, **4**(2), 1–12.

Taglietti, A., Dacarro, G., Barbieri, D., Cucca, L., Grisoli, P., Patrini, M., Arciola, C. R., Pallavicini, P. (2019). High bactericidal self-assembled nano-monolayer of silver sulfadiazine on hydroxylated material surfaces. *Materials*, **12**(2761), 1–13.

Tan, K. T., White, C. C., Hunston, D. L., Clerici, C., Steffens, K. L., Goldman, J., & Vogt, B. D. (2008). Fundamentals of adhesion failure for a model adhesive (PMMA/Glass) joint in humid environments. *Journal of Adhesion*, **84**(4), 339–367.

Tougaard, S. (1998). Accuracy of the non-destructive surface nanostructure quantification technique based on analysis of the XPS or AES peak shape. *Surface and Interface Analysis*, **26**(4), 249–269.

Tougaard, S., & Yubero, F. (2004). QUEELS software package for calculation of surface effects in electron spectra. *Surface and Interface Analysis*, **36**(8), 824–827.

Ulman, A. (1996). Formation and structure of self-assembled monolayers. *Chemical Reviews*, **96**(4), 1533–1554.

Wang, M., Liechti, K. M., Wang, Q., & White, J. M. (2005). Self-assembled silane monolayers: Fabrication with nanoscale uniformity. *Langmuir*, **21**(5), 1848–1857.

Wink, T., Van Zuilen, S. J., Bult, A., & Van Bennekom, W. P. (1997). Self-assembled monolayers for biosensors. *Analyst*, **122**(4), 43–50.

Yan, Z., Sun, Z., Lu, W., Yao, J., Zhu, Y., & Tour, J. M. (2011). Controlled modulation of electronic properties of graphene by self-assembled monolayers on SiO2 substrates. *ACS Nano*, **5**(2), 1535–1540.

Yang, Y., Bittner, A. M., Baldelli, S., & Kern, K. (2008). Study of self-assembled triethoxysilane thin films made by casting neat reagents in ambient atmosphere. *Thin Solid Films*, **516**(12), 3948–3956.

Chapter 3

Optimization of process conditions of SAM synthesis

After the identification of a proper formulation, the study of the process conditions represented the second part of the rationalization of SAM synthesis. The kinetics of glass functionalization with THIOL and AMINO silanes was studied combining XPS and time-of-flight secondary ion mass spectrometry (ToF – SIMS). Moreover, the impact of an increase in the reaction temperature (40 °C) on the surface properties of glass functionalized with THIOL silane was investigated with micro- and macro-characterization techniques, including contact angle, field emission scanning electron microscopy (FE – SEM), and XPS. The results of this part of the study pointed out that the key parameter to be manipulated to adapt the synthesis method to the specific silane chemistry was the reaction time. In order to verify the effective functionalization of glass with a single layer of THIOL silane molecules, the thickness of the functionalized layer was evaluated with XPS and ellipsometry.

3.1 Materials & Methods

3.1.1 Synthesis of SAMs

The synthesis of SAMs was performed as described in § 2.3.2 considering the optimized formulation. Surface activation was also carried out according to the optimized set-up (5:1 H_2SO_4 : H_2O_2, incubation time = 1 h). The silanization step was performed in anhydrous toluene, and the silane concentration was 0.054 M. Samples were prepared by modifying only one parameter. The reaction time ranged 1 h – 24 h for THIOL silane and 15 min – 15 h for AMINO silane. The reaction was carried out at room temperature (20 °C). To evaluate the impact of reaction temperature on surface functionalization, an additional test was carried out with THIOL silane setting the reaction temperature and time at 40 °C and 4 h, respectively. The rinsing step was unmodified. The detailed silanization conditions are listed in Tab. 10, together with the sample references. Samples were prepared in triplicate.

The results presented in this chapter have been partially published in (Artusio et al., 2020a).

Table 10 The detail of silanization conditions studied during the optimization of process parameters.

Sample code	Silane	Reaction time, h
T6	THIOL	1
T7	THIOL	5
T8	THIOL	24
T9*	THIOL	4
A4	AMINO	0.25
A5	AMINO	0.5
A6	AMINO	1
A7	AMINO	5
A8	AMINO	24

* The reaction temperature was 40 °C.

3.1.2 Physico-chemical characterization of SAMs

Contact angles and XPS analyses were performed as described in § 2.3.3.1 and § 2.3.3.3. In addition, angle-resolved XPS (AR-XPS) analyses were carried out setting take-off angle (ToA) at 45° and 73°. The depth of penentration of XPS is a function of ToA and can vary from approx. 10 nm at low ToA to few nm at high ToA. Tilting the sample maximized the instrument sensitivity towards the upper layers of the sample surface.

3.1.2.1 Time-of-flight secondary ion mass spectrometry (ToF – SIMS)

The surface chemistry of SAMs was additionally explored by ToF-SIMS (ToF IV, ION TOF GmbH, Germany). Bi^{3+} was selected as the source of primary ions, the raster area was 100 x 100 μm^2. The accelerating voltage of the liquid metal ion gun (LMIG) was set at 25 keV. All the analyses were performed in static conditions, and the ion dose was kept below 10^{12} ions/cm^2. The primary ion beam was in pulsed mode with beam current of 0.5 pA. The acquisition time was 45 s for each spectrum. The surface charging up during the acquisition of positive mass spectra was dissipated by using an electron flood gun. Seven different spots were analyzed per sample. The calibration peak-list included CH^+, CH_2^+, CH_3^+, $C_2H_3^+$, CHO^+, $C_3H_4^+$, $C_3H_5^+$, $C_4H_7^+$ and $C_5H_9^+$ mass fragments. Peak-lists of positive spectra were created on SurfaceLab software (ver. 6, IONTOF GmbH). More than 250 peaks could be detected in each spectrum. Data analysis techniques were used to help in the interpretation of data, given the large number of peaks and collected spectra. In particular, multivariate analysis (MVA) methods successfully reduced the size of large datasets, ensuring minimal loss of information (Graham & Castner, 2012; Trindade et al., 2017; Tyler et al., 2007). Non-negative matrix factorialization (NMF) was performed after the loading of the normalized selected peak intensities in the SimsMVA software (Trindade et al., 2018).

3.1.2.2 Ellipsometry

The SAM thickness was directly measured by ellipsometry (alpha-SE, J.A. Woollam Co., Lincoln, NE, USA). Measurements were performed at 65, 70, and 75 ° angles between the

source of incident light and the detector. The sample was placed on the dedicated stage and vacuum was applied to keep the sample in place during the measurement. The untreated glass was first analyzed to build a model describing the trends of light intensity as a function of the wavenumber on CompleteEASE software (ver. 4.63, J.A. Woollam Co.). The model was built starting from known parameters of the sample: refractive index = 1.523, surface roughness = 0.128 nm, and sample thickness = 0.15 mm. The unknown parameters of the Cauchy model, such as complex refractive indexes and angle offsets, were obtained by fitting the collected spectra. Then, glasses functionalized with SAMs were analyzed. The glass layer was described with the previously obtained model. The additional layer was described by means of a second Cauchy model, whose refractive index and thickness were obtained by fitting. The fitting procedure was refined until mean square error (MSE) was below 2.5. Three different spots were analyzed per sample, and measurements were performed on triplicates.

3.1.2.3 Field-emission scanning electron microscopy (FE – SEM)

The surface of untreated glass and THIOL SAMs was also investigated by means of FE – SEM (Merlin, ZEISS, Germany). In order to minimize the morphology alteration during the metallization step, platinum coatings were selected. Samples were coated with a few nm-thin layer of platinum and transferred to the SEM chamber. SEM operative parameters were 100 pA as tip current, 3 keV as operating voltage, and 2.2 mm as working distance. The InLens detector was employed. The analyses were performed on triplicates.

3.2 The impact of reaction time on SAM formation

The time of incubation of glass coverslips in the silanizing solution was first investigated. THIOL and AMINO silanes were selected as model molecules. The reference samples are T6 – 8 and A4 – 8. The preliminary results obtained in § 2.6 for silane concentration foresaw the possibility of having distinct reaction kinetics depending on the silane end group. Since contact angle analyses were not sensitive enough to discern among fine differences in surface chemistry, the kinetics of self-assembly was monitored with more sophisticated spectroscopy techniques.

3.2.1 XPS investigation of self-assembly kinetics

The kinetics of self-assembly was studied by stopping the silanization reaction at different time instants and analyzing the surface chemistry by XPS. The atomic composition was quantified, as reported in Tab. A2 (Appendix A), and the evolution of silicon, carbon, and sulfur/nitrogen at% was quantified. Results for THIOL and AMINO silanes are collected in Fig. 14. The initial values referred to activated glass. The evolution of characteristic elements of glass, i.e., silicon, and of the adlayer, i.e., carbon and sulfur/nitrogen, proceeded as expected. For both silanes, a decrease in silicon and an increase in carbon and characteristic element concentrations were observed as a function of time. Then, the surface chemistry stabilized around a plateau. Nevertheless, despite the general common trend, major differences could be evinced.

As far as THIOL silane was concerned, the at% of Si2p decreased from 25 to 20%. Conversely, C1s and S2s increased from 7 to 17%, and from 0 to 3%, respectively. The samples composition reached a plateau after 15 h. Samples prepared with AMINO silane, instead, displayed a much faster and noteworthy evolution. Si2p experienced a 2-fold larger decrease compared to THIOL silane. C1s increased up to more than 50% of relative composition, and N1s jumped to 10%. Plateau conditions were achieved in 1 h, as a result of the initial sharp variations in chemical compositions. Overall, it was inferred that AMINO silane led to roughly 3-fold lager extent of functionalization, compared to THIOL silane, in a fraction of the time.

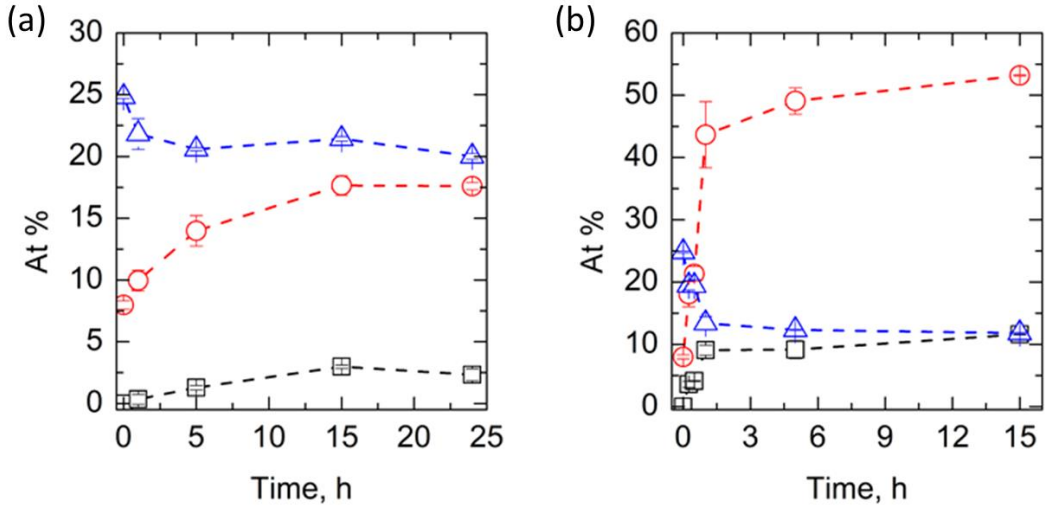

Figure 14 Atomic composition of glass functionalized with (a) THIOL and (b) AMINO silanes as a function of reaction time. The relative concentration of silicon (triangles, blue curve), carbon (circles, red curve), sulfur/nitrogen (squares, black curve) was calculated from XPS data. Synthesis was carried out with 0.054 M silane in anhydrous toluene at room temperature. The picture was taken from (Artusio et al., 2020a) with modification.

Self-assembly kinetics resulted to be governed by the polarity of the silane end group. On the one hand, thiol-terminated silanes displayed a slow assembly process. Plateau conditions were achieved smoothly, and the progress of self-assembly on the surface could be controlled. On the other hand, amino-terminated silanes resulted in fast and scarcely controlled functionalization. The comparison between the plateau compositions of the samples suggested that AMINO silane led to a multilayered structure on the glass surface as an excess of organic material was obtained for long incubation time.

The process of self-assembly on glass is composed of two main steps: the diffusion-controlled reaction of silanes with the active surface and the successive slow crystallization of the layer (Whitesides & Grzybowski, 2002). For THIOL silane, the process kinetics was dictated by the first step, as diffusion and reaction at the solid-liquid interface of silanes occurred slowly. Equilibrium was achieved within 15 h, and longer reaction times were not deleterious for the surface chemistry. Plateau conditions corresponded to monolayer conditions, as suggested by S/C ratios of about 0.2. As further discussed in § 3.4.3, multilayering of organic matter and silane self-polymerization were successfully avoided. When the interfacial reaction regarded amino-propyl chains, the first step was much faster. By comparing the relative compositions of samples prepared with AMINO silane to the plateau values of THIOL silane, monolayer conditions for glass functionalized with AMINO silane were identified. Such a comparison could be made since the two functionalizing agents displayed exactly the same chemistry, except for the characteristic

element of the end group, and XPS was not sensitive to light elements such as hydrogen. Monolayer conditions were achieved after 30 min (sample A5), but did not stabilize. Sample A5 was characterized by a smooth topography, with surface roughness comparable to the untreated glass However, for longer reaction time, the silanization reaction proceeded with the deposition of more material at the interface until equilibrium with the residual AMINO silane molecules in solution was achieved.

3.2.2 ToF-SIMS investigation of self-assembly kinetics

Self-assembly kinetics of THIOL and AMINO silanes was also followed by ToF-SIMS. Spectra collecting the results of sample cata-ionization were processed with NMF techniques. Endmembers were identified, corresponding to activated glass and functionalized glass. The results are sketched in Fig. 15. The X-axis refers to the "activated glass" endmember, which was equal to 1 at t = 0 h. The Y-axis, instead, referred to the "functionalized glass" endmember, which was equal to 1 at plateau conditions. Thus, its unitary value corresponded to monolayer conditions for THIOL silane and to multilayer conditions for AMINO silane.

The NMF analyses confirmed the controlled self-assembly underwent by THIOL silane and the fast deposition of AMINO silane on the glass surface. Fig. 15 (a) highlights a clear distinction among the scores of THIOL silane samples obtained after increasing incubation time. ToF-SIMS was very sensitive in detecting the first changes in surface composition after 1 h of reaction time. Glass lost approx. 60% of its initial features. Then, the evolution of samples chemistry was smoother and slowly progressed towards the features of 100% THIOL-functionalized glass. Samples obtained after 15 or 24 h displayed similar features, in agreement with XPS analyses.

A different trend was observed for AMINO silane, as sketched in Fig. 15 (b). Samples scores were much more dispersed than those of THIOL silane samples. Such a tendency denoted a strong dependence of surface chemistry on the analyzed spot. After 1 h, A6 sample displayed scores from 50 to 80% related to the "functionalized glass" endmember. The distribution of scores relative to longer times overlapped that of A6, confirming the uncontrolled progress of silanization.

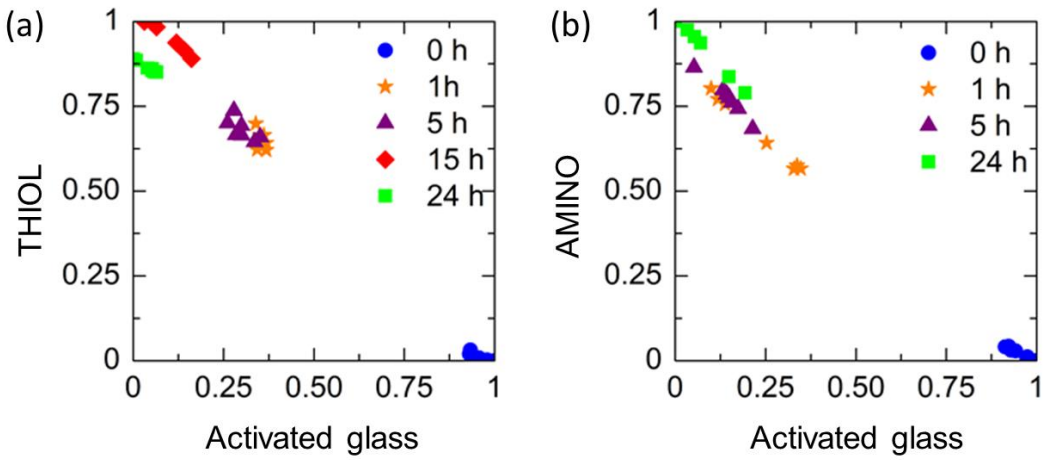

Figure 15 NMF analyses of ToF-SIMS data for glass functionalized with (a) THIOL and (b) AMINO silanes at different reaction times. The X-axis refers to the "activated glass" features, whereas the Y-axis refers to the "functionalized glass" features. Seven ToF-SIMS spectra were analyzed per condition. The picture was taken from (Artusio et al., 2020a) with modification.

The cross-comparison between XPS and ToF-SIMS data revealed a good agreement on the temporal evolution of surface chemistry. XPS allowed for the direct quantification of surface composition and the identification of monolayering conditions. ToF-SIMS enabled a qualitative evaluation of the character of the surface and the uniformity of surface chemistry.

In conclusion, the reaction time was a key parameter in the silanization process. The length of the functionalization step is fundamental for completing a silane monolayer. THIOL SAMs proved to be undisturbed by reaction times longer than 15 h. Conversely, AMINO SAMs were completed in 30 min, and longer incubation times led to multilayered structures. In this case, the equilibrium did not correspond to the monolayer formation but rather to the depletion of silane in solution. The higher reactivity of AMINO silane promoted its uncontrolled self-polymerization, and the reaction had to be stopped after 30 min to get monolayers.

3.3 The role of reaction temperature

The study on the optimization of process parameters was finally focused on the reaction temperature. In particular, the silanization reaction with THIOL silane was carried out for 4 h in anhydrous toluene at 40 °C (sample T9) to accelerate the silanization kinetics and reduce reaction time. Surface hydrophobicity and chemistry were investigated.

3.3.1 Contact angle

Water contact angles of T9 resulted to be 73.7 (± 3.5)°. T3 samples, instead, led to contact angles around 65°. The higher value and standard deviation of T9 highlighted a less controlled anchoring of THIOL silane. The reaction kinetics was boosted by heating, and surface hydrophobicity higher than that of sample T8 was obtained in a fraction of the time. Nevertheless, faster anchoring may result in less ordered layers, or even in localized deposits of silane. Therefore, surface chemistry and topography were further analyzed.

3.3.2 Investigation of sulfur oxidation with XPS

The samples were first analyzed with XPS by acquiring survey scans. The ratios between elements are reported in Tab. 11. The comparison to the corresponding ratios obtained for sample T3 highlighted a strong decrease in S/Si and S/C. Therefore, despite the higher hydrophobicity of the surface, the relative amount of sulfur was lower.

Table 11 Comparison between S/Si, C/Si, O/Si, and S/C ratios of T3 and T9 samples as evaluated from XPS survey scans taken at ToA = 0°.

Sample	S/Si	C/Si	O/Si	S/C
T3	0.14	0.82	2.60	0.17
T9	0.02	0.64	3.01	0.03

The chemical state of sulfur S2p was investigated by HR-XPS, as reported in Fig. 16. Two peaks centered at 164.3 and 169.0 eV were identified. The latter peak was attributed to oxidized sulfur, $S2p_{ox}$ (Beamson & Briggs, 1992). A predominance of the $S2p_{ox}$ component, which corresponded to 70%, was observed, indicating that the majority of the sulfur existed in the oxidized state, rather than as thiol groups. Heating the system while performing the silanization step revealed to be counterproductive. On the one hand, temperature speeded up reaction kinetics and allowed for a marked and fast increase in surface hydrophobicity. On the other hand, a deeper investigation of surface chemistry disclosed poor functionalization. All the evidence highlighted the high sensitivity of the process towards external factors. In order to achieve regular and high density of thiol groups, the self-assembly had to occur slowly and spontaneously. Kinetic boosting encouraged the formation of disulfide groups or other undesired reactions involving the sensitive thiol groups.

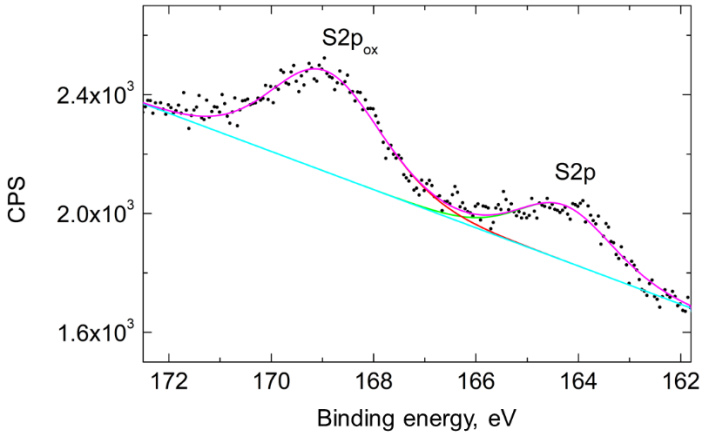

Figure 16 HR-XPS of S2p region of sample T9 at ToA = 0°. The oxidized state of sulfur was predominant.

3.3.3 Surface morphology

The morphology of untreated and functionalized glass was also investigated. Fig. 17 (a) and (b) display FE-SEM micrographs referring to untreated glass and sample T3, respectively. As expected, the two samples did not show any significant difference in their morphology. It was therefore demonstrated that the controlled surface functionalization with thiol groups did not alter the morphological attributes of glass, as the obtained surface was flat. When the silanization process was carried out in mildly heated systems, the superficial morphology significantly changed. Fig. 17 (c) highlights the presence of localized clusters on the surface of sample T9. Such deposits only interested local spots of the surface and were the result of the uncontrolled deposition of THIOL silane.

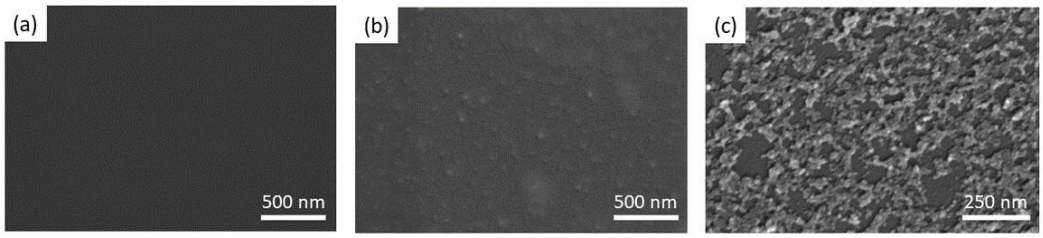

Figure 17 FE-SEM micrographs of (a) untreated glass, (b) T3, and (c) T9 samples.

3.4 Surface analysis of optimized THIOL SAMs

After the identification of the optimal set of synthesis parameters for thiol-terminated SAMs (sample T3), a more detailed analysis of the chemistry exposed by the surface was performed with AR-XPS and HR-XPS. In addition, the thickness of the functionalized layer was evaluated comparing XPS and ellipsometry results.

3.4.1 Characteristic element ratios vs. ToA

Characteristic elements of the organic adlayer, i.e., C and S, were referred to a bulk element, i.e, Si, and quantified from XPS survey scans recorded at increasing ToA. Also, C/S ratios were calculated. The results are collected in Fig. 18. The XPS sampling depth is inversely proportional to ToA, thus higher ToA guarantees higher sensitivity towards the upper layers of the sample. At high ToA, the quantity of photoelectrons coming from the bulk is reduced, favoring those coming from the most exposed layers of the sample. Thus, AR-XPS provides a useful tool to tackle the configuration of adlayers and understand the distribution of elements along the superficial layers of the sample. However, one of the drawbacks of a very high ToA is represented by the strong reduction of counts, and thus the greater uncertainty in quantification.

The trend of C/Si ratio underwent a remarkable increase with the ToA, going from 0.82 to 1.69. Similarly, S/Si ratio increased from 0.14 to 0.35. Thus, both ratios approx. doubled comparing scans recorded at ToA = 0 and 73°. C/Si ratio was much higher than S/Si because the presence of carbon was related to the propylic chain, whereas only one atom of sulfur was present per silane. Thus, it was demonstrated that THIOL silane molecules only reacted at the interface between activated glass and solution. Moreover, the XPS sampling depth at 73° is in the order of few nm. The marked increase in C/Si and S/Si showed that the thickness of the layer was smaller than the instrument sampling depth. Such a result represented the first clue of the confinement of thiol-propane chains to a less than few nm-thick layer on glass. The layer thickness will be quantified in § 3.4.3.

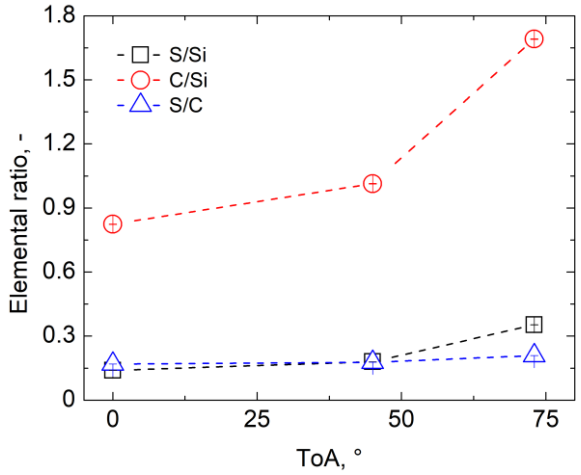

Figure 18 Element ratio of T3 sample vs. ToA. S/Si, C/Si, and S/C are reported. ToA was set at 0, 45, and 73°. Error bars refer to SD.

The ratio between two characteristic elements of the adlayer, i.e., S/C, displayed negligible deviations from 0.2 with ToA. The hypothetic structure of SAM foresees a

constant S/C ratio. As a matter of fact, if carbon and sulfur only belong to the adlayer, their ratio is independent of the sampling depth, provided that the latter is higher than the SAM thickness.

3.4.2 HR-XPS of characteristic elements

The surface chemistry of T3 sample was deeply investigated by HR-XPS, and the relative weight of components was quantified. C1s, S2p, and O1s peaks were analyzed at ToA = 0°. The C1s region is reported in Fig. 19 (a), and the quantification is reported in Tab. 12. A major peak relative to C1s was identified and fitted with two components. The most intense one referred to C-C at 285.0 eV and was due to the presence of propylic chains of THIOL silane. A less intense component was due to C-O bonds at 286.5 eV. The detection of ether bonds could be explained by the presence of unreacted methoxy groups within the layer. Residual -OCH_3 may be attributed to bond strain and steric hindrance issues. Ideally, the silane molecules should be anchored to the surface by means of three covalent bonds, but bond strain limit the actual number of bonds to one or two. The cross-polymerization of THIOL silane was thus proposed as the main mechanism contributing to the layer stability (Onclin et al., 2005). Moreover, as long as the anchoring proceeds, the glass surface becomes more and more populated by thiol-propane chains. At the same time, the labile surface hydroxylation may decay, making it is increasingly difficult for methoxy groups to meet the surface and participate to condensation reactions. Also, -OCH_3 may be due to THIOL silane molecules embedded in the highly packed layer. Therefore, C-O was attributed to incomplete THIOL silane conversion and, marginally, to carbon contamination.

As already discussed in § 2.4.3, the C1s region also included two minor peaks relative to K2p doublet. K2p is present as a glass bulk element and was employed as a reference in AR-HR-XPS analyses. Fig. 19 (b) displays the normalized HR spectra of C1s region recorded at different ToA. When ToA increased, the weight of C1s peak progressively increased, along with a progressive reduction of the intensity of K2p doublet. Carbon and potassium could be found in the adlayer and in the bulk of the sample, respectively. Considering the distinct location of the two elements and the decreasing depth of penetration of XPS with ToA, the drop of K2p signal confirmed that the organic layer was extremely thin.

Then, S2p region was analyzed. Peak fitting is reported in Fig. 19 (c). The double splitting typical of metal ions was observed. The main S2p peak was deconvoluted into two components centered at 162.8 and 164.1 eV. The minor component was half of the major one. The second main peak, centered at 168.4 eV, was attributed to oxidized sulfur, $S2p_{ox}$. $S2p_{ox}$ represented 13.8% of the total sulfur and indicated a partial oxidation of the thiol groups. Thus, the majority of sulfur was present in its elementary state, and only a fraction was oxidized. Lastly, O1s region was examined. Fig. 19 (d) reports the presence of a major peak at 532.0 eV related to the Si-O bonds of glass. Minor components were related to the presence of impurities in the glass or to unreacted methoxy groups.

The HR and AR-XPS study demonstrated the success of surface functionalization and explored the chemical state of typical elements, suggesting that silane molecules were confined to few nm on the glass surface.

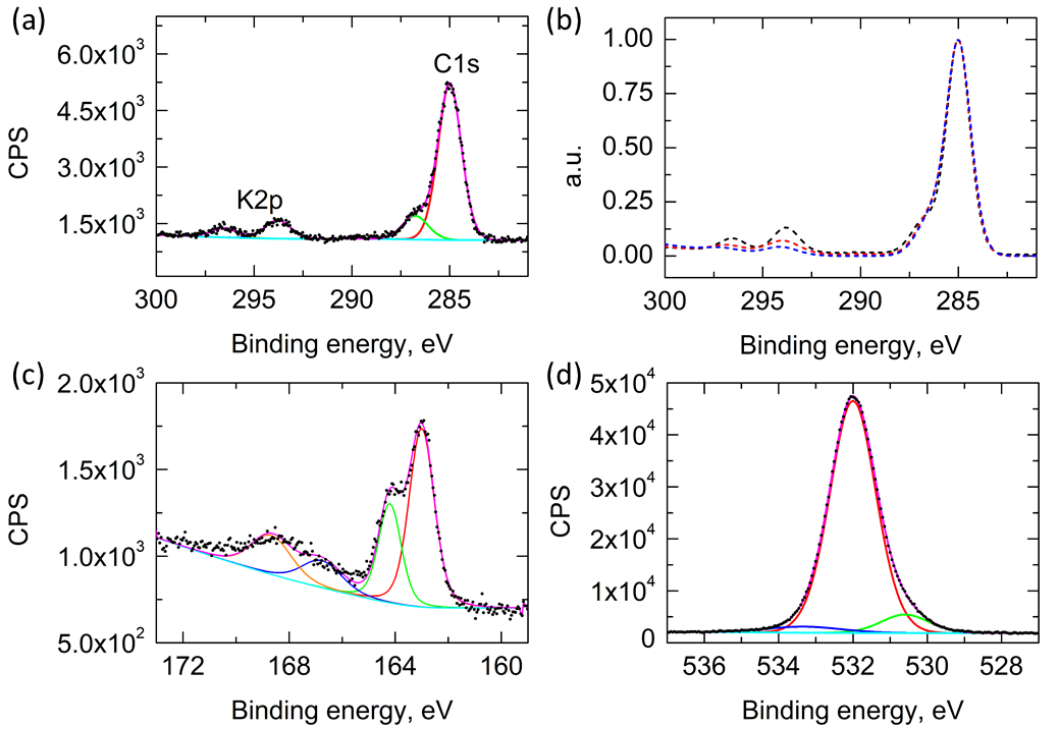

Figure 19 HR-XPS of (a) C1s region, (b) normalized C1s region at ToA = 0° (black), 45° (red), and 73° (blue), (c) S2p region, and (d) O1s region of sample T3. Dots refer to experimental data. A U-3 Tougaard background was used. Peak fitting was performed with Gaussian-Lorentzian functions. The picture was taken from (Artusio et al., 2020a) with modification.

Table 12 Detail of quantification of C1s region of sample T3. Results refer to spectra collected at ToA = 0°.

Sample	C-C (285.0 eV)	C-O (286.6 eV)	K2p3/2 (293.2 eV)	K2p1/2 (296.0 eV)
T3	80.2	16.8	2.1	1.0

3.4.3 Thickness of THIOL silane layer

The analysis of sample chemistry by AR-XPS pointed out that surface modification occurred within a layer no more than a few nm thick. The thickness of the modified layer was measured with two different techniques in order to quantify the number of THIOL silane layers deposited on the surface.

3.4.3.1 XPS

XPS not only provides an essential tool for surface analysis but can also be employed to estimate the thickness of thin adlayers (Cheng et al., 2008; Dhayal & Ratner, 2009; Herzer et al., 2010; Roldán et al., 2011). Different approaches have been proposed in the literature. In the present study, the electronic attenuation length (EAL) (Bain & Whitesides, 1989) and the thickogram (Cumpson & Zalm, 2000) models were selected.

The EAL approach assumes uniform thickness and exponential attenuation of electrons in the adlayer. In this case, EAL was the electronic attenuation length of silicon in the adlayer which was set at 0.48 nm as calculated from the NIST database (Powell &

Jablonski, 2002). 18 valence electrons, photoionization asymmetry parameter of 1.03, and bandgap equal to 2.5 eV for the adlayer were considered for the estimation of EAL. The thickness resulted to be 0.75 (± 0.01) nm.

The second approach for the estimation of layer thickness from XPS data relied on the use of a thickogram. Relative sensitivity factors (RSF) and kinetic energy (KE) of an element peculiar of the bulk and the adlayer must be known. S2s (RSF = 1.41, KE = 1258.6 eV) and Si2p (RSF = 1.18, KE = 1383.6 eV) were selected as peaks representing the adlayer and the bulk, respectively. Data referring to XPS survey scans recorded at ToA = 0° were considered. The graphical model has a precision of 1%. The layer thickness resulted to be 0.80 nm.

Both models led to thickness values slightly smaller than THIOL silane molecule length, corresponding to 0.9 nm (Ali et al., 2008). Such a finding was attributed to the loss of the methoxy groups after bonding to the surface. The estimation of layer thickness demonstrated that a single layer of silane molecules had been anchored to the glass surface.

3.4.3.2 Ellipsometry

The thickness of the functionalized layer was also measured by ellipsometry, as a comparison. The obtained value was 0.75 nm, in good agreement with the XPS results. Thus, it was demonstrated that the optimized synthesis protocol for THIOL silanes led to the controlled and robust functionalization of surfaces by means of SAMs.

3.5 Final remarks

The study of the process conditions of SAM synthesis, namely reaction time and temperature, highlighted several aspects. The self-assembly kinetics depended on the polarity of the trimethoxysilanes, since monolayers were obtained in 15 h for THIOL silane and 30 min for AMINO silane. Longer reaction times did not alter the single layer of THIOL silane, whereas they led to multilayered structures for AMINO silane. The influence of the reaction temperature on THIOL silane self-assembly was also studied, revealing the presence of oxidized sulfur and polymeric residues as a source of increased surface hydrophobicity. Overall, carrying out the silanization reaction at room temperature ensured a good compromise between the quality of functionalization and sustained reaction kinetics. The tuning of the reaction time was identified as the key for adapting the proposed synthesis protocol to different silane chemistries.

The study of formulation and process conditions supported the identification of an optimal set of synthesis conditions. The formation of a THIOL silane monolayer on the glass surface, suggested by AR and HR-XPS, was also demonstrated by the direct measurement of the thickness of the organic layer by ellipsometry. The thickness was in good agreement with the theoretical length of a silane molecule.

References

Ali, M. Ben, Bessueille, F., Chovelon, J. M., Abdelghani, A., Jaffrezic-Renault, N., Maaref, M. A., & Martelet, C. (2008). Use of ultra-thin organic silane films for the improvement of gold adhesion to the silicon dioxide wafers for (bio)sensor applications. *Materials Science and Engineering C*, **28**(5–6), 628–632.

Artusio, F., Fumagalli, F., Bañuls-Ciscar, J., Ceccone, G., & Pisano, R. (2020a). General and adaptive synthesis protocol for monolayers as tunable surface chemistry platforms for biochemical applications. *Biointerphases*, **15**(4), 041005.

Bain, C. D., & Whitesides, G. M. (1989). Attenuation lengths of photoelectrons in hydrocarbon films. *Journal of Physical Chemistry*, **93**(4), 1670–1673.

Beamson, G., & Briggs, D. (1992). XPS of Polymers Database. Surface Spectra (UK).

Cheng, F., Gamble, L. J., & Castner, D. G. (2008). XPS, TOF-SIMS, NEXAFS, and SPR characterization of nitrilotriacetic acid-terminated self-assembled monolayers for controllable immobilization of proteins. *Analytical Chemistry*, **80**(7), 2564–2573.

Cumpson, P. J., & Zalm, P. C. (2000). Thickogram: A method for easy film thickness measurement in XPS. *Surface and Interface Analysis*, **29**(6), 403–406.

Dhayal, M., & Ratner, D. M. (2009). XPS and SPR analysis of glycoarray surface density. *Langmuir*, **25**(4), 2181–2187.

Graham, D. J., & Castner, D. G. (2012). Multivariate analysis of ToF-SIMS data from multicomponent systems: The why, when, and how. *Biointerphases*, **7**(1–4), 1–12.

Herzer, N., Hoeppener, S., & Schubert, U. S. (2010). Fabrication of patterned silane based self-assembled monolayers by photolithography and surface reactions on silicon-oxide substrates. *Chemical Communications*, **46**(31), 5634–5652.

Onclin, S., Ravoo, B. J., & Reinhoudt, D. N. (2005). Engineering silicon oxide surfaces using self-assembled monolayers. *Angewandte Chemie - International Edition*, **44**(39), 6282–6304.

Powell, C. J., & Jablonski, A. (2002). The NIST Electron Effective-Attenuation-Length Database. *Journal of Surface Analysis*, **9**(3), 322–325.

Roldán, M. J. P., García, C. P., Marchesini, G., Gilliland, D., Ceccone, G., Mehn, D., Colpo, P., & Rossi, F. (2011). Chemical modification and patterning of self assembled monolayers using scanning electron and ion-beam lithography. *Microelectronic Engineering*, **88**(8), 1948–1950.

Trindade, G. F., Abel, M. L., & Watts, J. F. (2017). Non-negative matrix factorisation of large mass spectrometry datasets. *Chemometrics and Intelligent Laboratory Systems*, **163**(1), 76–85.

Trindade, G. F., Abel, M. L., & Watts, J. F. (2018). simsMVA: A tool for multivariate analysis of ToF-SIMS datasets. *Chemometrics and Intelligent Laboratory Systems*, **182**(10), 180–187.

Tyler, B. J., Rayal, G., & Castner, D. G. (2007). Multivariate Analysis Strategies for Processing ToF-SIMS Images of Biomaterials. *Biomaterials*, **28**(15), 2412–2423.

Whitesides, G. M., & Grzybowski, B. (2002). Self-assembly at all scales. *Science*, **295**(5564), 2418–2421.

Chapter 4

Validation of the protocol for SAM synthesis

In the present chapter, the general synthesis protocol identified in Chapter 3 is validated by applying it to trimethoxysilanes exposing methacrylate and glycidyloxy end groups. The quality of functionalization was confirmed by ToF-SIMS and XPS. Moreover, a comparison between samples prepared with trimethoxysilanes and triethoxysilanes is presented to demonstrate the better performance of the methoxy exit groups. The identification of a general synthesis route for SAMs enabled the preparation of four different SAMs exposing thiol, amino, glycidyloxy, and methacrylate groups. A detailed investigation of the surface properties of these SAMs is discussed at the end of this chapter. More specifically, SAM thickness and packing factor, surface zeta potential, and surface free energy will be addressed. The results will serve as a reference for the following part of the study dedicated to the determination of API/protein – surface interactions in the crystallization process.

4.1 Materials and Methods

4.1.1 Synthesis of SAMs

The synthesis of SAMs was performed as described in § 2.3.2. In addition to THIOL and AMINO silanes, 3-glycidyloxyopropyltrimethoxysilane (GLY, ≥ 98%), 3-glycidyloxyopropyltriethoxysilane (GPTES, ≥ 97%) and 3-(trimethoxysilyl) propylmethacrylate (ACR, 98%) were employed. Surface activation was carried out according to the optimized set-up (5:1 H_2SO_4 : H_2O_2, incubation time = 1 h). The silanization step was performed in anhydrous toluene at room temperature (20 °C), and the silane concentration was 0.054 M. The reaction time was 30 min for AMINO silane and 15 h for all the other silanes. The silanization conditions involving the additional silanes are listed in Tab. 13.

The results presented in this chapter have been partially published in (Artusio et al., 2020a).

Table 13 The silanization conditions studied for the validation of SAM synthesis.

Sample code	Silane	Concentration, M	Reaction time, h
M1	ACR	0.054	15
G1	GLY	0.054	15
G2	GPTES	0.054	15

4.1.2 Physico-chemical characterization of the surfaces

Static contact angles were measured as described in § 2.3.3.1. In addition to water, diiodomethane and glycerol were used as probing liquids. In this way, the surface energy and its component could be calculated thanks to the van Oss-Chaudhury-Good model (Berg, 1993; Rudawska & Jacniacka, 2018). XPS and ellipsometry were performed as described in § 2.3.3.3 and 3.1.2.2, respectively. ToF-SIMS analyses were carried out following the same procedure presented in § 3.1.2.1. For ToF-SIMS spectra, non-negative matrix factorialization (NMF) and principal component analysis (PCA) were performed after the loading of the normalized selected peak intensities in the SimsMVA software (Trindade et al., 2018).

4.1.2.1 Surface zeta potential (SZP)

A technique based on dynamic light scattering (DLS, Zetasizer NANO ZS90, Malvern Panalytical, Worcestershire, UK) was employed to evaluate surface zeta potential (SZP). SAM-functionalized coverslips were carefully cut into 4 x 6 mm^2 pieces and glued on dedicated sample holders. The sample holder was then mounted on the device for SZP measurements (ZEN1020, Malvern Panalytical, Worcestershire, UK). The sample was secured between two Pd electrodes. The device was coupled with a disposable polystyrene cuvette previously filled with 1 mL of standard microsphere latex. Particular care was taken to avoid the formation of bubbles during this step. The tracer mobility was measured at different positions away from the surface: 125, 250, 375, 500, and 1000 µm. The measurement carried out at 1000 µm corresponded to the mobility of the tracer unperturbed by the surface. A minimum of five measurements per sample was carried out. Analyses were performed in triplicate.

4.2 ToF-SIMS investigation of surface chemistry

Unlike XPS, ToF-SIMS is a rather qualitative technique and was applied to selected samples to study their mass fragmentation and verify the possibility of discerning among different surface chemistries starting from mass spectra. For this purpose, untreated glass, T3, A1, and M1 samples were analyzed. Representative positive mass spectra are reported in Fig. A1 in Appendix A.

All the samples displayed a significant number of hydrocarbon fragments. For the untreated glass, peaks referred to the hydrocarbon contamination highlighted by XPS analyses. As regards the functionalized glasses, the extracted carbon fragments included characteristic elements of the adlayer, such as sulfur, nitrogen, or oxygen. Given the large amount of data,

multivariate analyses (MVA) techniques were applied for data processing. Non-negative matrix factorialization (NMF) and principal component analyses (PCA) were performed, providing endmembers in the case of NMF and principal components in the case of PCA. Scores and loadings are the typical outcome of PCA and NMF analyses. The scores describe the relationship among the samples for each principal component/endmember, whereas the loadings provide information regarding how the variables (peak intensities) relate to each principal component/endmember (Henderson, 2013).

4.2.1 Multivariate analyses of ToF-SIMS data

As shown in Fig. 20 (a), ToF-SIMS spectra were successfully grouped and separated by NMF processing. Each axis of the box corresponded to an endmember, i.e., to a specific surface chemistry. The four surface chemistries were located at the distinct vertices of the box, which represented the endmember space. Such a result indicated that each spectrum was univocally related to the respective chemistry. Therefore, the surface modification was performed in an identifiable manner. The grouping of data referring to ACR SAMs turned out to be the most dispersed one, as demonstrated by the sparse purple points referring to SIMS spectra. This might be expected, because glass functionalized with ACR silane lacks easily identifiable elements which are peculiar to the molecule. Sample M1 displayed carbon and oxygen on the surface, which can also be found in the natural contaminants of untreated glass. Such a tendency was confirmed by the distribution of M1 spectra in the endmember space, pointing to more intense "untreated glass" features.

As a step further, PCA was employed for data processing in order to isolate the major components leading to differences among the samples, thanks to the evaluation of scores and loadings. Results are collected in Fig. 20 (b). The most intense and characteristic fragments isolated by PCA contained carbon, sulfur, and nitrogen. The characteristic elements of the adlayer were always detected as a part of hydrocarbon fragments. Fragments as CH_3S^+ or $C_2H_4N^+$ suggested that such elements were bound to a propylic tail.

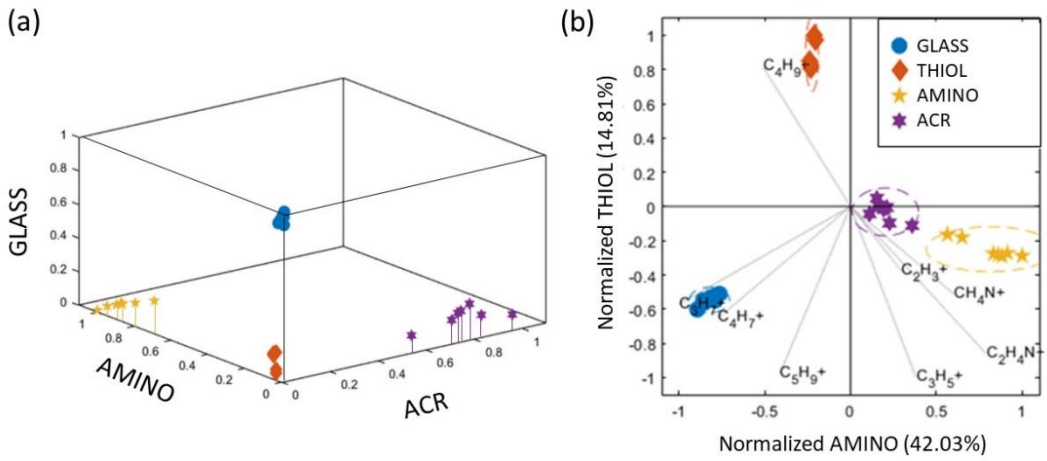

Figure 20 Outcomes of (a) NMF and (b) PCA analyses of ToF-SIMS spectra of untreated glass and glass functionalized with THIOL, AMINO, and ACR silanes. The picture was taken from (Artusio et al., 2020a) with modification.

As regards the untreated glass, PCA isolated characteristic components relative to hydrocarbon fragments. The majority of them had less than six atoms of carbon. Interestingly, the analysis of functionalized glasses revealed that the predominant fragments were characterized by three or less atoms of carbons. This finding was in agreement with the presence of propylic chains on the surface. Therefore, ToF-SIMS could also discern between carbon deriving from mere surface contamination and carbon coming from SAMs.

In addition, the excess of functionalization with AMINO silane typical of A1 samples was detected by ToF-SIMS. PCA revealed that three out of the ten most intense components relative to mass fragments contained nitrogen. Conversely, only one component containing sulfur was identified for T3 samples. Such a discrepancy could be explained by different extraction yields but also by the presence of a higher amount of AMINO-related material on the surface of A1. Therefore, the presence of multilayers of AMINO in A1 samples was also qualitatively confirmed by ToF-SIMS.

In conclusion, ToF-SIMS demonstrated the possibility to group and refer mass spectra to specific surface chemistries, proving a robust and reliable surface modification.

4.3 Validation of SAM synthesis protocol

The study carried out with THIOL and AMINO silanes for designing formulation and process parameters led to the identification of a set of synthesis conditions, summarized in Tab. 14, that can potentially be applied to other trimethoxysilanes. In order to validate the proposed protocol, GLY and ACR silanes were employed to prepare SAMs on glass using the same synthesis conditions of T3 samples. In the present section, the HR-XPS of C1s region of the optimized glass functionalization with AMINO (A5), GLY (G1), and ACR (M1) silanes will be discussed. Moreover, the choice of using methoxy-terminated silanes will be justified by comparing XPS data of glass functionalized with GLY silane (G1) and GPTES (G2).

Table 14 Optimized protocol for the synthesis of SAMs.

Solvent	Anhydrous toluene
Silane head group	Methoxy
Silane concentration	0.054 M
Reaction time	30 min for AMINO silanes 15 h for other silanes
Reaction temperature	Room temperature

4.3.1 HR-XPS of optimized samples

HR-XPS analyses of A5, M1, and G1 samples provided interesting insights into the surface chemistry. The C1s region was analyzed for all the samples and reported in Fig. 21. The

component quantification is summarized in Tab. 15. As already observed for THIOL SAMs in § 3.4.2, a major peak referring to C1s and minor peaks relative to K2p were identified. Results obtained for amino-terminated SAMs are depicted in Fig. 21 (a). The C1s peak was composed of four components. The most intense one referred to C-C (285.0 eV) and was due to the presence of propylic chains. Then, C-O, C=O, and COO-H/R components were identified at 286.6, 288.0, and 288.9 eV, respectively. Residual C-O bonds were attributed to the presence of unreacted methoxy groups. The two minor components were related to superficial contamination by carbon.

As reported in Fig. 21 (b), sample M1 displayed C-O and COO-H/R components, amounting to approx. 23 and 8 at%. The two components were attributed to the presence of methacrylate groups on the surface. As expected, the COO-H/R component of M1 resulted to be the most intense one among all the analyzed samples. Finally, Fig. 21 (c) reports the results obtained for sample G1. An inversion in the intensity ratio between C-C and C-O components was observed. The former dropped to 33 at%, whereas the latter increased to 59 at%, corresponding to a ratio of 0.6. The inversion was accompanied by a slight shift in the C-O (+ 0.1 eV) and COO-H/R (+ 0.2 eV) peaks positions. These results were taken as indicators of the presence of a large number of C-O bonds on the surface, due to the glycidyloxy groups (Beamson & Briggs, 1992).

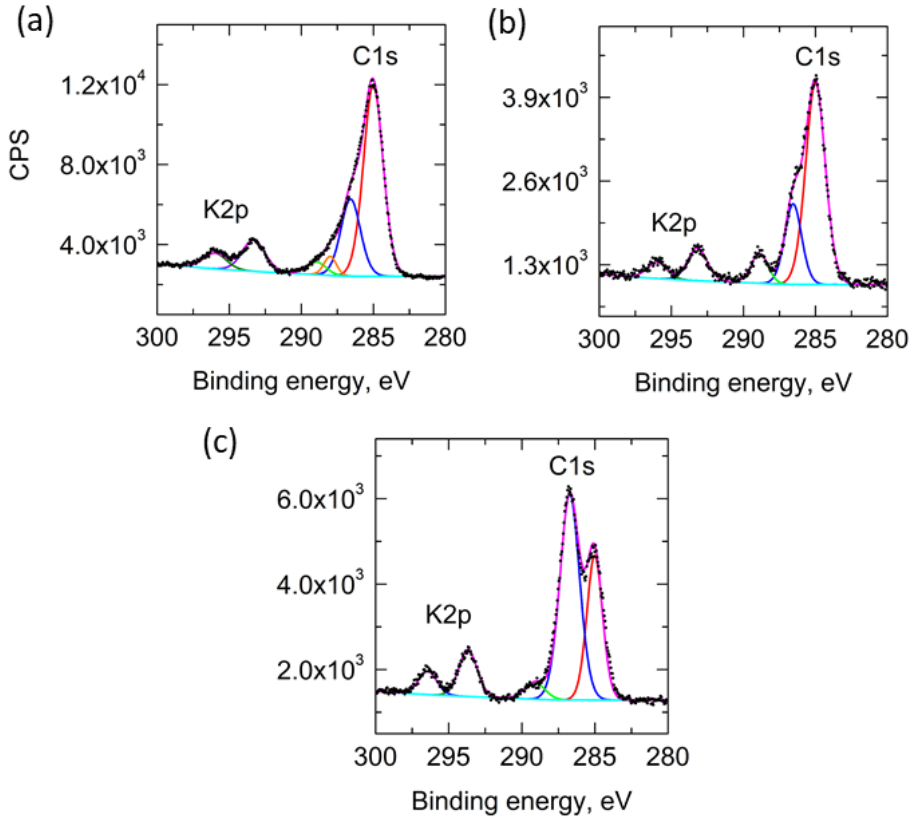

Figure 21 HR-XPS of C1s region of (a) A5, (b) M1, and (c) G1 samples. Spectra were recorded at ToA = 0°. Peak fitting was performed with Gaussian – Lorentzian functions (GL30) to identify components. The picture was taken from (Artusio et al., 2020a) with modification.

The investigation of C1s region confirmed the presence of the desired chemical groups on the surface. In addition, the relative atomic composition and the inversion in the intensity ratios provided useful tools to discern between surface modifications lacking characteristic elements, as samples M1 and G1. In addition, the doublet relative to K2p was always

clearly detected, and attested around 2 at% for $K2p_{3/2}$ and 1 at% for $K2p_{1/2}$. The obtained values agreed with the quantification of sample T3 previously reported in § 3.4.2. Therefore, thanks to the analogous chemistry of the functionalizing agents, it was concluded that the functionalization occurred in monolayers also for AMINO, ACR, and GLY silanes. As a matter of fact, the accurate and deep XPS investigation for THIOL silane was regarded as a reference calibration. Thus, the formation of SAMs with other exposed chemistries could be confirmed in a faster and easier way by XPS.

Table 15 Detail of components quantification of HR-XPS of C1s region at ToA = 0°.

Sample	C-C% (285.0 eV)	C-O% (286.6 eV)	C=O% (288.0 eV)	COO% (288.9 eV)	$K2p_{3/2}$% (293.2 eV)	$K2p_{1/2}$% (296.0 eV)
A5	63.0	25.4	4.0	4.1	2.3	1.1
M1	66.0	22.7	-	8.3	2.0	1.0
G1	32.9	58.6*	-	4.9**	2.4	1.2

*peak centered at 286.7 eV; **peak centered at 289.1 eV

4.4 The silane exit group

The chemistry of the functionalizing agent also played an important role in the formation of SAMs. In particular, the nature of the exit group can affect the reaction kinetics. In the present study, silanes carrying methoxy groups were employed. A comparison between the silanization performed with methoxy- or ethoxy-silanes is presented. GLY silane (sample G1) and GPTES (sample G2) were selected, keeping the same synthesis conditions reported in Tab. 13. After 15 h, the amount of carbon in sample G2 was only 7 at%, in contrast to 25 at% obtained for G1. The HR-XPS analysis of C1s region highlighted strong differences in the quantification of carbon components, listed in Tab. 16. Sample G2 was characterized by an inverse intensity ratio between C-C and C-O components, which was equal to 2.1. Also, binding energy shifts were not detected, and the relative amount of potassium was much higher than that obtained for G1.

Table 16 Comparison between components quantification of C1s region of G1 and G2 samples. Results refer to HR-XPS spectra collected at ToA = 0°.

Sample	C-C (285.0 eV)	C-O (286.6 eV)	COO (288.9 eV)	$K2p_{3/2}$ (293.2 eV)	$K2p_{1/2}$ (296.0 eV)
G1	32.9	58.6*	4.9**	2.4	1.2
G2	51.8	24.3	7.0	11.3	5.7

*peak centered at 286.7 eV; **peak centered at 289.1 eV

The ethoxy-silanes resulted to lead to poor surface modification after 15 h. The slower kinetics of self-assembly may be beneficial for the achievement of ordered and good quality

layers but could not guarantee a high density of groups exposed on the surface within a restricted amount of time. Therefore, it was demonstrated that methoxy-silanes guaranteed a higher and more robust extent of functionalization in a shorter time.

4.5 Thickness and packing of SAMs

Once the optimal synthesis protocol had been identified and validated by XPS, the four SAMs were analyzed with ellipsometry to quantify the thickness and the degree of packing of the layer, by evaluating the refractive index of SAMs, n_{SAM}. The packing factor of the organic layer, f_{mol}, was obtained from the comparison between n_{SAM} and n_{mol}, which is the refractive index of the specific silane molecule. f_{mol} was calculated from:

$$f_{mol} = \frac{n_{SAM} - n_{air}}{n_{mol} - n_{air}} \quad (2)$$

Knowing n_{air}, which is equal to 1.00027, and n_{mol}, provided by the chemicals' manufacturer, one can estimate and compare the packing behavior of different functionalizing agents. Results are summarized in Tab. 17.

Table 17 Thickness, refractive index, and packing factor of SAMs as calculated from ellipsometry.

Sample	Thickness, nm	n_{SAM}, -	n_{mol}, -	f_{mol}, %
T3	0.75	1.443	1.444	99.8
A5	0.76	1.429	1.424	100
M1	0.83	1.350	1.431	81.2
G1	0.90	1.423	1.429	98.6

The thicknesses were all below 1 nm, which represents the order of magnitude for the theoretical length of silane molecules. The vicinity of thickness values obtained for T3 and A5 samples reflected their similar molecule length, as the two silanes only differed for their characteristic atom (-SH and -NH_2 as end groups). Slightly thicker SAMs were obtained for M1 and G1, as expected considering the presence of bolder end groups.

The calculated packing factors highlighted a very high superficial density of functionalization that, together with the thickness values, pointed out that SAM chains were not significantly tilted. The tilt comes from the maximization of the van der Waals interactions between the chains, and denser packings require less tilt (Schreiber, 2000). A degree of packing close to 100% was obtained for T3 and A5 and was attributed to the slim configuration of the silane end groups. Bolder substituents, such as methacrylate groups, led to lower packing factors, namely around 80%. Therefore, the steric hindrance of the SAM terminal group governed the extent of layer packing, and thus the density of groups per nm^2.

4.6 Surface attributes of SAMs

The optimized synthesis protocol allowed the precise and controlled glass functionalization with selected chemical groups. The schematic representation of THIOL (T3), AMINO (A5), ACR (M1), and GLY (G1) SAMs is sketched in Fig. 22. The evaluation of the surface zeta potential and the surface energy of SAMs was performed as a conclusive step of the study of SAM synthesis.

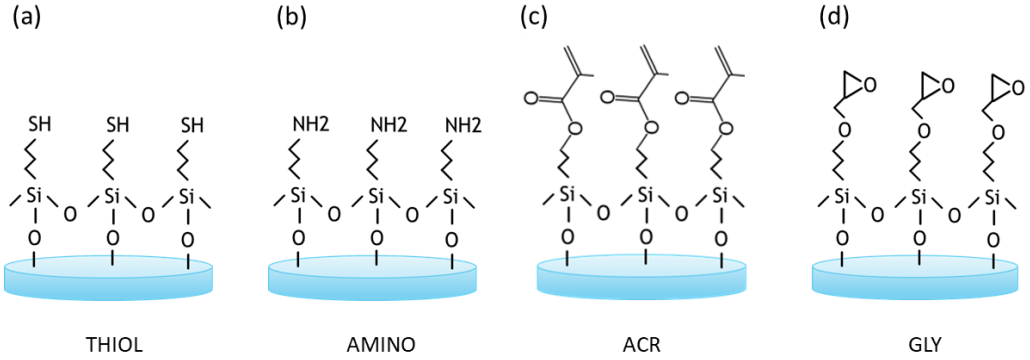

Figure 22. The schematic representation of (a) THIOL, (b) AMINO, (c) ACR, and (d) GLY SAMs.

4.6.1 Surface zeta potential of SAMs

In aqueous environments, surfaces display charges that attract ions from solution. Consequently, a layer consisting of strongly attracted ions is formed, called the Stern layer. Farther from the surface, a loosely attracted layer of ions is present, known as the diffuse layer. SZP is related to the surface charge of SAMs as it is defined as the electrical potential at the hydrodynamic shear plane, which belongs to the diffuse layer. The mobility of tracer particles was measured by DLS at different positions away from the SAMs. The effect of the surface charge decreases moving away from the SAM, and two main phenomena can be distinguished. As schematized in Fig. 23 (a), when an external electrical field is applied, the balance between electro-osmosis and electrophoresis forces governs the movement of the tracer particles. The tracer particles move directionally under the influence of the applied electrical field, $\vec{E}$. Particles are exclusively moving by electrophoresis far away from the surface. When particles closer to the SAM surface are considered, an electro-osmotic effect overlaps, and the modulus of the resultant particle mobility decreases. Next to the SAM, electro-osmosis becomes predominant, and a change in the versus of particles mobility occurs.

The apparent zeta potential was obtained at various distances from the SAM by measuring the tracer mobility. Linear fitting was performed on the experimental data, as reported in Fig. 23 (b) for THIOL SAM. Then, SZP was obtained by correcting the intercept value of the linear fitting with the zeta potential of the tracer, ZP_{tracer}:

$$SZP = -intercept + ZP_{tracer} \quad (3)$$

The value of ZP_{tracer} was measured 1000 µm away from the SAM, where the electro-osmosis contribution was zero. The correction was carried out to take into account that every apparent ZP includes the electrophoretic component of motion. Thus, the extrapolated intercept value was also including such a component.

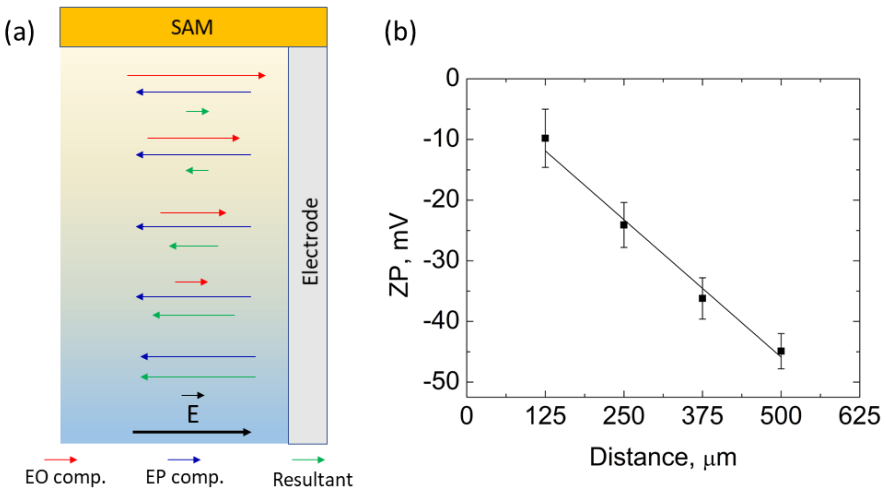

Figure 23 (a) Schematic representation of the predominant tracer mobility: the electro-osmosis (EO) component prevails next to the SAM surface, whereas the electrophoresis (EP) component prevails away from the SAM. (b) The zeta potential of the tracer particles vs. distance from THIOL SAM. Error bars refer to SD. Linear fitting was performed on experimental data.

The SZP values obtained for untreated glass and reference SAMs are collected in Tab. 18. The untreated glass was characterized by almost neutral values of SZP because of the lack of surface functionalization. THIOL and AMINO SAMs displayed the lowest and highest values of SZP, respectively. On the one hand, thiol groups can easily undergo protonation in aqueous environments. As a consequence, the $-SH_2^+$ groups attract negative ions, and an intense negative SZP was obtained. On the other hand, amino groups attracted positively charged ions. ACR and GLY SAMs were characterized by slightly negative SZPs due to the adsoprtion of hydroxide ions.

Table 18 SZP (± SD) of reference SAMs obtained from the measurement of the tracer mobility.

Sample	SZP, mV
Untreated glass	- 14.6 (± 3.9)
THIOL SAM	- 42.3 (± 2.1)
AMINO SAM	+ 14.9 (± 4.9)
ACR SAM	- 21.3 (± 2.5)
GLY SAM	- 24.7 (± 3.9)

4.6.2 Surface free energy of SAMs

Another aspect of surfaces that is helpful in the study of SAM – solute interactions regarded the surface energy of SAMs. In particular, the surface hydrophobicity and the acid, base, and van der Waals components of surface energy of SAMs were evaluated.

4.6.2.1 Water contact angle

Firstly, water contact angles were evaluated to test surface hydrophobicity. Literature reports controversial values of contact angle of silane-based SAMs (Nordin & Ahmad,

2015; Petri et al., 1999). As reported in Tab. 19, except for AMINO SAMs, all the SAMs exhibited comparable contact angles, which ranged from approx. 62 to 66°. Therefore, the formation of SAMs exposing different functional groups did not significantly alter the surface wettability. A specific consideration on AMINO SAMs has to be made since it displayed a much more hydrophilic surface, i.e., its contact angle was approx. half of the others. Such a behavior was attributed to the tendency to protonation of amino groups in aqueous environments. (Zhang et al., 1998). Nevertheless, contact angles of ~34° were only obtained when the measurement was carried out just after the synthesis of SAMs. AMINO SAMs resulted to be very sensitive to aging, and their contact angles experienced huge increases in few days. More specifically, contact angles started to increase after 10 hours from the synthesis and overcame 80° after a week. Such a tendency was attributed to the electrostatics of AMINO SAMs. As discussed in § 4.6.1, AMINO SAMs were the only surface displaying a positive SZP. The majority of impurities in the atmosphere is negatively charged, and particles may be favored to adsorb on the SAM surface. As a result, the contact angle would undergo an increase during time because of the deposition of contaminants on the sample surface. As regards the other SAMs, their contact angles resulted to be constant over time.

Table 19 Water contact angle (± SD) of untreated glass and reference SAMs.

Sample	Contact angle, °
Untreated glass	49.1 (± 1.9)
THIOL SAM	65.7 (± 1.7)
AMINO SAM	33.8 (± 2.6)
ACR SAM	65.4 (± 1.7)
GLY SAM	62.8 (± 1.5)

4.6.2.2 Polar and apolar components of surface free energy

As a second step, the surface free energy of SAMs was calculated, together with its components. To do so, the van Oss-Chaudhury-Good (VOCG) model was used (Berg, 1993). The model allows for the determination of polar and apolar components of surface free energy using contact angles obtained with selected probing liquids. The overall surface tension γ of SAMs was also estimated, which corresponded to the surface free energy per unit area. The model assumes that γ is the result of the contribution of different components that pertains to the physico-chemical nature of the interactions between the surface and the liquid. The Lifshitz-van der Waals component γ^{LW} is related to long-range interactions, including London, Keesom, and Debye forces, whereas the acid-base component γ^{AB} refers to the short-range interactions, which also include hydrogen bonding. The two components are additive and give the total surface tension:

$$\gamma = \gamma^{LW} + \gamma^{AB} \quad (4)$$

The Lewis acid-base interaction consists of acid and basic components referring to the electron donor and acceptor propensity of the surface, respectively. γ^{AB} can be expressed as follows:

$$\gamma^{AB} = 2\sqrt{\gamma^{+}\gamma^{-}} \quad (5)$$

where $\gamma^{+}$and γ^{-}refer to the acid and basic components of surface tension.

When cosidering a solid surface, the Young's equation relates the surface tension of the solid (γ_s) and the probing liquid (γ_l) to the interfacial tension between the solid and the liquid (γ_{sl}) as follows:

$$\gamma_s = \gamma_{sl} + \gamma_l cos\varphi \quad (6)$$

where φ is the contact angle between the solid-liquid pair. According to the VOCG theory, one can write:

$$\gamma_l(1 + cos\varphi) = 2\left[\sqrt{\gamma_l^{LW}\gamma_s^{LW}} + \sqrt{\gamma_l^{+}\gamma_s^{-}} + \sqrt{\gamma_l^{-}\gamma_s^{+}}\right] \quad (7)$$

where *l* and *s* subscripts refer to the liquid and the solid, respectively. To determine the SAM surface tension and components, three probing liquids were used, namely two polar liquids, i.e., water and glycerol, and a dispersive liquid, i.e., diiodomethane. The values of γ_l, γ_l^{LW}, γ_l^{+}, and γ_l^{-} of the three probing liquids are known and reported in Tab. A3 (Appendix A). According to the VOCG theory, the contact angle between each probing liquid and the SAM surface is measured, resulting in a set of three Eq. 7. In particular, the use of one dispersive liquid ($\gamma_l^{+} = \gamma_l^{-} = 0$) facilitates the resolution of the set of equations since γ_s^{LW}can directly be calculated. The overall SAM surface tension and its components were calculated and reported in Tab. 20.

Table 20 Surface tension and its dispersive, polar, acid, and base components of reference SAMs.

Sample	γ, mJ/m²	γ^{LW}, mJ/m²	γ^{AB}, mJ/m²	γ^{+}, mJ/m²	γ^{-}, mJ/m²
THIOL SAM	43.0	36.3	6.7	0.8	13.7
AMINO SAM	56.0	43.2	12.8	1.1	36.8
ACR SAM	47.6	38.6	8.9	2.3	8.7
GLY SAM	44.9	37.3	7.6	1.0	15.0

The four reference SAMs displayed comparable values of overall surface tension. Only amino-terminated SAMs were characterized by slightly higher values of γ. The calculation of γ^{LW} demonstrated that the Lifshitz-van der Waals component was affected by minimal variations among THIOL, ACR, and GLY SAMs. As expected, AMINO SAMs were out of range. The surface physico-chemical attributes of AMINO SAMs were found to be more affected by contamination. On the one hand, good results were obtained with spectroscopic techniques which required the use of vacuum, and thus had a lower risk for contamination. On the other hand, contact angle analyses were more affected by uncontrolled deposition of particles, even if all the measurements were carried out in clean room. Therefore, the surface tension values obtained for AMINO SAMs were affected by a higher degree of uncertainty but could, in any case, provide interesting qualitative insights.

With regard to the polar interactions, ACR SAMs displayed the highest γ^{+}component. Also, among all the SAMs, the relative contribution of acid and base components of surface tension resulted to be more balanced for ACR SAMs. AMINO SAMs, instead, were characterized by the highest γ^{-} component, as expected considering the presence of basic

amino groups on the surface. Therefore, even if the contact angles of AMINO SAMs were corrupted by some surface contamination, the qualitative trend still held true.

In conclusion, except for AMINO SAMs, all the SAMs displayed comparable contact angles with water and overall surface tension. At the same time, the ratio between acid and base components was successfully tuned for each SAM.

4.7 Final remarks

The comparison with XPS results concerning THIOL SAMs discussed in Chapter 3 allowed for the fast identification of monolayer conditions for two additional silanes by simply analyzing the C1s region. The more efficient anchoring of silanes leaving methoxy, rather than ethoxy, groups was also demonstrated. For the optimized SAM synthesis protocols, the organization of silane molecules in densely packed monolayers was demonstrated by ellipsometry, and surface zeta potential and surface free energy were determined. The four selected SAM end groups can provide different electrostatic and secondary interactions when placed in contact to solute molecules in solution. Such surface attributes are pivotal for the assessment of surface – drug/protein interactions and the identification of the predominant mechanisms influencing the nucleation processes discussed in the following chapters.

References

Artusio, F., Fumagalli, F., Bañuls-Ciscar, J., Ceccone, G., & Pisano, R. (2020a). General and adaptive synthesis protocol for monolayers as tunable surface chemistry platforms for biochemical applications. *Biointerphases*, **15**(4), 041005.

Beamson, G., & Briggs, D. (1992). XPS of Polymers Database. Surface Spectra (UK).

Berg, J. C. (1993). Wettability. (J. C. Berg, Ed.). New York: Dekker.

Henderson, A. (2013). Multivariate analysis of SIMS spectra. In J. C. Vickerman & D. Briggs (Eds.), TOF-SIMS: Materials analysis by mass spectrometry (p. 449). Surface Spectra (UK).

Nordin, N. H., & Ahmad, Z. (2015). Monitoring chemical changes on the surface of borosilicate glass covers during the silanisation process. *Journal of Physical Science*, **26**(2), 11–22.

Petri, D. F. S., Wenz, G., Schunk, P., & Schimmel, T. (1999). An improved method for the assembly of amino-terminated monolayers on SiO2 and the vapor deposition of gold layers. *Langmuir*, **15**(13), 4520–4523.

Rudawska, A., & Jacniacka, E. (2018). Evaluating uncertainty of surface free energy measurement by the van Oss-Chaudhury-Good method. *International Journal of Adhesion and Adhesives*, **82**(1), 139–145.

Schreiber, F. (2000). Structure and growth of self-assembling monolayers. *Progress in Surface Science*, **65**(5–8), 151–257.

Trindade, G. F., Abel, M. L., & Watts, J. F. (2018). simsMVA: A tool for multivariate analysis of ToF-SIMS datasets. *Chemometrics and Intelligent Laboratory Systems*, **182**(10), 180–187.

Zhang, H., He, H. X., Wang, J., Mu, T., & Liu, Z. F. (1998). Force titration of amino group-terminated self-assembledmonolayers using chemical force microscopy. *Applied Physics A: Materials Science and Processing*, **66**(1), 269–271.

PART II:

The crystallization of small-molecule drugs

Chapter 5

Application of SAMs to the crystallization of small molecules

Chapter 5 is devoted to the discussion of the crystallization of small-molecule drugs on SAMs. SAMs will be applied as heteronucleants for the batch crystallization of a model API. Aspirin (ASA) has been selected as a target because of its widespread diffusion, well-known structural properties, and massive industrial scale production. The solubility of ASA in different solvents was first evaluated, so as to identify a proper solvent composition. Particular attention was paid to the identification of a set of conditions allowing for the study of heterogeneous nucleation, in terms of supersaturation level and experimental set-up. The nucleation kinetics of ASA will be evaluated on different SAMs, and the nucleation time will be correlated to SAM surface properties.

5.1 Materials & Methods

5.1.1 Materials

Aspirin (ASA, USP grade), ethanol (EtOH, puriss. p.a., absolute, assay ≥ 99.8%), acetone (analytical reagent grade) and water (HPLC grade) were used for the crystallization trials and were procured from Sigma-Aldrich (Cesano Maderno, MI, Italy). The chemical structure of ASA reported in Fig. 24.

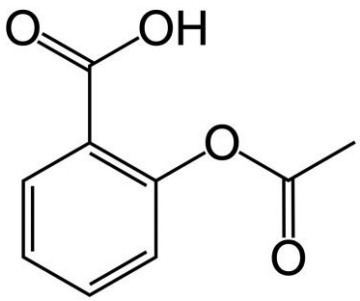

Figure 24. The chemical structure of aspirin (ASA).

The results presented in this chapter have been partially published in (Artusio et al., 2021).

5.1.2 Determination of aspirin (ASA) solubility curve

ASA solubility curve was determined with the help of gravimetric methods. The solubility curve of ASA was determined in three different solvents, namely ethanol, a mixture of ethanol and water (38/62 v/v), and acetone, to find suitable conditions for batch crystallization. The selected temperatures were 5, 10, 15, 25, and 35 °C. For each combination of solvent and temperature, two pre-weighted beakers loaded with 25 mL of solvent were placed inside an incubator with controlled temperature. One beaker served as a reference to calculate the amount of solvent mass evaporated during the test. In the other one, ASA was progressively added. The amount of ASA added to the system was weighted each time. Each addition was approx. 50 mg and was performed after the complete dissolution of the previously added solute. The beakers were sealed with parafilm to limit evaporation, and the liquid continuously stirred. When the ASA solution reached saturation, the system appeared turbid, and the experiment was stopped. The control beaker was weighted again to estimate the solvent evaporation. Then, 7 mL of ASA solution were withdrawn, filtered through 0.20 µm pore size PTFE syringe filters (Millex GV, Millipore), and dispensed in weighing boats. After the complete solvent evaporation, the boats were weighted again, and solubility was calculated. Each experiment was performed in triplicate.

5.1.3 Batch crystallization of ASA on SAMs

31.6 mg/mL of ASA were dissolved in an ethanol/water mixture (38/62 v/v), the selected solvent, at room temperature. The solution was passed through 0.45 and 0.20 µm pore size syringe filters (Millex GV, Millipore) to remove microparticles and contaminants. SAMs were synthesized on glass substrates following the optimized protocol summarized in § 4.3 and freshly prepared before each crystallization trial. SAMs were carefully placed at the bottom of each well of untreated 24-well plates (ThermoFisher Scientific). 125 µL of ASA solution were dispensed in each well with the help of an automatic pipette (M4 Multipette, Eppendorf) so as to avoid solvent evaporation during the filling step. The level of liquid in each well was approx. 1 mm. The plates were immediately sealed after solution dispensing. All the operations concerning the preparation of ASA solution and the loading of the plates were carried out under a laminar flow hood (Asalair 1500, Asal, Milan, Italy) to minimize the risk of sample contamination.

The plates were then transferred to an incubator, placed under a stereomicroscope (M125C, Leica Microsystems, Germany), and illuminated by transmitted light. During each crystallization trial, two plates were simultaneously housed in the incubator and monitored. The microscope was equipped with a motorized X-Y stage and a system for the automatic acquisition of time-lapse images (LAS-X, Leica Microsystems, Germany). The acquisition system was coupled to an in-house designed system for the temperature control. The crystallization temperature, T_c, was set at 15 °C. 47 wells were monitored every two hours, as one well was dedicated to the monitoring of the liquid temperature, for more than two weeks. The crystallization conditions in terms of temperature, initial cooling ramps, etc., were the same for all the trials. The unique variable was the surface inserted in the crystallizers. Crystallization trials were carried out on untreated glass and THIOL, AMINO, GLY and ACR SAMs. Each experiment was performed in duplicate.

5.2 Design of batch crystallization

The crystallization of a model API molecule, namely aspirin, was investigated in presence of SAMs to evaluate their impact on the nucleation step. The selected experimental design involved performing multiple batch crystallization trials in parallel to gain relevant statistics. The surface/volume ratio was maximized by loading the wells with small volumes of API solution (125 µL). In this way, the interaction between API molecules and SAM surface was enhanced and the risk of encountering foreign particles in the solution volume that could potentially act as heteronucleants was mitigated. The supersaturation conditions were achieved by cooling. On the one hand, knowledge on the solubility of ASA represented a primary need to select suitable supersaturation conditions. On the other hand, a system able to handle a high number of crystallizers at the same time was specifically designed.

5.2.1 The selection of supersaturation conditions

Solvent and crystallization temperature are decisive for guaranteeing a proper supersaturation level when performing crystallization with SAMs. The supersaturation degree, *S*, was defined as:

$$S(T) = \frac{C}{C_s(T)} \tag{8}$$

where *C* was the actual ASA concentration and C_s was the ASA solubility. C_s is a function of temperature, and so is *S.* The setting of the right *S* was dictated by different factors. On the one hand, the action of SAMs can be clearly discerned when heterogeneous nucleation is predominating in the crystallizer. If homogeneous nucleation occurred in bulk, the interaction of SAMs with ASA would be negligible. Most solute molecules would participate to crystal growth in the bulk, and the SAM contribution would be repressed. Such a phenomenon imposes an upper limit on the supersaturation degree to be implemented. On the other hand, nucleation must occur within a reasonable amount of time to shorten the length of the tests and limit the possibility of encountering disturbs, failures, etc. Such a requirement restricts the range of allowable *S* by introducing a lower constraint. Therefore, the selected *S* rises from a compromise between the setting of heterogeneous nucleation and the appearance of crystals within days or weeks. In this scenario, $S = 1.8$ has been selected to meet the boundary conditions, as it will be discussed in § 5.3.

In order to load each crystallizer with the correct amount of ASA, the solubility was evaluated. The solubility curve of ASA as a function of temperature was experimentally measured in ethanol, ethanol/water mixture (38/62 v/v), and acetone, as reported in Fig. 25. The experimental data were successfully fitted ($R^2 > 0.99$) with second order polynomials in the form of:

$$C_{S,ASA} = \mathrm{x_0} + \mathrm{x_1}T + \mathrm{x_2}T^2 \tag{9}$$

The fitting parameters are listed in Tab. 21. ASA solubility increased with the temperature and was the highest in acetone, in agreement with the literature (Maia & Giulietti, 2008). Conversely, the ethanolic mixture displayed the lowest solubility. Fitting parameters resulted to be slightly more uncertain, i.e., had a higher standard deviation, for acetone because of the high volatility of the solvent.

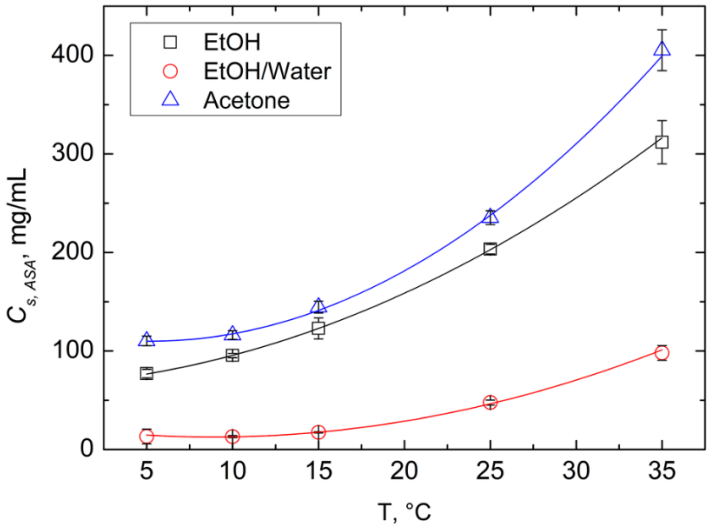

Figure 25 ASA solubility curves as a function of temperature in EtOH, EtOH/water mixture (38/62 v/v), and acetone.

Overall, the solubility curves pointed out that ASA was mostly soluble in acetone, followed by ethanol. Moreover, the addition of water to ethanol was found to drastically reduce ASA solubility. Ethanol has a much higher solubilizing power because of the formation of hydrogen bonds with the ASA carboxylic acid groups and dipole-dipole interactions with the ester groups. The hydrophobic hydrocarbon portion of ethanol enhances ASA dissolution by means of van der Waals interactions with the benzene ring. Conversely, water can only interact with the hydrophilic part of ASA, which is limited compared to the hydrophobic one. Such a feature was essential for the setting of crystallization conditions. As a matter of fact, the EtOH/water mixture allows to set up experiments with reduced contents of ASA. The achievement of the same S in pristine ethanol or acetone would require a much higher amount of ASA, thus increasing the probability of coherent solute clustering in bulk. Unlike acetone, the EtOH/water mixture was also fully compatible with the material of the multi-well plates, i.e., polystyrene.

Table 21 The fitting parameters and standard errors (SE) of the experimental solubility curve. Data referred to acetone, ethanol, and ethanol/water.

Solvent	x_0, mg/mL	x_0 SD, mg/mL	x_1, mg/(mL°C)	x_1 SD, mg/(mL°C)	x_2, mg/(mL°C^2)	x_2 SD, mg/(mL°C^2)
Acetone	118.73	5.48	-3.39	0.81	0.33	0.02
EtOH	66.10	1.79	1.27	0.26	0.17	0.01
EtOH / water	22.94	2.73	-2.30	0.32	0.13	0.01

The identification of the solubility curves guided not only the selection of solvent, but also the choice of crystallization temperature, T_c, which was set at 15 °C. The preparation of the ASA solution had to be preferentially performed at room temperature to minimize the extent of water evaporation, which would alter the final supersaturation value. Therefore, the crystallization experiment was carried out below room temperature. At the

same time, T_c could not be too low to avoid the condensation of atmospheric humidity on the crystallization chamber and disturbances during the monitoring of the samples.

5.2.2 Temperature control system

The maintenance of T_c at its set-point for a considerably long time required a temperature monitoring and controlling system. Multi-well plates were selected as supports for the crystallization trials. Therefore, an incubation chamber and a lab-scale plant for the temperature control were designed in-house.

The incubator was made of stainless steel and furnished with adjustable racks to sustain the plates and ensure proper focusing. The incubation chamber was connected to a nitrogen line to control the temperature. The control loop was governed by a controller implemented on LabVIEW which received the signal from a thermocouple (type T) immersed in the liquid of one of the wells. The well contained just the ethanolic mixture, without ASA, to avoid the thermocouple scaling because of the crystals. The scheme of the control loop is sketched in Fig. 26. The measured variable was the liquid temperature, whereas the manipulated variable was the ratio between the hot and the cold volumetric flows of nitrogen. The piping system was equipped with two mass flow controllers (MFC, EL-FLOW, Bronkhorst, Germany), which acted on the flow rate of nitrogen. In addition, the manual valve V1 served to isolate the plant from the general nitrogen distribution, whereas V2 served as a bypass in the transitory cooling stage. The cooler consisted of a heat exchanger placed inside a liquid nitrogen vessel. The cold lines and the incubator were insulated to minimize the thermal dispersions and increase the temperature stability inside the wells.

Two nitrogen lines guaranteed the set-point temperature inside the chamber. The “hot” nitrogen line was at room temperature, and directly came from the general distribution. The “cold” line passed through the cooler, and then was mixed together with the hot one before entering the incubating chamber. The temperature controller monitored T_c every second. The analogic signal was received from a thermocouple and transduced into a digital signal by a temperature input device (NI USB TC-01, National Instruments, Milan). The LabVIEW controller was designed according to a proportional control logics and commanded the degree of opening of FV1 and FV2 valves by analyzing the upper and lower temperature deviations from the set-point. Tolerance was set at 0.01 °C. The response of the controller was then transmitted to the valves to implement the regulating actions.

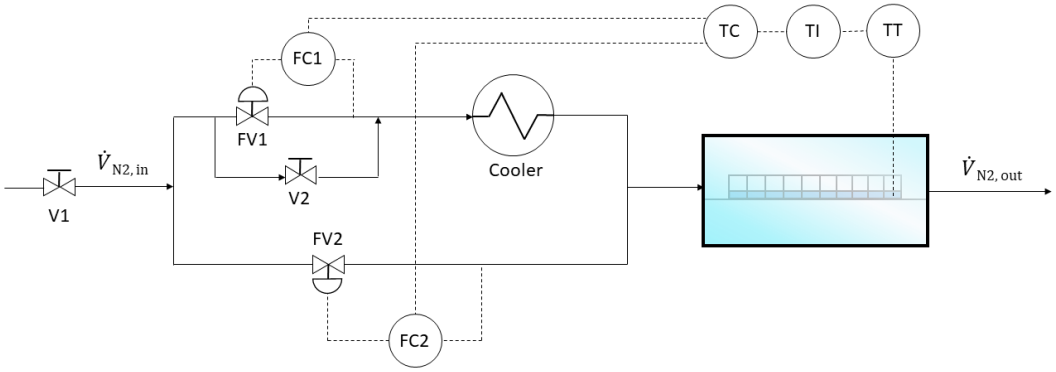

Figure 26 The control loop of the temperature control system. The manipulated variable was the ratio between the hot and cold flows of nitrogen, whereas the measured variable was the temperature of the EtOH/water mixture in one of the wells inside the incubator.

The selected gas carrier was nitrogen at 2 bar. Preliminary tests were carried out with compressed air, but ice plugging along the cold line were observed because of humidity. Therefore, an in-line desiccator was added, and air was replaced by nitrogen. The use of nitrogen also avoided the humidity condensation inside the chamber and on the plates.

Seal tests were first performed to ensure the absence of leakages from the piping. Then, the controller performances were tested before setting up crystallization trials. During the start-up phase, the controller response time, the ability to keep the temperature at its set-point and other parameters were studied. The controller was designed to allow for the selection of the initial cooling ramp by acting on the by-pass valve of FV1. Valve V2 was regulated manually to increase the volumetric flow, and thus the cooling power, of nitrogen during the initial cooling stage. According to the degree of opening of V2, faster or slower cooling ramps could be implemented. At the same time, this choice allowed for the use of MFCs acting on smaller flows and, consequently, a more precise temperature control during the stationary phase. The initial cooling ramp was –1.5 °C/min. This value allowed for a fast cooling transitory together with minor oscillations around the set-point and was compatible to the control system. As a matter of fact, because of the system thermal inertia, too fast cooling ramps would result in too deep undershoot temperatures which could be difficult to be handled by the automatic control system. The typical temporal evolution of T inside the well is reported in Fig. 27.

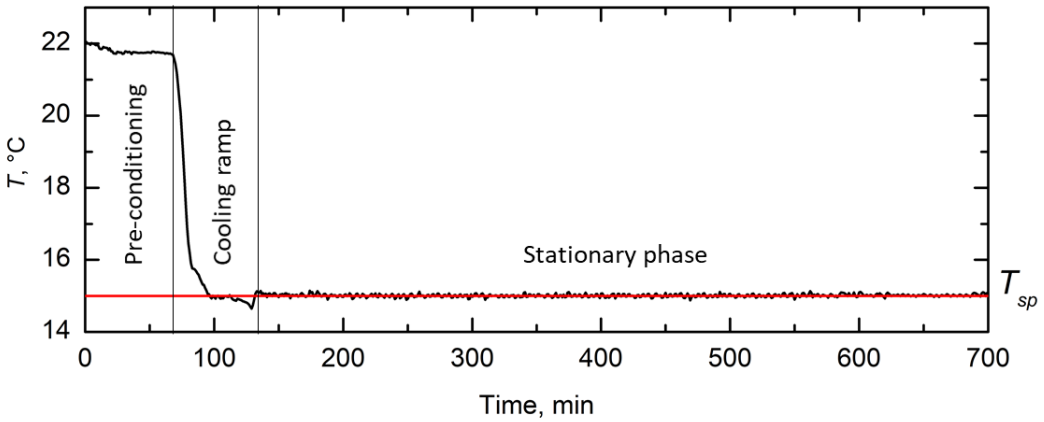

Figure 27 Temporal profile of temperature of the ethanolic mixture inside the incubator. The various phases of the process and the set-point temperature, T_{sp}, are highlighted.

The set-point temperature, T_{sp}, was achieved thanks to various steps. First, 1-hour pre-conditioning of the chamber was performed in order to equilibrate the temperature of the liquid, reduce the humidity inside the chamber and piping system, and clean the environment of crystallization. Then, the system underwent the transitory regime of cooling by implementing a fast cooling ramp. The slope of the ramp was tuned with V2. Lastly, the system entered the stationary regime. The transitory stage consisted of an approx. 10 min fast ramp (–1.5 °C/min) and an approx. 15 min slower ramp (–0.07 °C/min) to reach T_{sp}. Then, an oscillatory step with maximum undershoots of -0.4 °C followed. When the inlet thermal flux of the chamber had counterbalanced the outlet flux, a dynamic equilibrium was achieved, and the system entered the stationary phase. In this phase, the temperature deviations from T_{sp} were always below 0.2 °C, mostly below 0.1 °C.

In conclusion, a system for the implementation of controlled crystallization conditions was realized. The system was designed to monitor and control the temperature of the liquid

in the crystallizers and ensure the mitigation of external disturbances. An automatic controller was implemented on LabVIEW, and an in-house piping system was designed. The temperature was successfully controlled with ±0.1 °C deviations from the desired set-point.

5.3 Controlling the nucleation kinetics with SAMs

The ASA crystallization in batches containing SAMs was studied at 15 °C. The nucleation kinetics was evaluated thanks to cumulative distribution probability curves. The curves referred to the ensemble of the 47 wells, as one well was devoted to the *T* control. The wells which underwent heterogeneous nucleation during or just after the transitory stage were discarded as the presence of residual particles, dust or other impurities triggered crystallization, masking the action of SAMs. The experimental data were then analyzed considering Poisson statistics.

5.3.1 The Poisson distribution law

The Poisson distribution law represents an effective way of describing stochastic events in statistics. Its application to the nucleation datasets helps in the interpretation of the process kinetics (Jiang & ter Horst, 2011). The general form of the Poisson distribution is:

$$\mathrm{f}(\nu, n) = \frac{\nu^n \mathrm{e}^{-\nu}}{n!} \tag{10}$$

where ν and n are the expected and the exact number of events in a defined interval, respectively. At constant supersaturation, the nucleus formation is a random process. The nucleation induction time τ can be calculated from the nucleation rate J and the solution volume V as:

$$\tau = \frac{1}{JV} \tag{11}$$

The expected number of nuclei ν within time t is given by:

$$\nu = JVt = \frac{t}{\tau} \tag{12}$$

Thus, the probability $P(t)$ of not observing any nucleation event within the t timeframe can be obtained by setting $n = 0$ and $\nu = t/\tau$:

$$\mathrm{f}\left(\frac{t}{\tau}, 0\right) = P(t) = \mathrm{e}^{-\frac{t}{\tau}} \tag{13}$$

Considering a semi-logarithmic representation, $P(t)$ allows for the direct calculation of τ, which corresponds to the average nucleation induction time, from the slope of its temporal evolution:

$$\ln\big(P(t)\big) = -\frac{t}{\tau} \tag{14}$$

The nucleation kinetics results to be described by a first-order relationship, as recently demonstrated (Diao et al., 2011c). The average nucleation induction time, τ, can be obtained from the described procedure under certain boundary conditions. The present investigation of nucleation kinetics relies on optical microscopy, and thus on the detection of crystals, not nuclei. Rigorously, τ should be referred to as the average detectable nucleation induction time. However, the time needed for a nucleus to grow up to a detectable size is hypothesized to be negligible compared to the nucleation time. Moreover, the heat exchange rate has to be sufficiently high to reach the supersaturation conditions in a negligible amount of time (Diao et al., 2011c). The two boundary conditions will be verified in the following paragraph.

5.3.2 The inhibiting and promoting action of SAMs on nucleation

Preliminary tests of ASA crystallization in batch were carried out on untreated glass and were used as a reference. The cumulative probability of nucleation time was considered as the cumulative probability of finding crystallized wells. The nucleation time belonged to the range of several dozens of hours, whereas the crystal growth time was significantly shorter. As a matter of fact, the growth speed was in the range of hundreds of μm/h. Moreover, as discussed in § 5.2.2, stable supersaturation conditions were achieved in less than 25 min. The initial crash cooling ramp was followed by a smoother approach to T_{sp} from 1 °C above its value. The two boundary conditions were therefore realized in the experimental practice, allowing for the data processing with Poisson statistics.

The cumulative distribution curves of crystallized wells are reported in Fig. 28 (a) for the untreated glass and the four investigated SAMs. Major differences among the surfaces regarded the nucleation time and the number of successful nucleation events. As regards the reference surface, i.e., untreated glass, the onset of nucleation was observed after 200 h. All the functionalized surfaces turned out to induce nucleation in a shorter timeframe compared to bare glass. Moreover, the cumulative temporal distribution obtained for untreated glass resulted to be the broadest one. Nucleation events were registered over a time interval of 550 h.

ACR and AMINO SAMs were found to markedly restrict the time interval of nucleation events. The induction effect observed also led to 100% probability of getting crystals inside the wells, compared to 85% obtained for untreated glass. GLY SAMs had an intermediate effect: the onset of nucleation was rapidly achieved, but they were ineffective in promoting focused nucleation events, as already observed for untreated glass. The anticipated onset of nucleation was also observed on THIOL SAMs, but then a strong inhibition of the nucleation events occurred. Only 20% of the wells contained crystals after 375 h, and then the curve settled on a plateau.

The action of SAMs was clearly discerned and was not flattened by predominant homogeneous nucleation. The outpacing of heterogeneous over homogeneous nucleation was confirmed by the different percentages of the crystallized wells obtained after 600 h with SAMs. In particular, the inhibition effect would not have been observed for THIOL SAMs if homogeneous nucleation had occurred.

As a second step, the average nucleation induction time was evaluated according to Eq. (14). To do this, each cumulative curve was shifted to set the nucleation onset time at $t = 0$. As reported in Fig. 28 (b), the experimental data were successfully fitted with linear tendencies ($R^2 > 0.95$), and τ was obtained from their slope. However, τ only represented

the induction contribution after the onset of nucleation. The total nucleation induction time, t_{nuc}, was defined as:

$$t_{nuc} = t_{lag} + \tau \quad (15)$$

where t_{lag} represented the initial lag time elapsed from the achievement of supersaturation conditions to the recording of the first nucleation event. Despite the strong action of SAMs on ASA nucleation kinetics, changes in the habit or form of ASA crystals were not observed. Platelet-like monoclinic ASA crystals were obtained on all the SAMs, as shown in Fig. 28 (c)-(g).

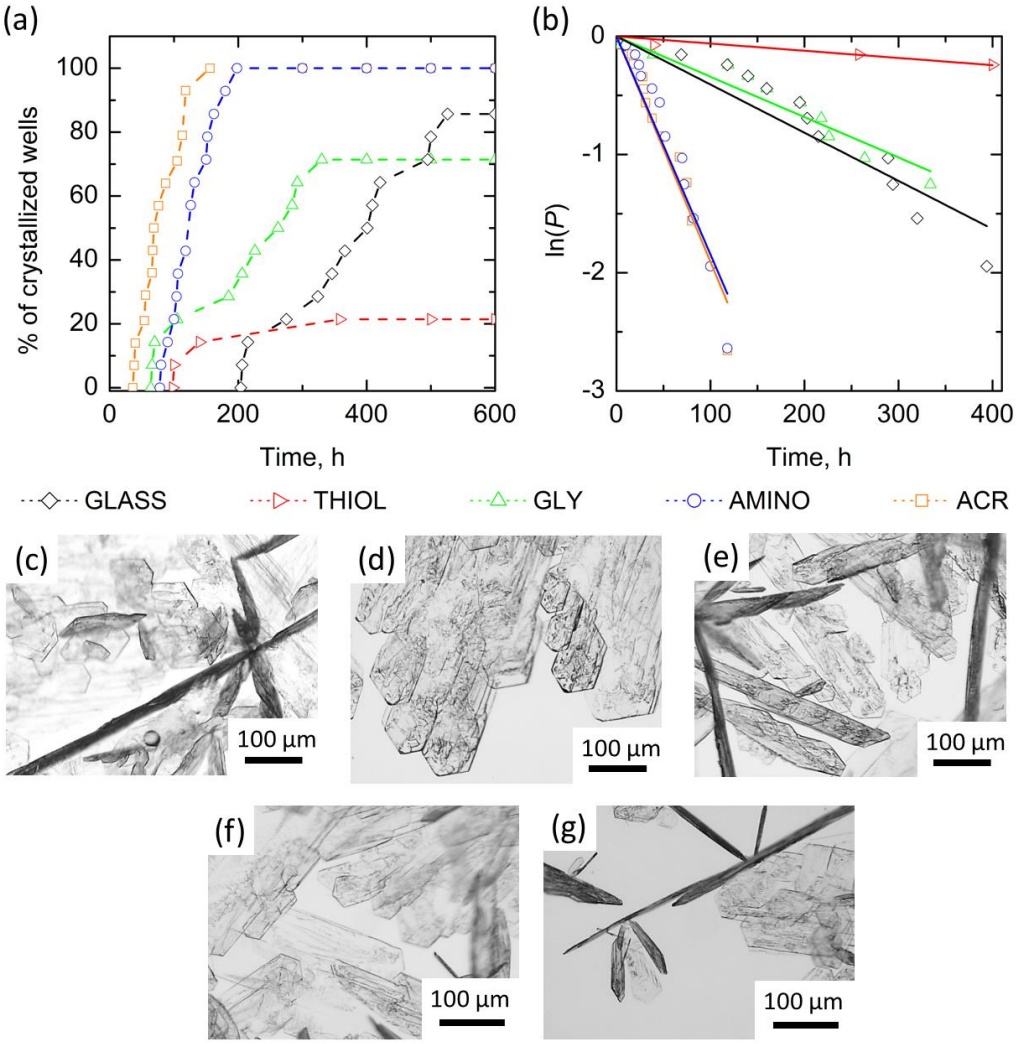

Figure 28 (a) Cumulative probability of finding crystals expressed as % of crystallized wells as a function of time. The curves were obtained on untreated glass, THIOL, AMINO, GLY, and ACR SAMs. 47 wells were monitored during each experiment. (b) Fitting of the experimental data obtained on different surfaces with the Poisson distribution law expressed as ln(P) vs time. t = 0 corresponded to the onset of nucleation. Representative optical micrographs of ASA crystals grown on (c) glass, (d) ACR, (e) AMINO, (f) GLY, and (g) THIOL SAMs. The figure was taken from (Artusio et al., 2021) with modifications.

The two nucleation time contributions and the total induction time are reported for each surface in Fig. 29. The most inducing active surface resulted to be the ACR SAM, leading to the shortest t_{nuc}, t_{lag}, and τ. The boosting effect promoted by the methacrylate

groups resulted in 5-fold faster nucleation kinetics compared to untreated glass. AMINO SAMs displayed similar performances, but lag time was approx. 50% higher. GLY SAMs successfully shortened the lag time, while displaying reduced effect on τ, compared to untreated glass. Finally, THIOL SAMs halved the time needed to observe the first nucleation event, compared to bare glass, but then exhibited a strong inhibition effect.

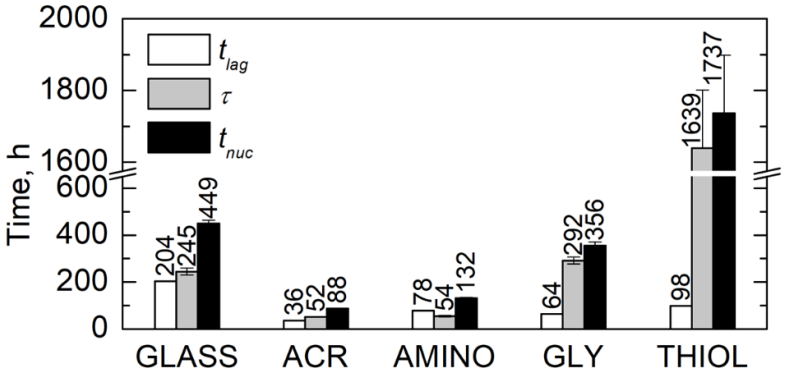

Figure 29 The overview of t_{lag}, τ, and t_{nuc} obtained on untreated glass, ACR, AMINO, GLY, and THIOL SAMs. The figure was taken from (Artusio et al., 2021) with modifications.

5.3.3 Interactions between ASA and SAMs

The high ratio between the ASA solution/SAM exposed groups interface and the volume of ASA solution (level of liquid in each well ~ 1 mm) allowed for the maximization of probability of encountering surface-induced nucleation. The nucleation inhibiting or inducing action provided by SAMs rises from interfacial phenomena occurring between the surface and the ASA molecules in solution. Among them, secondary bonds, acid-base interactions, and electrostatics effects were considered.

The predominant secondary interactions between ASA and SAMs were hydrogen bonds (HB). ASA molecules are characterized by three HB acceptor and one HB donor groups. The nucleation inducing ability of some SAMs was thus attributed to their higher affinity toward the solute molecules in terms of hydrogen bonding. The number of HB donor and acceptor groups of glass and SAM is reported in Tab. 22.

Table 22 Number of HB donor and acceptor groups per ASA molecule, glass, and SAM end groups.

	HB donor	**HB acceptor**
ASA	1	3
GLASS -OH	1	1
THIOL SAM	1	1
AMINO SAM	1	1
ACR SAM	2	0
GLY SAM	2	0

As regards ACR SAM, the methacrylate group could strongly interact with the HB acceptor groups of ASA. For example, surface carbonyl groups could bind to ASA carboxyl groups. It was also hypothesized that such HB could favor the formation of ASA dimeric synthon, which is built up by secondary bonds between ASA -COOH and -OH groups and

also between two -COOH groups (Przybyłek et al., 2015). In this perspective, SAM was playing a sort of molecular mimicking role. ASA molecules diffusing at the interface would be induced to self-assembly also because of a mild immobilization effect promoted by SAMs. Thanks to favorable HBs, ASA molecules can adsorb onto the surface, form synthons and nuclei. Thanks to the lowering of the nucleation barrier promoted by the surface, the energetic cost to form stable clusters could be reduced, and nucleation was more easily achieved. Such an explanation can partly justify the dramatic nucleation boosting effect promoted by ACR SAMs.

Acid-base interactions were believed to play a significant role in the nucleation inducing ability of AMINO SAMs, together with hydrogen bonds. As previously discussed, AMINO SAM resulted in slightly less efficient induction, but still comparable to ACR SAM. AMINO SAMs displayed only one HB donor group per molecule. However, as calculated in § 4.6.2, amino SAMs had a high γ^- component, revealing a highly basic character. ASA molecules in solution are known to exhibit a weak acid behavior. Therefore, the inducing effect of AMINO SAMs could be not only related to favorable HB, but also to acid-base interactions with ASA.

GLY SAMs were characterized by a different behavior since the shortening of t_{lag} was accompanied by a negligible effect on τ, compared to glass. The scarcer performance of glycidyloxy groups was related to the lack of beneficial acid-base interaction or mimicking effects. The HB interaction with surface ether groups was less effective in controlling nucleation kinetics.

Finally, an opposite tendency was evinced for THIOL SAMs, which were found to inhibit nucleation. 4-fold longer τ was obtained in presence of thiol groups. The absolute value of SZP was much higher for thiol SAMs, and this feature could be detrimental for the formation of stable nuclei at the interface. As a matter of fact, the strong accumulation of negatively charged ions on the no-slip plane may have prevented the ASA molecules from reaching the surface. Consequently, clusters did not experience the energetically beneficial action of SAM, and very few successful nucleation events were observed.

5.3.3.1 A correlation between surface properties and nucleation time

Finally, a correlation between the overall nucleation process and the SAM surface properties was identified. For this purpose, t_{nuc} was considered as representative of ASA nucleation on different surfaces. The nucleation time obtained on each SAM was then correlated with the corresponding acid surface energy component.

The trend is reported in Fig. 30 and provided interesting insights into the global mechanism of surface interaction with ASA molecules. It emerged that the surface acid character tuned ASA nucleation time in the considered range. SAMs displaying higher acidity, i.e., ACR, strongly induced the clustering of ASA into ordered structures. The inductive effect started to be less evident when the acidity decreased, as with AMINO SAMs. When γ^+ was below 1.0 mJ/m^2, inhibitive effects on nucleation were observed. This aspect will be further addressed in the next chapter.

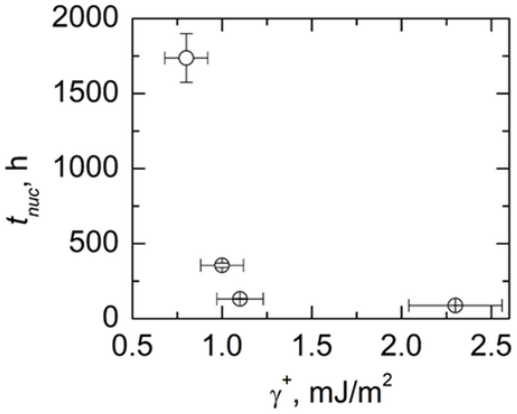

Figure 30 The nucleation time t_{nuc} of ASA as a function of the acid surface energy component of the corresponding SAMs. Error bars refer to standard deviation.

5.4 Final remarks

The crystallization of ASA was investigated in the presence of SAMs. An in-house platform to automatically monitor crystallization experiments, set and control the temperature of crystallization, and collect data has been designed and implemented. The description of plant configuration, the motivation of design choices, and the temperature control strategy and performances were illustrated. Supersaturation conditions were carefully selected thanks to the investigation of ASA solubility in different solvents. In this way, the heterogeneous nucleation of ASA on SAMs could have been tackled. On the one side, ACR and AMINO SAMs acted as nucleation promoters by boosting the nucleation kinetics and maximizing the probability of finding crystals in a defined timeframe. On the opposite side, THIOL SAMs acted as nucleation inhibitors by considerably reducing the probability of encountering nucleation events. GLY SAMs displayed an intermediate behavior.

In conclusion, it has been demonstrated that the tuning of surface attributes, such as the number and nature of HB groups, the components of surface tension, and the charge, represented an effective strategy in altering the nucleation pathway of APIs in solution. ΔG_{nuc} was successfully tuned by acting only on the surface chemistry and was not related to the morphological features. The two effects were thus successfully deconvoluted and the overall tuning of nucleation kinetics was related to the SAM acid surface energy component.

References

Artusio, F., Fumagalli, F., Valsesia, A., Ceccone, G., & Pisano, R. (2021). Role of self-assembled surface functionalization on nucleation kinetics and oriented crystallization of a small-molecule drug: Batch and thin-film growth of aspirin as a case study. Accepted for publication in *ACS Applied Materials & Interfaces*.

Diao, Y., Myerson, A. S., Hatton, T. A., & Trout, B. L. (2011c). Surface design for controlled crystallization: The role of surface chemistry and nanoscale pores in heterogeneous nucleation. *Langmuir*, **27**(9), 5324–5334.

Jiang, A., & ter Horst, J. H. (2011). Crystal nucleation rates from probability distributions of induction times. *Crystal Growth & Design*, **11**(1), 256-261.

Maia, G. D., & Giulietti, M. (2008). Solubility of acetylsalicylic acid in ethanol, acetone, propylene glycol, and 2-propanol. *Journal of Chemical and Engineering Data*, **53**(1), 256–258.

Przybyłek, M., Cysewski, P., Pawelec, M., Ziółkowska, D., & Kobierski, M. (2015). On the origin of surface imposed anisotropic growth of salicylic and acetylsalicylic acids crystals during droplet evaporation. *Journal of Molecular Modeling*, **21**(3), 1–12.

Chapter 6

A novel tool for the investigation of surface-API interactions: the spin-coating crystallization (SCC)

6.1 The spin-coating crystallization: a new paradigm for the evaluation of surface-API interactions

The batch crystallization of ASA highlighted the different actions of SAMs when employed as heteronucleants. Batch represents the most widespread technique for conducting lab-scale pharmaceutical research, but also for the mass production of drugs. As regards the former, batch experiments are usually tedious and difficult to perform. When heterogeneous nucleation has to be tackled, the risk of contamination with foreign particles is always very high, both during the solution preparation and the experiment set-up. Moreover, the number of crystallization trials needed to get relevant statistics is high, thus requiring the preparation and monitoring of multiple experiments in parallel, and a significant amount of API. Finally, the exploration of heterogeneous nucleation elongates the testing time, and a typical experiment can easily require several weeks.

In the framework of the results reported in Chap. 5 concerning the batch crystallization on SAMs, an innovative approach was proposed to investigate and gain mechanistic understanding of the interactions between SAMs and APIs. More specifically, the approach involved a shift from the temporal scale of batch crystallization to the spatial scale involved in the evaluation of SAM-API interactions at the interface. Firstly, API crystallization was confined to thin films, implementing a fast and reproducible process based on spin-coating crystallization (SCC). The interface between SAM and solution could be directly investigated by relating the structural properties of crystalline films to the superficial properties of SAMs. In this case, a macroscopic feature of the film was investigated. As a step further, the direct interaction between SAM end groups and a specific API crystal plane was evaluated by force spectroscopy. In this way, information on the mechanism of interaction was gathered at the atomic level.

Batch crystallization and crystallization in thin film are compared in Tab. 23. The two processes differ for the way in which supersaturation is reached. On the one hand,

---

The results presented in this chapter have been partially published in (Artusio et al., 2021).

pharmaceutical crystallization in batch is typically triggered by cooling of the solution. On the other hand, supersaturation is achieved by the progressive solvent evaporation induced by spinning in thin-film crystallization. It follows that the supersaturation implemented in batch is a defined value, provided that the experiment is properly designed. In thin film, instead, the exact supersaturation level at which nucleation starts in unknown as it is the result of spinning dynamics and stochasticity.

Table 23 The comparison of the main features of batch and thin-film crystallization for the lab-scale study of heterogeneous nucleation.

	Batch	**Thin film**
Achievement of supersaturation	cooling	solvent evaporation
Supersaturation	defined	unknown
Volumes of API solution	µL - mL	≤ 100 µL
Amount of drug required	mg - g	µg
Duration of experiment	few hours - months	≤ 5 min
Study in single-component solvents	depends on drug cost and solubility	yes
API – SAM interaction	anisotropic	isotropic
Post- treatment for XRD studies	rinsing and drying	none

Thin-film crystallization displays several advantages over batch to tackle the heterogeneous nucleation at lab-scale. One of the main advantages regards the volume of API solution required to carry out a single experiment. Typically, the majority of batch trials reported in literature require volumes in the mL-range. In some cases, the volume can be reduced, and even minimized, as presented in Chap. 5. The crystallization within thin films, instead, require the typical volumes of a spin-coating process, which are usually below 100 µl. It follows that the amount of API necessary for each spin-coating trial is significantly lower than the corresponding batch. Another important process parameter, when heterogeneous nucleation is investigated, is time. Conventional experiments carried out in batch usually require hours, days, or even months, to lead to the observation of the first crystals in solution. Crystallization in thin films, instead, can be accomplished in less than 5 min, thus minimizing process time and being a low-cost technique.

Thin-film crystallization also allows for the study of API crystallization in single-component solvents. As highlighted in § 5.2.1, the solubility of ASA is quite high is common solvents such as acetone or ethanol. Therefore, in previous batch experiments ethanol was mixed with water to reduce ASA solubility and the amount of requested ASA. Moreover, the reduced concentration of ASA was also beneficial for lowering the probability of solute clustering in the bulk. The study of single-component solvents in batch is thus limited by API solubility and cost. Conversely, thin-film crystallization opens up the possibility to tackle ASA crystallization in single-component solvents by using minimal amounts of API. Supersaturation is achieved very fast thanks to solvent evaporation, allowing the preparation of less concentrated starting solutions.

The spin-coating technique also avoids the anisotropy of interaction between API and SAM. Since the thickness of API solution is constant all over the SAM surface, all the nucleation sites on the surface are equally accessible by the API molecules, as schematized

in Fig. 31. At the same time, all the zones of the solution undergo the same increase in the API concentration during the spin step as the creation of any property discontinuity is repressed by the continuous rotation of the sample. Sample concentration is therefore uniform, and the presence of localized API gradients is avoided. Conversely, batch techniques are not exempt from local gradients or anisotropies. For example, referring to the trials of Chap. 5, the level of solution in each well may show minimal variations. Also, the cross-section profile of the liquid can be affected by curvature. In addition, the experiments were carried out under static conditions, thus lacking the homogenizing action induced by mixing. Therefore, batch crystallization on SAMs could be affected by an anisotropic interaction of ASA molecules with the SAM terminal groups.

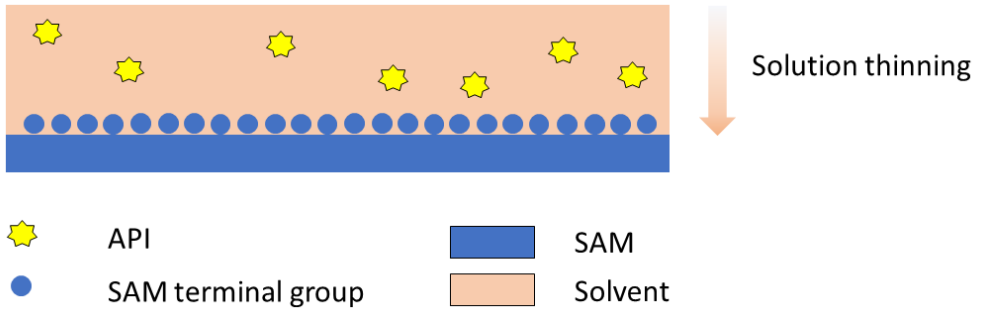

Figure 31 The isotropy of interfacial interactions between API and SAM end groups during SCC.

A final remark is dedicated to the preparation of samples for successive X-ray diffractometry (XRD) analyses. Crystals obtained by heterogeneous nucleation on external supports in batch require invasive pre-XRD treatments. The samples have to be thoroughly washed to remove unattached crystals that could corrupt the measurement. Then, samples have to be dried, and this step may trigger secondary nucleation, if not properly performed. Thin films of crystallized APIs, instead, do not require any pre-treatment, and XRD studies can be performed just after the spin-coating step. The absence of post-crystallization manipulation minimizes the risk of observing artifacts when collecting diffractograms.

Spin-coating is commonly used in micro-fabrication, photolithography, to prepare photonic crystals by progressive deposition of oriented layers or coatings with self-cleaning and self-sterilizing properties. Thin films can be obtained, ranging from few nm to several hundreds of µm. The main reason for the widespread application of spin-coating is due to the precise control of film features and repeatability, as well as to the precise dosage of chemicals and easy handling of substrates (Sahu et al., 2009; Tyona, 2013).

Nevertheless, the application of spin-coating techniques to the pharmaceutical field is nowadays still an emerging technique, but the literature reports many recent advancements. Thin-film phases have been studied by exploiting the ability of some substrates in modifying the structural order of materials near the interface (Jones et al., 2016). The investigation of API polymorphism and stabilization of amorphous forms (Guthrie et al., 2018), tautomerism (Wolnica et al., 2019), alteration of the texture of crystal forms (Röthel et al., 2016), crystallization behavior in different solvents (Van Eerdenbrugh et al., 2010) and with polymeric additives (Van Eerdenbrugh & Taylor, 2010) was successfully carried out in thin films. For example, when spin coating was followed by thermal treatments (Ehmann & Werzer, 2014) or performed on specific polymeric surfaces (Lopez-Mejías et al., 2011), metastable forms of acetaminophen were observed. Phenytoin was crystallized in thin films on silicon wafers to enhance the drug solubility and dissolution rate (Werzer

et al., 2014), obtain new polymorphs (Reischl et al., 2015), and alter the texture and form of the crystals by successive thermal treatments (Braun et al., 2019). In addition, the crystallization of aspirin deposited on oriented pyrolytic graphite resulted in dimer rods because of nonpolar interactions due to the underlying pattern (Mao et al., 2005). Most recently, thin composite layers of drug and matrix materials have been proposed as a drug delivery platform (Karki et al., 2016; Kellner et al., 2014). The application of thin films at industrial level has also been reported as a drying strategy for the continuous manufacturing of pharmaceuticals (Mesbah et al., 2014).

In the present thesis, to the best of our knowledge, the spin-coating crystallization of pharmaceuticals is firstly reported as a tool to investigate the interactions between engineered surfaces and APIs by evaluating the macroscopic properties of thin films. The evidence collected by the structural analysis of thin films was compared to the outcome of batch crystallization and force spectroscopy measurements.

6.2 Materials & Methods

6.2.1 Spin-coating crystallization of ASA on SAMs

Aspirin (ASA) solutions were freshly prepared and passed through 0.20 µm pore size syringe filters (Millex GV, Millipore). SAMs were freshly synthesized on glass substrates following the optimized protocol identified in § 4.3. A spin coater (Apogee, Cost Effective Equipment, Missouri, USA) was used to trigger ASA crystallization on SAMs. The process parameters were optimized before carrying out crystallographic studies on ASA thin films. The solvent composition, the concentration and the dispensed volume of ASA solution, the rotational speed, and the spin time were studied. The investigated range is outlined in Tab. 24. The process optimization was carried out on THIOL SAMs.

Table 24 Process parameters and respective conditions investigated to optimize the preparation of ASA thin films by spin-coating.

Parameter	Conditions
API solvent	EtOH, EtOH/water
ASA concentration, C_{ASA}	25 – 50 mg/mL
Dispensed volume of ASA solution, V_{ASA}	50 – 200 µL
Rotational speed, ω	500 – 6000 rpm
Spin time	5 – 10 min

The optimized process was carried out by setting the concentration of ASA at 50 mg/mL in ethanol. SAMs were placed on the spin coater chuck, and vacuum as low as 20 Pa was applied to keep the surface in place. 100 µL of ASA solution were pipetted on the surface. Spin process parameters involved initial acceleration = 500 rpm/s, spin speed = 1500 rpm, and spin time = 5 min. Such parameters ensured the complete solvent removal after the process.

6.2.2 Evaluation of the thickness of ASA films

The evaluation of the thickness of ASA films was performed with ellipsometry (alpha-SE, J.A. Woollam Co., Lincoln, NE, USA) and FE-SEM (FEI NOVA 600 Dual Beam, Hillsboro, OR, USA) techniques.

With regard to ellipsometry, measurements were carried out at 65, 70, and 75° to estimate the thickness of ASA films on SAMs. SAMs were described with the models already presented in § 3.1.2.2. As regards the ASA layer, a Cauchy film model was implemented, and the parameters were calculated by fitting the trends of the incident light. ASA refractive index was 1.562, as declared by the manufacturer.

The majority of the data was collected by ellipsometry. However, for samples prepared with $\omega \leq 750$ rpm, it was not possible to localize and detect the beam, and the measurement could not be performed. FE-SEM was therefore employed to investigate thick ASA films deposited on SAMs. Samples were carefully cleaved for cross-sectional investigation of the film. Then, samples were sputtered with a thin layer of gold to prevent charging effects. Coated samples were mounted on sample holders and transferred to the SEM chamber. The accelerating voltage was set at 2 keV, and the working distance was 5 mm. A through-lens detector (TLD) was used.

6.2.3 X-ray diffractometry (XRD) of spin-coated ASA

ASA thin films on SAMs were investigated by XRD (D8 Discover, Bruker AXC GmbH, Karlsruhe, Germany). XRD analyses were carried out in Bragg-Brentano configuration. A Cu K-α source and a LYNXEYE_XE detector in 0D mode were used. The measurements were carried out setting voltage and current at 40 kV and 40 mA, respectively. Physical slits were inserted on both the incident and the reflected beam path to parallelize the beams. A Göbel mirror and a 0.3 mm pinhole were mounted on the primary X-ray beam path. The pinhole was used to focus the X-ray beam on a small central area of the sample and avoid the signal contamination coming from the outer edges of the film. A 0.6 mm slit was mounted on the path of the secondary beam. In addition, a notch knife was mounted above the sample since, at small angles, the strong elastic scattering of electrons increases the detector counts and could easily lead to saturation. 2θ was varied between 6 and 40°. The step was set at 0.01°, and the acquisition time step was 15 s.

Diffractograms of powdered ASA were collected as a reference. ASA crystals were gently crushed with the help of a mortar and loaded into the sample holder. The sample holder was kept in a desiccator overnight to remove moisture and then transferred to the instrument. The sample rotation was set at 60 rpm to limit the disturbance due to the sample roughness and inhomogeneity. ASA thin films were directly analyzed after the spin-coating step. The same physical set-up and operative conditions were implemented, except for the absence of sample rotation. A narrower 2θ window was explored, namely $6° < 2\theta < 30°$.

XRD data were normalized and peaks were fitted with Voigt functions to evaluate the intensity ratios and the full width of the peaks at medium heights (FWMH).

6.2.4 AFM force spectroscopy

6.2.4.1 Functionalization of AFM tips

AFM Si_3N_4 tips were functionalized with THIOL or ACR silanes, which were responsible for major differences in ASA nucleation kinetics, as discussed in Chap. 5. The tips were exposed to UV light for 15 min. Tips were placed on a glass support to avoid deposition of adventitious material on the tip. The surface activation was achieved thanks to ozone. A dry activation route was selected to avoid damaging the tip with aggressive piranha treatment and rinsing steps. After the surface activation, tips were immediately immersed in individually closed tubes for surface functionalization. Each tube was pre-filled with 0.5 mL of 0.054 M silane solution in anhydrous toluene. Tips were incubated overnight and then rinsed with toluene, toluene : ethanol (1:1), and ethanol. Extreme care was taken during all the process to avoid the detachment of the cantilever from the tip.

6.2.4.2 Evaluation of force-distance curves by AFM

The functionalized probes were mounted on an AFM piezo (SMENA head, Solver electronics, NT-MDT Spectrum Instruments, Russia). Preliminary calibrations were carried out for each tip in semi-contact mode. In this way, sensitivity factors and spring constants of the cantilevers were determined on stiff and incompressible surfaces, i.e., silicon wafers. The tip positioning was equipped with a feedback controller. Then, an ASA crystal was placed on the AFM stage with the (100) face normal to the tip. Deflection-piezo height curves were acquired in contact mode and processed to obtain force-distance curves. Two types of tips were employed, differing for their elastic constant. Soft tips were used for reference and for the functionalization with ACR silane, whereas stiffer tips were functionalized with THIOL silane. As regards the latter, preliminary experiments involving soft tips were performed but led to the detachment of the tip because of the strong attraction forces with the crystal surface. Therefore, stiffer tips were employed. The experiments were carried out in clean room to limit the contamination of the crystal surface, and the measurements were repeated on at least 15 different spots of the crystal surface.

6.3 Design of the spin-coating process

The preparation of ASA thin films for crystallographic studies was carried out via spin coating. The various steps of the spin-coating process are sketched in Fig. 32. The first step consisted in the immobilization of SAM-functionalized coverslips onto the chuck thanks to vacuum. ASA solution was then directly pipetted on the SAM surface. Immediately after the dispensing step, the chuck was subjected to high rotational acceleration, $\dot{\omega}$. In this phase, the excess solution was removed thanks to centrifugal forces. A controlled thickness of ASA solution was obtained when the target rotational speed, ω, was achieved. During this stage, the solvent was progressively removed by evaporation, resulting in solution thinning. Supersaturation conditions high enough to trigger the formation of the first nuclei were soon achieved, and crystallization proceeded rapidly. After the total removal of solvent and the completion of crystallization, SAMs were withdrawn from the chamber and transferred to the XRD facility.

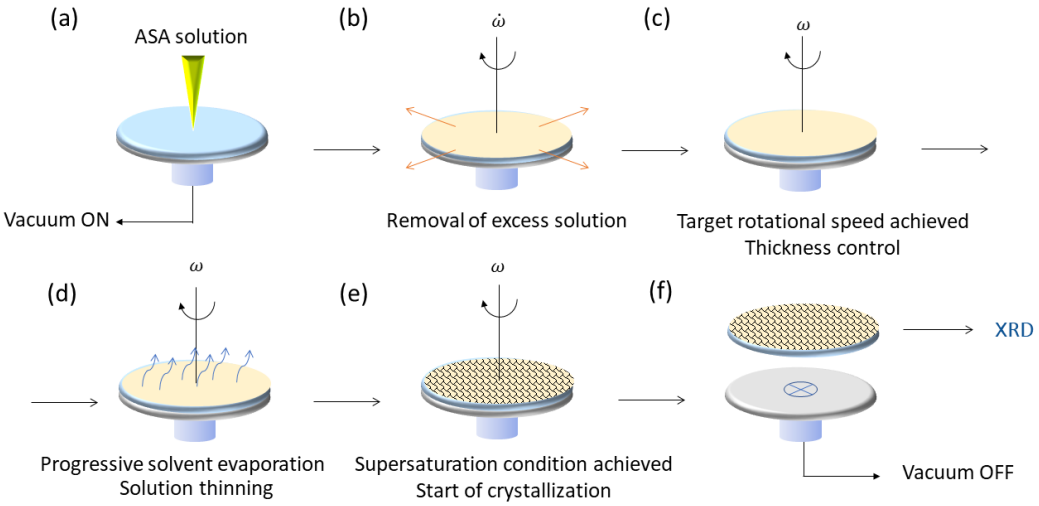

Figure 32 Overview of the spin-coating process for the preparation of ASA thin films. (a) Loading, (b)-(e) spinning, and (f) unloading phases are displayed. The figure was taken from (Artusio et al., 2021) with modifications.

Many variables can influence the spin-coating process and have to be carefully designed in order to ensure process robustness and sample quality. The following paragraphs present the process design in terms of API solvent, volume of API solution, spin time, and rotational speed.

6.3.1 Solvent and spin time

The model API selected for the study was ASA. A comparative study between the spin-coating outcome using a single-component solvent, namely ethanol, and a solvent mixture, such as ethanol/water (38/62 v/v), was performed. Several conditions were tested involving different rotational speed and spin times, as reported in Tab. 25. ASA concentration was set at 25 mg/mL for all the experiments.

The preliminary tests on ω and spin time highlighted several important points. Firstly, the ethanolic mixture used in Chap. 5 for batch crystallization was unsuitable to the formation of ASA thin films. All the conditions tested, i.e., samples EW1 - 4, did not lead to the formation of good quality ASA films. After the process, localized deposits of ASA crystals were observed, together with tiny liquid drops all over the glass surface. The former phenomenon was related to the localized nucleation of ASA promoted by the ethanol evaporation. The latter was attributed to the sparse formation of metastable drops of concentrated ASA aqueous solutions. The drops immediately led to crystals when perturbed. The number of drops per surface decreased increasing ω and spin time. The use of solvent mixtures impeded the formation of ASA films because of the different volatility and evaporation rates of the solvents.

The use of a single-component solvent like ethanol resulted in uniform evaporation of the solvent. Dry samples were obtained after 5 and 10 min. However, the resulting ASA film appeared to be discontinuous. The glass surface was covered by leopard-like areas of ASA thin films. Such a result was attributed to the insufficient amount of ASA retained on the sample surface after the removal of excess solution in the initial stages of spinning.

Table 25 List of spin-coating conditions for ASA dissolved in ethanol or ethanolic mixtures. Sample code, rotational speed ω, spin time, and aspect of obtained ASA films are reported. All the tests were carried out setting 100 µL as the ASA solution volume, C_{ASA} = 25 mg/mL, and $\dot{\omega}$ = 500 rpm/s.

EtOH / water			
Sample	**ω, rpm**	**Spin time, min**	**ASA film**
EW1	1500	5	Not formed
EW2	1500	10	Not formed
EW3	3000	5	Not formed
EW4	3000	10	Not formed
EtOH			
Sample	**ω, rpm**	**Spin time, min**	**ASA film**
E1	1500	5	Discontinuous
E2	1500	10	Discontinuous
E3	3000	5	Discontinuous
E4	3000	10	Discontinuous

6.3.2 API concentration and volume of dispensed solution

In order to obtain a continuous film from ethanol, the concentration of ASA was increased to 50 mg/mL, and the influence of the volume of pipetted solution, V_{ASA}, was studied. Three volumes were tested, and the outcome of spin-coating evaluated, as reported in Tab. 26.

Table 26 Sample code, ASA solution volume, and aspect of obtained ASA films. All the tests were carried out setting C_{ASA} = 50 mg/mL in EtOH, $\dot{\omega}$ = 500 rpm/s, ω = 1500 rpm, and spin time = 5 min.

Sample	**ASA solution, µL**	**ASA film**
E5	50	Discontinuous
E6	100	Continuous
E7	200	Continuous

The increased concentration of ASA promoted the formation of continuous films on the glass surface. However, when the volume of the dispensed solution was too small, discontinuities were encountered along the surface. As it was observed for the smaller C_{ASA}, such a behavior was related to the presence of insufficient amounts of API on the sample surface to form a continuous layer. The investigation of C_{ASA} and V_{ASA} allowed the identification of the respective threshold values for getting discontinuity-free ASA films.

The preliminary phase of the design of the process led to the identification of proper solvents, API concentrations, and amounts of dispensed solution before spinning. The following optimization of spin parameters will be performed by setting C_{ASA} = 50 mg/mL in EtOH, V_{ASA} = 100 µL, $\dot{\omega}$ = 500 rpm/s, and spin time = 5 min.

6.3.3 Rotational speed and API film thickness

The rotational speed controls the thickness of the retained layer of API solution over the sample surface and, thus, the final thickness of the crystallized film. However, the thickness of the API solution obtained after the thinning step depends on other factors, such as the viscosity of the solvent and the interfacial tension between the solution and SAM. One of the main advantages of spin coating for the preparation of crystallized thin films is represented by the uniformity of film thickness over the SAM. Once the API solution is selected, the film thickness will only depend on the spin speed and can easily be controlled. Such a feature ensures the reproducibility and the robustness of sample preparation, justifying the proposed application to crystallographic studies.

The thickness of ASA films obtained on THIOL SAMs was studied as a function of the spin speed, as displayed in Fig. 33. The optimized conditions highlighted in § 6.3.2 were employed. ω varied between 500 and 6000 rpm.

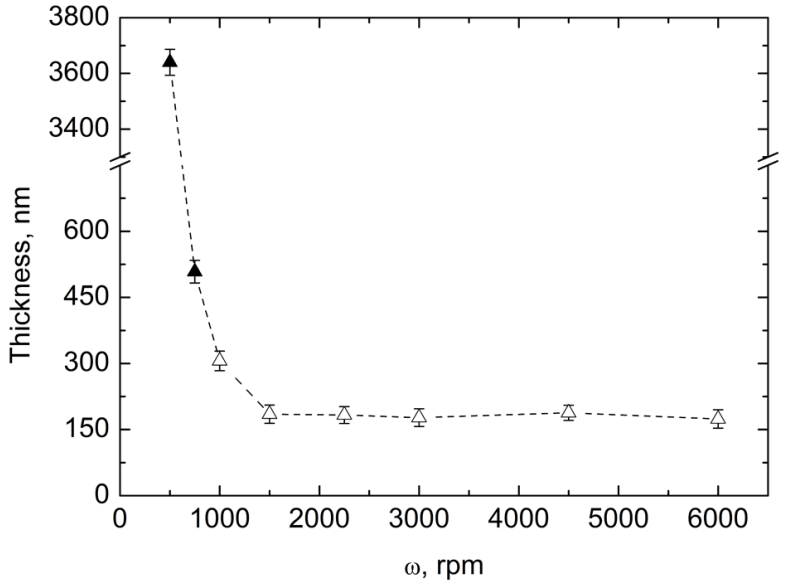

Figure 33 The thickness of crystallized ASA films as a function of the rotational speed ω. Full symbols refer to thickness estimated from FE-SEM micrographs, whereas empty symbols refer to thickness measured with ellipsometry. Error bars refer to SD. All the tests were carried out setting C_{ASA} = 50 mg/mL in EtOH and V_{ASA} = 100 µL.

The investigated range of ω led to ASA thin films belonging to the µm-range. As a general approach, thickness was calculated with ellipsometry but ASA films above a certain threshold thickness required the use of FE-SEM. The dramatic impact of ω on the thickness of the crystallized film was highlighted. Thick films up to almost 4 µm or more were obtained with low rotational speeds, i.e., ω = 500 rpm. Then, a more precise control and thinner films were obtained with higher ω. Finally, film thickness reached a plateau around 180 nm. It was therefore demonstrated that spin-coating techniques precisely control the thickness of the ASA films and that a tuning can be achieved by acting on the rotational speed. Continuous thin ASA films of approx. 180 nm were prepared by setting ω > 1500 rpm.

6.3.3.1 Morphology of ASA thin films

The morphological features of ASA thin films were investigated by FE-SEM after sample cleavage to study the cross-section of the films. Representative FE-SEM micrographs of ASA thin films grown on ACR SAMs and prepared at ω = 750 rpm are collected in Fig. 34. Fig. 34 (a) shows an overview of the coverslip and ASA thin film at the top of it. The ordered, compact, and defect-free structure of ASA films can clearly be discerned in higher magnification micrographs reported in Fig. 34 (b) and (c). Films were composed of elongated ASA crystals, and some crystalline fragments detached from the film, probably after sample cleavage, were also detected. The FE-SEM micrographs also highlighted the control over the thickness of the crystalline layer imposed by spin coating. The top of the film was indeed extremely regular. The lack of superficial asperities or crystal spikes proved that the crystal growth was successfully confined to a precise layer.

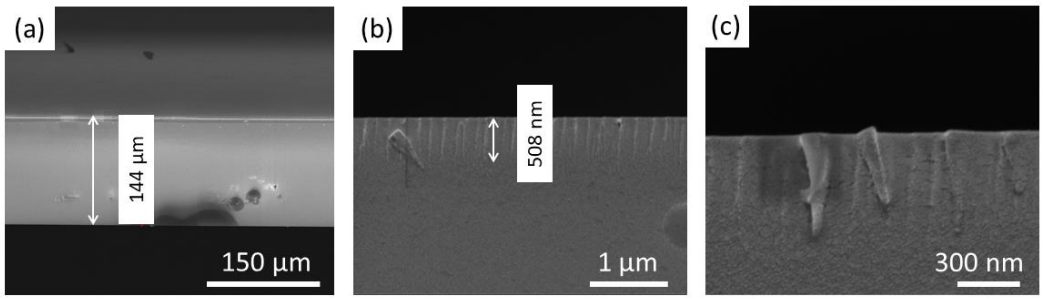

Figure 34 FE-SEM micrographs of ASA thin films grown on ACR SAMs. (a) 500 X, (b) 60k X, and (c) 160k X magnifications of samples prepared at ω = 750 rpm.

The design of the spin-coating process was vital for getting high-quality samples that could fit XRD requirements. Particular attention was devoted to the preparation of continuous ASA thin films. Process parameters including ASA solvent, dispensed solution volume, spin time, and rotational speed were adjusted. The thickness of ASA films was successfully tuned by acting on the rotational speed from 180 nm to few µms.

6.4 Crystallographic study of ASA thin films on SAMs

The crystallization of ASA in thin films was carried out on SAMs to investigate whether different SAM end groups could induce the face-selective nucleation of APIs. In this perspective, samples were prepared for XRD analyses and for the evaluation of the preferential orientation of crystal faces. The optimized spin-coating conditions were implemented, and the rotational speed was set at 1500 rpm for all the samples to deal with about 180 nm-thick films, which corresponded to the smallest thickness achievable with the selected experimental set-up. Such a thickness was selected so as to enhance the action of SAMs on ASA crystallization and avoid the risk of excessive growth of aspecific ASA crystals.

6.4.1 XRD of ASA thin films

As a preliminary step, the diffractogram of ASA powder was taken as a reference for the identification of the crystalline planes and the comparison with database values. Fig. 35 reports a representative diffractogram and the peak references. The structure of powdered ASA crystals belonged to the $P2_1/c$ monoclinic space group (a = 11.416(5) Å, b = 6.598(2) Å, c = 11.483(5) Å, α = 90°, β = 95.60(3)°, γ = 90°; CSD entry code: ACSALA07). A variety of crystal planes, attributable to the random orientation of the crystallites in space, was observed. The most intense peak was detected at 15.6° and was attributed to the convoluted signals coming from (002), (011), (110), and (200) planes. Less intense peaks were registered at 7.9, 22.3, and 26.9°. Minor peaks were also detected.

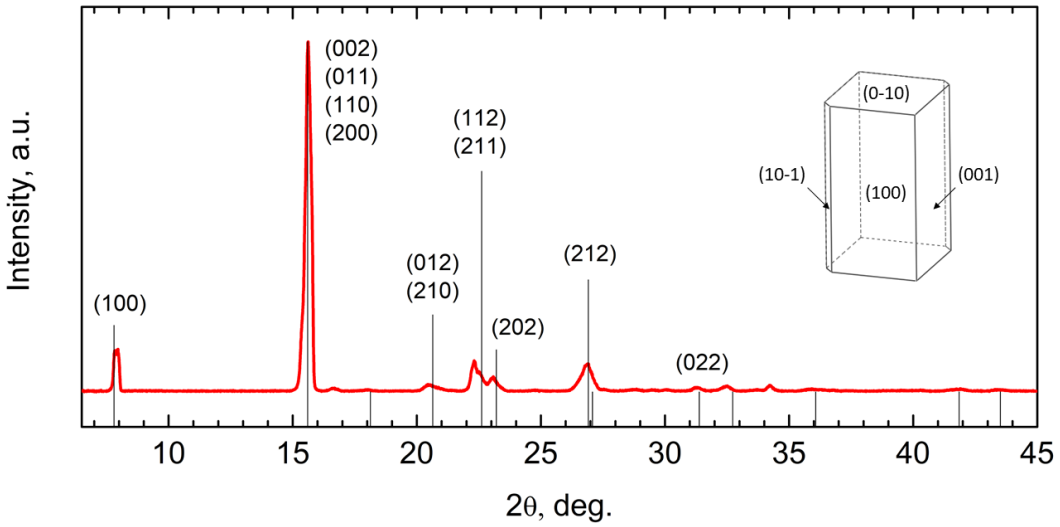

Figure 35 XRD of powdered ASA. Peaks were assigned to crystallographic planes by comparing the diffractogram (red curve) with ASA reference peaks in the database (black lines). Embedded is the BFDH prediction of ASA crystal morphology, as calculated with KrystalShaper.

ASA thin films were prepared on the four SAMs already used for batch crystallization in Chap. 5. ASA films on bare glass were used as reference, together with the ASA powder data. The diffractograms are collected in Fig. 36. The comparison between the diffractograms of powdered ASA and ASA thin films highlighted marked differences. In thin film samples, reflections from four groups of crystalline planes could only be observed, in contrast to ASA powder. Reflections corresponded to (100) planes at 7.7°, (002), (011), (110), and (200) planes at 15.4°, (112) planes at 23.3°, and (022) planes at 31.3°. The peak at 15.4° could not be deconvoluted, and the contribution of the dominant crystal planes (002) and (011) will be considered together.

The peak intensities and the respective positions in the diffractogram were used to investigate the preferential orientation of the crystalline planes as, in thin films, only crystal planes that are parallel to the substrate surface are able to reflect X-rays. Assuming that nucleation and crystallites formation during solvent evaporation in SCC proceeds governed by interfacial tensions between individual facets and SAM surface, solvent type and evaporation time, which are the same for all the substrates, one could look at the variation of the intensity ratios between different crystal facets as a consequence of their preferential interaction with SAMs surface chemistry and the resulting orientation of the ASA crystallites with respect to the surface normal.

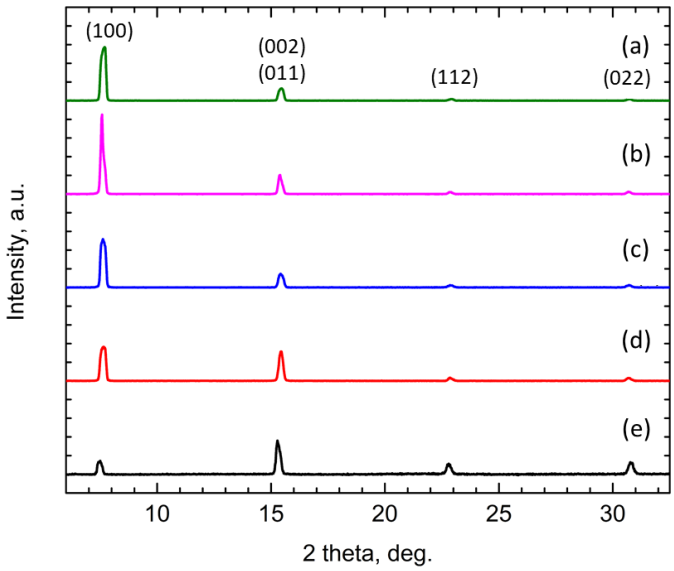

Figure 36 XRD of ASA thin films grown in ethanol on (a) AMINO, (b) GLY, (c) THIOL, (d) ACR SAMs, and (e) bare glass.

The intensity of the four peaks of ASA identified by XRD analyses was calculated and divided by the total peak intensity to evaluate the relative ratio among (*hkl*) planes. The results are reported in Fig. 37 (a). Compared to ASA crystals grown in bulk, ASA thin films displayed more intense peaks referred to (100) and (022) crystal planes. The relative ratio of (*hkl*) planes was related to the surface chemistry of the support used for SCC, as highlighted in Fig. 37 (b). The comparison among the relative intensity of (*hkl*) planes of ASA thin films grown on glass and on SAMs pointed out that the intensity of (100) planes was always higher on SAMs at the expense of (002)+(011), (112), and (022) planes. Regarding SAMs, the relative ratio of (112) and (022) planes was constant for all the ASA thin films.

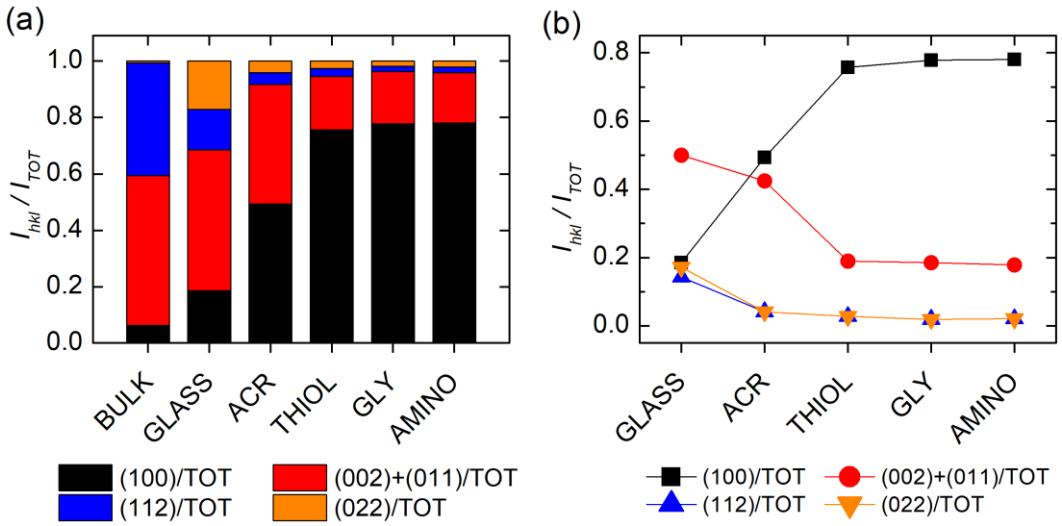

Figure 37 (a) Normalized peak intensity ratio of (*hkl*) planes referred to total intesity for ASA grown in bulk and as a thin film on surfaces. (b) Normalized peak intensity ratio of (*hkl*) planes of ASA thin films as a function of the glass/SAM surface chemistry.

The major effect of surface chemistry was observed on the relative ratio of (100) and (002)+(011) planes. Among all SAMs, ACR SAMs displayed the most intense signal related to (002)+(011) planes, whereas the signal of (100) planes was most intense in films grown on THIOL, GLY, and AMINO SAMs. Overall, the spin-coating induced the presence of preferential orientations of ASA crystals, whose relative contribution was dictated by SAM chemistry.

6.4.2 The face selective action of SAMs

A marked action of SAM's exposed chemistry on the orientation of ASA crystal faces was evinced from the comparison of the relative peak intensities, as highlighted in Fig. 37 (b). Such an observation was supported by the morphology of ASA thin films crystallized on ACR and GLY SAMs in cross sectional SEM images reported in Fig. 38 (a) and (b). On ACR SAMs, elongated crystals were observed, which corresponded to the growth of (011) crystal planes parallel to the SAM surface. Conversely, on GLY SAMs, the (100) crystal plane grew parallel to the SAM surface. The two ASA crystal planes display a markedly different character. The (011) face exposes carboxylic groups and is scarcely water soluble. The (100) face, instead, has a higher hydrophilic character, compared to the other ASA crystal faces, because of the exposed carbonyl and hydroxyl groups. The (100) face of ASA can easily interact via hydrogen bonding with the GLY SAM surface, which can, in turn, preferentially induce the nucleation of (100) faces. Since the (100) face is rather water soluble, it allows for fast and efficient drug administration, and it is also the most energetically stable face as regards cohesive and adhesive aspects (Mao et al., 2005).

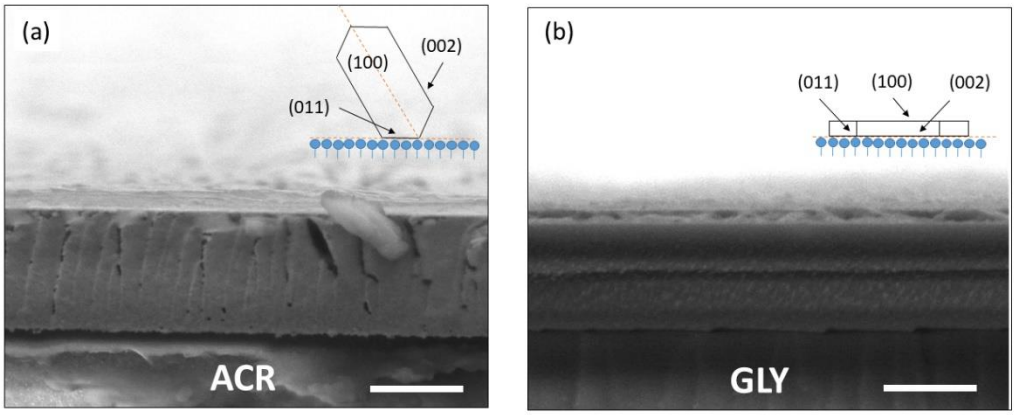

Figure 38 FE-SEM micrographs of ASA thin films grown on (a) ACR and (b) GLY SAMs. Scale bar is 1 μm. Diagrams in the inset show the relationship between film morphology and crystal orientation on the substrate. The figure was taken from (Artusio et al., 2021) with modifications.

The face-selective action towards ASA crystallization of SAMs was related to a specific SAM surface property. As outlined in Fig. 39, the ratio between (100) and the convolution of (002) and (011) planes of ASA thin films followed an opposite trend compared to the acid surface energy component of SAMs (Pearson's r = - 0.964). The minimum value of the ratio between (100) and (002) + (011) planes was found for bulk ASA. The spin-coating crystallization process slightly increased the signal of (100) peak, as seen for thin films prepared on glass. However, the superficial chemistry of the SAM turned out to have a dramatic selective effect. For ASA thin films grown on ACR SAMs,

the ratio between the two families of planes was approx. 1. Conversely, all the other SAMs led to 4-fold larger ratios.

On the one hand, ASA crystal faces are characterized by different polarity and acidity according to the exposed groups. On the other hand, SAMs are characterized by the ability to provide a different extent of acid/base interactions. SAMs displaying acceptor groups (THIOL, AMINO and GLY) determined stronger interactions with donor ASA crystal facets and thus preferentially grew (100) carbonyl terminated planes, whereas surfaces with donor groups (piranha-treated glass and ACR) preferentially interacted with acceptor ASA facets and favored the growth of (002) + (011) crystal features.

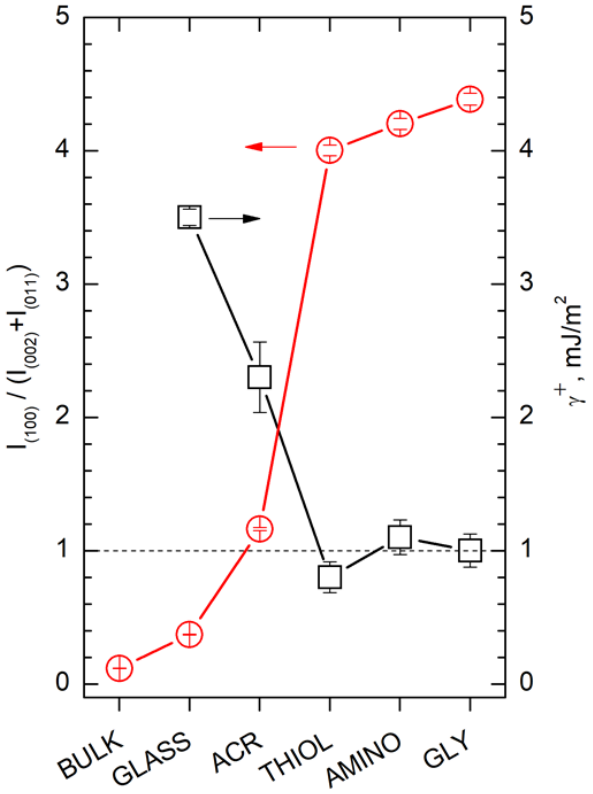

Figure 39 Ratio between the intensity of reflections from (100) and (002)+(011) planes of ASA thin films crystallized on different substrates and corresponding acid surface tension component. Error bars refer to SD. The figure was taken from (Artusio et al., 2021) with modifications.

6.5 Preferential interactions between ASA and specific chemical groups

As a final step, the preferential interaction between ASA molecules and specific chemical groups was investigated via force spectroscopy. AFM tips were functionalized with THIOL or ACR silanes, following a protocol similar to the optimized SAM preparation on glass. Particular care was taken during the surface activation and final rinsing steps to avoid damaging or detaching the AFM cantilever, as outlined in § 6.2.4. Fig. 40 represents a scheme of the set-up developed to probe the interaction between SAMs and the (100) ASA crystal face. Bulk ASA crystals of about 3x8x1 mm^3 were prepared by bulk crystallization in ethanol. Such crystals displayed a wide, regular and flat (100) face. The (100) face

displays carbonyl groups and a rather basic character. Silanes carrying thiol or methacrylate groups were selected since they led to the most distinct crystallization behaviors, both in batch and thin films.

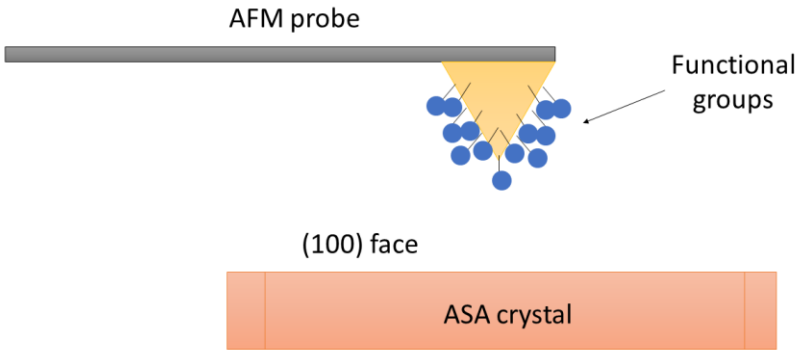

Figure 40 Schematic representation of the experimental set-up developed to study ASA – SAM interactions via AFM.

More specifically, the interaction between the functionalized tips and the crystal (100) face was evaluated by collecting force curves. In this way, precise information was gained on the specific affinity between the ASA groups exposed on the (100) face and SAM end groups in absence of solvents. To minimize the risk of crystal surface contamination, the experiments were carried out in clean room.

6.5.1 Force – distance curves

The force – distance, *F-d*, curves were obtained from the evolution of AFM cantilever deflection as a function of the piezo displacement along the z-axis. Such a technique is widely used in materials science to measure elasticity, Hamaker constants, hydrophobicity, Coulomb or van der Waals forces (Cappella & Dietler, 1999; Senden, 2001).

During the measurement, the piezo was ramped perpendicularly to the crystal (100) face, and the variations in tip height, δ, were collected. The AFM tip – crystal force, F, is given by the Hooke's law:

$$F = -k_e\delta \tag{16}$$

where k_e is the spring constant of the tip which was evaluated experimentally.

The force-distance curves reported in Fig. 41 were characterized by approaching and withdrawal phases. A more or less intense hysteresis was observed. Zero lines were obtained when the tip was far away from the crystal surface. In these regions, the cantilever deflection was nearly zero since the cantilever was not influenced by the surface. During the approaching phase, the tip progressively moved towards the crystal surface and long-range interactions could be explored, such as electrostatics. A sudden increase corresponded to the jump-to-contact, or snap-in. Here, the tip experienced a gradient of attractive forces larger than its spring constant. Strong van der Waals forces occurred between tip and crystal surface. The x-axis was set at 0 referring to a standard position of the AFM piezo corresponding to a three quarters way during the approaching phase. During the withdrawal phase, another discontinuity in the force value was observed and related to the jump-off-contact, or snap-out. Here, the interaction was tuned by adhesion forces.

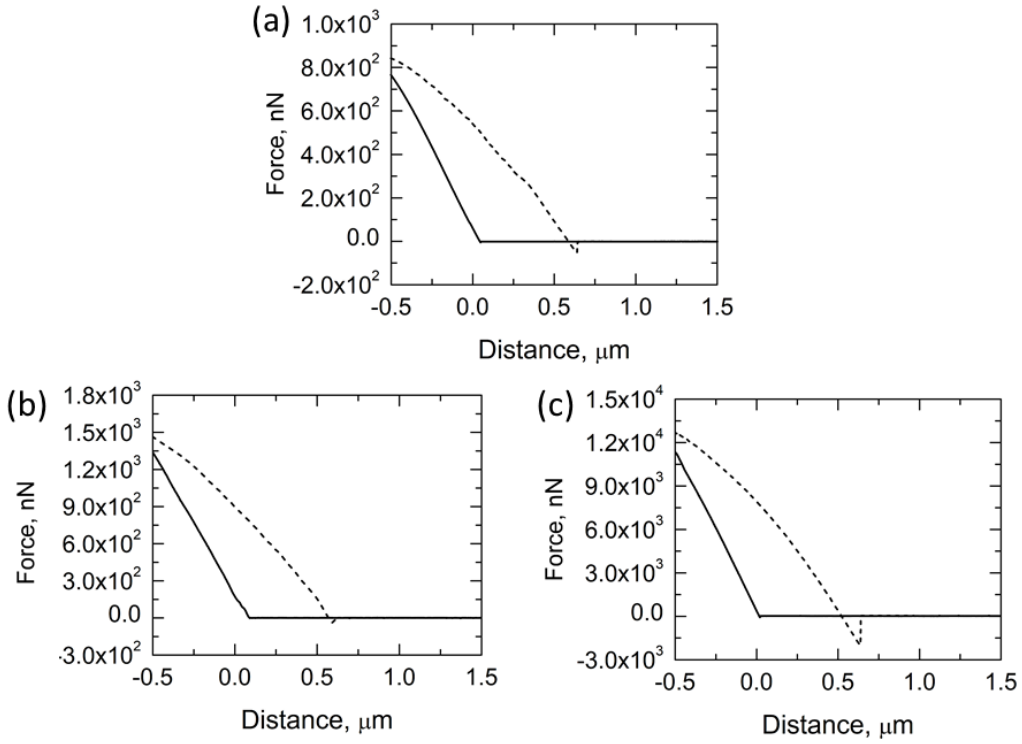

Figure 41 Force-distance curves as calculated with AFM. Tips were (a) UV cleaned or functionalized with (b) ACR and (c) THIOL silanes. The continuous line refers to the snap-in phase, whereas the dashed line refers to the snap-back phase. The figure was taken from (Artusio et al., 2021) with modifications.

The interaction between the tips and the ASA crystal resulted to be strongly dependent on the tip functionalization. Such a result was also confirmed by the values of adhesion force, F_{ad}. F_{ad} was obtained from the minimum of the withdrawal curve. The obtained values are listed in Tab. 27. UV cleaned tips were taken as reference as they only displayed a higher surface density of hydroxyl groups. The *F-d* curve reported in Fig. 41 (a) highlighted moderate interaction with the (100) face. The predominant interaction was attributed to the favorable hydrogen bonding between the tip -OH groups and the carbonyl groups of (100) face.

The presence of silanes on the AFM cantilever strongly altered *F-d* curves. Tips functionalized with ACR silanes displayed a much weaker interaction with the (100) face, as highlighted in Fig. 41 (b). The adhesion force resulted to be approx. half of the corresponding values found for the reference tips. Such a finding well agreed with the results obtained for ASA thin films. On ACR SAMs, the growth of (100) face turned out to be inhibited compared to other SAMs, and the ratio between (100) and (002) + (011) face was approx. 1. Conversely, such a ratio strongly increased when films were grown on THIOL SAMs. The result was reflected by much higher attractive and adhesive forces detected with AFM force spectroscopy. An intense hysteresis effect can be observed in Fig. 41 (c). The functionalization with THIOL silane required the use of much stiffer tips, as reflected by the higher spring constant, in order to successfully withdraw the tip from the ASA crystal during the retracting phase. F_{ad} increased of 2 and 3 orders of magnitude, respectively. The intense interaction was related to favorable hydrogen bonding and electrostatics.

Table 27 The spring constant and the adhesion force calculated from force-distance curves between functionalized tips and ASA (100) crystal face. SD is reported in brackets.

Tip	k_e, N/m	F_{ad}, nN
UV cleaned	1.455	52 (±7)
ACR SAM	1.789	28 (±6)
THIOL SAM	22.0	1800 (±550)

In conclusion, the interaction between ASA (100) face and SAMs was investigated by AFM force spectroscopy. Strong adhesion forces were evinced for THIOL SAMs, whereas significantly less intense interaction was obtained for ACR SAMs.

6.6 Final remarks

In this chapter, a new approach to tackle the fundamentals of interactions between drugs and specified chemical groups has been proposed. Spin-coating crystallization allowed for the creation of ASA thin films on different SAMs. The spin parameters and process conditions were optimized. The thickness of the ASA film was successfully tuned by acting on the rotational speed. Continuous crystalline films whose thickness varied from 180 nm to few μm were prepared. The crystallization of ASA in thin films was strongly related to the exposed chemistry of SAMs used as support. XRD investigation outlined the preferred orientations of ASA crystals, which was quantified by studying the intensity ratios between crystalline planes and confirmed by FE-SEM investigation of thin films morphology. A correlation between the acid surface energy component of SAMs and the oriented growth of ASA thin films was identified. Finally, the specific interaction between (100) ASA crystal face and SAMs was quantified with AFM force spectroscopy and force-distance curves.

References

Artusio, F., Fumagalli, F., Valsesia, A., Ceccone, G., & Pisano, R. (2021). Role of self-assembled surface functionalization on nucleation kinetics and oriented crystallization of a small-molecule drug: Batch and thin-film growth of aspirin as a case study. Accepted for publication in *ACS Applied Materials & Interfaces*.

Braun, D. E., Rivalta, A., Giunchi, A., Bedoya-Martinez, N., Schrode, B., Venuti, E., Della Valle, R. G., & Werzer, O. (2019). Surface induced phenytoin polymorph. 1. full structure solution by combining grazing incidence x-ray diffraction and crystal structure prediction. *Crystal Growth and Design*, **19**(11), 6058–6066.

Cappella, B., & Dietler, G. (1999). Force-distance curves by atomic force microscopy. *Surface Science Reports*, **34**(1), 1–104.

Ehmann, H. M. A., & Werzer, O. (2014). Surface mediated structures: Stabilization of metastable polymorphs on the example of paracetamol. *Crystal Growth and Design*, **14**(8), 3680–3684.

Guthrie, S. M., Smilgies, D., & Giri, G. (2018). Controlling polymorphism in pharmaceutical compounds using solution shearing. *Crystal Growth and Design*,

18(1), 602–606.

Jones, A. O. F., Chattopadhyay, B., Geerts, Y. H., & Resel, R. (2016). Substrate-induced and thin-film phases: polymorphism of organic materials on surfaces. *Advanced Functional Materials*, **26**(1), 2233–2255.

Karki, S., Kim, H., Na, S., Shin, D., Jo, K., & Lee, J. (2016). Thin films as an emerging platform for drug delivery. *Asian Journal of Pharmaceutical Sciences*, **11**(5), 559–574.

Kellner, T., Ehmann, H. M. A., Schrank, S., Kunert, B., Zimmer, A., Roblegg, E., & Werzer, O. (2014). Crystallographic textures and morphologies of solution cast ibuprofen composite films at solid surfaces. *Molecular Pharmaceutics*, **11**(1), 4084–4091.

Li, T., Li, B., & Tomassone, M. S. (2006). Surface characterization of aspirin crystal planes using molecular dynamics simulations. *Chemical Engineering Science*, **61**(1), 5159–5169.

Lopez-Mejías, V., Knight, J. L., Brooks, C. L., & Matzger, A. J. (2011). On the mechanism of crystalline polymorph selection by polymer heteronuclei. *Langmuir*, **27**(12), 7575–7579.

Mao, G., Chen, D., Handa, H., Dong, W., Kurth, D. G., & Möhwald, H. (2005). Deposition and aggregation of aspirin molecules on a phospholipid bilayer pattern. *Langmuir*, **21**(2), 578–585.

Mesbah, A., Versypt, A. N. F., Zhu, X., & Braatz, R. D. (2014). Nonlinear model-based control of thin-film drying for continuous pharmaceutical manufacturing. *Industrial and Engineering Chemistry Research*, **53**, 7447–7460.

Reischl, D., Röthel, C., Christian, P., Roblegg, E., Ehmann, H. M. A., Salzmann, I., & Werzer, O. (2015). Surface-induced polymorphism as a tool for enhanced dissolution: the example of phenytoin. *Crystal Growth and Design*, **15**(9), 4687–4693.

Röthel, C., Ehmann, H. M. A., Baumgartner, R., Reischl, D., & Werzer, O. (2016). Alteration of texture and polymorph of phenytoin within thin films and its impact on dissolution. *CrystEngComm*, **18**(4), 588–595.

Sahu, N., Parija, B., & Panigrahi, S. (2009). Fundamental understanding and modeling of spin coating process: A review. *Indian Journal of Physics*, **83**(4), 493–502.

Senden, T. J. (2001). Force microscopy and surface interactions. *Current Opinion in Colloid and Interface Science*, **6**(1), 95–101.

Tyona, M. D. (2013). A theoritical study on spin coating technique. *Advances in Materials Research*, **2**(4), 195–208.

Van Eerdenbrugh, B., Baird, J. A., & Taylor, L. S. (2010). Crystallization tendency of active pharmaceutical ingredients following rapid solvent evaporation - Classification and comparison with crystallization tendency from undercooled melts. *Journal of Pharmaceutical Sciences*, **99**(9), 3826–3838.

Van Eerdenbrugh, B., & Taylor, L. S. (2010). Small scale screening to determine the ability of different polymers to inhibit drug crystallization upon rapid solvent evaporation. *Molecular Pharmaceutics*, **7**(4), 1328–1337.

Werzer, O., Baumgartner, R., Zawodzki, M., & Roblegg, E. (2014). Particular film formation of phenytoin at silica surfaces. *Molecular Pharmaceutics*, **11**(2), 610–616.

Wolnica, K., Szklarz, G., Dulski, M., Wojtyniak, M., Tarnacka, M., & Kaminska, E. (2019). Studying tautomerism in an important pharmaceutical glibenclamide con fi ned in the thin nanometric layers. *Colloids and Surfaces B: Biointerfaces*, **182**(1), 110319.

PART III:

The crystallization of proteins

Chapter 7

An overview of the techniques used for the protein crystallization

In the present chapter, a general overview on the peculiarities of protein crystallization is given, focusing on the differences with small molecule crystallization and on the techniques employed. The results of the preliminary crystallization screening of lysozyme, catalase, and proteinase K are discussed. The optimal crystallization conditions were identified with different crystallization techniques and will guide the design of experiments involving SAMs and gel matrixes.

7.1 Differences between small-molecule and protein crystals

Despite sharing the crystalline state, small molecule and protein crystals display markedly different features. On the one hand, small molecule crystals, both organic and inorganic, are characterized by strong inter-reticular forces. The overall material is built up by a robust lattice, which makes the crystals brittle and robust. On the other hand, protein crystals are fragile and extremely sensitive to the external environment. Considering the molecular weight of a protein, each macromolecule can display a relatively small number of bonds in a lattice, resulting in crystals with scarce reticular energy (Durbin & Feher, 1996). The protein crystals retain a high content of solvent, typically from 30 to 80%, and can be regarded as ordered gels kept together by weak interstitial forces. Macromolecules in a crystal are essentially equivalent to their full solvation state. Solvent molecules, ions, or coenzymes can freely diffuse inside and outside the crystal thanks to cavities and channels.

From the process point of view, both small molecules and proteins require supersaturation as a driving force to trigger crystallization. However, the supersaturation conditions required by complex macromolecules to initiate crystallization are at least two orders of magnitude higher than for small molecules. At the same time, such conditions must not alter their natural state and have to be carefully tuned based on macromolecule stability (Mcpherson, Malkin, & Kuznetsov, 1995). Once nucleation is initiated, crystal growth occurs much slower in the case of proteins, as a consequence of smaller growth

kinetics coefficients (Chernov, 2003). An additional difference regards the limitations imposed by the solvent selection. On the one hand, only aqueous mother liquors are suitable for biological molecules as water represents the native environment of proteins, and variations are rarely tolerated. On the other hand, the selection of the solvent is mainly dictated by solubility for small molecules.

A final major distinction regards the scope of crystallization. As far as small molecule APIs are concerned, crystals possess a therapeutic value since the crystalline material is mostly employed to produce the final dosage forms and to investigate drug polymorphism and activity. On the other hand, crystals of complex biomacromolecules can be produced not only for therapeutic purposes, but also to understand the spatial conformation and structure of the macromolecules.

The two most important features of protein crystals are indeed stability and size. The former allows for safe crystal conservation over time and manipulation. The latter represents the target of many crystallization trials aimed at producing crystals suitable for the successive crystallographic investigations. The diffractive ability of crystals is directly related to the degree of order of molecular arrangement, thus being by far lower for proteins compared to small-molecule crystals. Nowadays, X-ray and neutron diffraction can provide structural images of macromolecules at atomic resolution. The diffraction quality is in turn a function of the crystal quality in terms of size and physico-chemical properties, pointing out the importance of protein crystallization in the proteomic and genomic fields (Burley et al., 1999). Nonetheless, protein crystallization has also industrial application in the field of downstream processes, as for the manufacturing of insulin (dos Santos et al., 2017).

7.2 Fundamentals of protein crystallization

Protein crystallization is a complex process relying on the slow and controlled precipitation of macromolecules from solution. However, the crystalline state, in which macromolecules rearrange their conformation and configuration to produce an ordered and coherent lattice, is not the only possible solid-state of proteins. Amorphous precipitates, oils or gels are other competitive phases. To achieve crystallization, the equilibrium conditions must be disturbed by increasing the interaction between the protein macromolecules in a controlled manner. The alteration of protein solubility is generally achieved by adding gentle precipitants, such as salts or polymers, or by modifying some crystallization parameters, such as temperature or pH. Also, substances like cofactors, ions, detergents, chemical protectants, osmolytes, cosmotropes, cross-bridging agents, or inhibitors may play an important role during crystallization as they can affect the physico-chemical state of the protein (McPherson & Gavira, 2014). In this scenario, a detailed comprehensive theory of protein crystallization is missing, and empirical evidence is still driving the growth of crystals of proteins and large biological conglomerate structures like viruses or ribosomes.

The selection of acid or basic conditions is pivotal for protein crystallization as pH strongly affects the protein charge and, thus, its solubility. At the isoelectric point, the protein displays a net charge equal to zero, which leads to minimum solubility and a strong tendency towards aggregation and uncontrolled precipitation (Chernov, 2003). Therefore, crystallization experiments have to be performed quite far from pI to keep a charge distribution on the surface of the protein and promote the controlled assembly of macromolecules.

The type and concentration of precipitant must also be carefully selected. Typically, salts, organic solvents, short and long-chain polymers, and nonvolatile organic compounds can be adopted as precipitants for proteins (Mcpherson, 2001; McPherson, 2004; Skálová et al., 2010). The function of the precipitating agents is to bring the protein molecules closer one to another and promote their assembly, which otherwise would not spontaneously occur. The forces acting in a system without precipitants can be well described by a DLVO (Derjaguin-Landau-Verwey-Overbeek) potential model and would not normally promote enough attraction to trigger macromolecule assembly (Tardieu et al., 2002). As far as salts are employed as precipitants, the mechanism of protein precipitation relies on protein dehydration. Salt ions and macromolecules are competing for binding water molecules which guarantee the protein stability. Proteins are indeed charged macromolecules and, when put in solution, the Coulomb electrostatic repulsion dominates. If the salt concentration is increased, the ionic strength of the system will increase as well, and the protein molecules will be progressively deprived of water. The extent of van der Waals interactions is therefore increased, and the electrostatic repulsion between the macromolecules is mitigated by constructive collisions leading to dimers and pre-nuclei in solution (Eberstein et al., 1994). However, salting-out is always accompanied by specific protein – anion/cation interactions, and the action of salts is difficult to predict (McPherson & Gavira, 2014). A different mechanism promotes protein precipitation when polymers like PEGs are employed as crystallizing agents. A volume-exclusion effect is produced because of the variable conformation of PEG chains in solution, and an attractive depletion potential is established (Tardieu et al., 2002). As a result, the space available for the solvent is strongly reduced, and macromolecules segregate. The achievement of nuclei critical size is followed by crystal growth, which can occur according to a variety of mechanisms, such as dislocation growth, normal growth, two or tridimensional nucleation, depending on the supersaturation level (Malkin et al., 1995). The addition of units is faster and less controlled at high supersaturation, leading to kinetic roughening (Sleutel et al., 2008).

Phase diagrams for protein crystallization are more complicated compared to small molecules, as several states are allowed for proteins. As schematized in Fig. 42, in addition to stable, metastable, and labile zones, precipitation and demixing areas are normally present. The former refers to high supersaturation levels where uncontrolled precipitation leads to an amorphous phase. The latter denotes the liquid-liquid demixing of the protein solution into two separate phases lacking order occurring at even higher supersaturation.

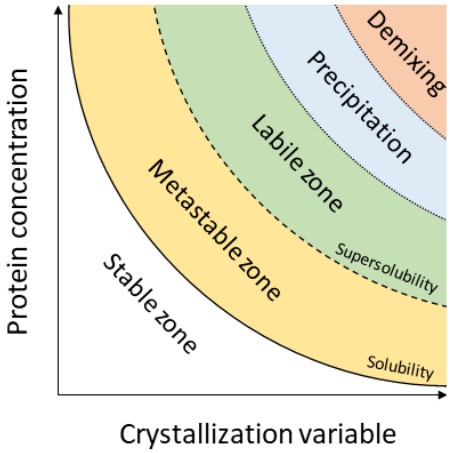

Figure 42 The phase diagram for protein crystallization reporting protein concentration vs. a crystallization variable, e.g., salt concentration. Stable, metastable, labile, precipitation, and demixing zones are reported. Solubility and supersolubility curves are also indicated.

7.3 Techniques for the crystallization of proteins

Protein crystallization requires the careful dosage and manipulation of all the species involved, including protein, precipitant, and buffers. Several techniques are available to carry out the process, allowing the investigation of static or dynamic conditions. The most popular ones are based on batch, vapor or liquid diffusion, and dialysis (Bergfors, 2009). Recent advancements in the experimental implementation of these methods were achieved thanks to the use of commercial kits for shotgun screening of crystallization conditions. Also, robotics and automated apparatuses for dispensing micro and nanoliters (Abola, Kuhn, Earnest, & Stevens, 2000) and evaluating crystallization trials (Cumbaa et al., 2003; DeLucas et al., 2003) paved the way to high-throughput macromolecular crystallography.

An overview of the techniques for protein crystallization employed in the present thesis is given in the following paragraphs.

7.3.1 Batch

Batch crystallization represents a common and simple technique to achieve protein crystallization, sharing the same experimental background of small molecule crystallization in batch. As a matter of fact, all the species are inserted inside the crystallizer at $t = 0$ and do not undergo any temporal evolution in their overall concentration before the onset of crystallization (Durbin & Feher, 1996). The rate at which supersaturation is achieved, J_{sup}, is infinite as the supersaturation is immediately reached by mixing the species. Such conditions correspond to point A in Fig. 43 (a). Once crystallization is initiated, equilibrium conditions are re-established going from A to B. Batch crystallization allows for the investigation of punctual conditions.

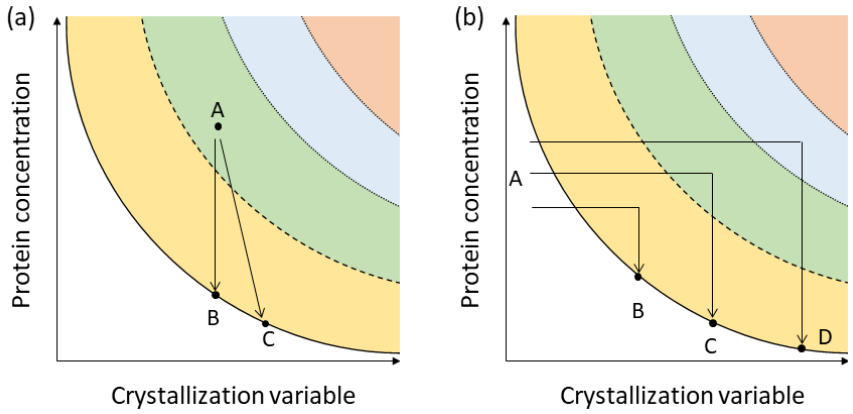

Figure 43 The typical pathway followed by a system in the protein phase diagram undergoing (a) batch (A to B) and vapor diffusion (A to C), and (b) counter-diffusion (A to B, C, D) crystallization.

7.3.2 Vapor diffusion (VD)

From a thermodynamic point of view, the optimal crystallization conditions are those minimizing the energetic barrier for nucleation. However, J_{sup} determines the position of the supersolubility curve and, thus, the width of the metastable zone where nucleation is forbidden, and crystal growth can only occur. J_{sup} is indirectly proportional to the

probability of nucleation because of its stochastic nature. As a result, the nucleation density, crystal quality, and size not only depend on supersaturation but also on supersaturation kinetics (García-Ruiz, 2003b). In order to slow down J_{sup} and guarantee good quality and large crystals, many protein crystallization techniques take advantage of diffusion.

Conversely to batch, vapor diffusion (VD) implies a dynamic system. Once the initial conditions are set, the system slowly evolves towards equilibrium conditions moving from A to C in Fig. 43 (a), as a consequence of mass transport (Martins *et al.*, 2008). Linbro plates are commonly adopted to carry out wide VD screening trials. Each well of the plate is partially filled with a reservoir solution of precipitant. Then, different set-ups are available to perform sitting or hanging drop experiments. The former requires micro-bridges or specifically designed wells, whereas the latter can easily be carried out with the help of siliconized coverslips. In both cases, the drop is formed by mixing protein and precipitant solutions and then is introduced in the system, before its closure. In this way, the drop can start its journey towards equilibrium facing the corresponding reservoir. A driving force for the vapor diffusive transport from the drop to the reservoir is established. The drop becomes more and more concentrated both in terms of protein and precipitant. However, the speed of the increase in concentration is very slow, opening up the possibility to explore a wide range of crystallization conditions, i.e., theoretically all the conditions between the initial and the equilibrium ones. If the volume of the precipitant and the protein solutions is the same, both concentrations are halved at $t = 0$. In this case, the evolution of crystallization conditions on the solubility diagram follows a line with a unitary slope. The slope may be modified by playing on the ratio between the two volumes. In this way, the explored range of conditions may be tuned according to the need of evaluating broader protein or precipitant concentrations. The system gradually evolves from one point to another and, if proper conditions are encountered along the path, crystallization occurs (Benvenuti & Mangani, 2007; Newman et al., 2007). Therefore, batch conditions may be regarded as the starting point of a vapor diffusion crystallization, the batch set-up being the $t = 0$ point of a vapor diffusion experiment. These two techniques allow the exploration of crystallization conditions in a static and in a dynamic way, respectively.

When a new protein has to be crystallized, an initial (micro)batch screening is generally performed. The conditions more likely to lead to crystals are identified and, then, a vapor diffusion experiment is designed. A wider set of crystallization conditions is thus explored and a refinement of the range of crystallization conditions may be achieved. Based on these results, one can go back to batch crystallization in order to determine precise crystallization conditions by designing experiments involving small variations of the studied parameters.

7.3.3 Counter-diffusion (CD)

The study of crystallization in batch and VD configurations is limited to a specific point in space in both cases. The introduction of the position-axis in the system was achieved by counter-diffusion (CD) crystallization. Such a technique enables the screening of crystallization conditions on both time and space-scales (Ng et al., 2003; Otálora et al., 2009). CD techniques rely on the separation between the precipitant and protein solutions. Their confinement enables the creation of a driving force both for the precipitant and the protein solutions, in opposite directions. Unlike batch and VD, the species must undergo only diffusive, rather than convective, mixing in CD to ensure the uniform propagation of

the supersaturation wave. To achieve this goal CD experiments must be carried out inside gels, high viscosity media, capillaries, or under microgravity conditions (Garciá-Ruiz, 2003a). Different set-ups have been proposed, such as the gel acupuncture method (GAME) (López-Jaramillo et al., 2001) or the 3-layers technique. In diffusive environments, the growth of crystals also proceeds with a reduced risk for the formation of defects, lattice mismatch, inclusion of impurities, etc.

A wide range of the phase diagram is explored thanks to the combination of local protein and precipitant concentrations, as highlighted in Fig. 43 (b). As a consequence, the crystal size will reflect the anisotropy of crystallization conditions. Moving away from the interface between the protein compartment and the precipitation cocktail, one could encounter precipitation, micro-crystals, and, eventually, large crystals. Such a gradient is the result of the protein being exposed to a continuum of different precipitant concentrations. CD experiments may be regarded as self-screeners for the best crystallization conditions and can easily be coupled to micro-seeding techniques (Gavira et al., 2011).

7.4 Materials & Methods

7.4.1 Materials

Lysozyme from hen egg white (HEWL, L6876, lyophilized powder, protein ≥ 90%, ≥40,000 units/mg protein), catalase C30 (aqueous suspension, 10,000-40,000 units/mg protein), and catalase C40 (lyophilized powder, ≥10000 units/mg protein) from bovine liver, as well as all the reagents used to prepare buffers and precipitant solutions were purchased from Sigma-Aldrich. Proteinase K obtained from *Tritirachium album* (A3830, lyophilized powder) was purchased from PanReac AppliChem GmbH (Germany). All the solutions were filtered with 0.22 μm pore size – low binding protein syringe filters. The protein concentration was measured spectrophotometrically at 280 nm before each experiment. All the experiments were performed in triplicate.

7.4.2 Batch crystallization

HEWL was crystallized both in PCR vials and in micro-batch plates. In every case, fresh concentrated solutions of HEWL were prepared in 50 mM Na acetate pH 4.5 and used as stock solutions. With regard to batch carried out in PCR vial, a single test was performed with 50 mg/mL HEWL and 4wt% NaCl in 50 mM Na acetate pH 4.5. The total volume was 100 μL. The schematic representation and a micrograph of the batch crystallization experiment in vials are reported in Fig. 44 (a) and (b).

To reduce the volumes of protein solution, the crystallization screening was carried out in micro-batch. The final concentration of NaCl in the batch ranged from 0.75 to 7.5wt%, and HEWL concentration was kept constant at 25 mg/mL in 50 mM Na acetate buffer pH = 4.5. The micro-batch plate was preliminary cleaned with compressed air and filled with a layer of mineral oil. To prepare the micro-batch, 2.5 μL of HEWL stock solution were individually mixed with 2.5 μL of NaCl stock solution and transferred into each well of the plate. The plates were incubated at 20 °C and periodically inspected by

optical microscopy. The scheme of a micro-batch experiment and pictures of the plate and wells are sketched in Fig. 44 (c) – (e).

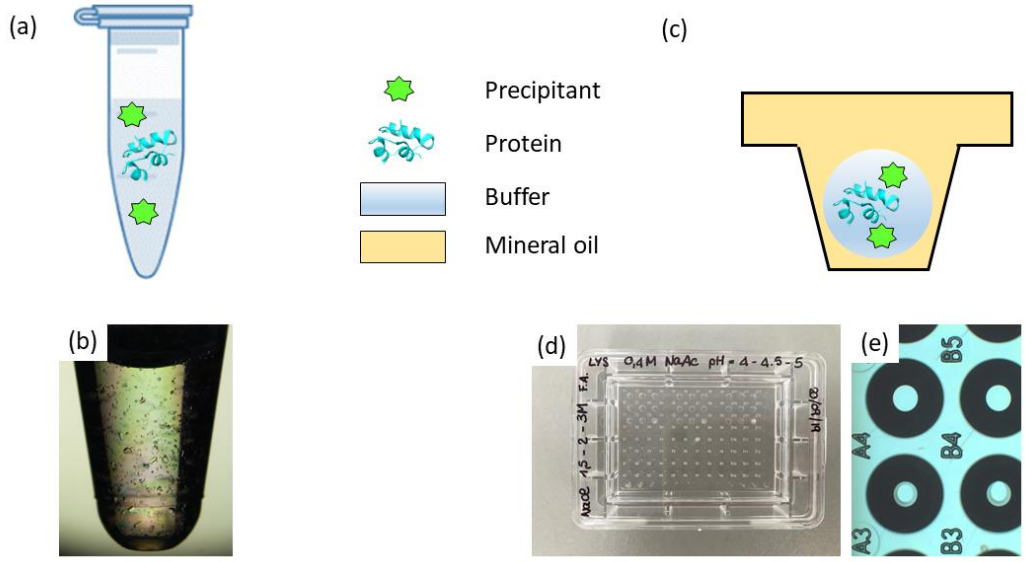

Figure 44 (a) Schematic representation of a batch crystallization experiment. (b) Micrograph of HEWL batch crystallization. (c) Schematic representation of a micro-batch crystallization experiment. (d) Micro-batch plate and (e) wells filled with micro-drops.

7.4.3 Vapor diffusion crystallization

VD crystallization was carried out in Linbro plates and *mushroom* crystallizers in the hanging and sitting drops configurations, respectively.

7.4.3.1 Linbro plates

HEWL, catalase, and proteinase K were crystallized in Linbro plates by hanging drop vapor diffusion. Each well was initially filled with 0.5 mL of precipitant solution. 5 µL drops were formed by mixing stock buffered solutions of protein and precipitant. Particular care was taken to avoid the formation of bubbles. Drops were carefully deposited on siliconized coverslips that were then placed on the top of vacuum-greased wells. Gentle pressure was exerted to hermetically seal the system. Plates were incubated at 20 °C and periodically inspected. The experimental set-up is represented in Fig. 45 (a).

The crystallization conditions and the sample codes for the three model proteins are summarized in Tab. B1 and B2 (Appendix B). HEWL starting conditions were the same of those implemented in micro-batch, with the addition of condition L8. Proteinase K was dissolved in 50 mM HEPES pH 7.0, whereas the precipitant stock solution was made of a variable amount of $NaNO_3$ and 50 mM Na citrate. HEWL and proteinase K were directly dissolved in their own buffer, freshly prepared before each experiment, and passed through 0.22 µm pore size syringe filters prior to mixing.

As regards catalase, two different formulations of the raw protein were used, i.e., C30 and C40. C30 consisted of a crystalline suspension containing 0.1% thymol as a preservative. The suspension was centrifuged at 11000 rpm for 1 min to pelletize the

crystals and quit thymol. The supernatant was discarded, and the pellet was resuspended in water. The suspension was centrifuged again, the supernatant discarded, and crystals resuspended in 50 mM K phosphate buffer pH 7.0. The suspension was gently warmed at 35 °C under agitation for 1 hour to completely dissolve the microcrystals. If needed, the so obtained protein solution was concentrated for 15 min at 4000 x g at room temperature (Amicon Ultra 15 centrifugal filter units, Merck). C40, instead, consisted of lyophilized protein and was directly dissolved in the phosphate buffer. At the end of the preparation step, both catalase solutions were filtered with 0.22 µm syringe filters. The solutions were freshly prepared before each experiment to minimize the risk of protein oxidation.

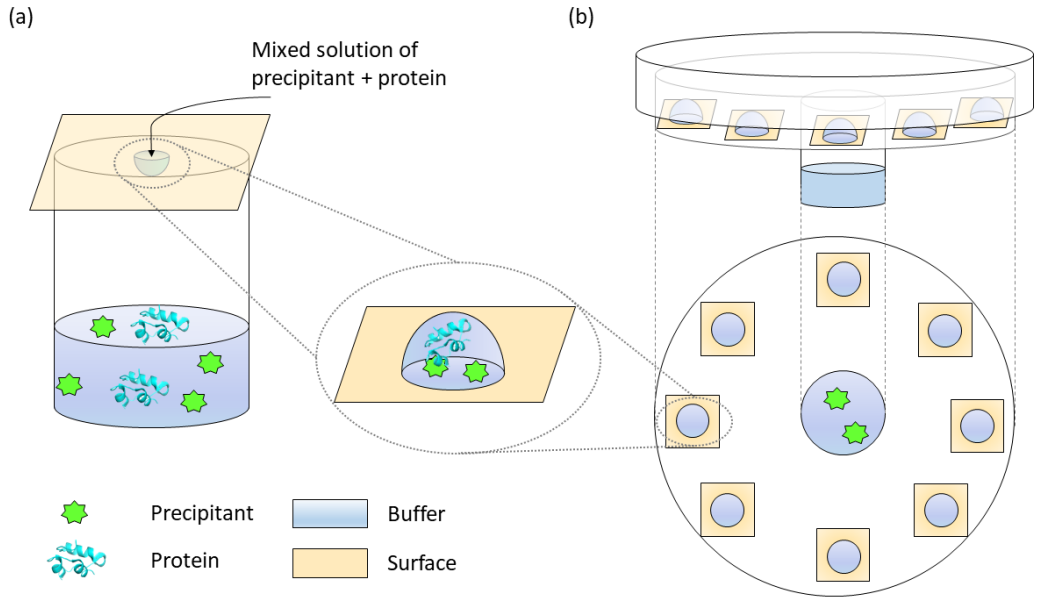

Figure 45 (a) Schematic representation of the experimental set-up of vapor diffusion crystallization in a well of Linbro plates. Drops were deposited on siliconized coverslips placed at the top of the well. (b) Schematic representation of the experimental set-up of vapor diffusion crystallization in *mushroom* crystallizers. Drops were deposited on mushroom glass (Chap. 7), EtOH-cleaned or SAM-functionalized coverslips (Chap. 8) depending on the experiment.

7.4.3.2 *Mushroom* crystallizers

The *mushroom* crystallization set-up is reported in Fig. 45 (b). HEWL was crystallized setting up L4, 9 and 10 conditions. 5 µL drops with a 1:1 ratio between protein and precipitant solutions were formed and carefully deposited on the crystallizer surface. Each *mushroom* was loaded with 12 drops arranged as a corona around the central reservoir. The unique reservoir was filled with 5 mL of precipitant solution, namely 6wt% NaCl in 50 mM Na acetate pH 4.5. The system was sealed with vacuum grease and incubated at 20 °C. The sample codes are reported in Tab. B1 (Appendix B).

7.4.4 Counter-diffusion crystallization

HEWL was selected as a model protein to perform crystallization under counter-diffusion (CD) conditions. Two different set-ups were tested based on the GAME and the 3-layers approach.

7.4.4.1 The gel acupuncture method (GAME)

GAME was implemented inside transparent Granada crystallization boxes (GCB Domino, Triana Science & Technology, Granada, Spain) (Garcia-Ruiz *et al.*, 2002) with the help of capillaries (I.D. = 0.7 mm). Each box was loaded with 2.2 mL of 10wt% NaCl in 50 mM Na acetate pH 4.5. A 0.5wt% agarose stock solution was prepared by dissolving the agarose in acetate buffer at 95 °C until a clear solution was obtained. Then, 0.5 mL of agarose solution was carefully pipetted on top of the precipitant. The system was kept at room temperature to trigger the agarose gelification overnight. Capillaries were loaded with HEWL solutions prepared at different concentrations, namely 25, 50, and 75 mg/mL in 50 mM Na acetate pH 4.5. One end of the capillaries was closed with sealing paste. Once the agarose gelification had been completed, the other end of the capillaries was passed through the agarose layer and inserted inside the box, as sketched in Fig. 46 (a). Up to six capillaries were loaded simultaneously per GCB. GCBs were incubated at 20 °C.

7.4.4.2 The 3-layers technique

The same HEWL crystallization conditions were selected to implement the 3-layers technique. The capillaries had a different configuration, as illustrated in Fig. 46 (b). A 50 mm long capillary (I.D. = 0.3 mm) was filled with protein solutions at different concentrations, and its end was sealed with pre-heated beeswax. Then, 3 µL of 0.5wt% agarose solution was poured into the upper reservoir to form the gel layer. Finally, 30 µL of 10wt% NaCl in 50 mM Na acetate pH 4.5 were pipetted on top of the gel. The top of the system was sealed with beeswax and incubated at 20 °C.

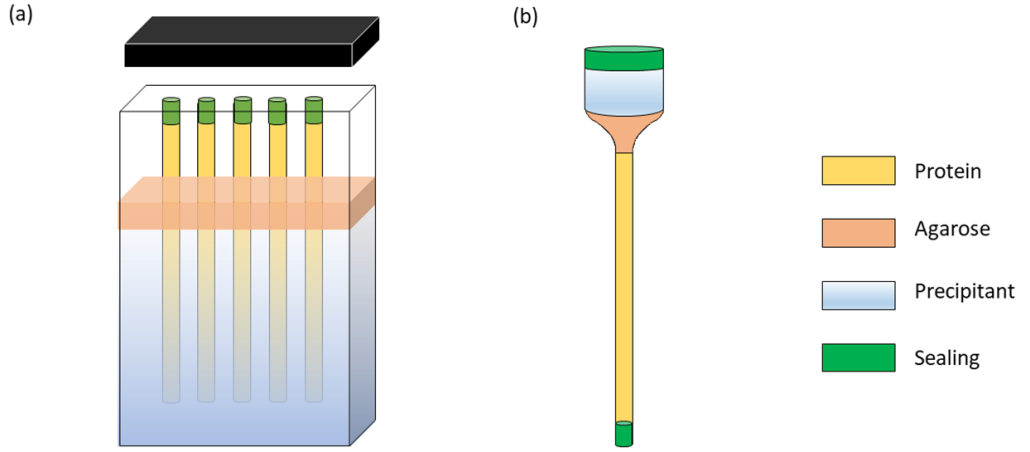

Figure 46 Schematic representation of the experimental set-ups used for CD crystallization: (a) GAME and (b) 3-layers techniques.

7.5 Batch crystallization of lysozyme (HEWL)

As a preliminary step for the design of protein crystallization with heteronucleants, the crystallization of model proteins was studied in the absence of heteronucleants to set reference crystallization conditions. In this chapter, the results obtained with batch, VD, and CD techniques are discussed.

HEWL crystallization was first studied in batch, and a typical outcome of a trial carried out in PCR vials is reported in Fig. 47 (a). HEWL crystals were obtained overnight by using NaCl as a precipitant salt, and the resulting crystal size varied between a few to 300 µm. For preliminary screening experiments, the dimensional uniformity of the crystals is not usually required since the main aim is to screen several precipitants and, for the selected ones, identify the optimal crystallization conditions. Conversely, when crystals are specifically grown for more advanced applications, requirements on crystal size become stringent. This aspect represents one of the major limitations of the batch technique applied to the preparation of reproducible and uniform crystals slurries.

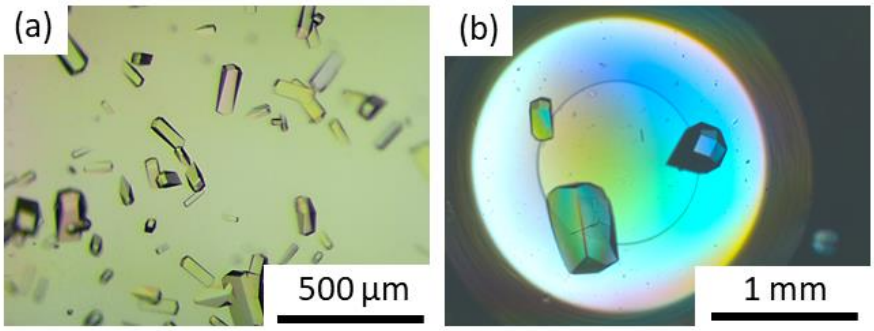

Figure 47 (a) Batch crystallization of HEWL in PCR vials loaded with 50 mg/mL HEWL and 4wt% NaCl in 50 mM Na acetate buffer pH 4.5. (b) Micro-batch crystallization of HEWL. Drops consisted of 25 mg/mL HEWL and 3 wt% NaCl in 50 mM Na acetate buffer pH 4.5.

Batch crystallization techniques require a significant amount of protein and are not suitable for wide screening tests. Micro-batch techniques can solve this issue. As suggested by the denomination, crystallization is carried out in micro-volumes, i.e., from 1 to 10 µL. In this way, a wide range of conditions could be covered, together with minimal waste of protein. As an example, a screening micro-batch crystallization experiment for HEWL has been designed to determine the minimal NaCl concentration needed to trigger crystallization. HEWL concentration was fixed at 25 mg/mL in the final drop. The protein crystallization was halved compared to the previous macro-batch trial to allow the observation of single crystals. NaCl concentration was varied between 0.75 and 7.5wt%. The minimal concentration of NaCl necessary to achieve crystallization was 3wt%. Single crystals were observed, as reported in Fig. 47 (b). In all the replicas, no more than three crystals were observed per micro-well. As already observed for batch, crystals were not dimensionally uniform. Some of them were also found to be broken or damaged because of their large size.

In conclusion, batch and micro-batch crystallization allowed for the investigation of single and defined crystallization conditions. Once the supersaturation and composition are set, the crystallization environment represents a closed system. The experiments are therefore dealing with static conditions as, provided that the oil was properly chosen to

prevent droplet evaporation, the concentration of the various components will remain constant throughout the experiment.

7.6 Vapor diffusion crystallization

Several experimental set-ups can be used to implement vapor diffusion trials. The most widespread technique involves the use of Linbro plates. Recently, a variation of the technique was also proposed, i.e., the *mushroom* crystallizer. In this thesis, the hanging drop vapor diffusion (HDVD) crystallization has been selected to identify reference crystallization conditions for the HEWL, catalase C30 and C40, and proteinase K, which were used as model proteins for the following part of the study.

7.6.1 Screening of HEWL

7.6.1.1 Crystallization in Linbro plates

The range of conditions implemented in the HEWL micro-batch was replicated in HDVD. The window of NaCl concentrations was expanded to set an upper threshold in NaCl concentration. In the following part of the discussion, the salt and precipitant concentrations are referred to the stock solutions. The explored conditions ranged from L1 to L8, as reported in Tab. B1 (Appendix B). The same conditions led to a different number of crystals compared to micro-batch, since they represented the $t = 0$ condition of HDVD. As shown in Fig. 48, tetragonal HEWL crystals were observed over the 4 – 15wt% NaCl range, whereas spherulites were observed above 17wt% NaCl. After 12 hours, large crystals were formed over the 6 – 15wt% NaCl range. More time was needed to observe the first crystals in the 4 – 6wt% NaCl range, namely between 1 and 3 days. Below 4wt% NaCl, crystals were not observed.

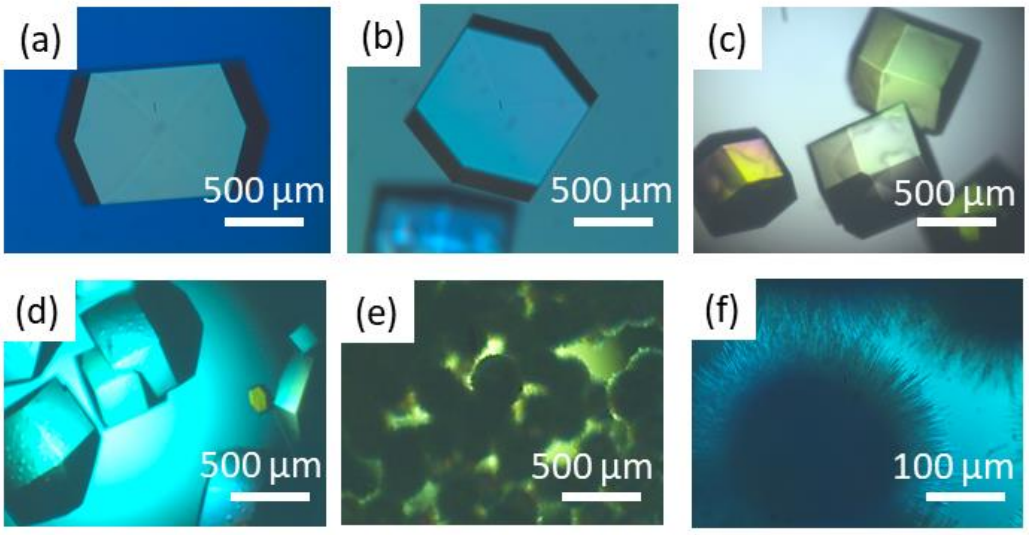

Figure 48 Optical micrographs of HEWL crystals grown by HDVD according to (a) L3, (b) L4, (c) L5, (d) L6, and (e) L8. (f) Enlarged micrograph of spherulites obtained with L8 conditions.

From the comparison between the results obtained with micro-batch and HDVD three intervals of stock salt concentrations were identified: those that did not lead to crystals in both cases, those that were responsible for crystallization in VD conditions, but not in micro-batch, and those that led to crystallization in both cases. Salt concentrations below 3wt% did not produce detectable crystals, whereas concentrations above 17wt% always produced crystals/spherulites. In the intermediate range of concentration, crystallization occurred depending on the method used. Whereas micro-batch was effective in leading crystals above 6wt% NaCl, vapor diffusion enabled the collection of crystals starting from 4wt% NaCl. The results were attributed to the different evolution of the two systems as HDVD crystallization progressively explored higher protein and salt concentration conditions.

The quality of the crystals for L7 crystallization conditions resulted to be lower as defects within the crystal faces were more likely to be observed. If the precipitant concentration was higher, the hydration sphere of a protein molecule became larger, thus hindering its diffusion. At the same time, the energy of the system would grow considerably. This resulted in fast crystal growth as, when a protein molecule came close to the face of a growing crystal, it did not have enough time to re-adjust itself and fit into the crystalline structure perfectly. The incorporation happened in an uncontrolled and fast manner. Crystals would therefore display defects as a consequence of the rapid growth, such as rough facets, irregular shapes and macro-defects. In other cases, crystal growth may also be incomplete because of the depletion of protein molecules available for being incorporated into the lattice.

7.6.1.2 Crystallization in *mushrooms*

Vapor diffusion crystallization of HEWL was also investigated inside *mushroom* crystallizers. Such devices provide a useful tool to study crystallization in multiple drops facing the same environmental conditions, as depicted in Fig. 45 (b). The precipitant concentration in the reservoir dictates the evaporation rate of water inside the drops. As a consequence, provided that the same starting conditions are set inside every drop, all the drops will evolve in the same manner. The explored areas of the phase diagram will be exactly the same, allowing for a more rigorous comparison of the crystallization trials. Conversely to HDVD where each drop refers to a corresponding reservoir, *mushrooms* allow for sitting drop vapor diffusion (SDVD) trials where all the drops are facing the same reservoir.

HEWL was crystallized inside *mushrooms* to identify the effect of three protein concentrations on crystallization, see conditions L4, L9, and L10 in Tab. B1. Crystals were observed in all the drops, as reported in Fig. 49. The number of crystals strongly increased with the protein concentration. Few crystals were obtained with 25 mg/mL HEWL stock solutions, whereas massive micro-crystallization occurred at 75 mg/mL HEWL. Also, the crystal morphology evolved with the protein concentration. Elongated crystals were grown with low HEWL concentrations. Crystals became less elongated as long as HEWL concentration increased. A final observation regarded the time needed to obtain crystals, which ranged from a few hours (L10) to several days (L4).

In conclusion, crystals density and aspect, as well as the time needed to grow crystals with detectable size, resulted to be strongly related to the HEWL concentration and, thus, to the supersaturation level of the system.

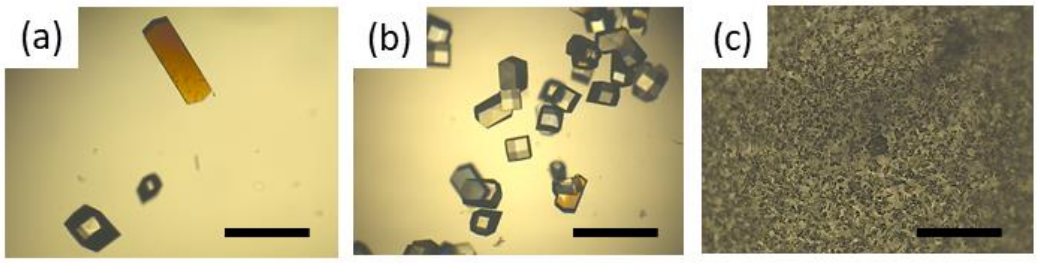

Figure 49 HEWL crystals grown in *mushroom* crystallizers according to conditions (a) L4, (b) L9, and (c) L10. The scale bar is 250 μm.

7.6.2 Screening of catalase

The crystallization of catalase in hanging drops was also studied to set reference crystallization conditions. Two different types of catalase have been studied, differing for their purity and formulation but not for their source. Both proteins were extracted from the bovine liver. Catalase from microcrystalline suspension (C30) and dry catalase (C40) were both buffered in 50 mM potassium phosphate pH 7.0 and crystallized with PEG4000. Compared to HEWL, catalase represents a trickier protein to be crystallized, and obtaining good quality crystals usually requires much more effort. In this perspective, a more detailed preliminary study was performed by considering more variables.

7.6.2.1 Crystallization of C30

The crystallization of C30 was screened according to different parameters, such as protein and precipitant concentrations, and the ratio between protein and precipitant solutions in the drop. The set of investigated conditions in Linbro plates is reported in Tab. 28, together with the time elapsed from the start of the experiments to the observation of crystals and the morphology of the crystals. The reservoir solution ranged from 10 to 30wt% PEG4000, whereas C30 stock concentration ranged from 1.0 to 3.7 mg/mL. The details of crystallization conditions are listed in Tab. B1.

Table 28 The time required for observing crystals and the morphology of the crystals according to the crystallization conditions.

Reference	Time required for observing crystals	Crystal morphology
C301	-	-
C302	3 days	Bad quality
C303	-	-
C304	2 days	Plates
C305	2 days	Extended plates
C306	1 day	Needles and rods
C307	1 day	Elongated rods

Low C30 concentrations led to crystals only when PEG was above 15wt%, i.e., C302 condition. Drops prepared with 1.0 mg/mL C30 led to few and bad quality crystals, as illustrated in Fig. 50 (a). The far ends of the bigger crystals were split in two parts, denoting the presence of a dislocation in the growing lattice. Therefore, the C301 – C303 range of conditions was found to be very far from the ideal ones. Moving toward higher protein and precipitant concentrations, i.e., range C304 –C307, it emerged that the amount of PEG in the system had a strong impact on catalase crystal habit and nucleation kinetics. In general, increasing the initial amount of PEG from 20 to 30 wt% halved the time needed for the appearance of the crystals. At the same time, the less concentrated drops led to plate-like catalase crystals, Fig. 50 (b). Larger and extended plates were observed when the protein to precipitant ratio was equal to 2, Fig. 50 (c). Conversely, drops formed by the mixing of 30wt% PEG led to needle-like or bar-like crystals, Fig. 50 (d) and (e). Again, crystals grew bigger and nucleation density was lower for protein on precipitant ratios equal to 2.

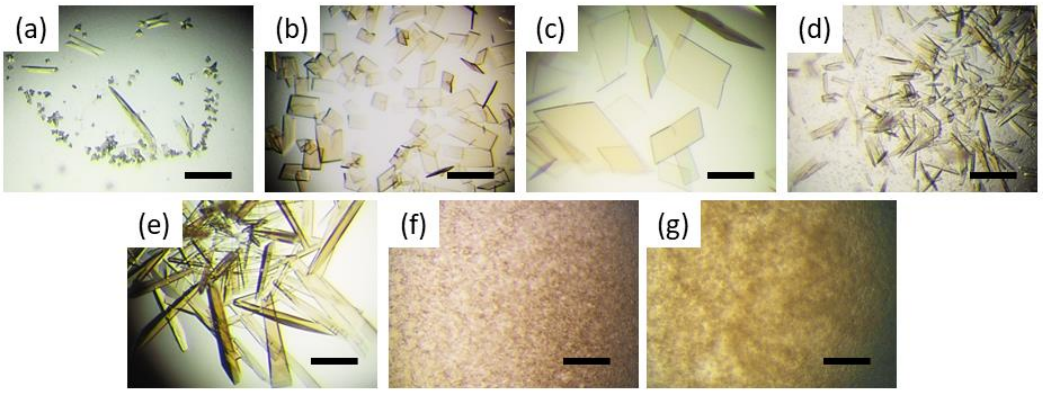

Figure 50 HDVD crystallization of catalase C30 involving the conditions (a) C302, (b) C304, (c) C305, (d) C306, and (e) C307. (f) and (g) refer to the HDVD trials carried out with C30 supernatant and 20 or 30wt% PEG4000, respectively. The scale bar is 250 μm.

As the last step, HDVD crystallization involving the supernatant discarded from C30 after the first centrifugation step was carried out. The aim was to demonstrate that the amount of catalase lost in the supernatant was negligible, and that the preliminary purification protocol was efficient. Drops were set mixing 2.5 μL of supernatant and 2.5 μL of PEG4000 20 - 30wt%. The results are sketched in Fig. 50 (f) and (g). Both conditions led to the massive formation of amorphous precipitate inside the drops. As expected, for smaller amounts of PEG, the extent of precipitation was reduced. In some cases, few small catalase crystals of extremely low quality appeared within the precipitate. Such results further confirmed the high purity of the final C30 catalase solution used in the HDVD experiments, which led to good quality crystals and the absence of precipitate.

7.6.2.2 Crystallization of C40

The second type of catalase considered for the study was C40, a less pure preparation of the protein commercially distributed as a lyophilized powder. Protein purity is a key variable in crystal growth. Microheterogeneities, such as post-translational modifications, oxidations, proteolysis, and conformational modifications, compromise the biochemical quality of the macromolecules and repress the crystallization success (Giegé et al., 1986).

C40 was directly dissolved in 50 mM K phosphate buffer pH 7.0, and HDVD crystallization was investigated. In particular, the first part of the experiments was carried out with comparable protein and precipitant concentrations to those used for C30, i.e., C401 and C402 conditions, whereas the second one involved higher protein concentration, i.e., C403 and C404. The detailed list of conditions is reported in Tab. B1, and the outcome of the experiments in Fig. 51.

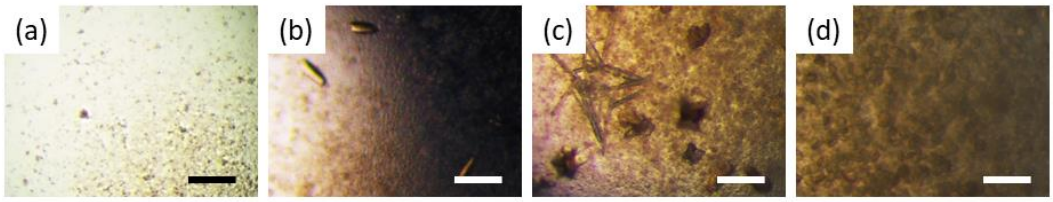

Figure 51 HDVD crystallization of catalase C40 involving the conditions (a) C401, (b) C402, (c) C403, and (d) C404. The scale bar is 250 µm.

In all the samples, precipitation was observed. The extent of precipitation increased along with the protein concentration. C40 concentrations between 3.5 and 7.0 mg/mL (C402 and C403 samples) led to some rod-like crystals embedded in the precipitate. Larger concentrations only resulted in precipitation, as well as smaller ones. Therefore, catalase crystals could only be grown at intermediate protein concentrations.

The preliminary crystallization tests in Linbro plates of C30 and C40 demonstrated the dramatically higher purity of catalase C30 preparation, which always led to crystals grown in the total absence of precipitate. Thanks to the higher quality of the initial stock of protein and the following separation and purification treatments, C30 gave the most reproducible and clean results. On the other side, C40 required larger concentrations to get fewer and scarce quality crystals, contaminated by amorphous precipitate. In the following chapters, C30 and C40 will be both crystallized in gels, whereas experiments on surfaces will only be performed with C30.

7.6.3 Screening of proteinase K

The crystallization of proteinase K in HDVD was first carried out by varying the protein concentration. Tab. B2 (Appendix B) lists the P1 – P4 conditions selected for performing the experiments. After one day, only the drops referring to P4 contained crystals. As reported in Fig. 52 (a), proteinase K crystals grew large and well-faceted. Single crystals were obtained in all the drops. Therefore, the mixing of 15 mg/mL proteinase K with 1 M $NaNO_3$ and 50 mM Na Citrate was selected as the optimal crystallization condition. None of the other tests led to crystals, even after more than two months.

Proteinase K was also successfully crystallized with another precipitation cocktail, consisting of $(NH_4)_2SO_4$ dissolved in 0.1 M Tris-HCl pH 8.0. Single crystals were grown with 1.2 M ammonium sulfate and 20 mg/mL proteinase K in 50 mM HEPES pH 7.0, Fig. 52 (b). However, it was found that the outcome of HDVD crystallization with ammonium sulfate strongly depended on the buffering of the precipitant solution.

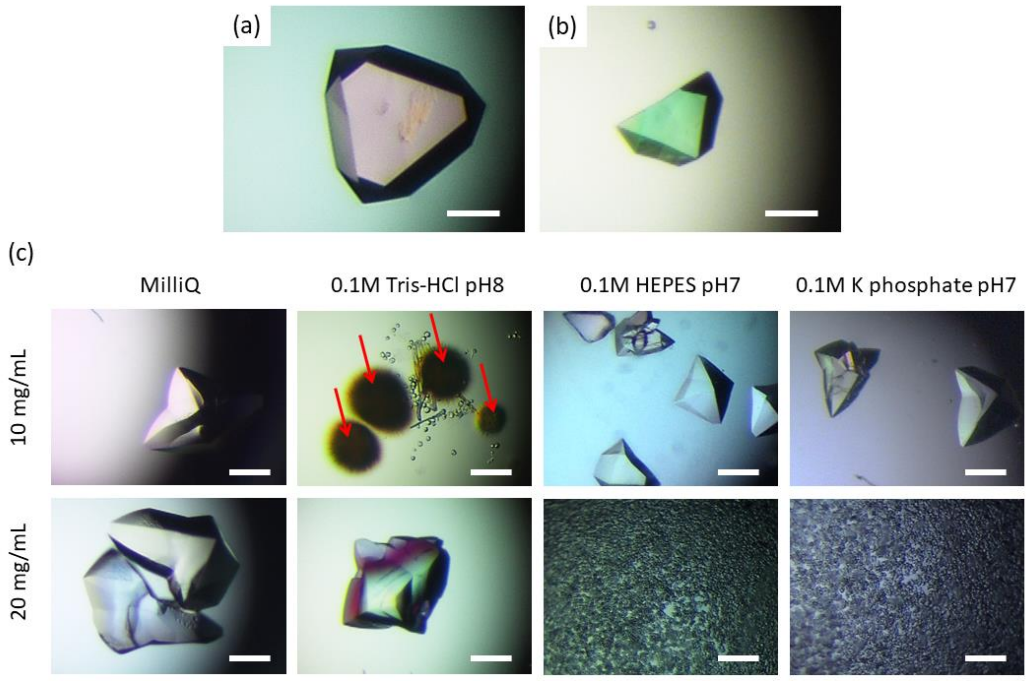

Figure 52 Proteinase K single crystals grown with HDVD crystallization. (a) Proteinase K initial concentration was 15 mg/mL in 50 mM HEPES pH 7.0, and the precipitant solution consisted of 1 M $NaNO_3$ and 50 mM Na citrate pH 6.5. (b) Proteinase K initial concentration was 20 mg/mL in 50 mM HEPES pH 7.0, the precipitation cocktail was 1.2 M $(NH_4)_2SO_4$ in 0.1 M Tris-HCl pH 8.0. (c) Screening of proteinase K crystallization in presence of different buffers. Proteinase K concentration before mixing was 10 or 20 mg/mL. The scale bar is 250 µm.

In order to investigate the influence of different buffers on proteinase K crystallization, several HDVD trials were performed. Two protein concentrations were tested, namely 10 and 20 mg/mL. 2 M $(NH_4)_2SO_4$ was set as precipitant concentration to ensure the appearance of crystals. The precipitant was directly dissolved in MilliQ water, 0.1 M Tris-HCl pH 8.0, 0.1 M HEPES pH 7.0, or 0.1 M K phosphate pH 7.0. The reference conditions were listed in Tab. B2. The absence of buffers in the precipitation cocktail led to the growth of large and irregular protein crystals. Generally, one or two single crystals were obtained with 10 and 20 mg/mL proteinase K, respectively. When Tris-HCl was added to the system, spherulites were observed at low protein concentrations, as indicated by the red arrows in Fig. 52 (c). Moreover, needle-like crystals grew from the spherulites because of a secondary nucleation step. At higher protein concentrations, the crystallization behavior resembled that of MilliQ trials. Lastly, the presence of HEPES or K phosphate resulted in a marked nucleation promotion. Crystal density was considerably higher, and massive micro-crystallization was registered at high protein concentrations.

In presence of ammonium sulfate as a precipitant, different buffering systems altered the crystallization outcome. It was demonstrated that Tris-HCl promoted the formation of a different polymorph of proteinase K at small protein concentrations. This could be related to the presence of Tris itself, but also to the slightly higher pH. Compared to the MilliQ case, phosphate and HEPES strongly induced the nucleation step, and high protein concentrations induced massive crystallization.

7.7 Counter-diffusion crystallization of HEWL

7.7.1 GAME technique

The gel acupuncture method enables the exploration of CD conditions. All the capillaries inside the box experience the same NaCl concentration wave. The set-up illustrated in Fig. 46 (a) enables the closure of capillaries with an agarose layer while passing across the agarose layer. In this way, the protein solution is prevented from escaping from the capillary. GAME also guarantees an infinite reservoir of precipitant since the volume of the precipitant solution is by far larger than the sum of all the volumes of protein solution inside the capillaries. In this way, the achievement of equilibrium inside each capillary is guaranteed, and crystallization conditions are explored along the length of the capillary.

Three concentrations of HEWL were tested in the GAME configuration, while keeping constant 10wt% NaCl concentration. The protein concentration had a dramatic impact on the crystal pattern obtained along the capillaries, as illustrated in Fig. 53.

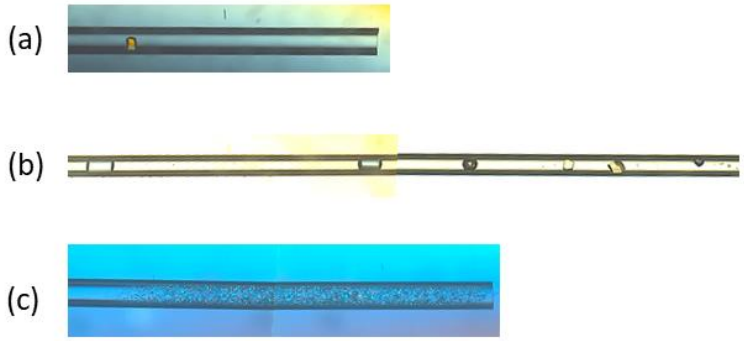

Figure 53 HEWL crystals grown with the GAME technique. Capillaries were loaded with (a) 25, (b) 50, and (c) 75 mg/mL of protein in 50 mM Na acetate pH 4.5. (a) and (c) micrographs were taken after 15 hours, whereas (b) referred to 70 hours.

After 15 hours, crystals were observed in all the capillaries. The density of crystals increased with the protein concentration. At low HEWL concentrations, very few crystals were observed. Typically, one single crystal was grown near the interface with the precipitant, which corresponded to the zone with the highest supersaturation. A pattern of crystal size was observed for the 50 mg/mL HEWL samples. The number of crystals was higher near the interface with the precipitant and then decreased. In the farthest regions of the capillaries, the growth of crystals was limited by the internal diameter of the capillary, and cylindrical crystals were observed. The highest protein concentration, i.e., 75 mg/mL, led to massive crystallization along all the capillary.

7.7.2 3-layers technique

Analogous experiments were carried out for HEWL with the 3-layers technique. Capillaries were loaded with 25, 50, and 75 mg/mL of HEWL, and 10 wt% NaCl. As reported in Fig. 54, after 50 hours, a pattern similar to the GAME trials was observed. Very few crystals were obtained at low protein concentrations. Crystal density increased for 50 mg/mL HEWL, and the size of the crystals increased moving away from the interface. Massive

micro-crystallization was observed with 75 mg/mL HEWL. For this condition, a zone with reduced crystal density was observed at the end of the capillary, conversely to GAME. Such evidence was due to the longer length of the capillary being almost twice for the 3-layers compared to GAME. When high supersaturation conditions were implemented, a long capillary allowed for the observation of gradients in crystal size.

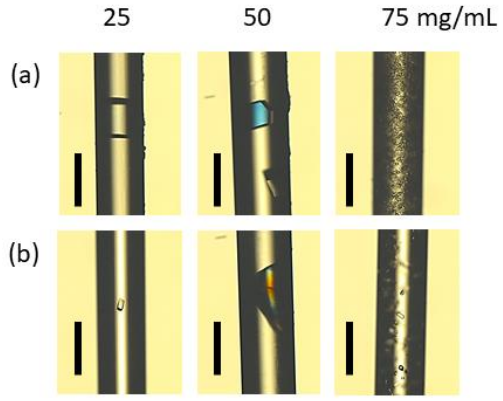

Figure 54 HEWL crystals grown inside capillaries with the 3-layers technique. Crystals grown (a) near and (b) far away from the precipitant compartment for 25, 50, and 75 mg/mL HEWL are sketched. The scale bar is 300 µm.

7.8 Final remarks

Chapter 7 was devoted to the introduction of protein crystallization and the preliminary screening of some model proteins according to various techniques. The differences between small molecule and protein crystals were outlined. Because of the intrinsic characteristics of protein crystals, more sophisticated crystallization processes had to be employed. Batch, vapor diffusion, and counter-diffusion approaches have been discussed, together with the experimental evidence collected. As a general trend, an increase in the supersaturation level of the system led to a larger number of crystals and reduced their average size. On the contrary, low supersaturation values promoted the growth of few and large crystals. The reference crystallization conditions of HEWL, catalase, and proteinase K have been identified and will guide the experimental design of the following part of the study.

References

Abola, E., Kuhn, P., Earnest, T., & Stevens, R. C. (2000). Automation of X-ray crystallography. *Nature Structural Biology*, **7**(11), 973–977.

Benvenuti, M., & Mangani, S. (2007). Crystallization of soluble proteins in vapor diffusion for x-ray crystallography. *Nature Protocols*, **2**(7), 1633–1651.

Bergfors, T. M. (2009). Protein Crystallization (second ed.). La Jolla: International University Press.

Burley, S. K., Almo, S. C., Bonanno, J. B., Capel, M., Chance, M. R., Gaasterland, T., Lin, D., Šali, A., Studier, F. W., & Swaminathan, S. (1999). Structural genomics: Beyond the human genome project. *Nature Genetics*, **23**(2), 151–157.

Chernov, A. A. (2003). Protein crystals and their growth. *Journal of Structural Biology*, **142**(1), 3–21.

Cumbaa, C. A., Lauricella, A., Fehrman, N., Veatch, C., Collins, R., Luft, J., DeTitta, G., & Jurisica, I. (2003). Automatic classification of sub-microlitre protein-crystallization trials in 1536-well plates. *Acta Crystallographica - Section D Biological Crystallography*, **59**(9), 1619–1627.

DeLucas, L. J., Bray, T. L., Nagy, L., McCombs, D., Chernov, N., Hamrick, D., Cosenza, L., Belgovskiy, A., Stoops, B., & Chait, A. (2003). Efficient protein crystallization. *Journal of Structural Biology*, **142**(1), 188–206.

dos Santos, R., Carvalho, A. L., & Roque, A. C. A. (2017). Renaissance of protein crystallization and precipitation in biopharmaceuticals purification. *Biotechnology Advances*, **35**(1), 41–50.

Durbin, S. D., & Feher, G. (1996). Protein crystallization. *Annual Review of Physical Chemistry*, **47**, 171–204.

Eberstein, W., Georgalis, Y., & Saenger, W. (1994). Molecular interactions in crystallizing lysozyme solutions studied by photon correlation spectroscopy. *Journal of Crystal Growth*, **143**(1–2), 71–78.

Garciá-Ruiz, J. M. (2003a). Counterdiffusion methods for macromolecular crystallization. *Methods in Enzymology*, **368**, 130–154.

García-Ruiz, J. M. (2003b). Nucleation of protein crystals. *Journal of Structural Biology*, **142**(1), 22–31.

Garcia-Ruiz, J. M., Gonzalez-Ramirez, L. A., Gavira, J. A., & Otálora, F. (2002). Granada Crystallisation Box: A new device for protein crystallisation by counter-diffusion techniques. *Acta Crystallographica Section D: Biological Crystallography*, **58**(10 II), 1638–1642.

Gavira, J. A., Hernandez-Hernandez, M. A., Gonzalez-Ramirez, L. A., Briggs, R. A., Kolek, S. A., & Shaw Stewart, P. D. (2011). Combining counter-diffusion and microseeding to increase the success rate in protein crystallization. *Crystal Growth and Design*, **11**(6), 2122–2126.

Giegé, R., Dock, A. C., Kern, D., Lorber, B., Thierry, J. C., & Moras, D. (1986). The role of purification in the crystallization of proteins and nucleic acids. *Journal of Crystal Growth*, **76**(3), 554–561.

López-Jaramillo, F. J., García-Ruiz, J. M., Gavira, J. A., & Otálora, F. (2001). Crystallization and cryocrystallography inside X-ray capillaries. *Journal of Applied Crystallography*, **34**(3), 365–370.

Malkin, J., Kuznetsov, Y. G., Land, T. A., Deyoreo, J. J., & McPherson, A. (1995). Mechanisms of growth for protein and virus crystals. *Nature Structural Biology*, **2**(11), 956–959.

Martins, P. M., Rocha, F., & Damas, A. M. (2008). Understanding water equilibration fundamentals as a step for rational protein crystallization. *PLoS ONE*, **3**(4), e1998.

Mcpherson, A. (2001). A comparison of salts for the crystallization of macromolecules. *Protein Science*, **10**(2), 418–422.

McPherson, A. (2004). Introduction to protein crystallization. *Methods*, **34**(3), 254–265.

McPherson, A., & Gavira, J. A. (2014). Introduction to protein crystallization. *Acta Crystallographica Section F:Structural Biology Communications*, **70**(1), 2–20.

Mcpherson, A., Malkin, A. J., & Kuznetsov, Y. G. (1995). The science of macromolecular crystallization. *Structure*, **3**(1), 759–768.

Newman, J., Xu, J., & Willis, M. C. (2007). Initial evaluations of the reproducibility of vapor-diffusion crystallization. *Acta Crystallographica Section D: Biological Crystallography*, **63**(7), 826–832.

Ng, J. D., Gavira, J. A., & García-Ruíz, J. M. (2003). Protein crystallization by capillary counterdiffusion for applied crystallographic structure determination. *Journal of*

Structural Biology, **142**(1), 218–231.

Otálora, F., Gavira, J. A., Ng, J. D., & García-Ruiz, J. M. (2009). Counterdiffusion methods applied to protein crystallization. *Progress in Biophysics and Molecular Biology*, **101**(1–3), 26–37.

Skálová, T., Dušková, J., Hašek, J., Kolenko, P., Tpánková, A., & Dohnálek, J. (2010). Alternative polymer precipitants for protein crystallization. *Journal of Applied Crystallography*, **43**(4), 737–742.

Sleutel, M., Maes, D., Wyns, L., & Willaert, R. (2008). Kinetic roughening of glucose isomerase crystals. *Crystal Growth and Design*, **8**(12), 4409–4414.

Tardieu, A., Bonneté, F., Finet, S., & Vivarès, D. (2002). Understanding salt or PEG induced attractive interactions to crystallize biological macromolecules. *Acta Crystallographica Section D: Biological Crystallography*, **58**(10 II), 1549–1553.

Chapter 8

Examples of crystallization of various proteins on SAMs

8.1 Introduction

In a typical VD experiment, proteins are crystallized in contact with a surface which is siliconized to avoid any undesirable effect. Glass siliconization guarantees a quasi-spherical drop shape thanks to moderate surface hydrophobicity, slowing down the water evaporation rate and being optimal for the growth of crystals in the system. Complementary strategies for controlling water evaporation rates have also been proposed, such as capillary or film barriers (Li et al., 2001) and oil layers above the reservoir (Chayen, 1997).

As outlined in Chap. 1, several attempts were carried out to study protein crystallization inside drops deposited on substrates different from siliconized glass or doped with foreign particles. However, the study of the interactions between external surfaces and proteins is by far more challenging than for small molecules. Proteins display hydrophobic and hydrophilic patches on their surfaces which in turn lead to different types of complex interactions. Thus, the surface properties of heteronucleants become even more important. Scarce attention has been paid to the deconvolution of surface chemistry and topography effects on protein nucleation. Surface functionalization is usually accompanied by alterations of surface roughness, impeding a rigorous study of the effect of different functional groups on the nucleation step. It has been demonstrated that the energetic penalty for heterogeneous nucleation increases with the contact angle between the surface and the drop. Conversely, it decreases when the surface roughness is more pronounced (Liu et al., 2007). As an alternative approach, the rational engineering of protein surface has been proposed as a tool to promote crystallization thanks to conformational entropy reduction (Derewenda & Vekilov, 2006).

A few studies reported the use of hydrophobic SAMs composed of hydrocarbon chains with variable terminal group or length to obtain faster crystallization rates and less stringent crystallization conditions compared to conventional coverslips thanks to the inhibition of amorphous precipitation (Ji et al., 2000; Pham et al., 2004). However, the substrates lacked detailed characterization and a topographic contribution to the enhancement of nucleation could not be excluded.

In the present chapter, SAMs have been applied as supports for the crystallization of HEWL, catalase, and proteinase K. Thanks to the demonstrated absence of surface defects and discontinuities which could act as potential nucleation sites, our supports allow for the isolation of the effect of SAMs end group on protein crystallization. Crystallization conditions were first adjusted without SAMs to identify the optimal nucleation induction time window. Then, crystallization was carried out on SAMs, and different supersaturation levels were explored to understand the action of SAMs on nucleation.

8.2 Methods

8.2.1 VD crystallization in *mushrooms*

Surfaces may be used to tackle nucleation phenomena of complex molecules, like proteins. However, the experimental investigation is by far more delicate than that concerning small molecules. From the point of view of the protein, its manipulation is vital for the preservation of stability (oligomerization state, bounded ligands, etc.) and prevention of denaturation. Extreme care must be taken when preparing the mother protein solution and to ensure that it is not exposed to environmental stresses (temperature, vibration, etc., depending on the specific protein). Moreover, when protein solutions are to be used for nucleation studies, the presence of impurities must be avoided so as not to interfere with the action of the surface. In this perspective, the purification of the solution by filtration and/or dialysis and, contextually, the preliminary cleaning of the surfaces helps in the creation of an impurity-free environment.

In order to investigate the nucleation phenomena of the chosen model proteins, we selected the vapor diffusion methods with the *mushroom* configuration. The device allows to carry on multiple experiments at the same time while ensuring the maintenance of exactly the same physico-chemical conditions. Among these, the maintenance of the same humidity degree in the crystallization environment and the same equilibration time are of utmost importance to cross-compare the final results. Even minimal variations in one of the afore-mentioned variables can have drastic consequences on the kinetics of nucleation.

Three model proteins were crystallized inside drops deposited on different surfaces. Drops deposited on *mushroom* glass and on EtOH-cleaned coverslips were taken as references to determine the effect of SAMs. SAMs were prepared with THIOL, GLY, and ACR silanes following the optimized procedure identified in Chap. 4. Each crystallizer was loaded with three SAMs and an EtOH-cleaned coverslip, and two drops were deposited on each surface. Then, the crystallizers were sealed with vacuum grease, incubated at 20 °C, and periodically inspected.

HEWL was buffered in 50 mM Na acetate pH 4.5, catalase C30 was prepared in 50 mM K phosphate buffer pH 7.0 following the same procedure described in § 7.4.3.1, and proteinase K was buffered in 50 mM HEPES pH 7.0. All the solutions were syringe filtered using 0.22 μm pore-size low protein-binding membrane filters. The list of crystallization conditions is reported in Tab. B3 (Appendix B). The total drop volume was set at 6 μL to minimize the evaporation of the drops before sealing the system. The reservoir volume was set at 5 mL, and its composition was the same as that highlighted in the “Precipitant” column of Tab. B3.

8.3 Crystallization of HEWL

The first model molecule selected for the study was HEWL. In order to identify the optimal nucleation induction time window for nucleation studies with surfaces, a preliminary screening without SAMs was performed.

8.3.1 Preliminary screening of nucleation induction time without SAMs

The goal of the preliminary tests was to identify the optimal combination of protein and precipitant concentrations which could guarantee the appearance of crystals in a reasonable amount of time. The experiments were designed to select a crystallization condition based on a limited amount of salt and the highest implementable concentration of protein, as will be further discussed below. The impact of protein and salt concentrations was studied separately.

8.3.1.1 Influence of protein concentration

Based on HEWL crystallization trials described in § 7.6.1, the precipitant concentration in the reservoir was set at 4 wt% NaCl in 50 mM Na acetate pH 4.5. Various concentrations ranging from 5 to 80 mg/mL of HEWL in the stock solution were tested. Each drop was made of 3 µL of HEWL solution and 3 µL of reservoir solution. The trend of the nucleation induction time according to HEWL concentration is reported in Fig. 55.

In the selected experimental conditions, a very good tuning of the time needed for the first crystal to become detectable by optical microscopy was achieved. By varying protein concentration, a range of induction time, from 12 hours to several days, was covered. Also, below a certain HEWL concentration (10 mg/mL), no crystallization events were detected after 20 days. This portfolio of nucleation times was fundamental for the choice of the proper HEWL concentration to be used in conjunction with the functionalized surfaces. Such a parameter emerged from a compromise. From the one side, the nucleation time has to be slow enough to allow the system equilibration, the diffusion of protein molecules towards the surface, and the tackling of the heterogeneous nucleation area of the phase diagram. On the other side, too long nucleation time is deleterious for the study of nucleation since other events may overlap with those related to the formation of stable clusters of protein molecules. Among these, one can count the perturbation of the system by external factors like vibrations, contaminants, the oxidation of the protein, or the leakages in the sealing resulting in excessive evaporation of the drops.

From the screening, it was also demonstrated that HEWL could be considered as an ideal model for nucleation kinetics studies. Thanks to its broad metastable zone, it is possible to investigate a wide range of supersaturation conditions and elucidate their effects on the crystal attributes.

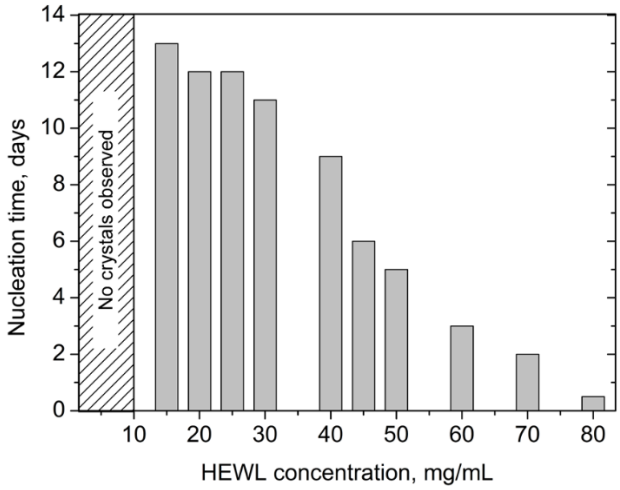

Figure 55 The nucleation time as a function of HEWL concentration in the mother protein solution. The nucleation time was defined as the time elapsed to observe the first crystals in the drops by optical microscopy investigations. Below 10 mg/mL HEWL, no crystals were detected within an experimental observation time of 20 days.

The nucleation time was correlated to the number and size of the crystals obtained in the drops. Fig. 56 sketches some representative drops in which HEWL crystals were grown starting from different protein concentrations, namely 80, 60, 50, and 30 mg/mL. Decreasing HEWL concentration had a major impact on the nucleation density. At high protein concentration (80 mg/mL, Fig. 56 (a)), single and large crystals were obtained, whereas smaller and more crystals were observed at lower protein concentration. This counter-intuitive phenomenon was attributed to the very low supersaturation level of the drops, confirmed by the elongated shape of the crystals, and the less amount of protein available for crystal growth in more diluted drops. The amount of salt in the precipitation cocktail guaranteed mild crystallization conditions. An excess in salt would have promoted the fast nucleation of many crystals whose (110) face had been shorter.

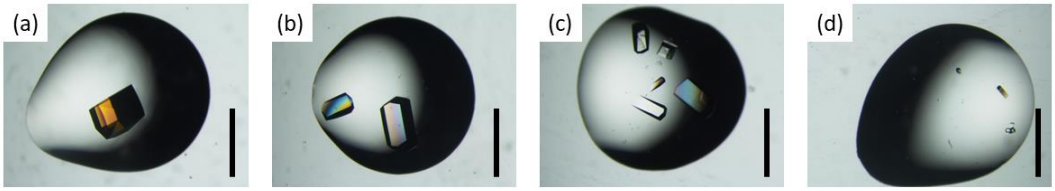

Figure 56 HEWL crystals grown in drops on mushroom glass starting from (a) 80, (b) 60, (c) 50, (d) 30 mg/mL of protein mother solutions. The scale bar is 1 mm.

The maximization of the nucleation extent over growth, keeping at the same time the low supersaturation conditions, the detection of crystals in a reasonable amount of time, and the presence of a high number of protein molecules in the system are all requirements to be fulfilled at the same time. In this way, crystallization experiments in the presence of surfaces can be successfully designed. A reasonable HEWL concentration to carry out experiments on SAMs turned out to be between 50 and 60 mg/mL to guarantee the appearance of crystals in 3-5 days in the reference samples, i.e., drops deposited on the *mushroom* glass. At the same time, this setting allowed the availability of a large number

of protein molecules in the drops to maximize the interaction with the surface and reduce the influence of salt over the nucleation step.

8.3.1.2 Influence of salt concentration

As a second step, the impact of NaCl concentration on HEWL nucleation time was evaluated. For this part of the study, HEWL concentration was set at 60 mg/mL, whereas the salt concentration was progressively increased. Reference conditions (LS1 – LS4) are reported in Tab. B3. The increase in the ionic strength shortened the nucleation time and increased the density of crystals inside the drops, as expected. At low supersaturation (LS1), few crystals were grown, as highlighted in Fig. 57 (a), and the first crystals were observed after three days. At higher supersaturation, the nucleation density increased (Fig. 57 (b), (c)), eventually leading to massive crystallization (Fig. 57 (d)). Crystallization was completed just after few hours on all the surfaces, and the variations in the nucleation time were too small to discern among samples. When salt exceeded 7wt%, the presence of a surface with specific attributes would not be able to alter the nucleation step, as the extent of interaction between protein and salt molecules by far exceeds that between protein and surface. Therefore, the optimal salt concentration for performing crystallization on SAMs was set at 4wt%.

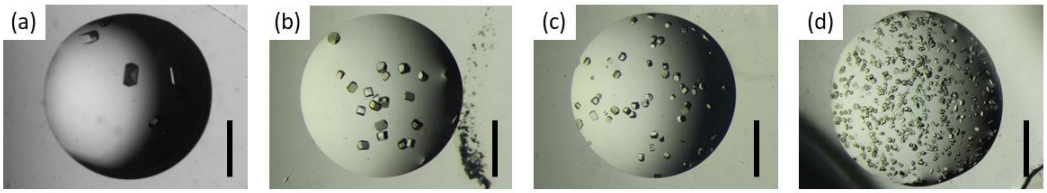

Figure 57 HEWL crystals grown in drops deposited on *mushroom* glass at progressively higher supersaturation. Protein concentration was 60 mg/mL and NaCl was (a) 4, (b) 7, (c) 11, and (d) 15wt%. Reference conditions are LS1 – LS4. The scale bar is 1 mm.

8.3.2 Crystallization of HEWL on SAMs

Following the previous results of the screening of HEWL crystallization in *mushrooms* without SAMs, an experiment involving condition LS1, i.e., 60 mg/mL of protein and 4wt% NaCl in buffered media, was performed. The total drop volume was kept at 6 µL, with a protein on precipitant ratio equal to 1. The drops deposited on the *mushroom* glass and the EtOH-cleaned coverslips served as a reference to compare the results. In fact, the two glasses significantly differed for their contact angle, and this, in turn, affects the drop shape and the nucleation kinetics. The surface-to-volume ratio of the drops is a function of the contact angle, and this feature determines the extent of water evaporation. Smaller contact angles result in enhanced evaporation and early equilibration of the drop. The protein solution had a contact angle of approximately 40° and 60° for the EtOH-cleaned glass and the *mushroom* glass, respectively. This discrepancy is a consequence of the glass commonly selected for building protein crystallization devices. A slightly more hydrophobic surface is beneficial for the creation of more “rounded” drops, which are more stable and ensure ideal evaporation rates. All the SAMs were designed to generate similar contact angles in order to set-up coherent crystallization experiments.

8.3.2.1 Evaluation of nucleation time

The nucleation time for the two reference glass surfaces and the three SAMs is reported in Fig. 58, black bars. The comparison with the preliminary screening results confirmed that the crystallization experiment proceeded as expected. In the drops deposited on *mushroom* glass, the first crystals appeared after 3 days, which fell in the time range previously discussed. This condition corresponded to the reference state for the crystallization of HEWL occurring without alterations promoted by engineered surfaces.

All the other substrates led to shorter nucleation times. The growth of detectable crystals in the drops deposited on the standard glass coverslips was completed in 2 days. All the evidence pointed out the importance of the hydrophobicity of the surface, and its major role in governing the drop equilibration time. Therefore, the presence of this second reference state was essential for data comparison. The highest nucleation-active surface was found to be THIOL SAM, leading to crystals in approx. 12 hours. Crystals appeared on GLY and ACR SAMs after 1 and 2 days, respectively.

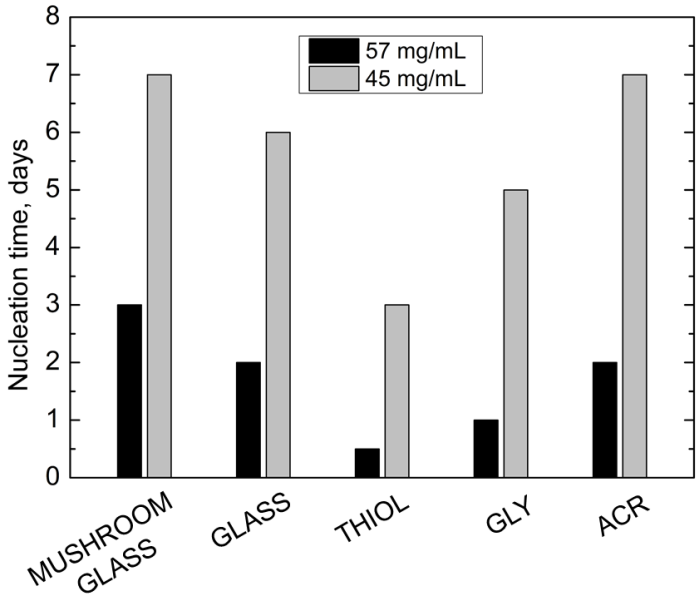

Figure 58 Comparison among the HEWL nucleation time on different surfaces at 60 (LS1, black bars) and 45 mg/mL (LS5, grey bars) HEWL and 4wt% NaCl.

Once the beneficial effect of the functionalized surfaces on the kinetics of HEWL crystallization had been demonstrated, further investigation was carried out to better isolate the effect of each surface. HEWL concentration was reduced to 45 mg/mL (condition LS5), keeping the experimental set-up constant, to emphasize and verify the nucleation ability of each surface. As can be seen in Fig. 58 (grey bars), the trend of the induction of nucleation time was preserved. It was confirmed that THIOL SAMs were the most active surfaces for nucleation, followed by GLY SAMs. ACR SAMs, instead, showed a slight inhibitory effect, leading to crystals one day later than the untreated coverslips. It also emerged that, at lower supersaturation, the action of the SAMs was much more evident compared to not functionalized glasses. The gap in nucleation time obtained with SAMs was markedly enlarged, whereas the two reference glasses still differed for 1 day. Therefore, at lower supersaturation the effect of a mere change in hydrophobicity of the glass was flattened, whereas the effect of different surface functionalization was predominant.

8.3.2.2 Interactions between SAMs and HEWL

The ability in accelerating nucleation of some surfaces was attributed to the interplay between protein and surface charge. At pH 4.5, the overall charge of HEWL is positive. Thiol groups become increasingly protonated if pH is below 8.0. The positive charge of THIOL SAMs was confirmed by the large negative SZP measured at neutral pH, as reported in § 4.6.1. The early stabilization of nuclei was probably due to an initial electrostatic attraction between the positively charged protein molecules and the anions adsorbed on THIOL SAMs and forming the Stern layer. As regards the other surfaces, they all displayed a much smaller negative SZP, pointing out a less important electrostatic interaction with the protein. Such a finding agreed with the lower influence on HEWL nucleation kinetics displayed by these substrates. Other parameters may also come into play, such as the chemical affinity between surface and protein. This mechanism of interaction was probably predominant in drops deposited on GLY SAMs. Having approximately the same SZP of ACR SAMs, but resulting in halved nucleation times, it was hypothesized that the glycidyloxy group might display some secondary interactions with the protein molecules, favoring their accumulation next to the surface. As a result, an increase in the local supersaturation could enhance nucleation kinetics. In parallel, we hypothesize that glycidyloxy groups may also promote the stabilization of pre-nucleation clusters, resulting in shorter nucleation times. In fact, proteins are supposed to adsorb on flat surfaces and migrate until the formation of a monolayer. Aggregates may simultaneously form on the surface and, if bond angles correspond to protein crystals, they can grow into nuclei and crystals (Kim *et al.*, 2002; Yau & Vekilov, 2000). The presence of a flat surface functionalized with specific groups may have promoted the early aggregation of protein macromolecules by lowering the energetic penalty.

In conclusion, SAMs displayed a distinct action on HEWL nucleation, resulting in up to 6-fold faster nucleation compared to *mushroom* glass. Depending on the SAM end groups, nucleation time was successfully tuned. The effect was strongly dependent on the supersaturation level of the system.

8.4 Crystallization of catalase

In order to extend the validity of our approach, the crystallization of other proteins was studied in the presence of SAMs. Compared to HEWL, catalase represents a more challenging protein to be crystallized because of its strong tendency to oxidation and consequent loss of activity, and the lower level of control over nucleation.

8.4.1 Preliminary screening of crystallization in *mushrooms*

We followed a similar strategy as with HEWL to identify suitable crystallization conditions. A preliminary screening in *mushrooms* was carried out. The results obtained for C30 by HDVC presented in § 7.6.2 served as a starting point for setting the experimental design. Differently from HEWL, the screening was performed varying the concentration of the protein mother solution and the ratio between the protein and the precipitant solution. Such a choice was dictated by the possibility to explore a wider range of conditions with

the second parameter and the more challenging crystallization of catalase. All the drops were equilibrated against the same precipitant reservoir, made of 15 wt% PEG4000.

The initial catalase concentration was varied between 1.8 and 3.7 mg/mL, as summarized in Tab. B3. After one day, crystals were observed in all the drops. The screening pointed out that, despite the implementation of mild crystallization conditions, it was not possible to achieve fine tuning of the nucleation time, as obtained for HEWL. At higher protein concentrations, i.e., CS1, the nucleation density was large as reported in Fig. 59 (a). Reduced supersaturation conditions, i.e., CS2, led to fewer and larger crystals as reported in Fig. 59 (b). A further reduction of catalase and/or PEG concentration was not beneficial for the enlargement of the waiting time for the appearance of the first crystals but, rather, it hindered their formation.

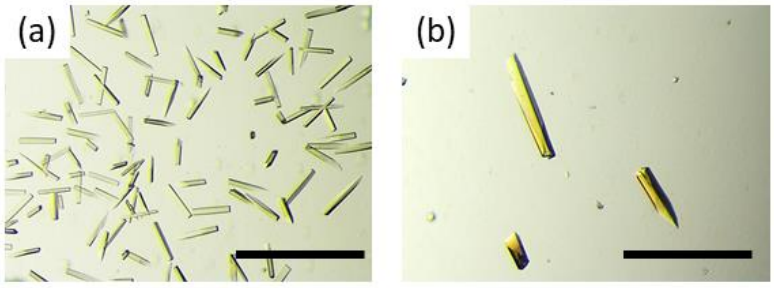

Figure 59 Optical micrographs of catalase crystals grown under (a) CS1 and (b) CS2 conditions. The scale bar is 500 μm.

8.4.2 Crystallization of catalase on SAMs

Two concentrations of catalase were selected to carry out low and high supersaturation experiments with SAMs. Low supersaturation guaranteed the appearance of crystals in one day and reasonable nucleation density to evaluate the effect of surface chemistry. Higher supersaturation was implemented to validate the hypothesis of surface inactivity during homogeneous nucleation.

The need for a second reference surface is even clearer in cases such as this one, in which the protein metastable zone is narrow, and the impact on nucleation density due to the mere hydrophobicity of the surface becomes more relevant. As already discussed, the average contact angle of drops on *mushroom* glass was about 20° higher than on EtOH-cleaned coverslips. On the one hand, the smaller surface-to-volume ratio of the former was responsible for slower drop equilibration. The slower crossing of the metastable zone led to reduced nucleation density. On the other hand, for drops having a larger surface available for vapor mass transfer, the metastable zone was reached faster, and a higher number of nuclei were formed. All the evidence further confirmed the need for two reference states. The *mushroom* glass is used for the comparison to the preliminary screening data, the untreated coverslip is directly compared to the functionalized surfaces. In this way, the nucleation step on SAMs could have been studied cutting out hydrophobicity effects.

8.4.2.1 Low supersaturation

The crystallization of catalase on surfaces was initially carried out at low supersaturation to maximize the impact of SAM chemistries. Condition CS3 involving a low amount of

PEG4000 (15wt%) and moderate protein concentration (2.4 mg/mL) was implemented in a *mushroom* crystallizer. After 12 hours, crystallization was completed on the two reference glasses and on GLY and ACR SAMs. No crystals were observed on THIOL SAMs. The catalase nucleation induction time was thus significantly shorter than that of HEWL, complicating the kinetics studies. However, some interesting insights into catalase nucleation behavior were obtained. On the one hand, when nucleation occurred, it did in a comparable time window on the different surfaces. On the other hand, the observed populations of crystals differed among the surfaces. A common feature regarded the presence of elongated bar-like crystals, as can be seen in Fig. 60. However, plate-like crystals were also observed on GLY (Fig. 60 (a)-(b)) and ACR SAMs. The final population of crystals reflected a distinct equilibration pathway. A single ensemble of nucleation events occurred on reference glasses, leading to a uniform population. Conversely, on GLY and ACR SAMS, two morphologically different populations denoted a first ensemble of early nucleation events, which occurred at high supersaturation and led to rod-like crystals. Then, a second ensemble of belated nucleation events took place at lower supersaturation and led to plate-like crystals.

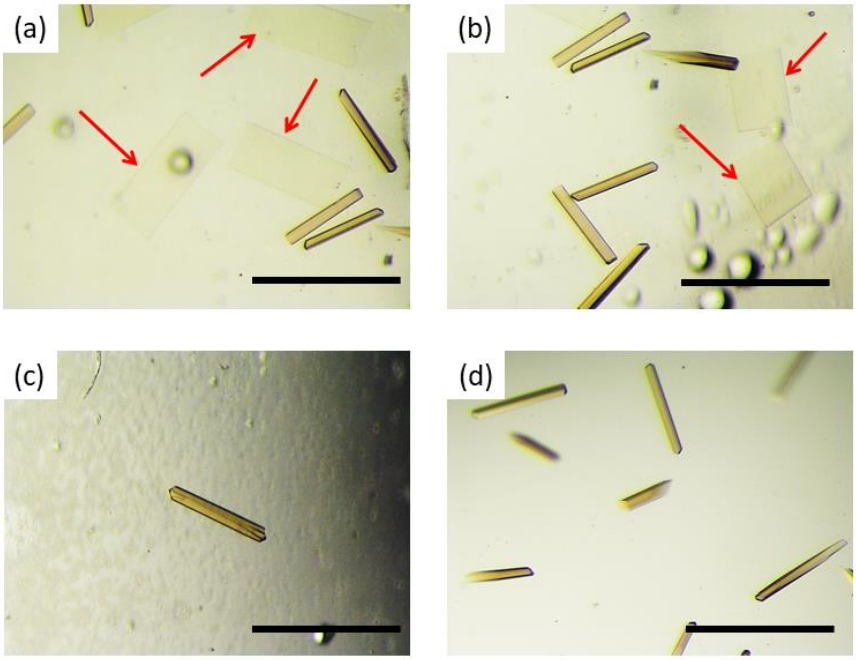

Figure 60 (a), (b) Catalase crystals grown on GLY SAMs. Two nucleation steps were observed and led to bar and plate-like (indicated by the red arrows) crystals. Reference catalase crystals grown on (c) *mushroom* glass, and (d) untreated coverslips. The scale bar is 500 µm.

Catalase nucleation was substantially affected by surfaces. When glasses lacking specific functionalization were employed, nucleation occurred in bulk, and no interactions with the surface were present. The two ensembles of nucleation events observed on GLY and ACR SAMs was related to adsorption phenomena. A certain amount of protein molecules could have interacted with SAMs, forming an adsorbed layer on the surface. After the first nucleation event which led to bar crystals, the decrease in solvated protein molecules in the drop due to fast crystal growth may have promoted the release of the adsorbed catalase. Thanks to the interaction with the residual PEGs, the released

macromolecules led to the plates. A second hypothesis regards the surface stabilization of the plates as a consequence of ΔG lowering.

Electrostatic interaction played a major role for THIOL SAMs, which were found to inhibit catalase nucleation in the time window of observation. At the crystallization pH of 7.0 the net charge of the protein is negative, whereas THIOL SAMs displayed a strong and negative SZP. The electrostatic repulsion prevented the interaction of catalase molecules with the surface. Therefore, the surface was prevented to exert its ΔG-lowering action, resulting in retarded nucleation.

In conclusion, it was demonstrated how SAMs could have been employed to indirectly tackling nucleation phenomena for proteins that unsuited the requirements to carry out kinetics studies. The crystal population mirrored the events taking place before nucleation, thus enabling an indirect investigation of the surface action during the early stages of crystallization.

8.4.2.2 High supersaturation

The area of the phase diagram dominated by homogeneous nucleation was investigated by selecting the more aggressive crystallization condition CS4. Catalase concentration was increased to 3.7 mg/mL and PEG4000 to 20wt%. After a few hours, showers of crystals were observed on all the surfaces, blanks included, as reported in Fig. 61. Similar to what had been observed for HEWL, high supersaturation flattened the effect of surface functionalization. The nucleation step was characterized by the aggregation of protein molecules occurring homogeneously in the bulk because of the large protein and polymer concentrations. The extent of interaction with the surface was minimal, and the control of nucleation was no longer possible.

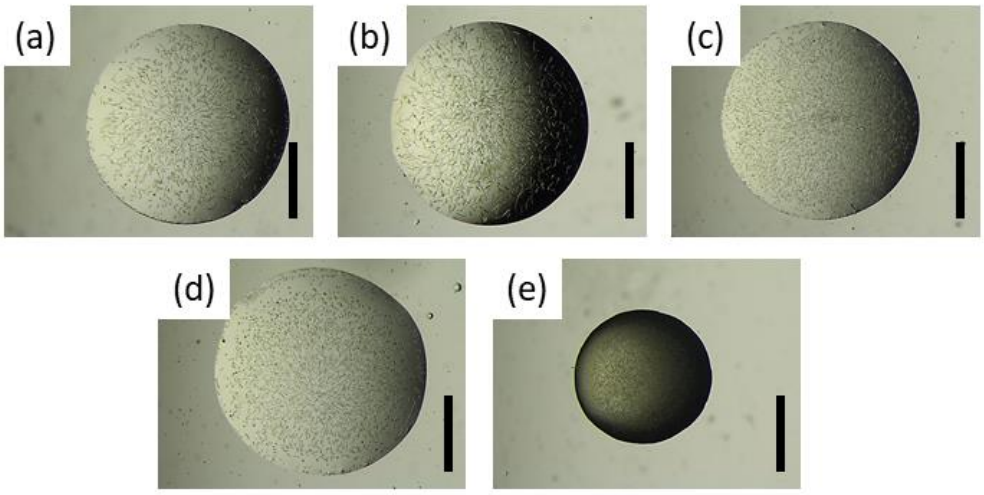

Figure 61 Massive crystallization of catalase carried out at high supersaturation (3.7 mg/mL of catalase, 20 wt% PEG4000) on (a) THIOL, (b) ACR, (c) GLY SAMs, (d) EtOH-cleaned coverslip, and (e) *mushroom* glass. The scale bar is 1 mm.

In conclusion, catalase represented a more challenging case-study compared to HEWL for nucleation studies. Its reduced metastable zone made it unsuitable for the direct evaluation of nucleation kinetics on SAMs. However, it also demonstrated the possibility offered by SAMs to indirectly investigate the nucleation step and to be used as

crystallization promoters or inhibitors. The final crystal population mirrored the history of crystallization, and the interaction between the protein and the surface could be addressed by studying the morphology of the crystals.

8.5 Crystallization of proteinase K

The implementation of SAMs for the study of the nucleation step of proteins was also carried out for proteinase K. A preliminary screening in *mushrooms*, followed by the study in the presence of surfaces, was performed.

8.5.1 Preliminary screening of proteinase K crystallization in *mushrooms*

Keeping as reference the HDVD screening presented in § 7.6.3, the crystallization of proteinase K in *mushrooms* was studied with two different precipitation cocktails. The first one involved 0.25 M $NaNO_3$ as a precipitant and 25 mM Na citrate as an additive. The second one involved 2 M $(NH_4)_2SO_4$. The protein concentration ranged between 10 and 30 mg/mL. The experiments are listed in Tab. B3.

Two salts were selected to carry out the crystallization of proteinase K because of experimental design reasons. If comparable nucleation kinetics were obtained with two different salts, one could investigate the influence of different ions, and thus different charges, on the nucleation of the same protein on the same surface. According to the Hofmeister series, sulfates are more able to alter the protein solubility than nitrates. The reservoir conditions were carefully selected in order to set-up *mushrooms* in which the expected nucleation rates would have been the same, even if the chemical composition of the precipitation cocktail differed. The nucleation time is reported in Tab. 29.

Table 29 The nucleation time for the various crystallization conditions screened for proteinase K. The total volume of the drops was 6 µL. The observation time was 15 days.

Experiment reference	Proteinase K, mg/mL	Precipitant	Nucleation time
PS1	30	0.25 M $NaNO_3$ 25 mM Na citrate	5 min
PS2	20	0.25 M $NaNO_3$ 25 mM Na citrate	12 h
PS3	15	0.25 M $NaNO_3$ 25 mM Na citrate	-
PS4	10	0.25 M $NaNO_3$ 25 mM Na citrate	-
PS5	30	1.7 M $(NH_4)_2SO_4$	5 min
PS6	20	1.7 M $(NH_4)_2SO_4$	12 h
PS7	15	1.7 M $(NH_4)_2SO_4$	-
PS8	10	1.7 M $(NH_4)_2SO_4$	-

The periodic investigation of the drops by optical microscopy revealed a good matching between the nucleation of the two systems. High supersaturations (PS1 and PS5), reported in Fig. 62 (a) and (e), led to quasi-immediate micro-crystallization of the protein which filled the drops with showers of tiny crystals. Moderate supersaturations (PS2 and PS6), reported in Fig. 62 (b) and (f), slowed nucleation time down to 12 hours and produced a countable number of crystals. Crystals of around 150 and 300 µm were observed in the presence of nitrate and sulfate, respectively. Nucleation density was clearly reduced in both cases when protein concentration was lowered by 30%. If the protein was lowered an extra 20% or more (PS3, PS4, PS7, PS8), nucleation was completely avoided regardless of the type of precipitant used. Such an observation was attributed to the insufficient driving force for nucleation provided by the protein and the precipitant concentration. The observation time was 10 days.

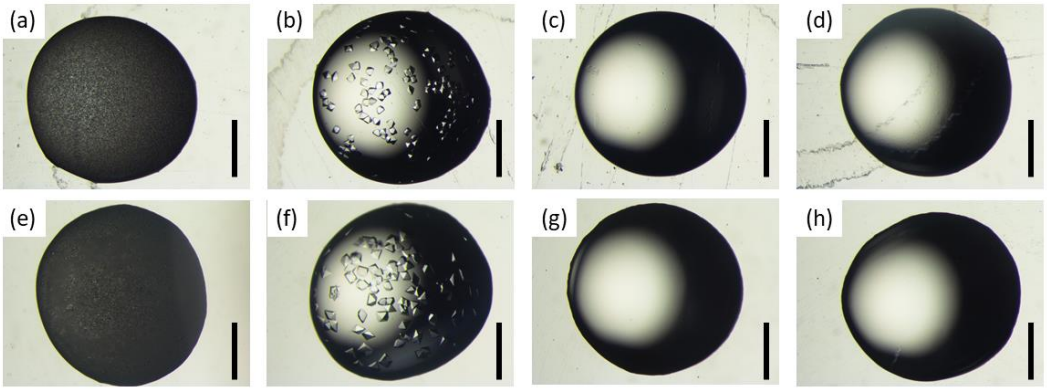

Figure 62 Outcome of crystallization of proteinase K for experiments involving (a)-(d) nitrate and (e)-(h) sulfate. Crystallization conditions follow Tab. B3. The scale bar is 1 mm.

The investigation of crystallization of proteinase K in *mushrooms* evidenced the major influence of protein concentrations on the nucleation step. The window of accessible concentrations for nucleation is narrower than for HEWL, reflecting a much more constricted metastable zone. Therefore, proteinase K is expected not to be a good model protein for nucleation studies.

8.5.2 Crystallization of proteinase K on SAMs

The window of suitable protein concentrations was identified to be 15 – 20 mg/mL. As usual, this consideration emerged from the compromise between nucleation kinetics and time available for the interaction with the surface. Two protein concentrations, namely 17 and 19 mg/mL, were tested. The detailed list of conditions is reported in Tab. B3.

The selected conditions did not lead to crystals on any of the SAMs and glasses tested. These results showed that even a small variation in the protein concentration, i.e., 1 mg/mL (less than 5%), was able to completely repress the nucleation step. Interestingly, the trend was found to be the same for both salts and all the surfaces. Therefore, for proteinase K, protein concentration played a pivotal role in dictating nucleation. The alteration of the system with salts differing in the Hofmeister series or surfaces, offering different electrostatics, had no role in the promotion of nucleation. These pieces of evidence

demonstrated the narrowness of proteinase K metastability zone and the unsuitability of this model protein to tackle the effect of functionalized surfaces on nucleation.

8.6 Final remarks

Chapter 8 presented the alteration of the nucleation pathway of proteins through SAMs. The comparative experiments were carried out inside *mushroom* crystallizers to ensure that all the drops followed exactly the same equilibration path and experienced the same environment of crystallization. Firstly, the reference conditions of crystallization were studied without SAMs, to identify the supersaturation regime able to ideally guarantee a decent lag time in the formation of crystals. Then, SAMs were implemented, and mild and high supersaturations were compared. Three model proteins were selected to carry out the study on nucleation kinetics. Thanks to the presence of a surface inside the crystallization system, provided that the supersaturation conditions were carefully selected, the early appearance of the first crystals of HEWL was induced, shortening the experimental time and the risk of disturbances affecting the crystallization outcome. Nevertheless, SAMs were found to be nucleation-active, able to shorten nucleation time and to tune the crystal population attributes only at low supersaturation. HEWL, catalase, and proteinase K resulted to be decreasingly suitable for kinetics investigations. For proteins having a narrower metastable zone, an indirect investigation of surface effects was carried out considering the morphology of crystal populations.

References

Artusio, F., & Pisano, R. (2018). Surface-induced crystallization of pharmaceuticals and biopharmaceuticals: A review. *International Journal of Pharmaceutics*, **547**(1–2), 190–208.

Chayen, N. E. (1997). A novel technique to control the rate of vapour diffusion, giving larger protein crystals. *Journal of Applied Crystallography*, **30**(2), 198–202.

D'Arcy, A., Mac Sweeney, A., & Haber, A. (2003). Using natural seeding material to generate nucleation in protein crystallization experiments. *Acta Crystallographica - Section D Biological Crystallography*, **59**(7), 1343–1346.

Derewenda, Z. S., & Vekilov, P. G. (2006). Entropy and surface engineering in protein crystallization. *Acta Crystallographica Section D: Biological Crystallography*, **62**(1), 116–124.

Georgieva, D. G., Kuil, M. E., Oosterkamp, T. H., Zandbergen, H. W., & Abrahams, J. P. (2007). Heterogeneous nucleation of three-dimensional protein nanocrystals. *Acta Crystallographica Section D: Biological Crystallography*, **63**(5), 564–570.

Guo, Y. Z., Sun, L. H., Oberthuer, D., Zhang, C. Y., Shi, J. Y., Di, J. L., Zhang, B. L., Cao, H. L., Liu, Y. M., Li, J., Wang, Q., Huang, H. H., Liu, J., Schulz, J. M., Zhang, Q. Y., Zhao, J. L., Betzel, C., He, J. H., & Yin, D. C. (2014). Utilisation of adsorption and desorption for simultaneously improving protein crystallisation success rate and crystal quality. *Scientific Reports*, **4**(1), 7308.

Hodzhaoglu, F., Kurniawan, F., Mirsky, V., & Nanev, C. (2008). Gold nanoparticles induce protein crystallization. *Crystal Research and Technology*, **43**(6), 588–593.

Ji, D., Arnold, C. M., Graupe, M., Beadle, E., Dunn, R. V., Phan, M. N., Villazana, R. J., Benson, R., Colorado, R., Randall, L., & T. Friedman, J. M. (2000). Improved protein

crystallization by vapor diffusion from drops in contact with transparent, self-assembled monolayers on gold-coated glass coverslips. *Journal of Crystal Growth*, **218**(2), 390–398.

Kallio, J. M., Hakulinen, N., Kallio, J. P., Niemi, M. H., Kärkkäinen, S., & Rouvinen, J. (2009). The contribution of polystyrene nanospheres towards the crystallization of proteins. *PLoS ONE*, **4**(1), e4198.

Kim, D. T., Blanch, H. W., & Radke, C. J. (2002). Direct imaging of lysozyme adsorption onto mica by atomic force microscopy. *Langmuir*, **18**(15), 5841–5850.

Li, G., Xiang, Y., Zhang, Y., & Wang, D. C. (2001). A simple and efficient innovation of the vapor-diffusion method for controlling nucleation and growth of large protein crystals. *Journal of Applied Crystallography*, **34**(3), 388–391.

Liu, Y. X., Wang, X. J., Lu, J., & Ching, C. B. (2007). Influence of the roughness, topography, and physicochemical properties of chemically modified surfaces on the heterogeneous nucleation of protein crystals. *Journal of Physical Chemistry B*, **111**(50), 13971–13978.

Pham, T., Lai, D., Ji, D., Tuntiwechapikul, W., Friedman, J. M., & Lee, T. R. (2004). Well-ordered self-assembled monolayer surfaces can be used to enhance the growth of protein crystals. *Colloids and Surfaces B: Biointerfaces*, **34**(3), 191–196.

Sugahara, M., Asada, Y., Morikawa, Y., Kageyama, Y., & Kunishima, N. (2008). Nucleant-mediated protein crystallization with the application of microporous synthetic zeolites. *Acta Crystallographica Section D: Biological Crystallography*, **64**(6), 686–695.

Thakur, A. S., Robin, G., Guncar, G., Saunders, N. F. W., Newman, J., Martin, J. L., & Kobe, B. (2007). Improved success of sparse matrix protein crystallization screening with heterogeneous nucleating agents. *PLoS ONE*, **2**(10), e1091.

Weichsel, U., Segets, D., Janeke, S., & Peukert, W. (2015). Enhanced Nucleation of Lysozyme Using Inorganic Silica Seed Particles of Different Sizes. *Crystal Growth and Design*, **15**(8), 3582–3593.

Yan, E. K., Zhao, F. Z., Zhang, C. Y., Yang, X. Z., Shi, M., He, J., Liu, Y. L., Liu, Y., Hou, H., & Yin, D. C. (2018). Seeding Protein Crystallization with Cross-Linked Protein Crystals. *Crystal Growth and Design*, **18**(2), 1090–1100.

Yau, S. T., & Vekilov, P. G. (2000). Quasi-planar nucleus structure in apoferritin crystallization. *Nature*, **406**(6795), 494–497.

Zhou, R. Bin, Cao, H. L., Zhang, C. Y., & Yin, D. C. (2017). A review on recent advances for nucleants and nucleation in protein crystallization. *CrystEngComm*, **19**(8), 1143–1155.

Chapter 9

The crystallization of proteins in environments with altered pH

9.1 Introduction

Crystallization by salting-out depends on several factors, such as protein concentration, ionic strength, temperature, and pH, which can affect the protein phase behavior (Grigsby et al., 2001; Popova et al., 2008). For example, it has been found that lysozyme displays a phase transition from soluble aggregates to macroscopic clusters when ionic strength is increased, and that the specific transition depends on salt identity and pH (Kuehner et al., 1997). The charge displayed by a protein in solution depends on the extent of ionization of the acid and basic groups of its amino acids side chains. The alteration of the pH of the solution acts on these chemical equilibria and modifies the protein net charge. Generally, proteins are positively charged at low pH and negatively charged at high pH. The crossing from one condition to the other is the isoelectric point, where the protein net charge is zero.

The choice of the optimal pH for crystallization experiments derives from a series of factors. Among these, ensuring that the system is far from the isoelectric point to increase its solubility (Retailleau et al., 1997), and that the protein is stable are two of the most relevant ones. The optimal pH of crystallization is specific to the protein and is generally associated with a specific buffer. However, very little attention has been paid to the study of the crystallization of a buffered protein according to various pH. One of the plausible reasons is represented by the unclear effects that varying pH has on protein solubility, especially when narrow pH windows are considered (Forsythe et al., 1999). The solubility of triclinic crystals of lysozyme was also studied by coupling pH and pressure effects, and was found to increase with pressure because of the decrease in pH of the buffer (Suzuki et al., 2011). pH may also help in the discovery of new polymorphs since a change in the space group of insulin crystals was found to be pH-dependent (Norrman & Schluckebier, 2007). Also, pH limits defining the crystal growth range can be finely-sliced to suppress nucleation and avoid microcrystallization (McPherson & Cudney, 2014).

In this chapter, the evaluation of protein charge vs. pH and the crystallization of two model proteins at different pH is presented. Furthermore, such a study will be transferred to *mushrooms* containing selected SAMs, and the combination of surface and pH effects

will be discussed. Lysozyme and catalase were selected as case studies for the implementation of pH-affected crystallization trials. The choice was carried out keeping in mind the different range of pH in which the two proteins are known to crystallize well, and the different extent of charge affection by pH.

9.2 Materials and Methods

9.2.1 Crystallization in Linbro plates

HEWL and catalase were first crystallized using Linbro plates and buffers with controlled pH. Each well was filled with 500 mL of precipitant solution. Drops were prepared with 1:1 ratio between protein and precipitant solution, and their total volume was 3 µL. Drops were deposited on siliconized coverslips on top of the reservoirs, which were then sealed with vacuum grease. Plates were incubated at 20 °C and periodically checked *via* optical microscopy.

Na acetate buffers were prepared for HEWL crystallization within the pH range 3.0 – 8.0. pH was corrected using acetic acid and sodium hydroxide. 4.5wt% NaCl was used as a precipitant, and it was buffered in 400 mM of Na acetate at a defined value of pH. HEWL was prepared in 50 mM Na acetate pH 4.5 at an initial concentration of 50 mg/mL.

As regards catalase C30, the protein was buffered in 50 mM K phosphate pH 7.0. Two concentrations were tested, namely 1.8 and 2.4 mg/mL. The precipitation cocktail was made of 15wt% PEG4000 buffered in 400 mM K phosphate with pH ranging from 6.0 to 8.0. The pH of all the buffers was checked before setting up each trial. All the solutions were passed through 0.22 µm syringe filters before setting up the experiments.

9.2.2 Crystallization with SAMs in *mushrooms*

The two model proteins were crystallized on THIOL SAMs in *mushrooms* at different pH. Among all the SAMs studied in the present thesis, THIOL SAMs were selected since they provided an ideal platform for tackling charge effects as the degree of protonation of thiol groups progressively increases by lowering the pH below 8. To prepare the experiments, the same procedure described in § 8.2.1 was applied. The reservoir was filled with 5 mL of precipitant solution, and the drop volume was 6 µL. Each crystallizer was loaded with drops deposited on *mushroom* glass and THIOL SAMs.

HEWL concentration was 60 mg/mL in 50 mM Na acetate pH 4.5, the precipitation cocktail was made of 4wt% NaCl in 400 mM Na acetate at a defined value of pH. pH was varied between 3.0 and 7.0. Drops were equilibrated against 4wt% NaCl aqueous solution.

The catalase concentration was set at 3.7 mg/mL. The precipitation cocktail was composed of 15wt% PEG4000 in milliQ water for the reservoir and 15wt% PEG4000 in 400 mM K phosphate at defined pH for the mother precipitant solution of the drops.

9.3 The protein charge as a function of pH

As a first step of the study of the affection of protein crystallization by pH, the charge trend vs. pH for some common proteins was evaluated and reported in Fig 63. The values were calculated with Protein Calculator (v. 3.4), knowing the sequence of amino acids for each protein. The maximum difference in the protein charge (Δq) was defined as the difference between the charge carried by the protein (q) at pH 4 and pH 10:

$$\Delta q = q\ (\text{pH } 4) - q\ (\text{pH } 10) \tag{17}$$

As can be seen, Δq fell within the 20 – 40 coulomb range for the majority of proteins. However, a much more marked dependence of charge from pH can also be identified for specific proteins. A particular case is represented by catalase, whose Δq was around 90 coulomb.

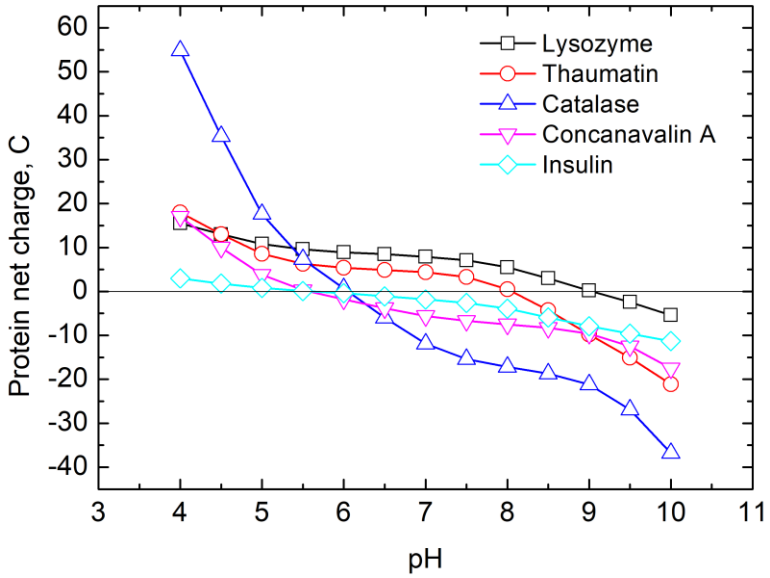

Figure 63 The protein net charge as a function of pH for lysozyme, thaumatin, catalase, concanavalin A, and insulin.

Crystallization is usually carried out under conditions where the trend of the protein charge vs. pH is as flat as possible, in order to avoid excessive fluctuations in the ionization of amino acids. For example, lysozyme crystallization is usually carried out at acidic pH, whereas catalase is crystallized at neutral or slightly basic pH.

The evaluation of the protein net charge as a function of pH guided the selection of two proteins to be adopted as models. Lysozyme was selected as a representative protein for the most general tendency. Catalase was chosen because of its strong charge dependency on pH and to test a more challenging crystallization process at different pH.

9.4 Crystallization of HEWL at different pH in HDVD

The surface charge distribution of HEWL was first simulated with PyMOL, as displayed in Fig. 64 (a), to evaluate its nature. The macromolecule resulted to be characterized by a

diffused positive charge across the surface and a localized and strong negative charge in the enzyme active pocket. The absolute value of the local charges is a function of pH.

As will be discussed below, pH had a major impact on the relative growth of tetragonal HEWL crystal faces. This effect was quantified by introducing the *AR* parameter which referred to the aspect ratio of the (110) crystal face. More specifically, *AR* was defined as:

$$AR = \frac{l_{max}}{l_{min}} \tag{18}$$

where l_{max} and l_{min} were defined as the maximum extension and the minimum extension of the (110) crystal face, as shown in Fig. 64 (b). The nomenclature of the parameters was given considering a HEWL crystal grown at low supersaturation conditions, i.e., elongated (110) face.

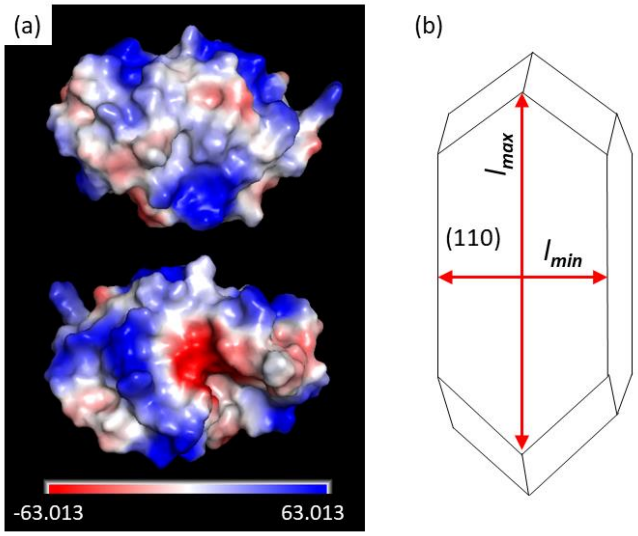

Figure 64 (a) Representation of the surface charge distribution of HEWL. Front and back views of the molecule are sketched. Red areas refer to the negatively charged zones of the molecule, white areas to the neutral ones, blue zones to positively charged areas. (b) Schematic representation of a tetragonal HEWL crystal. l_{min} and l_{max} are highlighted on the (110) face.

HEWL was buffered in Na acetate, which is suitable for the maintenance of acidic and neutral pH. The buffering system had to be the same for all the crystallization trials to compare the results obtained at different pH. Such a requirement represents a limitation in the width of the window of explorable pH. Other limitations regarded the choice of the buffer, which had to guarantee the protein stability over a range of pH, and its concentration, as it had to be high enough to maintain the desired pH but, at the same time, not to favor protein precipitation with salt excess. In this scenario, the explored pH window ranged from 3.0 to 8.0. Na acetate buffering systems are generally used between pH 3.6 and 5.6. However, it was decided to test it over a pH range wider than its safe buffering window to expand the area of investigated crystallization conditions. Such an aspect will be further discussed after the evaluation of the *AR* parameter. pH of Na acetate solutions was always checked for stability before setting the experiments. At the same time, the stability of protein solutions mixed with pH-corrected buffers was also visually checked.

The precipitation cocktail was designed to provide the necessary amount of NaCl to observe fast protein crystallization and the necessary amount of Na acetate to maintain the pH stability. Namely, the cocktail was made of 4.5wt% NaCl in 400 mM Na acetate buffer

at a defined value of pH. Protein concentration was set at 50 mg/mL. HDVD crystallization set-up was chosen in order to deal with individually closed systems. Any cross-contamination among the drops was thus avoided, and the punctual action of pH could have been investigated as a first step.

At pH below 4, the amorphous precipitation of HEWL was detected, reflecting the protein instability when facing very acidic pH values. From pH 4 to 8, crystals were obtained after achieving drop equilibration. It was observed that pH strongly affected the shape of the crystals, as highlighted by the trend of *AR* vs. pH in Fig. 65 (a).

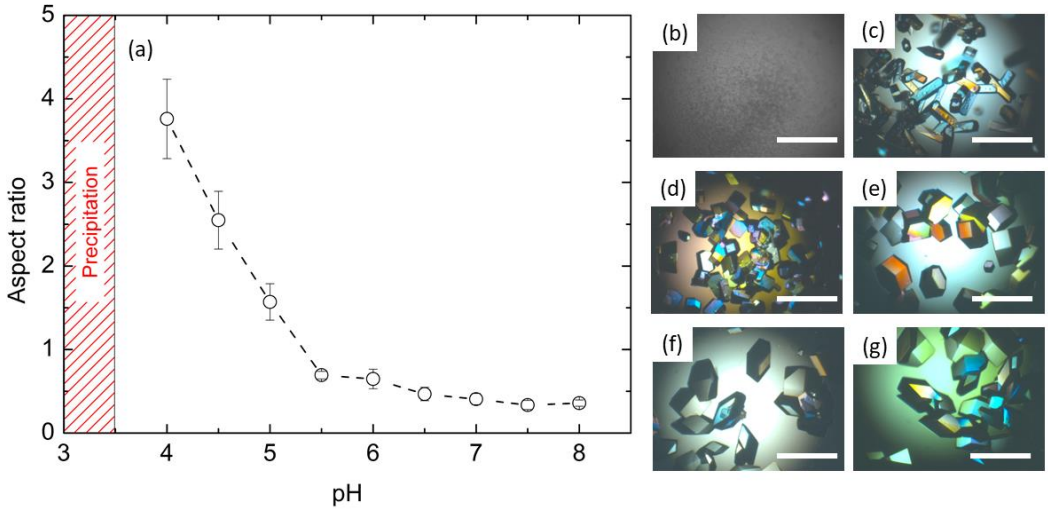

Figure 65 (a) The aspect ratio of HEWL crystals vs. pH trend. pH below 4 led to amorphous precipitation. Error bars refer to SD. HEWL concentration was 50 mg/mL in 50 mM Na acetate pH 4.5, the precipitation cocktail was made of 4.5wt% NaCl buffered in 400 mM Na acetate at defined pH. The ratio between protein and precipitant solutions was 1. The total volume drop was 3 µL. On the right side, representative micrographs of drops referring to pH (b) 3, (c) 4, (d) 5, (e) 6, (f) 7, and (g) 8 are illustrated. The scale bar is 500 µm.

AR showed a steep decrease in the range of pH from 4.0 to 5.5. HEWL crystals moved from elongated to more compact habits. A linear decrease in *AR* was observed. In the higher pH range, the decrease was progressively smoother and finally reached a plateau around 0.4 for pH values > 6.5. Also, the *AR* deviation was significantly smaller in this area. The plateau referred to the minimum elongation of the (110) face, which corresponded to the total absence of its central sector in HEWL crystals.

The presented results all referred to the same amount of precipitant (4.5wt% NaCl) and buffer concentration (400 mM Na acetate) in the precipitation cocktail, which corresponded to the same degree of supersaturation. It was therefore demonstrated how playing with the pH of the precipitation cocktail could alter the nucleation and growth pathway of HEWL, starting from ideally the same supersaturation. Extremely acidic pH conditions were responsible for the destabilization of the protein, probably because of a too high positive charge of the system and led to amorphous precipitation. When the crystallization zone was encountered, at milder acidic conditions, crystals began to appear. The linear decrease in *AR* was observed within the safe buffering window of acetate and, thus, such an effect could be only attributed to the increase in pH.

It was also discovered that pH had a strong influence on the growth step. In general, the more visible crystal faces are those that have grown slower and, thus determine the final

habit of the crystal. Conversely, the faces that tend to disappear are those growing faster. The relative growth rate of each crystalline face is determined by several factors, both internal and external to the crystal. The former includes the crystal structure and connections, whereas the latter refers to the composition of the solution and the supersaturation level. At high supersaturation, the faces carrying higher surface energy show higher incorporation rates, whereas those with lower energy determine the final shape of the crystal (Durbin & Feher, 1996). In our case, the (110) face is less visible at high pH. Therefore, the growth of the (110) prismatic face relative to the bipyramidal ones was strongly increased by the increase of pH. This output is generally obtained when different supersaturations are employed: elongated crystals reflect low supersaturation, whereas compressed crystals reflect high supersaturations (Grimbergen et al., 1999; Yoshizaki et al., 2001). As a thumb role, the farthest the system is from equilibrium, the more nucleation prevails over growth. In our case, this seemed not to be the case. On the one hand, nucleation density was enhanced in drops containing elongated crystals, which is contradictory to the previous statement. On the other hand, compact crystals grew bigger than the elongated ones. These pieces of evidence reflected a complex interplay between nucleation and growth in systems with modified pH. Certainly, a role could have been played by the higher amount of acetic acid used to stabilize the more acidic pH. This could have affected HEWL solubility and, consequently, its supersaturation degree at low pH. However, it did not explain the observed trends. As regards nucleation, in every case crystals were obtained overnight, with no differences in kinetics. It was therefore inferred that the protein net charge could have played a pivotal role. As presented in Fig. 63, the HEWL net charge initially decreased from pH 4.0, and it stabilized around pH 5.5. Such a trend was in very good agreement with that of *AR* vs. pH. The value of the protein charge could have governed the rate of the 4-molecular reaction involving the formation of tetramers from 4_3 helices (Nadarajah *et al.*, 1997), directly affecting the growth of the (110) face. The kinetics of the reaction could have been strongly repressed at lower pH and promoted at higher pH, leading to large and small (110) face areas, respectively.

9.5 Crystallization of HEWL at different pH on THIOL SAMs

The previous section highlighted how environments with modified pH can affect HEWL crystallization. As a further step, a narrowed pH screening was implemented in mushrooms with and without SAMs. pH was screened from 3.0 to 7.0. The crystallization conditions mirrored the first described experiment of HEWL crystallization in presence of surfaces. The protein concentration was 60 mg/mL in 50 mM Na acetate pH 4.5, the precipitation cocktail was made of 4wt% NaCl in 400 mM Na acetate at a defined value of pH. In a *mushroom* crystallizer, all the drops must be equilibrated against a unique reservoir. In order to get rid of pH effects on the evaporation rate, the reservoir was composed of 4wt% NaCl prepared in MilliQ water.

The nucleation time of HEWL on *mushroom* glass and on THIOL SAMs is reported in Tab. 30. The comparison between the corresponding pH conditions carried out on the *mushroom* glass, which served as reference, and THIOL SAMs evidenced striking differences in nucleation kinetics. Generally, THIOL SAMs were very active in inducing

the nucleation of HEWL, as already noticed in § 8.3.2. However, here it was demonstrated that such an ability could have been extended over the whole range of pH explored. THIOL SAMs generally induced HEWL crystallization in half of the time required to obtain crystals on the *mushroom* glass. At very acidic pH, i.e., 3.0, crystals were obtained on THIOL SAMs and not on *mushroom* glass. Interestingly, on THIOL SAMs the nucleation time was found to be minimum at pH 5.0 and to increase according to the same trend when moving up or down from this point. On the *mushroom* glass, the nucleation time was found to be minimum at pH 5.0 too.

Table 30 The nucleation time of HEWL on *mushroom* glass and THIOL SAMs, as observed at different pH. The total volume drop was 6 μL. The observation time was 15 days.

pH	Nucleation time on *mushroom* glass	Nucleation time on THIOL SAM
3.0	-	5 days
4.0	3 days	12 hours
5.0	1 day	6 h
6.0	13 days	1 day
7.0	10 days	5 days

The pH-altered nucleation time also had massive consequences on the number of crystals obtained per drop. As can be seen in Fig. 66, the crystal density vs. pH trend agreed with that of nucleation time, as expected. Both on *mushroom* glass and THIOL SAM, the largest number of crystals was obtained at pH 5.0. Therefore, the tuning of pH, by itself, could successfully tune the time in which crystals start to nucleate and grow. However, the introduction of a functionalized surface in the system produced a higher level of control on nucleation phenomena, both as regards kinetics and density of nucleation.

The nucleating ability of THIOL SAMs towards HEWL was attributed to favorable electrostatic interactions in § 8.3.2. Here, the additional variable of pH enabled a deeper understanding of these interactions. The nucleation step was believed to be affected by the interplay between protein net charge and surface degree of protonation. In the pH range 6 – 7, the net charge of HEWL is practically constant and equal to approx. 10 coulomb. On the surface side, the protonation is less extended than at low pH. The interaction would not be drastically enhanced, as demonstrated by the small number of crystals and the long nucleation times. Around pH 5, the interaction was maximized thanks to the electrostatic matching between surface and protein, resulting in the fastest nucleation time and the highest nucleation density. Further decreases in pH are affected by the rising of the protein net charge, which is detrimental for the stable assembly of molecules to form pre-nucleation clusters, thus enlarging again the nucleation time and lowering the number of successful nucleation events. However, even in these hostile crystallization conditions, THIOL SAM still played a role. Firstly, it kept its accelerating ability towards nucleation. More interestingly, it was able to facilitate the formation of crystals in extreme pH conditions. At pH 3, crystals were only obtained on the functionalized surface, whereas the *mushroom* glass turned out to be inert.

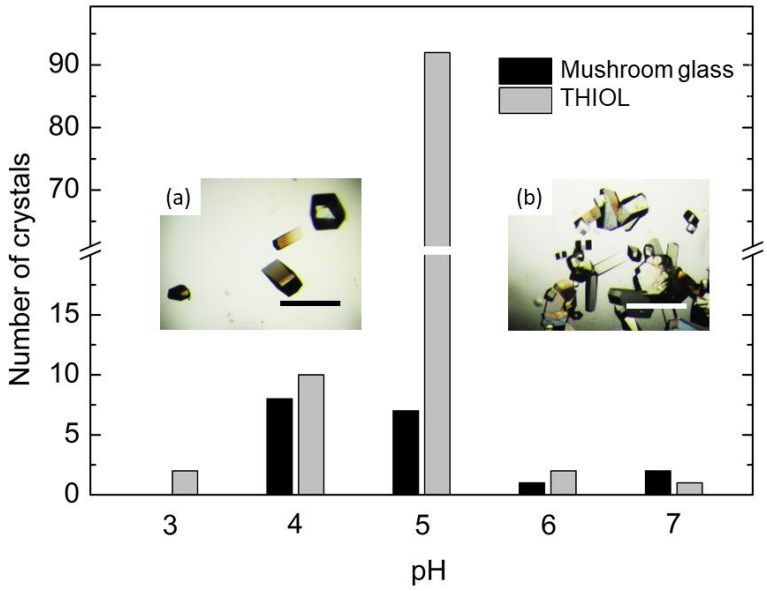

Figure 66 The number of crystals nucleated in drops deposited on mushroom glass and THIOL SAMs as a function of pH. Embedded are two representative micrographs illustrating crystal density on (a) mushroom glass at pH 5 and on (b) THIOL SAMs at pH 5. The scale bar is 500 µm.

To conclude, it was demonstrated that HEWL crystallization behavior strongly depended on the pH of the precipitation cocktail. In the absence of foreign surfaces, the homogeneous nucleation of HEWL was studied at different pH, and the aspect ratio of the crystals was found to be a function of pH. A second study demonstrated that the nucleation kinetics of HEWL was also affected by the pH conditions. In this case, the nucleating ability of THIOL SAMs was preserved. Many protein crystals were obtained in reduced time, even in conditions that would not lead to crystals in the absence of SAMs.

9.6 Crystallization of catalase at different pH in HDVD

The protein crystallization in environments with tuned pH was carried out for as a second case-study. Catalase was selected as a model because of the strong dependence of protein charge on pH, as discussed in § 9.3. Compared to HEWL, the surface charge distribution of catalase, sketched in Fig 67, is markedly different. Instead of a negatively charged zone confined to a single area of the protein, both negative and positive charges are distributed all over the enzyme surface. Preferential orientation of the macromolecule on a foreign surface would thus be more difficult to predict. On the other side, as catalase charge is more spread, it represents an ideal system to investigate the effect of pH.

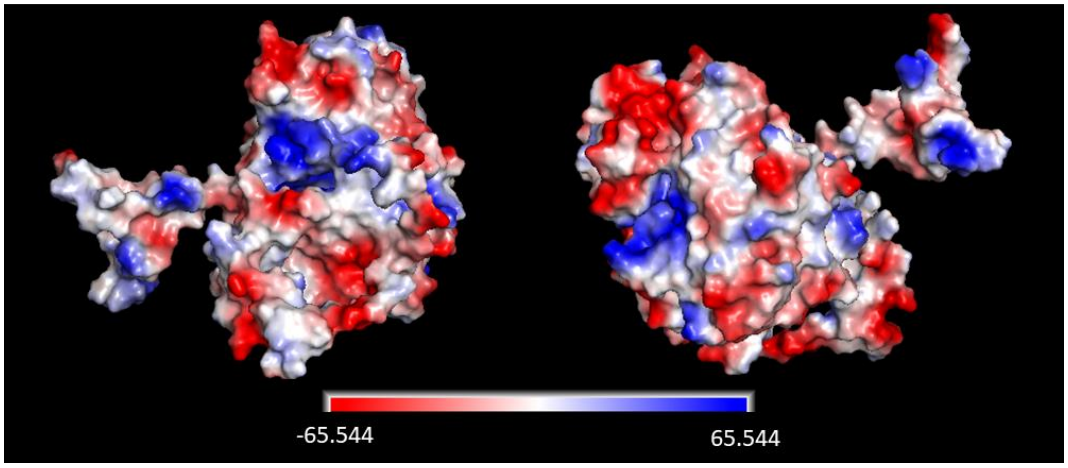

Figure 67 The surface charge distribution of catalase. Two views of the same protein molecule are displayed. Red areas refer to the negatively charged zones of the molecule, white areas to the neutral ones, blue zones to positively charged areas.

In order to test the crystallization of catalase altered by pH, HDVD crystallization trials were performed. Catalase was buffered in 50 mM K phosphate pH 7.0. The precipitation cocktail was made of 15wt% PEG4000 buffered in 400 mM K phosphate at a defined pH between 6.0 and 8.0. Two catalase concentrations were tested, namely 1.8 and 2.4 mg/mL. The crystals obtained after the complete droplet equilibration are shown in Fig. 68.

The pH played a major role on the success of nucleation events and the exploitation of catalase macromolecules to grow crystals. Up to pH 6.5, at both protein concentrations tested, many plate-like crystals were observed. When the pH was raised, a transition from crystalline sheets to more compact habits was detected. At intermediate pH of 7.0, rod-like crystals were observed, which evolved towards iso-dimensional crystals at higher pH. Such a trend very closely resembled that of HEWL, discussed in § 9.4.

It was concluded from HEWL and catalase VD trials that pH tuned the aspect ratio of protein crystals, and that the increase in pH led to more compact crystal habits. This latter aspect was accompanied by the destabilization of the system after crystallization had occurred. Fig 68 (d), (e), (i), and (j) show the concomitance of catalase crystals and phase separation events. Such an insight revealed that under high pH conditions, i.e., 7.5 and 8.0, catalase crystallization preceded protein segregation into another phase. This two-step temporal evolution of the system reflected the scarce affinity of the protein towards basic crystallization conditions.

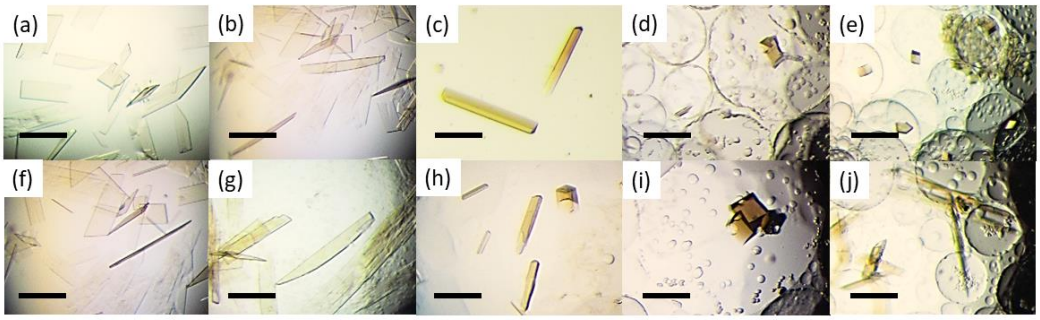

Figure 68 Representative catalase crystals grown at increasing pH. The first row refers to 1.8 mg/mL of protein and pH equal to (a) 6.0, (b) 6.5, (c) 7.0, (d) 7.5, and (e) 8.0. The second row refers to 2.4 mg/mL of protein and pH equal to (f) 6.0, (g) 6.5, (h) 7.0, (i) 7.5, and (j) 8.0. Phase separation was observed for experiments performed at pH 7.5 and 8.0. The scale bar is 500 μm.

9.7 Crystallization of catalase at different pH on THIOL SAMs

In a parallel fashion to the experimental set designed for HEWL, the crystallization of catalase at altered pH was implemented in *mushrooms*, with and without the presence of a foreign surface. The protein crystallization was studied on *mushroom* glass and on THIOL SAMs. The preliminary investigation of the nucleation phenomena on functionalized surfaces evidenced an inhibitory effect provided by THIOL SAMs, as discussed in § 8.4.2. This inhibition was overcome when high supersaturation conditions were implemented.

In this scenario, the selection of THIOL SAMs for the study of pH-altered crystallization on a model surface might seem counterproductive. This type of surface functionalization would require higher supersaturation conditions to be investigated, lowering the extent of interaction between the protein and the surface. However, despite representing a challenging case-study, THIOL SAMs are very interesting from a nucleation point of view. In the considered pH window, thiol groups experience a shift in their protonation state. Below pH 7.0, the degree of protonation increases. Above pH 7.0, the thiol groups would be in their fundamental state, without exposing net charges.

The catalase concentration was increased to 3.7 mg/mL to counteract the inhibitory action of THIOL SAMs, whereas the precipitation cocktail composition was unaltered. 15wt% PEG4000 was dissolved in milliQ water or in 400 mM K phosphate at defined pH to be used for the reservoir and for the mother precipitant solution of the drops, respectively. The crystallization outcome was first evaluated in terms of nucleation kinetics, reported in Tab. 31.

Table 31 The nucleation time of catalase on mushroom glass and THIOL SAMs, as observed at different pH. The total volume drop was 6 μL.

pH	Nucleation time on mushroom glass	Nucleation time on THIOL SAM
6.0	5 days	3 days
6.5	1 day	12 hours
7.0	12 hours	12 hours
7.5	12 hours	12 hours
8.0	12 hours	12 hours

Nucleation occurred very fast both on mushroom glass and SAMs for pH above 7.0. Differences in nucleation kinetics emerged only at lower pH, enlarging the temporal window needed to observe the first crystals in the drops. The effect was maximized at pH 6.0, where a two-day difference in nucleation time was detected. In these conditions, it was evident that the inhibitory effect previously reported for THIOL SAMs overturned in an inducing effect. Further insights into these apparently contradictory results were gained from the optical micrographs of the crystals, shown in Fig. 69. At neutral and basic pH, no substantial differences were noticed in the crystal populations grown on *mushroom* glass and SAMs, as expected since the time range for nucleation resulted to be the same for both surfaces. However, when a slightly acidic pH of 6.0 was tested, the crystallization outcomes on *mushroom* glass and SAMs showed some differences. The enhanced nucleation kinetics on THIOL SAMs was related to the appearance of tiny and less elongated crystals in the

drops. After a few days, these nucleation events were followed by the formation of sheet-like crystals of catalase, as can be seen in Fig. 69 (f). On the *mushroom* glass, instead, the population of crystals was dominated by sheet-like crystals, Fig. 69 (a). All the evidence pointed out a peculiar action promoted by the surfaces at more aggressive supersaturation conditions. It was hypothesized that thanks to the electrostatic repulsion promoted by the THIOL SAMs, occurring only at acid pH, the catalase macromolecules were concentrated in the bulk of the drops. Initially, at high supersaturation, the repulsion favored homogeneous nucleation events leading to tiny crystals. Then, when supersaturation dropped, the formation of single and giant sheet crystals occurred next to the surface. This second step was not related to a favorable interaction with the surface but just to the non-specific lowering of ΔG for nucleation promoted by a foreign interface.

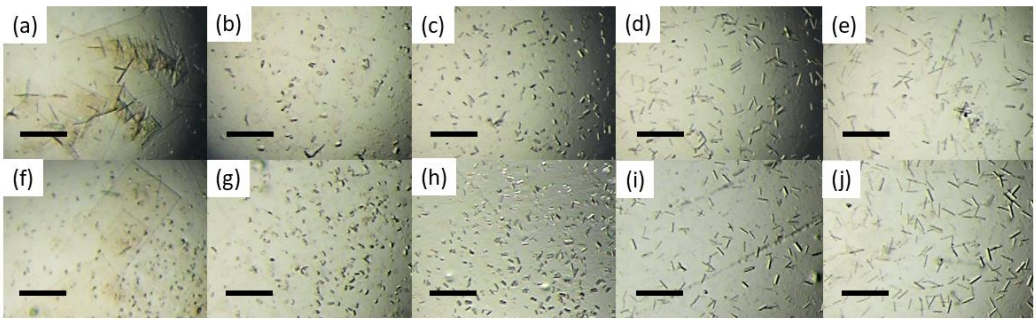

Figure 69 Representative catalase crystals grown at increasing pH. The protein concentration was 3.7 mg/mL. The first row refers to drops deposited on *mushroom* glass and pH equal to (a) 6.0, (b) 6.5, (c) 7.0, (d) 7.5, and (e) 8.0. The second row refers to drops deposited on THIOL SAMs and pH equal to (f) 6.0, (g) 6.5, (h) 7.0, (i) 7.5, and (j) 8.0. The scale bar is 500 μm.

The presence of THIOL SAMs showed beneficial effects in terms of nucleation kinetics at low pH. Moreover, the test of crystallization conditions corresponding to higher supersaturation than those employed in HDVD screenings led to the absence of the phase separation phenomena described under basic conditions.

9.8 Final remarks

In Chap. 9, the effect of pH on the crystallization of proteins was analyzed. It turned out that the surface charge of the protein had a major role in governing the aspect ratio of the crystals at different pH. The pH-altered crystallization of two proteins, HEWL and catalase, was also implemented on surfaces. SAMs were integrated to study the cross influence of charge screen on the protein and on the surfaces. For HEWL, the crystal density followed a “bell-like” tendency according to pH, being maximized at pH 5.0. In these conditions, THIOL SAMs raised the number of crystals obtained in the drops by an order of magnitude, confirming its strong activity towards HEWL nucleation. For catalase, a much more complex behavior was observed as a shift in surface charge occurred in the considered pH window.

In conclusion, despite the very limited amount of works reported in literature dealing with detailed studies on crystallization with altered pH, it has been demonstrated that pH plays a pivotal role in protein crystallization. It may be used to control the number, the size,

and the shape of crystals. Moreover, the careful tuning of pH may help in working with the protein solution more efficiently and increasing the probability of getting good quality crystals.

References

Durbin, S. D., & Feher, G. (1996). Protein crystallization. *Annual Review of Physical Chemistry*, **47**(1), 171–204.

Forsythe, E. L., Judge, R. A., & Pusey, M. L. (1999). Tetragonal chicken egg white lysozyme solubility in sodium chloride solutions. *Journal of Chemical and Engineering Data*, **44**(3), 637–640.

Grigsby, J. J., Blanch, H. W., & Prausnitz, J. M. (2001). Cloud-point temperatures for lysozyme in electrolyte solutions: Effect of salt type, salt concentration and pH. *Biophysical Chemistry*, **91**(3), 231–243.

Grimbergen, R. F. P., Boek, E. S., Meekes, H., & Bennema, P. (1999). Explanation for the supersaturation dependence of the morphology of lysozyme crystals. *Journal of Crystal Growth*, **207**(1), 112–121.

Kuehner, D. E., Heyer, C., Rämsch, C., Fornefeld, U. M., Blanch, H. W., & Prausnitz, J. M. (1997). Interactions of lysozyme in concentrated electrolyte solutions from dynamic light-scattering measurements. *Biophysical Journal*, **73**(6), 3211–3224.

McPherson, A., & Cudney, B. (2014). Optimization of crystallization conditions for biological macromolecules. *Acta Crystallographica Section F:Structural Biology Communications*, **70**(1), 1445–1467.

Nadarajah, A., Li, M., & Pusey, M. L. (1997). Growth mechanism of the (110) face of tetragonal lysozyme crystals. *Acta Crystallographica Section D: Biological Crystallography*, **53**(5), 524–534.

Norrman, M., & Schluckebier, G. (2007). Crystallographic characterization of two novel crystal forms of human insulin induced by chaotropic agents and a shift in pH. *BMC Structural Biology*, **7**(1), 1–14.

Popova, E., Watanabe, E. O., Filho, P. A. P., & Maurer, G. (2008). Phase equilibria for salt-induced lysozyme precipitation: Effect of salt concentration and pH. *Chemical Engineering and Processing: Process Intensification*, **47**(6), 1026–1033.

Retailleau, P., Riès-Kautt, M., & Ducruix, A. (1997). No salting-in of lysozyme chloride observed at low ionic strength over a large range of pH. *Biophysical Journal*, **73**(4), 2156–2163.

Suzuki, Y., Konda, E., Hondoh, H., & Tamura, K. (2011). Effects of temperature, pressure, and pH on the solubility of triclinic lysozyme crystals. *Journal of Crystal Growth*, **318**(1), 1085–1088.

Yoshizaki, I., Sato, T., Igarashi, N., Natsuisaka, M., Tanaka, N., Komatsu, H., & Yoda, S. (2001). Systematic analysis of supersaturation and lysozyme crystal quality. *Acta Crystallographica Section D: Biological Crystallography*, **57**(11), 1621–1629.

Chapter 10

The crystallization of proteins in gels

10.1 Introduction

In the previous chapters, crystallization was tuned through engineered surfaces. Depending on the final application of the crystals, it can be convenient to grow crystals with the help of 3D systems, such as particles or gels.

Even if protein crystallization is carried out under static conditions, convection may emerge for several reasons. Firstly, the depletion of solute molecules around the crystals can generate buoyancy-driven convection. Secondly, temperature or concentration gradients within the drops can be responsible for interfacial flows known as the Marangoni effect (Provost & Robert, 1991). Lastly, the sedimentation of large crystals also generates convective rolls. The gelification of the medium selected to achieve the crystallization of a protein creates an environment dominated by a diffusive mass transport regime, which is beneficial for the controlled growth of crystals. The precipitation of macromolecules is forced to proceed smoothly as it is governed by the mass transport of the reactants (García-Ruiz et al., 2001), which in turn is a function of the gel pore size and distribution, and molecular size of the species involved in the process (Gutenwik et al., 2004). The introduction of foreign material, i.e., the gel itself, but also residual monomers, reaction by-products, or impurities, must be carefully evaluated. An analogous environment for protein crystallization can only be established under microgravity conditions encountered in space (McPherson & Delucas, 2015).

Gels may act as promoters or inhibitors of the nucleation of proteins. Nucleation density can be limited by silica gels or enhanced inside the large channels of agarose gels (Provost & Robert, 1991). Pioneer studies of protein-gel interactions carried out with small-angle neutron scattering (SANS) pointed out a strong dependence of nucleation on the kind of gel precursor. On the one hand, the charged (sulfate) or hydrophobic (methyl) moieties of the agarose gel network did not interact with lysozyme molecules (Vidal et al., 1998a). On the other hand, strong electrostatic and hydrogen bonding interactions were responsible for the adsorption of lysozyme on the surface of silica gel, thus reducing its nominal concentration in solution and preventing nucleation (Vidal et al., 1998b).

The results presented in this chapter have been partially published in (Artusio et al., 2020b).

Agarose, silica, poly(ethylene oxide) (Choquesillo-Lazarte & García-Ruiz, 2011), PEG-crosslinked hydrogels (Gavira et al., 2014), lipidic phases, and cellulose derivatives (Mirkin et al., 2005) are few examples of gels that have been tested in the frame of protein crystallization. The incorporation of the fibers within the crystal has been used to build reinforced crosslinked enzyme crystals (Gavira et al., 2013), self-healing crystals with integrated polymer networks (Zhang et al., 2018), conductive protein crystals incorporating single-walled carbon nanotubes (Contreras-Montoya, et al., 2019a), and to protect the protein sensitive groups such as disulfide bonds and methionines (Contreras-Montoya, et al., 2019b). Moreover, it has been demonstrated that the incorporation of fibers does not affect the diffraction-quality of the crystals since they are randomly distributed within the crystalline latex (Gavira & García-Ruiz, 2002). Agarose is certainly one of the most investigated media, as demonstrated by its applications as a simulating medium for biomineralization (Yin et al., 2019), selector for polymorphism (Song et al., 2020), facilitator of soaking of different molecules such as ligands, co-factors, cryo-protectants, and heavy atoms (Gavira et al., 2002; Sugahara, 2014; Sugiyama et al., 2015). A phase transition from needle to polyhedral crystals leading to unusual patterns, a phenomenon known as the Morse code effect, was also studied in agarose gels (Lisgarten & Marks, 2018).

The general focus of the present thesis regarded the identification of tools for the control of crystallization. In this context, it was hypothesized that gels could be used for this purpose. In Chap. 10, a preliminary investigation on the use of silica and agarose gels is presented. Two model proteins were selected, depending on the gel chemistry. On the one hand, lysozyme was crystallized in silica gels because its optimal crystallization conditions require slightly acid pH (4.5). The gelification kinetics of the silica precursor depends on the solution pH and is enhanced by setting acid conditions. The choice of lysozyme as a model protein ensured that the gelification time was smaller than the nucleation time. On the other hand, proteinase K was crystallized in agarose gels. As already discussed in the previous chapters, proteinase K crystallizes very well, leading to well-faceted crystals, but it has a narrow metastability zone. Such a feature made very difficult the study of crystallization on SAMs because of the “on/off” crystallization behavior of the protein. For the study in gel, this may be regarded as the worst-case scenario, but it also represents an optimum benchmark for testing the power of agarose.

10.2 Materials & Methods

10.2.1 Batch experiments

Tetramethyltrimethoxysilane (TMOS) was employed as the silica precursor. TMOS was first dispersed in 50 mM Na acetate pH 4.5 by mechanical agitation at high speed for about 20 min. Each batch was prepared by adding and mixing HEWL stock solution, Na acetate, TMOS sol, and NaCl stock solution to obtain a final volume of 100 µL. The final conditions of the batches were: 25 mg/mL HEWL, 3wt% NaCl, 0 – 5% TMOS. The order of addition was kept the same for all the batches. In particular, NaCl was the lastly added solution to mix it with the diluted protein + TMOS solution so as to avoid precipitation. The batches were prepared in Eppendorfs and left at room temperature for one day to crosslink the silica

precursor. In a parallel fashion, batches containing only TMOS (1 – 10%) dissolved in acetate were prepared.

Agarose (OmniPur 2120) was purchased from Calbiochem (San Diego, CA, USA). 40 mg/mL of proteinase K were dissolved in 50 mM HEPES pH 7.0 to get the protein stock solution. The final crystallization conditions involved 0.5 M $NaNO_3$ and 50 mM Na citrate pH 6.5. The range of explored protein concentration was 3 – 8 mg/mL. The agarose content was fixed at 0.5wt% for all the experiments. All the solutions were filtered with 0.22 μm pore size syringe filters. The experiments were set up by preparing a 3% (w/v) agarose stock solution. Agarose was weighted in an Eppendorf, milliQ water was added to it and gently mixed with a pipette at room temperature. Then, the Eppendorf was placed on a thermoblock at 95 °C for 10 min to prepare the agarose sol. The temperature was decreased to 45 °C, and all the stock solutions were added to the thermoblock to allow equilibration before mixing. Na citrate, Na nitrate, milliQ water, protein, and agarose stock solutions were added one at a time and carefully mixed after each addition to ensure the homogeneity of the system and the absence of concentration gradients. The order of addition was the same for every sample. Particular care was taken for pipetting agarose. Tips were cut to facilitate dispensing and pre-heated at 45 °C to avoid local cooling of the sol. The prepared volume was 100 μL. Then, 80 μL were transferred to a PCR vial, the system was closed and incubated at 20 °C. Agarose gelification was achieved in less than 30 min. Extreme care was taken to avoid the formation of bubbles in the system. Since the gelification of agarose is very fast, they would remain entrapped in the final gel and alter its uniformity. All the experiments were performed in triplicate.

10.2.2 Counter-diffusion experiments

TMOS was first dispersed in the HEWL buffer by mixing at high speed for about 20 min. The TMOS stock was prepared at double concentration than the desired one in 50 mM Na acetate pH 4.5. All the operations regarding the preparation of TMOS sol were carried out avoiding the use of glass. In the meantime, fresh HEWL solutions were prepared at double concentration than the desired one and filtered (pore size 0.22 μm). Then, equal amounts of TMOS sol and HEWL solution were mixed together to achieve a homogeneous solution. The final conditions were 75 mg/mL HEWL and 5 or 10% TMOS. 500 μL of this solution were transferred to a preliminary parafilm-sealed tube with the aid of a syringe. Particular care was taken in order to avoid the formation of bubbles, which would compromise the uniformity of the gel. The gelification of the solution was achieved overnight. Then, 100 μL of 5% TMOS in 50 mM Na acetate pH 4.5 were added on top of the gel to create a ~0.5 cm silica plug. After the plug gelification was completed, 500 μL of 12wt% NaCl buffered in Na acetate were added on top of the gel phase. The system was sealed with parafilm at both ends of the tube and incubated at 20 °C.

10.3 Silica gels: nucleation inhibitors

Silica gels act as inhibitors toward protein nucleation. When the crystallization environment is doped with silica precursors and successively gelled, the nucleation density is strongly inhibited. One of the main limitations in the use of silica gels for protein

crystallization is represented by the strong influence of salts, proteins, and pH on silica gelification.

10.3.1 Batch crystallization in silica gel

The preliminary investigation of HEWL crystallization in silica gel was carried out in batch. Initially, only batches containing TMOS concentration in the range from 1 to 10% in acetate were analyzed to test the physical aspect of the crosslinked silica. In the 1 – 3% TMOS range, the samples showed a liquid-like behavior. At 4% the samples started to show resistance to flow, which was more and more evident as 10% was approached. After the gelification, all the samples were transparent, which made them potentially suitable for crystallization studies.
After the assessment of TMOS gelification, HEWL crystallization in gelled silica batches was investigated. The addition of protein and salt to the system was found to be detrimental to the formation of transparent and uniform gels. TMOS ranged from 1 to 5% and, even with the minimum silane content, massive flocculation of silica was observed. The extent of flocculation increased with the amount of TMOS in the system, as shown in Fig. 70.

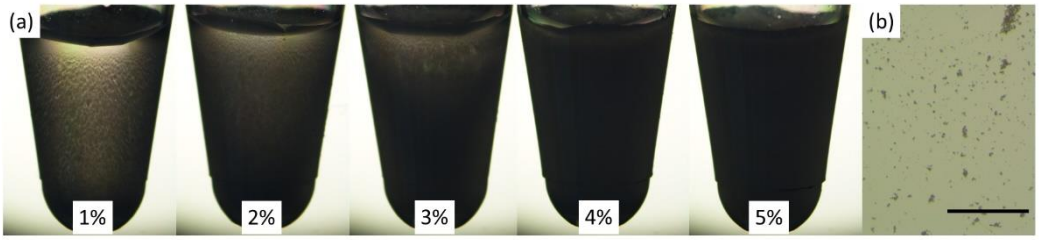

Figure 70 (a) The increasing TMOS concentration, as indicated by the labels, studied in batches containing 25 mg/mL HEWL and 3wt% NaCl in 50 mM Na acetate buffer pH 4.5. (b) Magnification of flocculated silica. The scale bar is 500 µm.

In order to identify the chemical species that hindered the formation of the silica gel network, the previous conditions were replicated in two sets of experiments: the first one without the addition of NaCl and the second one without the addition of HEWL. Results showed that, given that all the other variables of the two sets of experiments were unaltered, the interaction between HEWL and TMOS led to matt gels. When TMOS and salt systems were considered, undisturbed gelification occurred, and transparent gels were obtained. Thus, the chemical interaction between the silica precursor and the protein led to the uncontrolled aggregation and flocculation of silica. Additional experiments were carried out in batch involving decreased concentrations of HEWL (20, 15, and 10 mg/mL) and 5% TMOS to test whether less protein content could avoid interference with the gelification of silica. Unfortunately, flocculation was always observed. These pieces of evidence pointed out that the strong interaction between gel and protein was a stringent limitation on the design of HEWL batch crystallization in silica gels.

In this perspective, additional trials were performed with lower TMOS concentration and higher protein and salt concentration. The tested HEWL concentrations were 75 and 100 mg/mL, in 2% TMOS and 7wt% NaCl. Such an experimental choice was dictated by the need to deal with highly supersaturated batches, which corresponded to increased protein and salt concentrations, to counteract the inhibiting action of silica. At the same

time, the extent of interaction between protein and silane was stemmed by reducing TMOS content. Under these conditions, the flocculation of silica was observed, as expected, but protein crystallization was forced too. In samples involving 75 mg/mL HEWL, shown in Fig. 71 (a), some protein crystals appeared embedded in a partially flocculated silica matrix. Even if HEWL strongly interacted with silica, it was possible to grow single and well-faceted crystals. When HEWL concentration was increased to 100 mg/mL, Fig. 71 (b), tetragonal crystals were not obtained anymore. Crystalline micro-domains of acicular crystals, indicated by the red arrows, were only detected, suggesting a reduced affinity between the protein and the environment of crystallization.

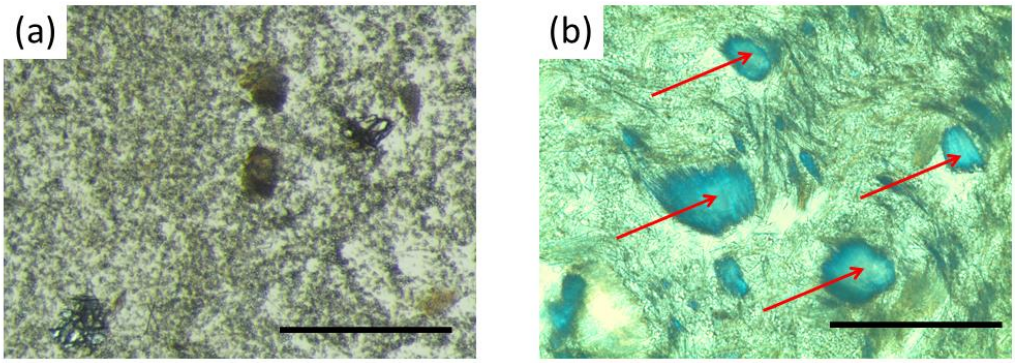

Figure 71 Optical microscope images of HEWL batch crystallization in silica gels. The conditions were (a) 75 mg/mL HEWL, 7wt% NaCl, 2% TMOS and (b) 100 mg/mL HEWL, 7wt% NaCl, 2% TMOS. The scale bar is 500 µm.

The preliminary study of HEWL in silica gel according to the batch technique emphasized major limitations rising from the non-ideal coupling of crystallization medium and crystallization technique. Single HEWL tetragonal crystals could only be grown in a tiny window of crystallization conditions including silica gel. In order to overcome these limitations, the counter-diffusion technique was applied to silica gels. Such a coupling would guarantee the set-up of concentrated crystallization experiments and the exploration of a wide area of the protein phase diagram.

10.3.2 Counter-diffusion crystallization in silica gel

The schematic representation of the counter-diffusion (CD) experiments is sketched in Fig. 72, together with two tubes prepared with 5 and 10% TMOS. The nucleation of HEWL resulted to be strongly inhibited by the presence of silica gel. Only one and two crystals were obtained inside gels referring to 10 and 5% TMOS, demonstrating that the increase in silica concentration was deleterious for the nucleation step. On the other side, crystals grew big and, after a month, reached even 0.4 cm in length. The growth of crystals inside gels is governed by diffusive phenomena, avoiding the disturbances caused by convective flows which would compromise the growth of good quality crystals. Moreover, protein crystals grown in silica gels incorporate the silica fibers, resulting in reinforced crystals. Such a feature increases their stability toward external factors, minimizing the possibility of breakage during manipulation. Shocks deriving from changes in osmotic pressure, vibrations, and manipulation with tools are strongly mitigated by the presence of silica.

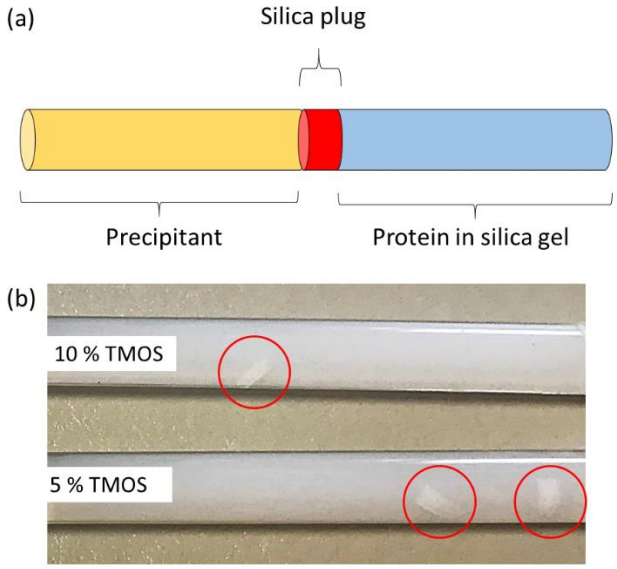

Figure 72 (a) Schematic representation of CD carried in tube. The gelled protein solution and the precipitant solution are separated by a silica plug (5% TMOS in protein buffer). (b) The protein + silica gel compartment of two tubes prepared with 5 and 10% TMOS. The red circles highlight the presence of crystals.

The growth of crystals inside silica gels represents a convenient strategy for the preparation of crystals for neutron diffraction analyses. Such a technique requires large, i.e., above 1 mm, and good quality crystals, and this represents one of its main limitations. The growth of protein crystals in conventional media is subjected to a series of adverse phenomena. Firstly, the attainment of large dimensions may be impeded by excessive nucleation. Then, large crystals are prone to breakage, impeding the analysis of the crystals even before their harvesting. Lastly, if a crystal was successfully grown and harvested, it would undergo the constant risk for drying and breakage during manipulation. Despite all the limitations concerning sample preparation, neutron diffraction is a very powerful technique to diffract crystals. One of its main advantages regards the minimal damage induced by the neutron beam during the data collection. This non-destructive analysis allows the complete sample recovery and is one of its main advantages. In this perspective, the use of silica gels for the growth of protein crystals overcomes the limitations rising from sample preparation, together with the assurance of good diffraction power of the reinforced crystals. It has been shown that silica does not alter the diffraction of crystals. Therefore, despite the incorporation of silica, the crystalline structure is preserved.

10.4 Agarose gels: nucleation promoters

Agarose gels are composed of inter-connected uncharged linear polysaccharide chains, thus allowing the study of nucleation in the absence of important electrostatics effects. The material is widely used in biologics for electrophoresis and separation processes, but also in food technology and pharmacy. Conversely to silica gels, the agarose gel formation is temperature driven and relies on liquid-liquid phase separation. The agarose sol is initially prepared at high temperatures. Then, the gel is obtained by simply cooling the sol below

its gelling temperature, triggering agarose association into dimers, helixes and finally fibers thanks to hydrogen bonding (Braudo et al., 1991). The whole process follows a nucleation and growth mechanism and typically goes through three stages: induction, gelation, and pseudo-equilibrium (Narayanan et al., 2006; Xiong et al., 2005). Therefore, agarose gels can be regarded as physical, rather than chemical, gel since the phase transition from sol to gel is not triggered by chemical reactions but from a change in physical state (Zhou et al., 2006).

A lot of different types of agarose are commercially available, differing in their gelling and melting temperatures. Such tuning is achieved by modifying the polysaccharide chain with the addition or substitution of specific chemical groups. For example, the addition of methyl or sulfate groups can lower the gelling temperature. Gels may be obtained at temperatures even below 20 °C.

Agarose gels can promote the nucleation step of proteins but can also act as filters to limit the incorporation of impurities (Mirkin et al., 2005; Van Driessche et al., 2008) and parent macromolecules in the crystal lattice (Provost & Robert, 1995). The gel network is beneficial for the clustering of protein macromolecules and could exert a control action over crystallization. However, the mechanism of promotion is still debated and the crystallization process in agarose gel is regarded as a "black-box".

10.4.1 Induction of crystallization at low supersaturation in agarose gels

The first part of the investigation of protein crystallization in agarose gels was devoted to the test of the inducing ability of the gelled medium. A series of crystallization conditions were selected for proteinase K, taking as reference the supersaturation conditions identified with the HDVD experiments presented in § 7.6.3. The low supersaturation region of proteinase K phase diagram was investigated by implementing small protein concentrations, i.e., from 3 to 8 mg/mL.

Proteinase K was crystallized according to the batch technique, and the same conditions were implemented in gel-free and gelled systems. The precipitant composition (0.5 M $NaNO_3$ and 50 mM Na citrate pH 6.5) and, for gels, the agarose content (0.5%) were kept constant, whereas protein concentration was progressively increased. Results are reported in Fig. 73.

Differently from batches involving silica gels, presented in § 10.3.1, the addition of agarose did not lead to separation phenomena, nor altered the system continuity on the macro-scale. The gelled batches resulted perfectly transparent, allowing a clear sample investigation by optical microscopy. Moreover, thanks to the fast gelification of agarose, being completed in less than 30 min, the gelification and nucleation steps were temporally separated. The confinement of the two processes on distinct timescales and the succession of events are vital for the study of crystallization. If nucleation occurred within the same time interval of gelification, the two processes would have inexorably affected each other, and their deconvolution would be impossible. If nucleation occurred before gelification, the outcome of crystallization would be independent of the gel and just be the result of the protein interaction with salts and, maybe, agarose sol. If nucleation followed gelification, then the protein molecules would experience the modification of the medium and undergo different nucleation pathways. The last condition represents the desired set-up of crystallization in gel and the one studied in this thesis.

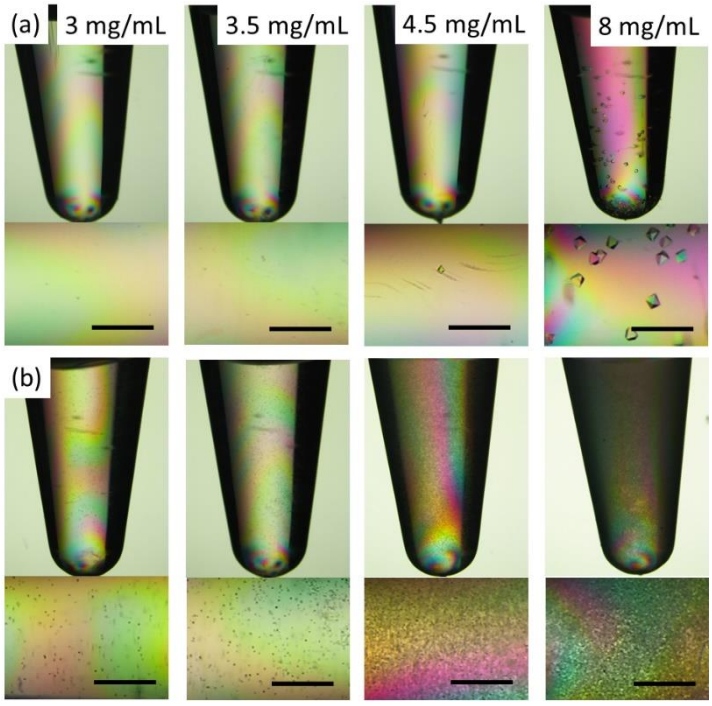

Figure 73 Batch crystallization of proteinase K carried out with increasing protein concentration (3, 3.5, 4.5, 8 mg/mL), 0.5 M $NaNO_3$ and 50 mM Na citrate pH 6.5. Analogous concentrations, reported in the labels, were implemented in (a) gel-free medium and (b) 0.5% agarose gel. Below each Eppendorf an enlarged micrograph is reported. Optical micrographs were collected using polarized light. The scale bar is 500 μm.

The agarose ability in promoting protein nucleation appeared evident at every protein concentration. Most interestingly, it was found that agarose induced the nucleation in conditions that normally would not lead to crystals. At protein concentrations equal to 3.0 or 3.5 mg/mL, a supersaturation level high enough to allow nucleation was not reached in gel-free batches. When 0.5% agarose was added, not only crystals were observed but also the nucleation density was large. Crystals were obtained after 4 days in agarose, whereas the total observation time for gel-free batches was 5 months.

The protein concentration was gradually increased up to the appearance of crystals in gel-free samples in order to identify its threshold value. It resulted that a single crystal of proteinase K was successfully grown at 4.5 mg/mL. On the gel side, this corresponded to higher nucleation density and the shortening of the waiting time to get crystals to one day.

When protein concentration was even higher, up to 8 mg/mL, the nucleation density in the gel-free samples started to increase too. Overall, the increase in protein concentration was reflected by the enhancement in nucleation density, both in gel-free and gelled samples. In the gel-free samples, such an increase was detected only above the threshold value of 4.5 mg/mL, which corresponded to the minimum amount of protein necessary for growing crystals in batch. The presence of agarose gel extended the crystallizability of proteinase K and allowed one to obtain crystals even at very low supersaturations.

10.5 Final remarks

Chap. 10 was devoted to the introduction of protein crystallization in gels. Chemical and physical gel were tested to identify the optimal set-up for designing controlled crystallization experiments. Silica gels strongly interacted with the target protein, HEWL, being responsible for massive flocculation in batch and minimal nucleation probability in CD. In contrast, agarose gel provided an ideal tool for studying the crystallization of another target protein, proteinase K, in diffusive environments. It was demonstrated that agarose could induce protein nucleation even under conditions that did not lead to crystals in gel-free batches. Therefore, agarose gel was selected as an effective platform to tune the nucleation step of proteins, as it will be discussed in the following chapters.

References

Artusio, F., Castellví, A., Sacristán, A., Pisano, R., & Gavira, J. A. (2020b). Agarose gel as a medium for growing and tailoring protein crystals. *Crystal Growth & Design*, **20**(8), 5564-5571.

Braudo, E. E., Muratalieva, I. R., Plashchina, I. G., Tolstoguzov, V. B., & Markovich, I. S. (1991). Studies on the mechanisms of gelation of kappa-carrageenan and agarose. *Colloid & Polymer Science*, **269**(11), 1148–1156.

Choquesillo-Lazarte, D., & García-Ruiz, J. M. (2011). Poly(ethylene) oxide for small-molecule crystal growth in gelled organic solvents. *Journal of Applied Crystallography*, **44**(1), 172–176.

Contreras-Montoya, R., Castellví, A., Escolano-Casado, G., Juanhuix, J., Conejero-Muriel, M., Lopez-Lopez, M. T., Cuerva, J. M., Álvarez de Cienfuegos, L., & Gavira, J. A. (2019a). Enhanced stability against radiation damage of lysozyme crystals grown in Fmoc-CF hydrogels. *Crystal Growth and Design*, **19**(8), 4229–4233.

Contreras-Montoya, R., Escolano, G., Roy, S., Lopez-Lopez, M. T., Delgado-López, J. M., Cuerva, J. M., Díaz-Mochón, J. J., Ashkenasy, N., Gavira, J. A., & Álvarez de Cienfuegos, L. (2019b). Catalytic and electron conducting carbon nanotube–reinforced lysozyme crystals. *Advanced Functional Materials*, **29**(5), 1–10.

García-Ruiz, J. M., Novella, M. L., Moreno, R., & Gavira, J. A. (2001). Agarose as crystallization media for proteins I: Transport processes. *Journal of Crystal Growth*, **232**(1–4), 165–172.

Gavira, J. A., & García-Ruiz, J. M. (2002). Agarose as crystallisation media for proteins II: Trapping of gel fibres into the crystals. *Acta Crystallographica Section D: Biological Crystallography*, **58**(10 II), 1653–1656.

Gavira, J. A., Toh, D., Lopéz-Jaramillo, J., García-Ruíz, J. M., & Ng, J. D. (2002). Ab initio crystallographic structure determination of insulin from protein to electron density without crystal handling. *Acta Crystallographica Section D: Biological Crystallography*, **58**(7), 1147–1154.

Gavira, J. A., Van Driessche, A. E. S., & Garcia-Ruiz, J. M. (2013). Growth of ultrastable protein-silica composite crystals. *Crystal Growth and Design*, **13**(6), 2522–2529.

Gavira, J. A., Cera-Manjarres, A., Ortiz, K., Mendez, J., Jimenez-Torres, J. A., Patiño-Lopez, L. D., & Torres-Lugo, M. (2014). Use of cross-linked poly(ethylene glycol)-based hydrogels for protein crystallization. *Crystal Growth and Design*, **14**(7), 3239–3248.

Gutenwik, J., Nilsson, B., & Axelsson, A. (2004). Effect of hindered diffusion on the adsorption of proteins in agarose gel using a pore model. *Journal of Chromatography A*, **1048**(2), 161–172.

Lisgarten, J. N., & Marks, J. A. (2018). The Morse code effect: A crystal–crystal transformation observed in gel-grown lead (II) oxalate crystals. *Journal of Crystal Growth*, **490**(1), 35–40.

McPherson, A., & Delucas, L. J. (2015). Microgravity protein crystallization. *Npj Microgravity*, **1**(7), 1–20.

Mirkin, N., Moreno, A., Química, I. De, Nacional, U., México, A. De, Exterior, C., & Coyoacán, C. U. (2005). Advances in Crystal Growth Techniques of Biological Macromolecules. *Revista de La Sociedad Química de México*, **49**(1), 39–52.

Narayanan, J., Xiong, J. Y., & Liu, X. Y. (2006). Determination of agarose gel pore size: Absorbance measurements vis a vis other techniques. *Journal of Physics: Conference Series*, **28**(1), 83–86.

Provost, Karine, & Robert, M. C. (1991). Application of gel growth to hanging drop technique. *Journal of Crystal Growth*, **110**(1–2), 258–264.

Provost, K., & Robert, M. C. (1995). Crystal growth of lysozymes in media contaminated by parent molecules: influence of gelled media. *Journal of Crystal Growth*, **156**(1–2), 112–120.

Song, S., Wang, L., Yao, C., Wang, Z., Xie, G., & Tao, X. (2020). Crystallization of Sulfathiazole in Gel: Polymorph Selectivity and Cross-Nucleation. *Crystal Growth and Design*, **20**(1), 9–16.

Sugahara, M. (2014). A technique for high-throughput protein crystallization in ionically cross-linked polysaccharide gel beads for x-ray diffraction experiments. *PLoS ONE*, **9**(4), e95017.

Sugiyama, S., Shimizu, N., Kakinouchi, K., Hiraoka, O., Matsumura, H., Yoshikawa, H. Y., Takahashi, Y., Maruyama, M., Yoshimura, M., Adachi, H., Takano, K., Murakami, S., Inoue, T., Murata, M., & Mori, Y. (2015). Development of protein seed crystals reinforced with high-strength hydrogels. *CrystEngComm*, **17**(42), 8064–8071.

Van Driessche, A. E. S., Otálora, F., Gavira, J. A., & Sazaki, G. (2008). Is agarose an impurity or an impurity filter? In situ observation of the joint gel/impurity effect on protein crystal growth kinetics. *Crystal Growth and Design*, **8**(10), 3623–3629.

Vidal, O., Robert, M. C., & Boué, F. (1998). Gel growth of lysozyme crystals studied by small angle neutron scattering: Case of agarose gel, a nucleation promotor. *Journal of Crystal Growth*, **192**(1–2), 257–270.

Xiong, J. Y., Narayanan, J., Liu, X. Y., Chong, T. K., Chen, S. B., & Chung, T. S. (2005). Topology evolution and gelation mechanism of agarose gel. *Journal of Physical Chemistry B*, **109**(12), 5638–5643.

Yin, X., Griesshaber, E., Fernández-Diáz, L., Ziegler, A., Garciá-Garciá, F. J., & Schmahl, W. W. (2019). Influence of Gelatin-Agarose Composites and Mg on Hydrogel-Carbonate Aggregate Formation and Architecture. *Crystal Growth and Design*, **19**(10), 5696–5715.

Zhang, L., Bailey, J. B., Subramanian, R. H., & Tezcan, F. A. (2018). Hyperexpandable, self-healing macromolecular crystals with integrated polymer networks. *Nature*, **557**(7703), 86–91.

Zhou, J., Zhou, M., & Caruso, R. A. (2006). Agarose template for the fabrication of macroporous metal oxide structures. *Langmuir*, **22**(7), 3332–3336.

Chapter 11

The agarose gel as a tool to design batch crystallization

11.1 Introduction

Agarose gels were proposed as an alternative means to silica gels for growing protein crystals in 1991. Provost and Robert (1991) found that the agarose concentration promoted a linear increase in the nucleation density of lysozyme crystals in the range of 0 – 0.15% (w/v). Contemporaneously, Thiessen (1994) showed that lysozyme nucleation was repressed independently of supersaturation in gels containing more than 0.4% (w/v). Similarly, Tanabe et al. (2009) reported a non-linear relationship between agarose concentration and lysozyme nucleation rate. Induction between 0.2 – 0.4%, inhibition up to 0.8%, and induction again up to 2% were observed.

In this thesis, a rationalization of the effect of agarose concentration on protein nucleation was performed and the application of agarose as a controller for protein crystallization was proposed for the first time. In Chap. 11, various aspects of protein crystallization in agarose gel will be investigated, ranging from the fine-tuning of crystal size and nucleation density to the mathematical modeling of their respective trends as a function of the agarose concentration. Agarose gels will also be proposed not only as a crystal growth medium, but also as a delivery medium for serial crystallography analyses. The versatility of agarose gel as a crystallization medium for proteins and the fine-tuning of crystal properties were demonstrated by considering three model proteins, namely, proteinase K, insulin, and HEWL. Nevertheless, the applicability of agarose gels can be limited by the chemical nature of the precipitants needed for protein crystallization, as in the case of catalase. This aspect will be discussed in Chap. 12.

The results presented in this chapter have been partially published in (Artusio et al., 2020b).

11.2 Materials & Methods

11.2.1 Batch crystallization in PCR vials

Three model proteins were crystallized in batches containing agarose gels. The crystallization conditions are reported in Tab. 32. 6.0 mg/mL of proteinase K in 50 mM HEPES pH 7.0 were crystallized with 0.5 M $NaNO_3$ and 25 mM Na citrate. 5.0 mg/mL of insulin in 25 mM HCl were crystallized with 5 mM $ZnCl_2$, 35.2 Na citrate pH 6.5, and 5% (v/v) acetone. 27.6 mg/mL HEWL in 50 mM Na acetate pH 4.5 were crystallized with 0.75 M NaCl. The agarose gel content was varied between 0 and 1.9% for proteinase K, 2.1% for insulin and HEWL. The maximum agarose concentration was limited by the concentration of the stock solutions, and the dilution factors to be employed to pursue the batch conditions. The stock concentrations, in turn, were calibrated in order to avoid protein precipitation when mixing it with concentrated salt stocks. The order of addition of the species was particularly important and was not varied. Generally, the concentrated protein was first inserted in the system and then diluted with its buffer. Then, precipitants were added, followed by agarose. For insulin, $ZnCl_2$ was directly added to the concentrated protein in order to allow the formation of hexamers. Acetone was added after agarose because of its high volatility. Batches were made of 80 µL of the mixture prepared in PCR vials at 45 °C. As agarose undergoes a thermal gelification, samples were let to cool down to room temperature to achieve the formation of a gel network, following the same procedure described in § 10.2.1. After 1 day, crystals were obtained in all the samples and their average size was measured by analyzing optical microscope images. All the experiments were performed in triplicate.

Table 32 Reference batch crystallization conditions of the three model proteins selected for the study in PCR vials. The protein concentration and buffer, the precipitant cocktail, and the range of agarose concentrations are listed.

Protein	Protein concentration, mg/mL	Protein buffer	Precipitant	Agarose concentration, (w/v) %
Proteinase K	6.0	50 mM HEPES (pH 7.0)	0.5 M $NaNO_3$ 0.025 M Na citrate (pH 6.5)	0 – 1.9
Insulin	5.0	25 mM HCl	5 mM $ZnCl_2$ 35.2 mM Na citrate (pH 7.0) 5 % (v/v) acetone	0 – 2.1
HEWL	27.6	50 mM Na acetate (pH 4.5)	0.75 M NaCl	0 – 2.1

11.2.2 Batch crystallization in flat capillaries

The three model proteins were also employed for the evaluation of the nucleation density as a function of the agarose concentration. The sample preparation followed the same protocol for the batch crystallization in vials, described in § 10.2.1. When the final mixture was obtained at 45 °C, it was loaded inside a pre-heated flat capillary (path length 0.3 mm). The ends of the capillary were plugged with sealing paste and covered with a layer of nail enamel to prevent water evaporation and drying of the gel. The capillaries were incubated at 20 °C and periodically inspected. The length of the capillary was 6 cm and it was divided into 12 segments of 0.5 cm each. Three segments were analyzed per sample, and the position of the selected segments was the same for all the samples. Proteinase K was crystallized under the same conditions as the previous batches in vials. For large agarose concentrations, the nucleation density was very high and the size of the crystals around 10 μm. For these samples, the images of the selected segments were taken at three focal planes and then merged. In this way, all the crystals present in the segment volume could be detected. For gels less concentrated in crystals, the use of a single focal plane was enough to catch all the crystals. As regards insulin and HEWL, milder crystallization conditions were used to grow larger crystals and facilitate the counting process. Crystallization conditions are summarized in Tab. 33. The images were then processed with ImageJ to create a grid whose mesh size was adapted to the size and number of crystals. The crystals were counted in each mesh, their number averaged and then divided by the considered volume to get the nucleation density.

Table 33 The crystallization conditions of the batch experiments in flat capillaries. The protein concentration, buffer, precipitation cocktail, and agarose concentration are reported.

Protein	Protein concentration, mg/mL	Protein buffer	Precipitant	Agarose concentration, (w/v) %
Proteinase K	6.0	50 mM HEPES (pH 7.0)	0.5 M $NaNO_3$ 0.025 M Na citrate (pH 6.5)	0.1 – 1.9
Insulin	4.0	25 mM HCl	5 mM $ZnCl_2$ 35.2 mM Na citrate (pH 7.0) 5 % (v/v) acetone	0.1 – 2.1
HEWL	22.0	50 mM Na acetate (pH 4.5)	0.75 M NaCl	0.1 – 2.1

11.3 Batch crystallization in gelled media

The crystallization of three model proteins in batches containing increasing concentrations of agarose is here discussed. The action of agarose on crystal size provided insight into the mechanism of interaction between protein and gel.

11.3.1 The tuning of crystal size with agarose concentration

Batch crystallization of proteinase K, insulin, and HEWL in gel-free and gelled samples was successfully accomplished. In every case, gelification time was significantly shorter than nucleation time. The samples were studied by optical microscopy, and the results are collected in Fig. 74. Agarose had a key role in the crystallization process. The same crystallization conditions, implemented in systems with different gel contents, led to different crystals populations. The presence of agarose, even at the largest concentrations, did not hinder the formation of good quality and faceted crystals, nor promoted precipitation phenomena. These pieces of evidence further confirmed the suitability of agarose in carrying out nucleation studies in batch, opposite to what had been observed for silica gels.

Gelling the crystallization medium had several beneficial consequences over protein crystallization. The direct comparison of images of crystals grown in the absence of gel to any of those referring to gelled batches pointed out the avoidance of sedimentation promoted by the gel. When crystals grow over a certain threshold size, sedimentation can occur. In gel-free batches, larger crystals tended to sediment at the vial bottom, whereas smaller ones were floating in the liquid. The convective flow generated by the fall of the crystals and their accumulation in the batch bottom very often promote crystal breakage. On the other side, the presence of even minimal amounts of agarose gel, i.e., 0.05 or 0.1%, guaranteed the preservation of the *locus* of nucleation. Big crystals were trapped inside the gel network and could grow up to large size without the risk of damages.

Another beneficial effect promoted by the gel regarded the uniformness of the crystal populations in terms of size, imposing control over the extent of growth of the crystals. Lastly, the diffusive environment created by the gel was ideal for the investigation of nucleation because all the disturbances due to convective flows were excluded.

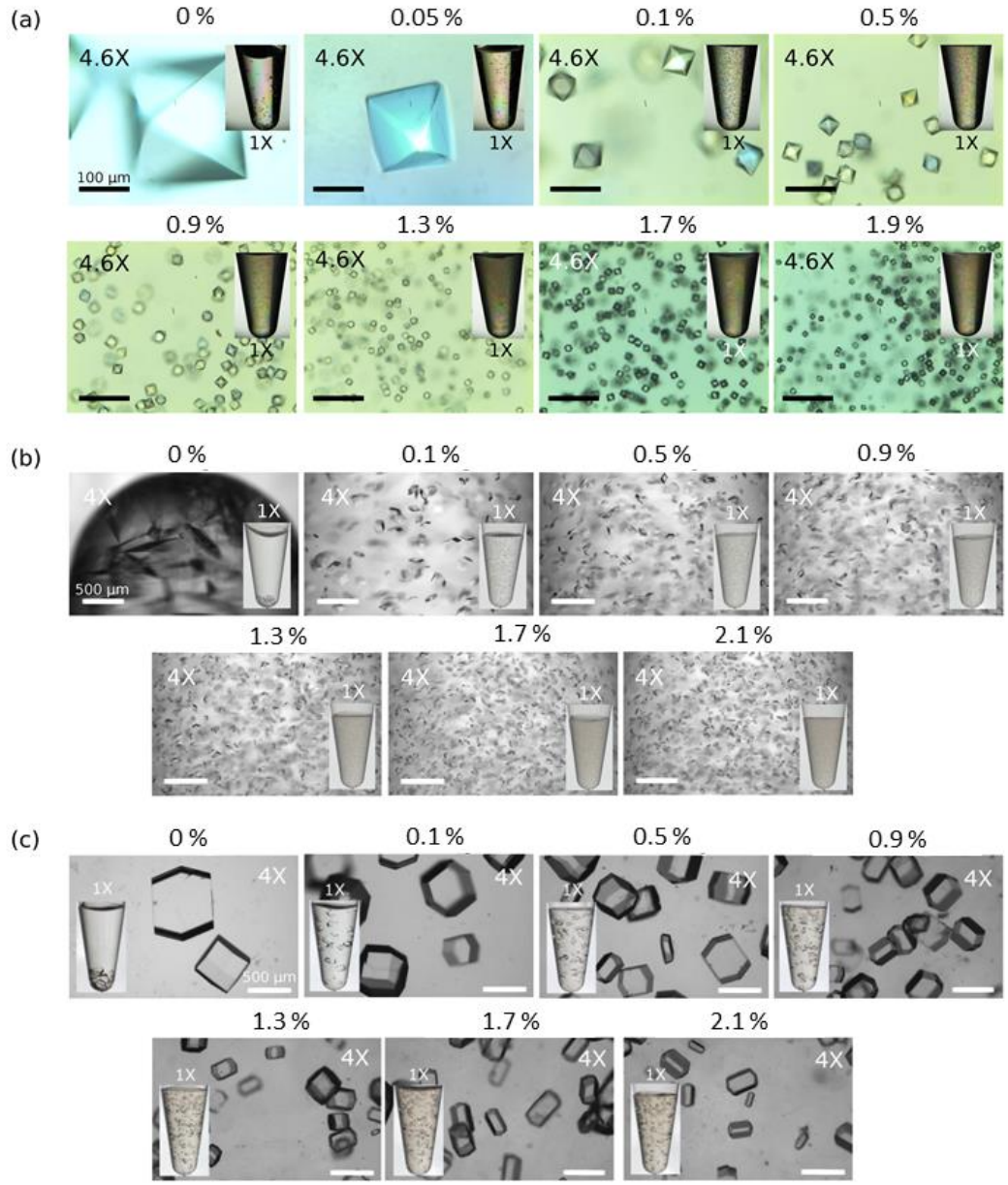

Figure 74 The crystallization of the three model proteins in batches containing agarose gels: (a) proteinase K, (b) insulin, and (c) HEWL. The zoom is directly reported on each image, the scale bar is 100 µm for proteinase K and 500 µm for insulin and HEWL. Embedded in each zoom is the overview of the crystallization batch. The picture was taken from (Artusio et al., 2020b) with modification.

In order to quantitively evaluate the action of agarose on nucleation phenomena, the crystal size at equilibrium was measured. The average values emerged from the analysis of at least 70 crystals per condition. A characteristic length was identified for the three proteins: the distance between the two vertexes of proteinase K bipyramidal crystals, the height of insulin polyhedron, and the width of (110) face of HEWL crystals (corresponding to l_{min}, introduced in § 9.4). Hereinafter, the term "crystal size" will be used to indicate the characteristic length of the crystals for simplicity. The crystal size trend as a function of the agarose concentration in the system is reported in Fig. 75 for the three model proteins.

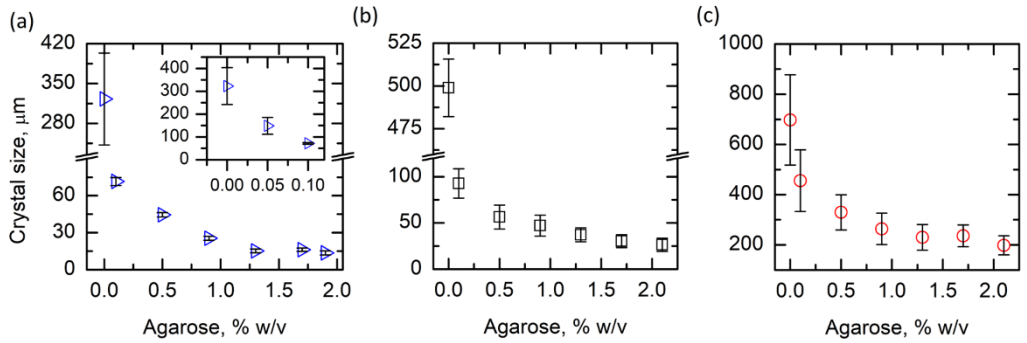

Figure 75 The (a) proteinase K, (b) insulin, and (c) HEWL crystal size as a function of the agarose concentration in the system. Error bars refer to SD. Embedded in panel (a) is the detail of the crystal size trend for agarose concentration < 0.10%. The picture was taken from (Artusio et al., 2020b) with modification.

Without agarose, a few crystals were obtained per sample. Crystal growth predominated over nucleation and, on average, crystals larger than hundreds of µm were observed. However, the crystal size showed major variations among the samples, leading to high SDs. When agarose was added to the crystallization environment, a dramatic effect on crystal size was observed. A fine-tuned dimensional gradient was obtained by increasing the amount of gel in the system. More specifically, the dimension of the crystals was strongly affected up to 1.3% agarose and then reached a plateau. Minimal addition of agarose in the system, such as 0.05% for proteinase K, led to more than 50% reduction in both crystal size and SD if compared to the gel-free conditions. Considering 0.1% for insulin and HEWL, this led to 5-fold and 40% reduction in crystal size, respectively. It has to be noticed that very low amounts of agarose, i.e., 0.05%, are quite difficult to handle in so small crystallization volumes, thus making these conditions more prone to scarce reproducibility or need for more trials. As a general trend, increasing the content of agarose gel was beneficial not only for the reduction of the average crystal size, but also for the monodispersity of the crystal population. Dimensional plateau conditions corresponded to 15 (±1), 26 (±7), and 200 (±38) µm for proteinase K, insulin, and HEWL, respectively. Such a behavior denoted a strong influence of the gel network over the interactions among protein macromolecules, which led to clustering. The presence of a network in the crystallization environment strongly promoted nucleation and was essential for precisely controlling crystal size and narrowing the dimensional distribution of crystals.

The crystals obtained inside the gel for the three model proteins differed in their size. Proteinase K and insulin led to sub-100 µm crystals, whereas HEWL grew larger than 200 µm. Curiously, the crystal size of all the proteins seemed to follow the same trend when agarose concentration increased independently from the dimension of the crystal. This point will be further discussed in the following section.

Agarose gel was able to uniformly distribute crystals all over the batch, avoiding sedimentation and breakage of the crystals. At the same time, the gelled systems provided an ideal platform to tune crystal size in a very fine and reproducible manner.

11.3.2 Mathematical modeling of crystal size

The dimensional data collected for the study of agarose concentration were normalized between 0 and 1. Data referring to gel-free batches were excluded from the analysis. The considered agarose range was 0.1 % - 1.9/2.1%. As can be noticed in Fig. 76 (a), the general trend was found to be the same for the three model proteins. The experimental data were successfully fitted with exponential decay laws ($R^2 > 0.99$):

$$\widehat{l_c} = A_c e^{-\frac{C_{aga}}{B_c}} \tag{19}$$

where $\widehat{l_c}$ was the normalized crystal size and C_{aga} was the agarose content. $\widehat{l_c}$was defined as:

$$\widehat{l_c} = \frac{l_c}{l_{c,max}} \tag{20}$$

where $l_{c,max}$ was the maximum crystal size. A_c and B_c were two fitting parameters, representing the pre-exponential factor and the decay constant, respectively. The values of parameters A_c and B_c for the three proteins are reported in Tab. 34. The fitting of the experimental data confirmed that all the proteins behaved in the same manner. The fitting curves of insulin and HEWL overlapped, whereas proteinase K showed a slight deviation. This finding proved that the action of agarose was independent of both the specific protein and the crystal size obtained.

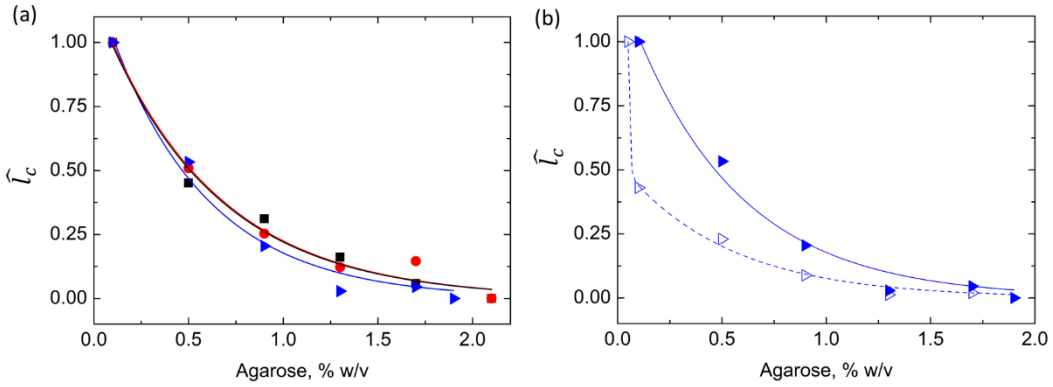

Figure 76 (a) Fitting of the normalized data of crystal size of proteinase K (blue triangle), insulin (black square), and HEWL (red circle) with exponential decay laws. (b) Comparison between the single (continuous line) and the double (dashed line) decay exponential law used to fit crystal size data referring to the 0.1 – 1.9% (full symbols) and the 0.05 – 1.9% (empty symbols) agarose range. Data refer to proteinase K. The picture was taken from (Artusio et al., 2020b) with modification.

Table 34 The fitting parameters of the single exponential decay law used to fit the experimental data of the crystal size vs. agarose gel trend. A_c is the pre-exponential factor, and B_c is the decay constant.

Protein	A_c	SD	B_c	SD
Proteinase K	1.238	0.074	0.515	0.051
HEWL	1.176	0.058	0.605	0.049
Insulin	1.165	0.060	0.601	0.051

An interesting observation could be made considering agarose contents < 0.1%. Considering proteinase K as a case-study, the inclusion of the 0.05% agarose point in the normalization and fitting process required a double-decay exponential law for the accurate description of the tendency:

$$\widehat{l_c} = \mathrm{A_{c1}} e^{-\frac{C_{aga}}{\mathrm{B_{c1}}}} + \mathrm{A_{c2}} e^{-\frac{C_{aga}}{\mathrm{B_{c2}}}} \quad (21)$$

The modification of the fitting curve was remarkable, as reported in Fig. 76 (b). The discrepancy between the two fittings rising from the inclusion of data referring to 0.05% agarose was attributed to the physical behavior of the gel. Below 0.12%, agarose gel is known to behave as a non-Newtonian fluid. Above such a concentration, the gel enters the viscoelastic regime (García-Ruiz, Novella, Moreno, & Gavira, 2001). Therefore, the different tendency highlighted at small agarose concentrations was related to the presence of two different diffusive regimes in the gel physics. For agarose contents lower than 0.12%, the fluid viscosity is mainly responsible for the diffusive transport, whereas, for higher agarose contents, the porous structure becomes predominant. This, in turn, would lead to different extents of interaction between the gel matrix and the protein, which was mirrored by the double exponential decay fitting law. On the one side, in the non-Newtonian fluid region, the agarose fibers are more dispersed, the structure is less compact and more mobile. This kind of "soft" confinement can strongly impact the nucleation step of the proteins, as demonstrated by the sharp decrease in crystal size, but still permits some freedom to the system. On the other side, when the viscoelastic regime is approached and achieved, the conformational movements of the fibers are reduced, and the gel structure is by far stronger. The "hard" confinement promoted by the gel can control more precisely the nucleation step and all the diffusive processes, as demonstrated by minimal deviations in crystal size and higher reproducibility.

11.3.3 Insights into the mechanisms of interaction between gel and proteins

The experimental observations and their mathematical processing provided insights into the mechanism of interaction between the protein macromolecules and the agarose gel. In general, gels can interact physically or chemically with the proteins to promote clustering.

Chemical interactions involve secondary bonding between gel groups and amino acids, with the prevalence of hydrogen bonds. This interaction is protein-specific since it is based on chemical affinity and matching between the two species. For example, silica gels interact chemically with HEWL macromolecules. The silica precursors display -OH groups that are available as hydrogen bond donors. The same groups should participate in the condensation reactions required for building the 3D network. HEWL molecules are supposed to be entrapped in the gel structure, affecting its formation and being not available for clustering. Thus, the nominal supersaturation inside the gel is lower than expected, and nucleation is inhibited. Physical interactions, instead, are not protein-specific as they do not involve the aminoacidic sequence of the macromolecules or the chemical groups of the gel.

Following the discussion introduced in the previous section, a specular trend to the one reported in Fig. 76 (a) has been previously reported for the evolution of the homogeneous nucleation rate of NaCl in aqueous solutions as a function of supersaturation, as obtained

with molecular dynamics simulations (Jiang et al., 2018). This parallelism suggests that the increment in agarose concentration can be assimilated to an increment in the effective supersaturation experienced by the protein in the gel.

The mathematical analysis of the data pointed out the absence of specificity in the action of agarose. The replica of the same experiment with proteins having different molecular weights, charges, aminoacidic sequences, etc., always led to the same trend. Thus, the increase in supersaturation was regarded as the effect of the physical interaction between protein and gel and as the cause of the enhanced nucleation phenomena.

The supersaturation increase was attributed to the entrapment of water inside the double helices of the gel fibers. This would have decreased the activity of water in the whole system, increasing the overall supersaturation. If the solvent displays extensive interaction with the agarose matrix, a decrease in solubility of any solute can be obtained (Velásquez-González et al., 2019). As the fibers are randomly distributed, the effect on the overall supersaturation is the same in the whole system. This could explain why nucleation was initiated at the same time in the totality of the batch and crystals with constant size were obtained. Increased agarose contents led to higher extents of water entrapment and smaller crystals.

A final remark has to be done on the plateau conditions observed for agarose. The inducing ability of the gel resulted to be saturated for agarose concentrations above 1.3%, whatever the protein and the crystallization conditions. At the plateau, agarose forced nucleation to such an extent that all the other effects were leveled off, i.e., decrease in crystal size and increase in nucleation density. This could explain why a further reduction in crystal size was not possible.

In conclusion, the protein molecules in solution experienced a much higher supersaturation than the nominal one and nucleated more easily. The mechanism which promoted this process was identified to be physical and related to the water entrapment inside the gel fibers.

11.4 The design of batch crystallization in agarose gel

For many technological applications the flexibility of the sample preparation technique is of utmost importance. The addition of agarose to the crystallizing environment was demonstrated to be a valid tool to control the nucleation step and tailor the size of protein crystals. In order to extend the potential of the technique, agarose gel was not only proposed as a medium for the controlled growth of crystals, but it was also hypothesized that it could serve as a delivery medium for crystallography analyses. Several aspects had to be considered. On the one hand, constraints on the size of the crystals are imposed by many crystallographic analyses, such as serial millisecond (SMX) and serial femtosecond (SFX) crystallography, and X-ray free electron laser (XFEL) experiments. On the other hand, the amount of gel used for preparing the crystals can limit the applicability of the technique. Thus, the design of the crystallization cocktail was performed. Two parameters were studied, namely the protein concentration and the precipitant concentration, and their influence on crystal size was evaluated. Both parameters were studied at fixed agarose concentrations in order to study their impact separately from that of the gel.

11.4.1 Growth and delivery of crystals for serial crystallography (SX)

One of the major bottlenecks of the crystallographic investigation is the small amount of protein available for growing high-quality crystals for collecting single crystals diffraction patterns. To counteract this limitation, alternative techniques based on cryocrystallography (Garman & Schneider, 1997) or synchrotron radiation (Helliwell & Mitchell, 2015) have been proposed, reducing the size and number of required crystals. In particular, SMX and SFX represent recent techniques for the analysis of protein crystals. The crystalline structure has been commonly studied through single crystals diffractometers. One large protein crystal is cryo-cooled and mounted on the sample holder and the diffractograms are collected at different diffraction planes. On the other side, serial crystallography implemented at synchrotron sources has overcome many of the limitations of the conventional X-ray techniques. Among them, one of the most important ones regards the damage dose per crystal. In serial crystallography, many micro-crystals are analyzed for milli- or femto-seconds. The analysis of a large number of randomly oriented crystals in a flux allows the radiation damage of the crystals to be negligible. The technique can be considered as non-destructive since the crystal structure is determined from the sum of single diffractograms collected on hundreds of randomly oriented crystals, rather than hundreds of diffractograms collected per single crystal.

Besides many advantages, serial crystallography techniques are also burdened by limitations as they require a micro-fluidic injector to govern the flux of crystals entering the chamber, and only micro-crystals can be analyzed. In this perspective, agarose gels could be used for the controlled growth of micro-crystals but also for their delivery at SMX. It was hypothesized that setting low agarose contents and playing with protein and precipitant concentrations could represent a new platform for sample delivery in serial crystallography. The agarose content was set at 0.1% to ensure reproducibility and easy handling of agarose but, most importantly, that the gel was in the non-Newtonian fluid regime. This design would ensure the good flowability of the gel and a higher level of flow control compared to gel-free liquids, thanks to slightly larger viscosity. Higher agarose contents would trigger the transition to the viscoelastic regime, impeding the piping in the micro-fluidic channels. As a general reference, microcrystals suitable for SMX are normally smaller than 25 μm. As previously discussed, at 0.1% agarose, the crystals grew significantly larger than this threshold. In order to reduce the crystal size, the increase in protein and precipitant concentrations was studied.

11.4.2 The increase in protein concentration

The protein concentration represents one of the parameters directly related to the degree of supersaturation in a crystallizing system. The flexibility of the agarose gel technique was first tested by tuning protein concentration at fixed agarose concentrations. In this perspective, a further level of control could be introduced. Proteinase K, HEWL, and insulin were crystallized setting three different agarose contents, 0.5, 1.0, and 1.5%, respectively. In this way, since the action of agarose was demonstrated not to be protein-specific, a wide range of conditions could have been tested, including different crystal size, protein concentrations, and gel contents. The results are collected in Fig. 77.

The smaller protein concentrations derived from the previous study on agarose gradients and were fixed as reference points. The higher protein concentrations corresponded to the achievement of a crystal size reduction larger than 50%. As regards proteinase K and insulin, an approx. 30% increase in concentration led to a halved crystal size, which was below 20 µm. The reduced crystal size was accompanied by a marked increase in nucleation density, as illustrated in Fig. 77 (b) and (c) for proteinase K. A regards HEWL, the crystal size reduction was more important. The protein concentration was increased by almost 50%, and the crystals were 4-fold smaller.

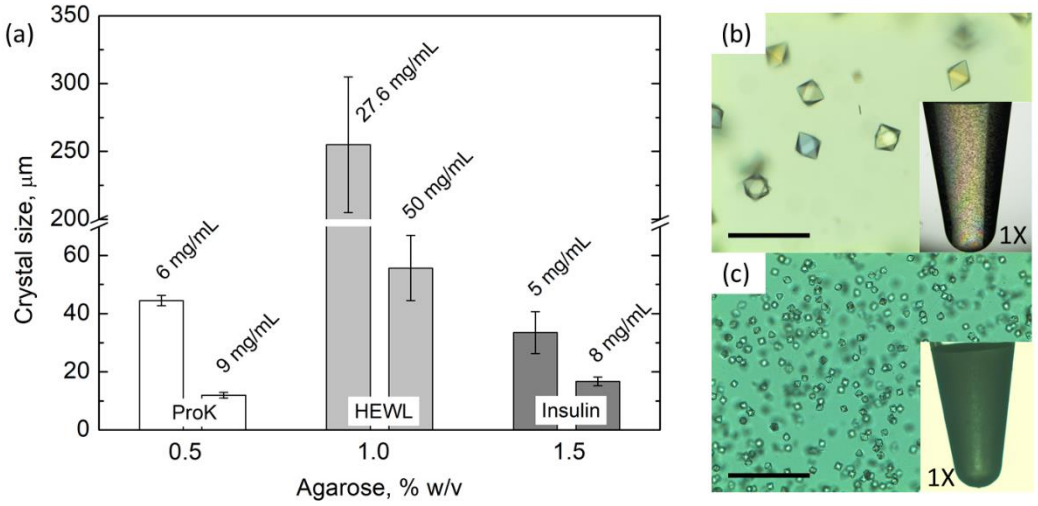

Figure 77 (a) The crystal size obtained with increased protein concentration. Each protein was crystallized at fixed content of agarose: 0.5% for proteinase K (white), 1% for HEWL (light grey), and 1.5% for insulin (dark grey). Optical micrographs of proteinase K crystals grown in 0.5% gel with (b) 6 mg/mL and (c) 9 mg/mL protein concentration. The scale bar is 100 µm. Embedded is the 1X view of the batch. The picture was taken from (Artusio et al., 2020b) with modification.

The tuning of protein concentration was successfully carried out in gelled batches. The same results that would normally be expected in the absence of gel were collected. The nucleation density increased with the protein concentration at every agarose concentration. As a general trend, the crystal size population resulted to be more dimensionally uniform, as revealed by smaller SDs. The synergy between the gel and the increase in protein concentration proved to be a reliable tool to tune the nucleation step and decrease crystal size. Also, this tuning allowed the growth of crystals whose dimensions could have only been achieved with large agarose contents, see plateau conditions in Fig. 75., in less concentrated agarose environments.

11.4.3 The increase in precipitant concentration

The versatility of the technique was also tested by fixing the amount of agarose gel in the system and varying the concentration of the precipitant solution. In particular, the proteinase K concentration was set at 6 mg/mL and the agarose content at 0.1%. The precipitation solution was made of 0.1 – 0.5 – 1 – 2 M $NaNO_3$ and 25 mM Na citrate. The crystal size trend according to the salt concentration is reported in Fig. 78, together with optical micrographs of the crystal population.

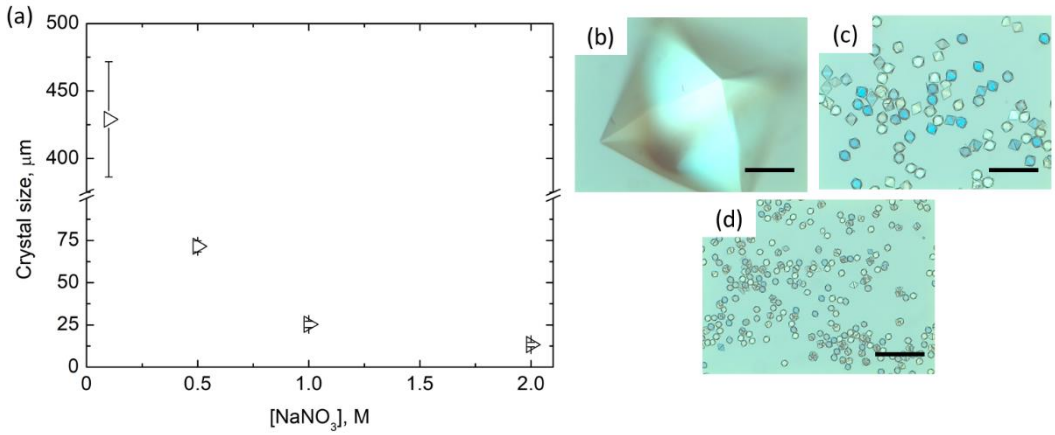

Figure 78 (a) The proteinase K crystal size vs. salt concentration in batch crystallization experiments carried out with 0.1% agarose. The optical microscope images of crystal populations obtained with (b) 0.1, (c) 1, and (d) 2 M $NaNO_3$. The protein concentration was 6 mg/mL and 25 mM Na citrate was used in all the samples. The scale bar was 100 µm. The picture was taken from (Artusio et al., 2020b) with modification.

Lowering the salt concentration in the system down to 0.1 M led to protein crystals of about 430 µm. Compared to the crystals prepared with 0.1% gel and 0.5 M salt, an increase of more than 4 times in crystal dimension was achieved. On the other side, increasing salt concentration was beneficial for the limitation of crystal growth down to 25 and 13 µm for samples involving 1 and 2 M salt, respectively. These conditions are particularly interesting from the perspective of serial crystallography. Such a technique requires high-densely concentrated micro-crystals slurries to carry out femtosecond analyses on a large number of single crystals. In particular, the 0.1% agarose gel condition was selected taking into consideration the transition between two different flow regimes of aqueous agarose gels. Thus, the samples ensured the good flowability required to allow the injection into the microfluidic channel for XFEL. Besides, the crystals showed very good dimensional coherency and reproducibility among the prepared batches. Such evidence confirmed the reliability and robustness of the technique in getting the target crystals.

The tuning of precipitant concentration led to the same trends expected for gel-free batches, as already noticed for the study on protein concentration. Further confirmation of the ability of the agarose network to induce nucleation was obtained. Thanks to its physical action, the real supersaturation in the system was always higher than the nominal one, and this impacted on nucleation. Along this, agarose did not provide side effects during crystallization. In other words, the crystallization of proteins underwent the same rules of the gel-free batch, in an enhanced way.

The design of crystallization inside agarose gel was successfully carried out highlighting the impact of agarose, protein and precipitant concentrations on the nucleation step. The technique was proven to be adaptive and able to meet a wide range of applications ranging from the preparation of microcrystals to large single crystals. The potential of agarose as a growth and delivery medium for a variety of crystallographic techniques, from SMX to neutron scattering has been presented.

11.4.4 Side strategies for obtaining microcrystals for SX

Along with the tuning of protein and precipitant concentration, other strategies were also tested to reduce crystal size while maintaining the medium flowability for SX. On the one hand, the use of a different kind of agarose having a lower gelling point was proposed. On the other hand, the addition of glycerol to the agarose was performed in order to work with high agarose concentrations but keep the gel more liquid-like. Proteinase K was selected as a model to carry out the experimentation.

As regards the use of low melting point (LMP) agarose, the formulation used was the reference one (6 mg/mL proteinase K in 50 mM HEPES pH 7.0, 0.5 M $NaNO_3$, 25 mM Na citrate) and the gel content was set at 1.3%. The amount of agarose was selected considering the crystal size obtained in Fig. 75 with the standard agarose. At 1.3% agarose, the crystal size was approx. 15 µm. Therefore, LMP agarose was believed to have the potential to preserve crystal size but ensure higher flowability of the gel. The lowering of melting and gelling temperatures is obtained by the introduction of methyl and sulphate groups in the polysaccharide chain. Therefore, a different interaction between the LMP gel matrix and the protein must be considered. As a matter of fact, under the same nominal conditions, crystals of approx. 35 µm were grown in LMP gels, Fig. 79 (a). Only a few single and well-faceted crystals could be observed. The majority displayed twinning or the concomitant growth of randomly interconnected crystalline planes. This behavior was attributed to the modification of protein – agarose interactions. Stronger interactions probably due to chemical matching between the side aminoacidic chains of the protein and the dopant group of the LMP gel led to larger crystal size and uncontrolled crystal growth. Such a technique was demonstrated to be inefficient for the growth of good quality microcrystalline slurries, even if the LMP gel displayed a liquid-like behavior.

As regards the inclusion of an additive, i.e., glycerol, into the standard gel matrix, two tests were carried out. The formulation and the overall gel content were the same as the LMP set of experiments. The agarose stock included 10 or 20% (v/v) glycerol. The addition of glycerol restricts the applicability of the technique for sample preparation because not all the proteins are compatible with it. However, its inclusion can increase the flowability of the gel for selected proteins. The samples prepared with 10% glycerol in the agarose stock enabled the preservation of the size of proteinase K crystals which was around 10 µm, Fig. 79 (b). The strength of the gel appeared to be slightly reduced but still not enough to reach good flowability conditions. The amount of glycerol in the agarose stock was therefore doubled, i.e., 20%. In these conditions, crystals were detectably grown after a few days. The strength of the gel was considerably reduced and approached the desired flowability, but the observed crystals grew up to 75 µm, Fig. 79 (c). This phenomenon was attributed to the increase in the protein solubility caused by the presence of an excess of glycerol. As a consequence, it was not possible to reach the supersaturation required to strongly induce nucleation, although the promoting action of agarose. On the one hand, the increase in glycerol was beneficial for getting less strong gels and promote the transition to the liquid regime. On the other hand, glycerol compromised the achievement of a supersaturation level high enough to obtain microcrystals.

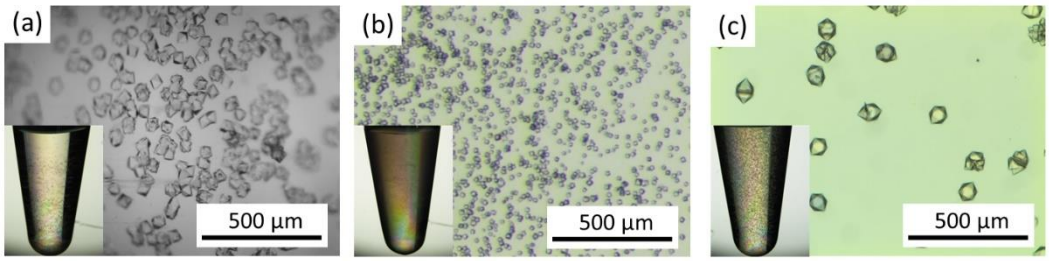

Figure 79 Optical micrographs of proteinase K crystals grown in (a) 1.3 % LMP agarose gel and 1.3 % standard agarose gel with (b) 10 and (c) 20 % glycerol. The scale bar is 500 µm.

The investigation of the two presented alternative routes for the preparation of microcrystalline slurries confirmed that the tuning of the precipitation conditions was the easiest and most efficient approach for getting monodispersed microcrystalline slurries.

11.4.5 Limitations of the technique

The crystallization of proteins in agarose gels represented a reliable technique, provided that sample preparation was carried out rigorously. A monodispersed crystal population was obtained when the nucleation onset was achieved at the same time throughout the sample and after the complete gel setting. Particular care has to be taken during the set-up of crystallization as many parameters can disturb the success of the experiments. Of course, the solutions have to be pre-filtered to avoid the presence of impurities that could trigger undesired nucleation events. The maintenance of 45 °C as the temperature of the mixing step ensures that gelification does not start in this step. The gelification of agarose is a very fast process and, for the type of agarose selected for the study, it begins very few degrees below. Fig. 80 shows the outcome of proteinase K crystallization when the temperature was lowered down to 40 °C for just a few seconds and then immediately brought back to 45 °C. The temperature step was carried out after the addition of agarose. As can be seen, the crystals showed major dimensional variations. At least two distinct populations could be identified. This was an indication that the incipient agarose gelification already triggered the formation of some crystals that were not dissolved by the temperature increase. At the same time, the early formation of some fibers was not fully reversible. Once the total gelification was accomplished, a second nucleation step, the target one, was triggered, and the second population of nuclei was formed.

The effect of temperature on the success of batch crystallization in the gel was even more striking when performing experiments in flat capillaries, Fig. 80 (c) and (d). It can be seen how, after the filling of the capillary with the hot solution, the manipulation of the system with cold tweezers promoted a gradient of crystal size. The localized cool spot had a double effect. On the one hand, it triggered the early and fast gelification of agarose because of the higher ΔT. On the other hand, it increased the local supersaturation since the HEWL solubility decreased. Overall, the supersaturation was pushed both by the gel and the cool spot, and the nucleation density reached its maximum in the area of contact with the tweezers. Moving away from the cool spot, the nucleation density progressively decreased in favor of fewer and larger crystals. The resulting crystals provided a picture of the radial heat distribution.

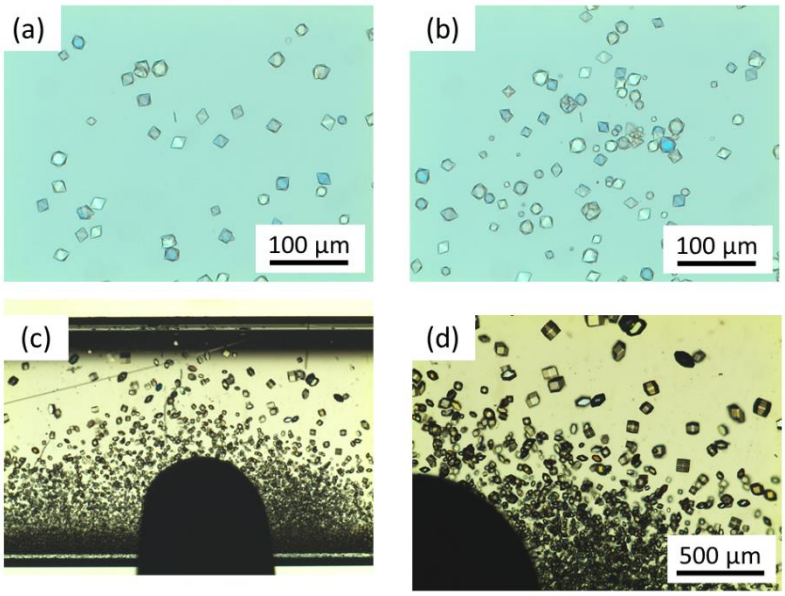

Figure 80 Uncontrolled crystallization of proteinase K in 0.1% agarose gels with (a) 1 M and (b) 2M $NaNO_3$. The protein concentration was 6 mg/mL, and 25 mM Na citrate was used as an additive. (c), (d) The effect of a localized cool spot on batch crystallization of HEWL in flat capillaries.

Overall, the design of agarose was optimized not only in terms of the formulation but also from the preparation point of view. Particular care must be taken when mixing the stock solution and manipulating the samples, and to the maintenance of a uniform temperature inside the batch.

11.5 Evaluation of nucleation density in batch

Rigorously, the ideal parameter that has to be correlated with the agarose content would be the nucleation density, which is obtained by counting the crystals in a defined volume. This represents a very challenging limitation of batch crystallization experiments since it is impossible to precisely count crystals in these systems. However, as the final crystal size mirrors the nucleation events, it was regarded as a good first estimation of the agarose action on nucleation. To tackle nucleation phenomena more rigorously, the batch crystallization was implemented in flat capillaries. Such systems allowed for the direct counting of the crystals, provided that some precautions were taken when carrying out image analysis, thanks to the drastic reduction of the height of the sample. The totality of crystals could thus be visualized by using no more than three distinct focal planes (for the most crystal-concentrated samples) under the microscope.

11.5.1 Crystallization in flat capillaries

The batch crystallization carried out in flat capillaries represents a powerful tool for the experimental estimation of the nucleation density. The agarose gradient was implemented in flat capillaries for the same model proteins of the dimensional study. Fig. 81 collects

representative micrographs of crystals obtained increasing the agarose concentration in batch. Crystallization conditions were selected to cover a wide range of crystal sizes with the three model proteins, ranging from a few to hundreds of µms. The average crystal size increased moving from proteinase K to insulin and HEWL.

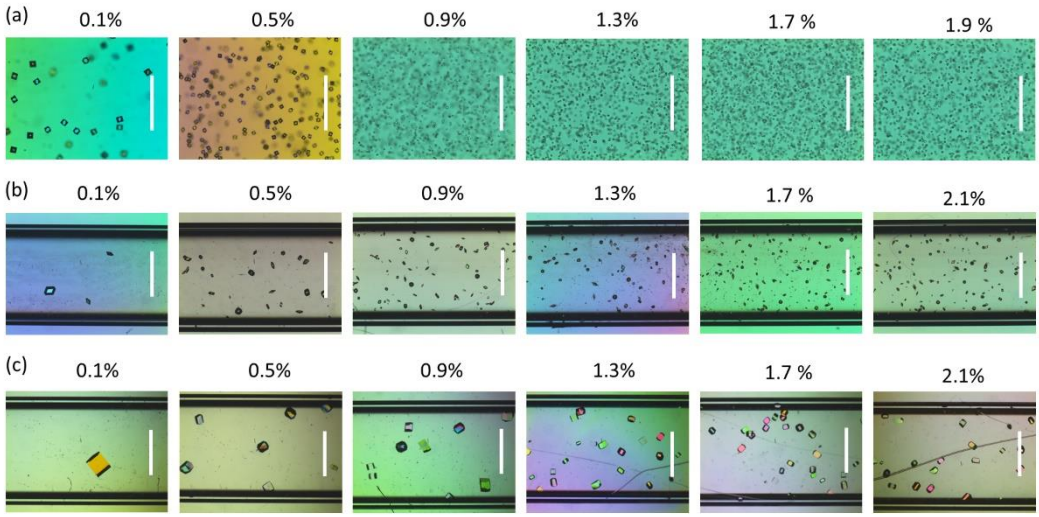

Figure 81 Batch crystallization of (a) proteinase K, (b) insulin, and (c) HEWL in flat capillaries prepared with increasing agarose concentration. The scale bar is 250 µm for proteinase K series, and 500 µm elsewhere.

In order to quantify the number of nuclei obtained in a defined volume the nucleation density, *N*, defined as the number of crystals per mm^3, was introduced. The number of nuclei was confused with the number of crystals since the analyses were performed after all the systems reached the equilibrium. The trends of *N* vs. agarose concentration are reported in Fig. 82. Thanks to the tuning of crystal size, three different order of magnitudes of *N* could have been explored, namely 10^3, 10^0, and 10^{-1} for proteinase K, insulin, and HEWL, respectively. The large window of explored *N* enabled the generalization of the results over a wide length scale, as discussed below.

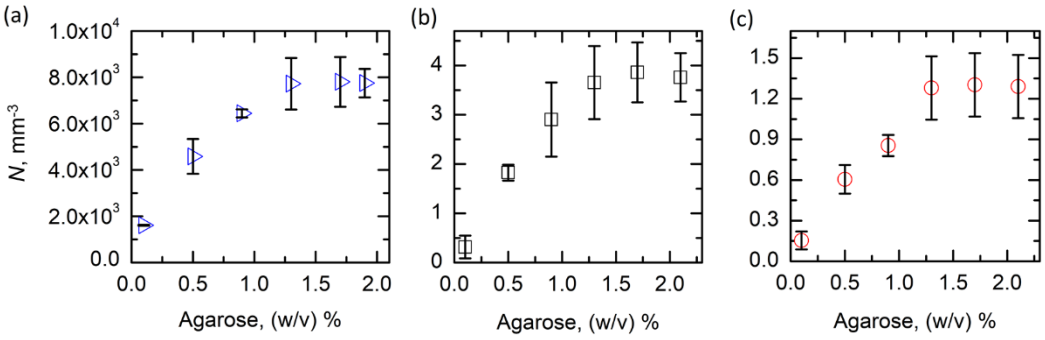

Figure 82 The nucleation density, *N*, as a function of the agarose content for (a) proteinase K, (b) insulin, and (c) HEWL. Error bars refer to SD.

The analyzed range of agarose started from 0.1% since, as observed in § 11.3.2, nucleation in systems with lower gel contents was affected by many factors. Thus, the investigation was carried out in the viscoelastic regime of the gel to avoid the copresence of transitory effects on nucleation deriving from the gel physics. Proteinase K had the highest nucleation density and the smallest crystals. *N* was successfully tuned from 1.8 to

$7.9 \cdot 10^{3}$ crystals/mm^3. Similar behavior was observed for insulin and HEWL, even of the nucleation density was reduced by over than 3 and 4 orders of magnitude, respectively. The results were expected because of the milder crystallization conditions employed for these two proteins. On the one hand, the creation of a data set covering a wide numerical range enabled the generalization of the laws governing the phenomena, as it will be discussed below. On the other hand, dealing with less crystal-concentrated systems made it by far easier and faster the counting of crystals.

Overall, for the three proteins, N sharply increased from 0.1 to 1.3% of agarose, and then stabilized on a plateau for higher gel contents. The statistical dispersion of data was higher at large gel content for all the sets of data, as demonstrated by larger error bars. The analysis of samples having a large number of crystals appeared to be more affected by the sampling method.

11.5.2 Mathematical modeling of nucleation density

In a similar fashion to the modeling of crystal size, the nucleation densities of the three proteins were normalized between 0 and 1, as sketched in Fig. 83 (a). An exponential law ($R^2 > 0.98$) in the form:

$$\widehat{N} = A_N e^{\frac{c_{aga}}{B_N}} \tag{22}$$

was found to give the best fit of the experimental data. $\widehat{N}$ was the normalized nucleation density, defined as:

$$\widehat{N} = \frac{N}{N_{max}} \tag{23}$$

where N_{max} was the maximum nucleation density. A_N and B_N were two fitting parameters, whose values and SD are reported in Tab. 35.

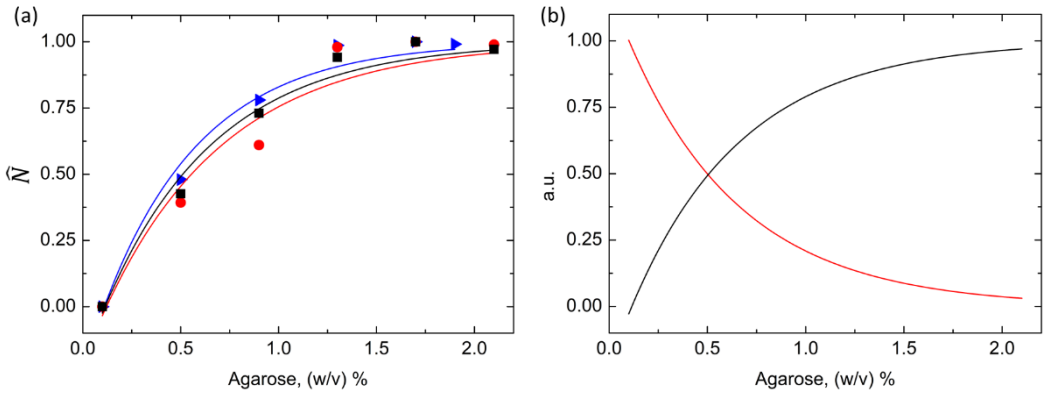

Figure 83 (a) The normalized nucleation density as a function of the agarose content of proteinase K (blue triangle), insulin (black square), and HEWL (red circle). The experimental data were fitted with exponential laws. (b) The normalized crystal size (red curve) and the normalized nucleation density (black curve) vs. agarose content. The parameters of the two curves resulted from the average of the corresponding parameters found for the three proteins.

Table 35 The fitting parameters of the exponential law used to fit the experimental data of the nucleation density vs. agarose concentration trend. A_N is the pre-exponential factor, and B_N is the decay constant.

Protein	A_N	SD	B_N	SD
Proteinase K	1.244	0.083	0.503	0.055
HEWL	1.213	0.133	0.626	0.112
Insulin	1.220	0.080	0.572	0.061

As already noticed for the normalized trends of crystal size, no significant differences were identified among each protein trend. The fitting parameters were again very similar for the three systems. The obtained values of A_N and B_N were in very good agreement with the values of A_c and B_c. Such an evidence confirmed that the effect of agarose on crystal size and nucleation density was the same, and that the two parameters were strongly correlated. The nucleation density followed an opposite trend compared to the evolution of crystal size as a function of agarose. The general laws of the trends were obtained by averaging the fitting parameters and resulted to be:

$$\widehat{l_c} = 1.193\ \mathrm{e}^{-\frac{C_{aga}}{0.574}} \tag{24}$$

$$\widehat{N} = 1.226\ \mathrm{e}^{\frac{C_{aga}}{0.567}} \tag{25}$$

The laws are represented in Fig. 83 (b). As can be seen, the normalized crystal size and the normalized nucleation density mirrored each other and could have been described by analogous laws. The pre-exponential factors and the decay ratio were quasi-identical, meaning that $\widehat{l_c}$ and $\widehat{N}$ underwent the same initial alteration by the gel and reached a plateau at the same agarose content.

This finding demonstrated that the nucleation density and the crystal size are correlated by a linear relationship in gelled media. From a modeling point of view, it enables the *a priori* prediction of the crystallization outcome in gels. Moreover, it demonstrates that the nucleation phenomena in the gel are mirrored by the final crystal size. If the nucleation step is to be investigated, it will be enough studying the size of the crystals, which is by far easier, less time-consuming, and can be carried out in any kind of system.

11.6 Final remarks

Chap. 11 presented the use of agarose gels as tools to fine-tune the protein crystal size in batch. Several model proteins significantly differing in their MW, charge, amino acid sequence, etc. were crystallized with different agarose concentrations to demonstrate the independence of the action of agarose from the protein chemistry. A mechanism relying on the physics of the gel was proposed to justify the nucleation inducing power of agarose thanks to the mathematical analysis of the crystal dimensional trends. A parallel study carried out on the nucleation density confirmed such a hypothesis. Crystal size and nucleation density displayed inverted dependencies on the agarose content, as expected. The versatility of the technique has been highlighted by designing protein and precipitant

concentrations according to the final crystallographic application. Crystals could thus not only be prepared but also delivered using agarose as a medium, potentially covering the full range of application from neutron diffraction to SX. The limitations of the technique have also been pointed out, such as the sensitivity of the preparation technique to temperature and sample manipulation.

References

Artusio, F., Castellví, A., Sacristán, A., Pisano, R., & Gavira, J. A. (2020b). Agarose Gel as a Medium for Growing and Tailoring Protein Crystals. *Crystal Growth & Design*, **20**(8), 5564-5571.

García-Ruiz, J. M., Novella, M. L., Moreno, R., & Gavira, J. A. (2001). Agarose as crystallization media for proteins I: Transport processes. *Journal of Crystal Growth*, **232**(1–4), 165–172.

Garman, E. F., & Schneider, T. R. (1997). Macromolecular Cryocrystallography. *Journal of Applied Crystallography*, **30**(3), 211–237.

Giegé, R., Dock, A. C., Kern, D., Lorber, B., Thierry, J. C., & Moras, D. (1986). The role of purification in the crystallization of proteins and nucleic acids. *Journal of Crystal Growth*, **76**(3), 554–561.

Helliwell, J. R., & Mitchell, E. P. (2015). Synchrotron radiation macromolecular crystallography: Science and spin-offs. *IUCrJ*, **2**(1), 283–291.

Jiang, H., Haji-Akbari, A., Debenedetti, P. G., Panagiotopoulos, A. Z. (2018). Forward flux sampling calculation of homogeneous nucleation rates from aqueous NaCl solutions. *J. Chem. Phys.*, **148**(4), 1–17.

Provost, K., & Robert, M. C. (1991). Application of gel growth to hanging drop technique. *Journal of Crystal Growth*, **110**(1–2), 258–264.

Tanabe, K., Hirose, M., Murai, R., Sugiyama, S., Shimizu, N., Maruyama, M., Takahashi, Y., Adachi, H., Takano, K., Murakami, S., Mori, Y., Mizohata, E., Inoue, T., & Matsumura, H. (2009). Promotion of crystal nucleation of protein by semi-solid agarose gel. *Applied Physics Express*, **2**(12), 12551.

Thiessen, K. J. (1994). The use of two novel methods to grow protein crystals by microdialysis and vapor diffusion in an agarose gel. *Acta Crystallographica Section D Biological Crystallography*, **50**(4), 491–495.

Velásquez-González, O., Campos-Escamilla, C., Flores-Ibarra, A., Esturau-Escofet, N., Arreguin-Espinosa, R., Stojanoff, V., Cuéllar-Cruz, M., & Moreno, A. (2019). Crystal growth in gels from the mechanisms of crystal growth to control of polymorphism: New trends on theoretical and experimental aspects. *Crystals*, **9**(433), 1-23.

Chapter 12

The agarose gel as a tool to design counter-diffusion crystallization

12.1 Introduction

The design of protein crystallization in gelled batches was demonstrated to be a reliable tool for the tuning of nucleation phenomena. The technique is flexible and versatile, as supported by the several investigations carried out on process parameters, such as precipitant and protein concentration, as well as gel content. However, an important limitation comes from the chemistry of the precipitant cocktail.

Some species, such as salts, i.e., ammonium sulfate, and polymers, i.e., PEGs, may strongly interact with agarose, and finally interfere with the gelification process. The success of agarose gelation in presence of different salts has been related to the lyotropic effect, i.e., the Hofmeister series (González-Rámirez et al., 2008). The anion-specific action is known to disturb protein solubility (Ries-Kautt & Ducruix, 1989). During gelation, the preferential adsorption of certain anions on the agarose surface contributed to the stabilization or destabilization of the double helices because of salting-in or salting-out effects, respectively. Inorganic salts as NaCl can stabilize the helices, whereas ammonium sulfate disturbs the proper gelification of the network (Letherby & Young, 1981; Piculell & Nilsson, 1989). Instead, the destabilizing action of polymers like PEG is the consequence of the competition for water molecules. Agarose tends to condensate into a thick precipitate during the gelation step and leads to heterogeneous gels (Charlionet et al., 1996; Crowley et al., 2008).

In this chapter, a variation of the crystallization in batches containing agarose gel is proposed to potentially extend the technique to the entire pool of proteins. In particular, an approach based on counter-diffusion (CD) was explored. The protein was confined inside the gel, whereas the precipitation cocktail represented a separate phase. The precipitant was let to diffuse into the gel, and crystallization was achieved.

The results presented in this chapter have been partially published in (Artusio et al., 2020b).

12.2 Materials & Methods

12.2.1 Compatibility between agarose and precipitants

The gelification of agarose was first investigated in presence of PEGs with different molecular weights or ammonium sulfate. The mixture between agarose and precipitant was prepared following the previously described procedure. Briefly, the agarose stock was prepared at 95 °C and the mixture was prepared at 45 °C in 1.5 mL tubes. The precipitant solutions were freshly prepared and filtered with a 0.22 µm pore size filter. The mixture was cooled down to room temperature, and samples were analyzed via optical microscopy. PEG content was fixed at 30% (v/v) whereas molecular weight ranged from 300 to 8000 Da. Ammonium sulfate concentration ranged from 0.1 to 2 M. Agarose content varied between 0.1 and 2% for $(NH_4)_2SO_4$ experiments and between 0.1 and 1% for PEG experiments.

12.2.2 Batch crystallization of catalase in vials

A preliminary tests of C30 crystallization in gel was carried out in gelled drops. The precipitant and the protein solutions were mixed at 45 °C, agarose was added to the mixture, and 3 µL drops were produced for HDVD. The crystallization conditions were C304 (3.7 mg/mL of protein and 20% PEG4000 as stock solutions) with 0.1% agarose gel. The ratio between protein and precipitant solutions was 1.

Catalase was then crystallized in gelled batches. The protocol for the sample preparation was the same as previously described. Experiments were carried out with 1.8 mg/mL of C30 and 15% PEG4000. 0.1 and 0.5% agarose contents were tested.

12.2.3 Counter-diffusion crystallization in PCR vials

Counter-diffusion experiments were first carried out in PCR vials. Two model proteins which require PEG as a precipitant were selected, namely catalase and trypsin. The former was used to carry out proof-of-concept experiments and, later, to optimize the technique. The latter was implemented for technique validation.

The confinement of catalase crystallization inside gels was a two-step process. The first step involved the gelification of a solution containing catalase and agarose. A 3% agarose stock was prepared. Agarose was dissolved in MilliQ water at 95 ° C for 10 min. The solution was then cooled down to 45 °C. The protein and the agarose solutions were mixed at 45 °C and then 50 µL of solution were pipetted in each PCR vial. The vials were incubated at 20 °C and gelification was achieved overnight. The precipitation cocktail was composed of PEG4000 and 50 µL were added on top of the gel. The schematic representation of the system is illustrated in Fig. 84 (a). Crystallization and/or precipitation of catalase were observed as long as the diffusion of PEG inside the gel proceeded.

Firstly, the catalase concentration was varied to identify the optimal crystallization conditions. The agarose gel content was fixed at 0.5% and PEG4000 at 50% (w/v). It was observed that catalase successfully crystallized in the gel for C30 concentrations equal to 2.5 and 3.0 mg/mL. Smaller concentrations did not lead to crystals.

As a second step, the increase in agarose concentration was investigated. C30 concentration was set at 3.0 mg/mL. Samples were prepared with 0.1, 0.5, and 1.0% gel, without varying the protein and the precipitant concentrations, as well as the ratio between their volumes.

Further investigation was carried out with catalase C40, the less pure source of the protein. Initially, the agarose gel content was set at 0.5%, and C40 concentration was varied between 2 and 60 mg/mL to compare the results. The samples were prepared with the same experimental conditions, involving gel content, precipitant concentration (50% PEG 4000), the volume of gel and precipitant (50 µL), and temperature.

In conclusion, the technique was validated by implementing analogous experiments with trypsin (Sigma-Aldrich). Agarose concentration covered the 0.1 – 1.5% range. Trypsin required 30% (w/v) PEG800 and 0.2 M $(NH_4)_2SO_4$ in its precipitation cocktail. The preparation procedure followed the same protocol. The volumes of the protein + gel phase and the precipitation solution were 50 µL each. The reference conditions of crystallization of catalase C30 and trypsin are summarized in Tab. 36.

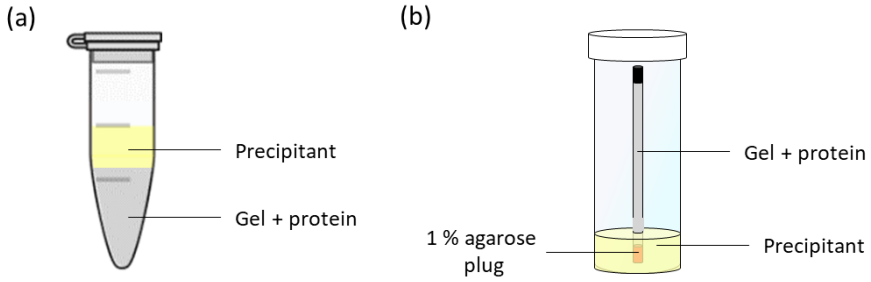

Figure 84 Schematic representation of CD crystallization carried out in batch inside (a) PCR vials and (b) capillary tubes.

In order to quantify the effective protein concentration along the gel, 0.5% agarose gels loaded with 2.5 mg/mL C30 were prepared. The gel was carefully cut into three parts and transferred to pre-weighed vials loaded with 5 µL of MilliQ water. The vials were weighed again to calculate the gel mass loaded into each of them. The gels were incubated in MilliQ for two weeks. The concentration of protein in the incubation medium was measured spectrophotometrically. Knowing the gel mass and the protein concentration in the medium, the C30 concentration in the gel was finally calculated. The experimental procedure is schematized in Fig. 85.

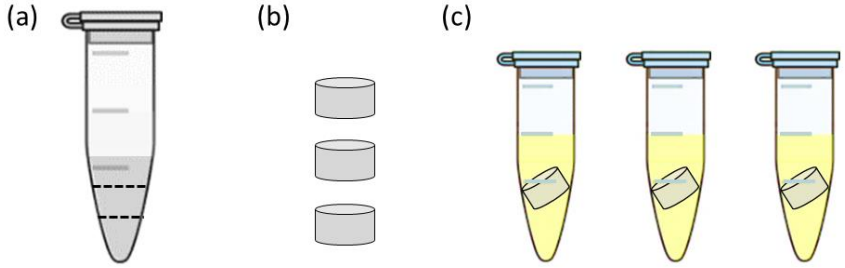

Figure 85 Schematic representation of the procedure used to measure the nominal protein concentration inside the gel. (a) The protein and agarose mixture underwent gelification. (b) The gel was cut into three parts. (c) The three sections were incubated in MilliQ water for two weeks.

12.2.4 Counter-diffusion crystallization in capillaries

CD was also implemented in circular capillary tubes (I.D. = 0.7 mm, Triana Science & Technology, Spain). The tested protein was proteinase K that was crystallized with $(NH_4)_2SO_4$, as reported in Tab. 36. The mixture of agarose and protein was prepared as usual. The hot mixture (45 °C) was loaded inside pre-heated capillaries. One end of the capillary was plugged with 1% agarose, and with a sealing paste at the other end. The capillary was let to cool down at room temperature to achieve gelification. The capillary was then inserted into a vial placing the end containing the agarose plug in contact with 150 µL of 3 M $(NH_4)_2SO_4$, as illustrated in Fig. 84 (b). Capillaries were prepared with varying amounts of agarose, namely 0.1, 0.5, 1.0, and 1.5%.

Table 36 Crystallization conditions used for CD experiments. The crystallization method, the protein concentration and buffer, the precipitant, and the agarose concentration range are reported.

Protein	Crystallization method	Protein concentration, mg/mL	Protein buffer	Precipitant	Agarose concentration, (w/v) %
Catalase C30	Counter-diffusion in PCR vial	3.0	50 mM K phosphate (pH 7.0)	50 % (w/v) PEG4000	0.1 – 1.0
Trypsin	Counter-diffusion in PCR vial	20.2	15 mM HEPES (pH 7.5) 5 mM $CaCl_2$ 5 mg/mL benzamidine	0.1 M HEPES (pH 7.5) 30 % PEG8000 0.2 M $(NH_4)_2SO_4$	0.1 – 1.5
Proteinase K	Counter-diffusion in capillary	25.0	50 mM HEPES (pH 7.0)	3 M $(NH_4)_2SO_4$	0.1 – 1.5

12.3 The incompatibility between agarose and some precipitants

The presence of certain substances including polymers like PEG, or salts like ammonium sulfate, may alter the gelification of agarose, thus hindering the creation of a proper gel network. Nevertheless, PEGs and $(NH_4)_2SO_4$ are commonly employed as precipitants in the field of protein crystallization. Batch crystallization may not be feasible when the interaction between the precipitant and the agarose sol was too strong. On the one hand, the formation of the gel could be altered, and the formation of flocculates could not be

excluded as well. On the other side, the amount of precipitant available for protein crystallization could be significantly lower than its nominal value.

As a first step, the investigation of agarose – precipitant mixtures was carried out to build phase diagrams. To do this, mixtures were prepared with various agarose and precipitant concentrations and the outcome of the gelification step was studied. A map of potentially allowable conditions for batch crystallization was created for PEG and $(NH_4)_2SO_4$.

12.3.1 The PEG case

The system composed of PEG and agarose was first explored. PEGs with different MWs were mixed with the polysaccharide (0.1 – 1.0%), while keeping constant the amount of PEG at 30%. The MWs and concentration of PEGs were selected considering the most commonly used crystallization conditions.

It was observed that the agarose gelification depended solely on PEG MW, and not on agarose concentration. Three different outcomes could have been identified. For low MW PEGs, i.e., from 300 to 400 Da, gelification occurred undisturbed, and homogeneous and clear gels were obtained. For intermediate MW PEGs, i.e., between 600 and 1000 Da, a suspension of agarose fibers was observed. When high MW PEGs were employed, i.e., between 1500 and 8000 Da, the mixture underwent phase separation, and precipitation was observed at the bottom of the tubes.

The interaction of PEG with agarose was found to be exclusively dependent on MW, and not on agarose concentration. In this perspective, protein crystallization in gelled batches may be feasible when low MW PEGs are implemented. When longer PEG chains are necessary to achieve crystallization, the implementation of counter-diffusion techniques is required. The crystallization of proteins requiring PEG4000 and PEG8000 will be presented in § 12.4 and 12.5.

12.3.2 The ammonium sulfate case

Mixtures between $(NH_4)_2SO_4$ and agarose were also investigated. The range of $(NH_4)_2SO_4$ and agarose concentrations were 0.5 – 2 M, and 0.1 – 2.0%, respectively. As with PEGs, the range of explored conditions for ammonium sulfate was selected considering the most commonly performed crystallization screenings.

The results are collected in Fig. 86, where the outcome of the gelification step performed at different agarose and $(NH_4)_2SO_4$ concentrations is illustrated. The phase diagram highlighted three different regions. For $(NH_4)_2SO_4$ concentrations below 0.5 M, the mixtures led to transparent gels, regardless of the agarose content. When $(NH_4)_2SO_4$ concentration was increased to 1 M, gels resulted to be inhomogeneous and not clear, except at 0.1% of agarose. At 0.5% of agarose, aggregation of the polysaccharide fibers was detected. A suspended phase appeared to be entrapped in a matrix still exhibiting a gel behavior (orange). At higher agarose concentrations, massive precipitation occurred at the bottom of the vials (red), and gels did not form properly. Lastly, when $(NH_4)_2SO_4$ concentration was further increased to 2 M, precipitation occurred with every agarose content.

Unlike PEGs, the mixtures between ammonium sulfate and agarose exhibited a strong dependence on the agarose concentration. In general, a low concentration of salt did not hinder agarose proper gelification. The admissible conditions for gelification were progressively restricted as long as the salt and the agarose concentrations were increased.

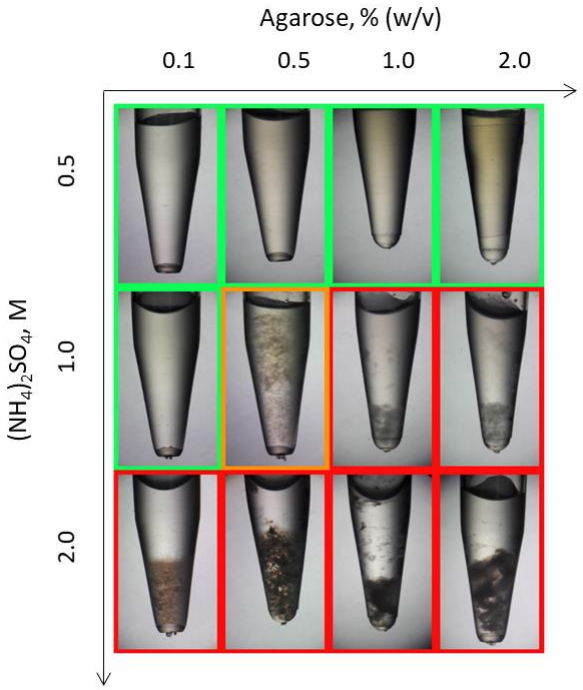

Figure 86 The mixtures between various agarose and ammonium sulfate concentrations. Transparent gels (green), aggregated fibers (orange), and strong precipitation (red) were observed. Image taken from (Artusio et al., 2020b) with modification.

In conclusion, high MW PEGs and concentrated $(NH_4)_2SO_4$ solutions were found to be deleterious for agarose gelification. The shift from batch to counter-diffusion was therefore proposed to extend the crystallization in gelled media to proteins which require the aforementioned precipitants.

12.4 Crystallization of catalase

The counter-diffusion crystallization of catalase was carried out in vials thanks to a two-step procedure. As a first step, the protein was immobilized inside the gel phase. As a second step, the gel was put into contact with the precipitation cocktail which was allowed to slowly diffuse inside the gel matrix. In this way, a wide range of crystallization conditions could be screened within a single experiment.

Preliminary experiments were carried out in gelled drops and vials. Then, the counter-diffusion crystallization of catalase C30 and C40 was explored.

12.4.1 Crystallization of catalase in gelled drops

The crystallization of catalase was first studied in drops containing agarose gels, according to the HDVD method. Such a preliminary screening aimed to test the feasibility of catalase crystallization in gels employing very small amounts of protein. The molecular weight of catalase is around 250 kDa, and this may represent a limitation to the use of agarose gel because of dimensional incompatibility between the protein and the pore size of the gel.

Before implementing CD crystallization, a preliminary test was performed with the help of HDVD with agarose. To verify whether catalase crystallization could be corrupted by the presence of a gel matrix, a trial was carried out with the crystallization condition C304 and 0.1% agarose. Despite the incompatibility between agarose and PEG highlighted in the previous section, precipitation was not observed probably because of the fast gelification of the system due to the micro-volume. Representative optical microscope images of the drops are presented in Fig. 87.

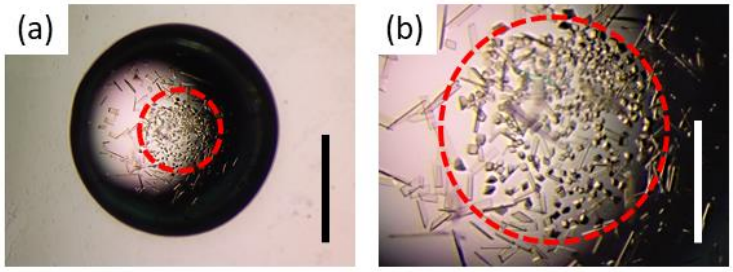

Figure 87 (a) Drop containing catalase crystals grown according to the condition C304 plus 0.1% agarose gel. The circled area encloses the region with tiny iso-dimensional crystals. The scale bar is 1 mm. (b) Zoom of the circled area. Iso-dimensional and plate crystals can be distinguished. The scale bar is 500 μm.

The introduction of agarose into the system modified the nucleation and growth of C30 crystals. Two separated areas could have been identified within the same drop. In the central zone, corresponding to the bottom of the drop, smaller and iso-dimensional crystals were observed. In the upper part of the drop, elongated and plate-like crystals were obtained. Likely, the creation of two distinct crystal populations was due to the formation of a biphasic system inside the drop. The introduction of agarose gel could have promoted the segregation of a highly concentrated gel drop inside the bigger drop. This may be due to different reasons. First, the scarce affinity between PEG and agarose could promote phase segregation. Also, agarose could have been more concentrated in the bottom of the drop. This zone of the drop undergoes faster evaporation, and the mass and heat transport are enhanced because of the higher surface area exposed. The gelification of the concentrated agarose could have been faster in this area, leading to a small, gelled drop. The protein molecules were trapped inside the gel network and crystallized thanks to the diffusion of PEG. The nucleation density was largely higher compared to the other areas of the drops because of the presence of the gel. Control over the crystal size and habit was achieved. As a matter of fact, the crystals grown in the network were dimensionally and morphologically homogeneous. The same protein crystals grown in the absence of gel displayed various habits, and it was not possible to impart reproducible limitations over the growth of each crystal face. Thus, the crystallization of catalase inside a gelled network was demonstrated to be physically possible.

12.4.2 Batch crystallization of catalase

As a step further, catalase was crystallized in gelled batches using mild crystallization conditions. More specifically, 1.8 mg/mL of C30 and 15% PEG4000 were employed. Since catalase required a high MW PEG as precipitant, the trials were carried out keeping the polymer concentration as low as possible. The PEG concentration was by far lower than the one used for the assessment of polymer – agarose interactions, i.e., 30%, to limit the precipitation phenomena. The results are collected in Fig. 88 for 0.1 and 0.5% agarose contents.

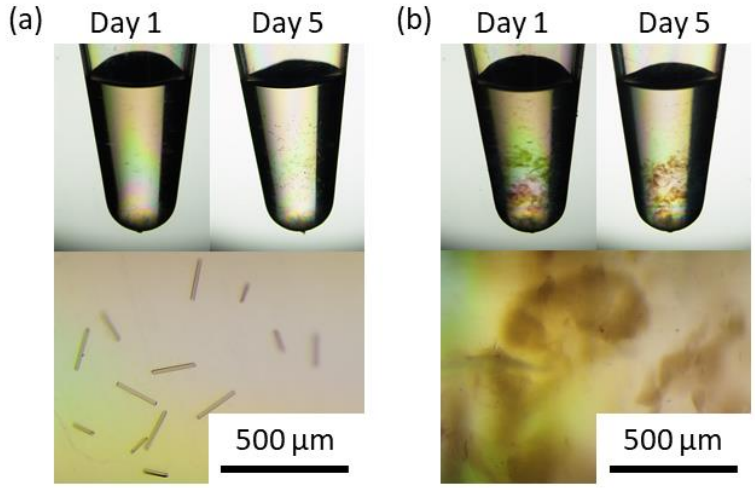

Figure 88 Catalase C30 crystals grown in (a) 0.1 and (b) 0.5% agarose gels. The outcome of crystallization is displayed after 1 and 5 days. Below the vials pictures is reported a zoom relative to day 5.

Due to the mild crystallization conditions, the time needed for obtaining crystals was longer compared to previous batch experiments. The first crystals were observed after 5 days in 0.1% agarose samples, in contrast to 1 day for the older sets. The crystallization of catalase in gelled batches evidenced the unsuitability of the technique when high MW PEGs are to be employed. When the agarose content was above 0.5%, massive precipitation was observed in the system and the gel did not form properly, as highlighted in Fig. 88 (b). The observation was similar to that described in § 12.3.2. It was therefore demonstrated that the drastic reduction in PEG4000 content, namely from 30 to 15%, was not sufficient to prevent the precipitation of agarose fibers. Proper gelification and crystallization were achieved only at very low agarose contents, i.e., 0.1%.

In conclusion, the batch technique was proven not to be reliable with high MW PEGs and medium-high agarose contents. The need to modify the previous batch technique emerged from the preliminary tests of catalase crystallization. In this scenario, the counter-diffusion crystallization in agarose gel was introduced.

12.4.3 Crystallization of catalase in counter-diffusion

The counter-diffusion technique required much more concentrated protein and precipitant solutions, compared to the batch. On the one hand, in the batch technique, all the species, i.e., protein and precipitants, were in the same phase from the beginning of the experiment. On the other hand, when two phases are present as in CD, the species have to undergo mass

transfer and pass from one phase to another. A gradient of concentration has to be created to make this happen. The confinement of protein and precipitant to separate phases established the concentration gradients. Also, the immobilization of the protein inside a gel matrix not only helped its crystallization but also hindered its diffusion in the upper layer of the precipitant solution. In this way, the diffusion of PEG inside the network represented the predominant process responsible for the achievement of proper crystallization conditions. The consequence of the experimental set-up in vials was the creation of a gradient of PEG concentration inside the gel, which, in turn, resulted in a wide screening of different precipitant concentrations within the same sample. At the same time, it was possible to play with the gel content, and study its impact on crystallization.

Both C30 and C40 were crystallized in agarose gel. C30 was crystallized involving very small protein concentrations, whereas C40 was used to carry out a wider screening over protein concentration. The HDVD conditions identified in § 7.6.2 guided the selection of protein and precipitant concentrations for CD crystallization.

12.4.3.1 Crystallization of C30

C30 was first crystallized in CD with 2.5 mg/mL of protein, 50% PEG4000, and 0.5% agarose. It was possible to discern different areas in the gel, as reported in Fig. 89. More specifically, the crystal size and the nucleation density followed the diffusion scheme of PEG4000 inside the gel. Higher nucleation density was observed near the interface with the precipitant solution. A large number of tiny crystals were obtained because of the high precipitant concentration in such an area. Moving away from the interface, the nucleation density decreased, and bigger crystals were grown in zones with less precipitant. The crystal habit shifted from bar-like to plate-like as long as the concentration of the precipitant at the early stage of nucleation decreased. Such an evidence agreed with the preliminary HDVD experiments highlighting a difference in crystal habit related to the amount of PEG.

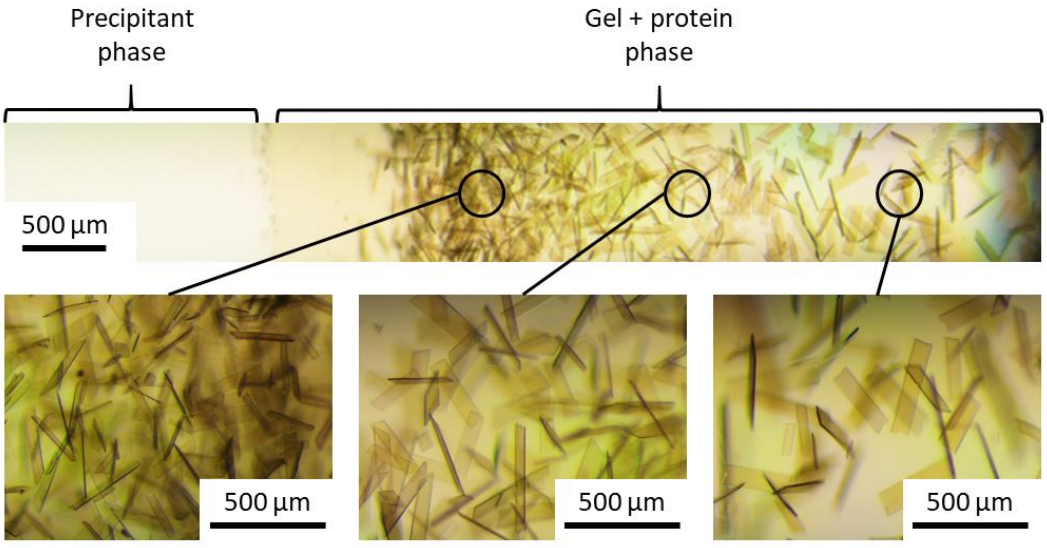

Figure 89 CD crystallization of catalase in 0.5% (w/v) agarose gel. Enlarged micrographs of highlighted areas are reported. The yellowy zone of the vial refers to the gel with immobilized protein, the white one refers to the precipitant solution..

Interestingly, the formation of crystals did not occur directly at the interface between gel and PEG solution, but an empty area was detected. Such a trend was found to be

reproducible and independent of the gel content in the system. The absence of crystals in this area was attributed to a smaller C30 concentration with respect to the target one. In an ideal system, after agarose gelification, one should obtain a homogeneous gel, both in terms of protein and water contents. However, in the real system, when agarose gelification occurs, a sudation of the gel may happen. Because of the formation of the network, some water could be expulsed from the matrix and migrate in the upper part of the gel. In a parallel fashion, the interconnection between the agarose fibers makes them heavier and promotes their sedimentation, trapping protein molecules inside them.

To verify such a hypothesis, a gel was prepared with 0.5% agarose and the same concentration of catalase (2.5 mg/mL). After gelification, the gel was dissected into three parts, and, following the procedure presented in § 12.2.3, the concentration of protein in each part was calculated. As reported in Tab. 37, the concentration of catalase did not result uniform along the gel height but increased from the top to the bottom. The upper layers of the final gel were less concentrated in protein, thus explaining the lack of crystals at the interface. The inhomogeneity of the protein concentration along the gel was related to the gelification step that, in combination with the high MW of catalase, resulted in an accumulation of protein at the bottom.

Table 37 The concentration of catalase along the gel. The protein displayed a concentration gradient moving from the top to the bottom of the vial.

Reference part	C30 concentration, mg/mL
1 (top)	2.34
2 (middle)	2.47
3 (bottom)	2.83

12.4.3.2 CD crystallization with increased agarose concentration

After the proof-of-concept tests carried out with catalase in § 12.4.3.1, CD crystallization was carried out with increased agarose concentrations, as for batch experiments presented in § 11.3.1. The study aimed to investigate whether the design of crystallization could also be carried out under CD conditions. In contrast to batch, CD represents a dynamic environment. The concentration of the various species evolves, and designing the crystallization can be more challenging.

C30 concentration was set at 2.5 mg/mL, and agarose contents equal to 0.1, 0.5, and 1.0% were implemented. The protein and the precipitant concentrations were constant for all the experiments, and the ratio between the two volumes of the phases was set at 1. After one day, crystals were observed in all the samples, as highlighted in Fig. 90. A marked increase in the C30 nucleation density was observed in the upper part of the gels when the agarose content was increased. Such a result was expected considering the strong impact of the gel on crystallization, which facilitated the nucleation step thanks to the increase in the actual supersaturation. The enhancement of nucleation with increased gel content was reflected by the smaller crystal size in the upper part of the samples. In addition, after one day of incubation at 20 °C, the crystallization scheme was completed only for samples involving less than 0.5% of agarose. For higher agarose concentrations, crystallization was confined to the higher layers of gel. Moreover, the amount of not crystallized and free C30 in the gel increased with the agarose content, as demonstrated by the more and more intense yellowy color of the gel. These results proved that the kinetics of crystallization strongly

depended on the gel content. As long as the number of fibers increased, the diffusion of PEG slew down, and also the diffusion of the protein became more and more hindered. The stronger and more interconnected the network, the slower the diffusion and crystallization of catalase. As a matter of fact, in 1.0% agarose samples, crystals started to nucleate and grow in the lower levels of the gel after 3 days, reducing the amount of free C30 in the gel.

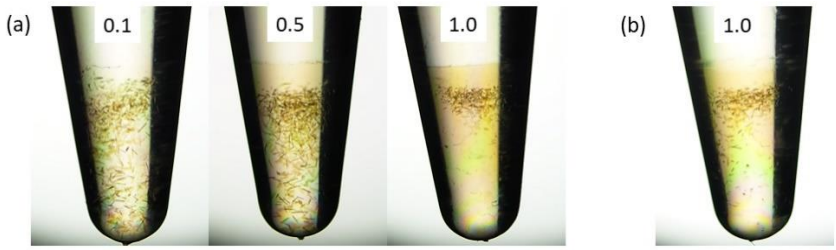

Figure 90 (a) CD crystallization of C30 with increasing agarose concentration (0.1, 0.5, and 1.0%) after one day. C30 concentration was 2.5 mg/mL, and 50% PEG4000 was employed. The volumes of the gel and the precipitant solution were 50 µL each. (b) The 1% sample after 3 days of incubation.

In CD experiments, the agarose gradient displayed an analogous action as observed in batch. As long as the concentration of agarose increased, the nucleation density increased. However, in CD, a kinetic effect exerted by the gel was also identified. A competition between the induction of nucleation and the slowdown of diffusion was highlighted at high agarose content. As a result, nucleation was promptly induced near the interface with the PEG phase, where the first effect prevailed. Moving away from this region, the second effect became more and more important, and nucleation kinetics depended more strongly on diffusion kinetics.

12.4.3.3 Counter-diffusion crystallization of C40

The batch crystallization in gel was found to be drastically affected by the purity of the protein stock solution, as reported in § 11.3.4. A similar investigation was carried out in CD for catalase. Tests were carried out with a less pure source of catalase, i.e., C40. Therefore, the model protein was the same as the previous study, enabling a direct comparison of the outcome of CD crystallization under the same conditions. A first set of experiments was carried out setting the agarose content at 0.5%, and C40 concentration between 2 and 4 mg/mL. All the other conditions, i.e., precipitant concentration (50% PEG4000), individual volume of gel and precipitant (50 µL each), and temperature were the same of C30 crystallization. In all the samples, amorphous precipitation was observed after one day, and crystallization did not occur. The samples were periodically monitored over three months but did not show any evolution. The C40 trial experiments confirmed the lower purity of C40 and its unsuitability to perform crystallization tests at low protein concentrations. The results are collected in Fig 91.

Further tests have been carried out increasing the C40 concentration from 8 to 60 mg/ml. The appearance of C40 crystals was observed in the tested range of protein concentration. As a first step, the protein precipitated, and then, after a few days, crystals began to appear in the gel. Overall, the number of crystals was proportional to the protein concentration. In contrast to C30, C40 did not display any diffusion scheme for the growth of crystals. The mechanism of nucleation was therefore different from conventional CD. The diffusion of PEG within the gel network was first responsible for the precipitation of

the protein. Then, crystals probably nucleated from the precipitate rather than in solution. As nucleation started when the system had already reached equilibrium, i.e., the diffusion of PEG had been completed, the crystals grew under static conditions. The second phase of the experiment could be compared to a conventional batch crystallization.

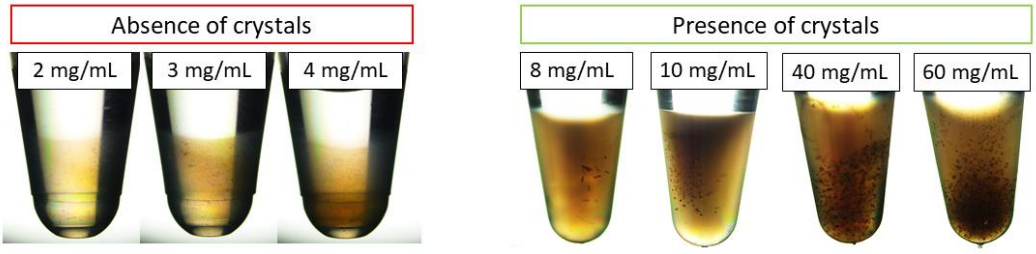

Figure 91 CD crystallization tests for C40 concentrations equal to 2, 3, 4, 8, 10, 40, and 60 mg/mL. All the samples were prepared with 0.5% agarose and 50% PEG4000. Precipitation was observed in all the samples. The formation of crystals was related to C40 concentration.

The C40 set of experiments proved that the presence of agarose gel was beneficial for the promotion of catalase crystallization, even in systems with high impurity loadings. Also, C40 crystallized in a more reproducible manner compared to the uncontrolled crystallization encountered in HDVD preliminary experiments (see § 7.6.2.2). The agarose filtering action was also demonstrated in CD environments.

All the evidence further confirmed that the purity of the source of protein was extremely important to maximize the performance of gels. The same protein, commercialized under different forms, led to dramatically different crystallization outcomes. On the one hand, the purer system enabled the control of crystallization even under CD conditions and the achievement of high nucleation density with minimum amounts of protein. On the other hand, systems characterized by scarce purity were less performant and required a higher concentration of "dirt" protein to get crystals. Alongside this aspect, precipitation always contaminated the samples.

12.5 Validation of CD crystallization in gels: trypsin

The design of counter-diffusion crystallization was carried out with catalase, a protein which required PEG4000 as precipitant. In order to validate the approach, a second protein was selected. Trypsin is commonly crystallized with PEG8000. The protein was selected to test the feasibility of CD in gels with even higher MW PEGs. Trypsin was crystallized increasing the concentration of agarose, as displayed in Fig. 92.

The nucleation density was higher near the interface with the PEG reservoir. Moreover, it progressively increased moving from low to high agarose contents, as already observed for catalase C30. The crystal size trend along the gel mirrored the diffusion scheme of PEG8000. Thus, the feasibility of protein crystallization in gels was demonstrated even in the presence of different MW PEGs.

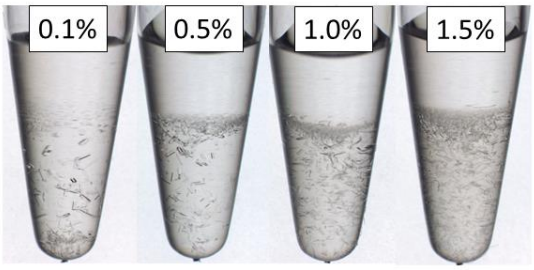

Figure 92 CD crystallization tests of trypsin with increasing agarose concentration (0.1, 0.5, 1.0, and 1.5%).

12.6 CD crystallization of proteinase K in capillaries

As presented in § 12.3, in addition to PEG, also ammonium sulfate unsuited the agarose gelification, particularly at high salt and agarose concentrations. Counter-diffusion approaches were implemented with ammonium sulfate too. The selected model protein was proteinase K. Such a choice also permitted a comparison between batch and CD crystallization of the same protein. A different precipitation cocktail was used, but this did not affect the crystal morphology, as discussed in §7.6.3 and 8.5.1.

Proteinase K was first crystallized in CD inside vials, in a similar way to catalase and trypsin. Then, crystallization inside capillaries was proposed as an alternative technique to solve the issues that emerged from the first part of the experimentation. Lastly, the design of crystallization inside capillaries was discussed.

12.6.1 Preliminary tests in PCR vials

Initially, the crystallization of proteinase K under CD conditions was implemented in vials. Gels were loaded with the protein, and the concentrated precipitant solution was added on top of the gel. However, some issues were encountered. Fig. 93 collects the results obtained for CD experiments after 1 and 5 days carried out with 13 mg/mL of proteinase K in 50 mM HEPES pH 7.0 and 0.5% agarose as the gel phase. The precipitant phase was composed of 1.8 M $(NH_4)_2SO_4$ and 0.1 M Tris pH 8.0.

After 1 day the crystals already grew to a detectable size, but only one or two nuclei were formed in the gel phase. After 5 days anomalous crystals were observed in the precipitant compartment. Thanks to the slow release of the protein from the agarose network into the precipitant compartment, the nucleation of a distinct crystal form was obtained. It was hypothesized that that the tuning of the protein mass transport imposed by the agarose gel played a pivotal role in the early stabilization of pre-nucleation clusters characterized by a different spatial arrangement of the macromolecules. The kinetic interplay between the selective nucleation and the mass transport of the protein in solution could have been modified to get diffraction-quality crystals of a metastable form.

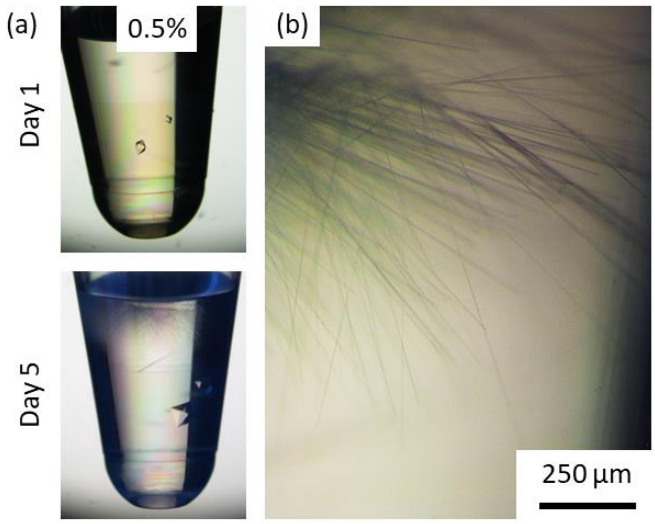

Figure 93 (a) CD crystallization of proteinase K after 1 and 5 days. Crystallization conditions were 13 mg/mL proteinase K, 0.5% agarose, 1.8 M $(NH_4)_2SO_4$, 0.1 Tris – HCl pH 8.0. (b) Enlargement of acicular proteinase K crystals.

Nevertheless, the preliminary screening of CD crystallization of proteinase K in vials evidenced two main limitations. Firstly, the protein was found to be slowly released from the gel and migrate towards the upper compartment of the system. On the one hand, the excessive escape of protein from the gel matrix reduces the number of macromolecules available for nucleation and growth in the protein compartment. On the other hand, if the protein escape from the gel phase was not negligible, the isolation of the agarose action on nucleation could not be achieved. As a consequence, the design of protein crystallization through agarose gradients would not be convenient. In this case, too many variables would undergo variations at the same time, i.e., the protein concentration in the gel and precipitant compartments, the precipitant concentrations in the two phases.

The second drawback was related to the presence of $(NH_4)_2SO_4$ in the system. The deleterious effect of the salt on agarose gelification was discussed in § 12.3.2. When proteins that do not require the presence, such as catalase, or require minimal amounts of $(NH_4)_2SO_4$, such as trypsin, were used, the massive protein migration towards the upper compartment was not observed. Conversely, when concentrated solutions of $(NH_4)_2SO_4$ were put into contact with protein-loaded gels, the migration was significant. It was hypothesized that $(NH_4)_2SO_4$ not only had a deleterious effect on agarose gelification but also could interact with the gel network. The diffusion of the salt in the gel was not believed to directly damage and break the network but, rather, to be responsible for the partial subtraction of water molecules from the agarose helices. The fibers would undergo progressive compaction because of the reduced degree of hydration. Such a premise could explain the enhanced escape of the protein in environments put into contact with concentrated $(NH_4)_2SO_4$ solutions. The compacted fibers of the gel would increase the average pore size and diminish the retention ability of the gel. Moreover, the water activity in the gel compartment would increase because of the release of the entrapped water molecules from the fibers, and the supersaturation level would drop. In this way, the absence of nucleation induction experimentally observed could also be explained.

At the end of the preliminary tests of CD crystallization in vials with $(NH_4)_2SO_4$, the need for a different experimental set-up was evident, and round capillaries were introduced.

12.6.2 CD crystallization in capillaries

The implementation of CD in capillaries aimed at obtaining a versatile and robust set-up for the crystallization of proteins inside gels and in presence of concentrated $(NH_4)_2SO_4$ solutions. The gel loaded with the protein was confined inside the capillary tube, which was in turn immersed in the precipitant solution.

The first point to be solved regarded the protein escape from the gel. A 1% agarose plug was added to the end of the capillary facing the $(NH_4)_2SO_4$ solution. Such a simple ploy was fundamental for the success of the CD experiments. The plug contained the protein migration by slowing down its diffusion out of the capillary. The appearance of crystals outside the capillary was therefore avoided, maximizing the number of protein macromolecules available for nucleation and growth. At the same time, the plug could be regarded as a physical buffer because of the ability to mitigate the initial high supersaturation wave pervading the gel. Uncontrolled precipitation in the first part of the capillary could be avoided or, at least, strongly reduced. The presence of the plug was also beneficial to reduce the deleterious action of $(NH_4)_2SO_4$ on the gel network, acting as a "sacrificial" pre-crystallization chamber.

The synergy between the increased protein concentration inside the gel and the presence of a physical buffer strongly enhanced the nucleation step. Compared to the previous investigation in vials, the protein and the salt concentration were almost doubled, going from 13 mg/mL and 1.8 M to 25 mg/mL and 3 M, respectively. Such aggressive crystallization conditions could be implemented thanks to the robustness of the new experimental set-up. Also, the experiments were performed in the absence of Tris to avoid the effect of different buffers on proteinase K crystallization and focus on the nucleation step.

12.6.2.1 Design of CD crystallization in capillaries

The design of CD crystallization in capillaries was carried out increasing agarose concentration to tune crystal size. The agarose content ranged from 0.1 to 1.5%. Representative optical micrographs of the samples are reported in Fig. 94. The agarose influence on nucleation was striking. The density of crystals increased together with the agarose content in the system. Few and large proteinase K crystals were grown in 0.1% agarose, having an average size of around 500 μm. Well-faceted and intact crystals were observed. The presence of a minimal amount of gel was enough to keep the crystals suspended and prevent their sedimentation. As already discussed, such a gel ability is particularly important for large protein crystals as protects them from damage and breakage. In addition, for every gel content, crystals were observed all along the capillary. The lack of preferential nucleation zones indicated that the system was perfectly homogeneous and that gelification successfully occurred. At the same time, no crystals were observed in the precipitant phase. Such pieces of evidence proved the suitability of the experimental set-up to perform efficient crystallization trials.

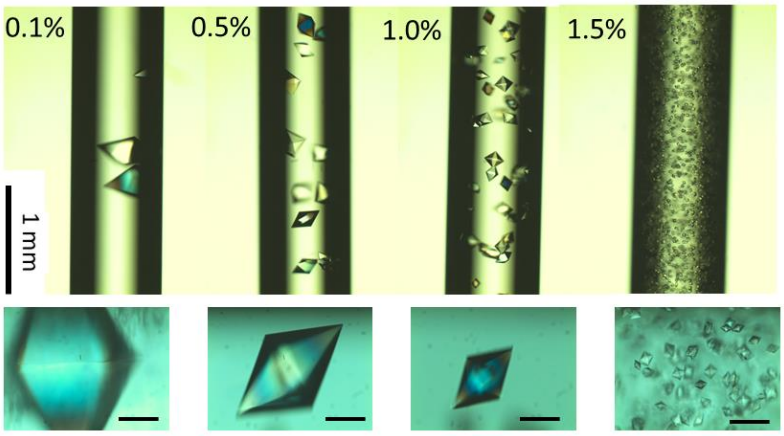

Figure 94 Capillaries prepared with increasing agarose concentrations: 0.1, 0.5, 1.0, and 1.5%. Below each capillary is reported the relative zoom of representative crystals. The scale bar of the zooms is 250 µm. Crystallization conditions were 25 mg/mL proteinase K in 50 mM HEPES pH 7.0 and 3 M $(NH_4)_2SO_4$ as precipitant.

In contrast to conventional CD experiments or to the previous experiments in vials, a gradient of nucleation density along the capillary was not observed. At constant agarose content, the systems were characterized by the same average number of crystals per volume in every zone. This result could be explained considering the precipitation cocktails used in each trial. The gradients of nucleation density were only observed for proteins requiring PEGs as precipitants. In particular, since high MW PEGs were employed, the diffusion of the precipitant species within the gel network was slow. Conversely, $(NH_4)_2SO_4$ is a small molecule compared to the long polymer chains of PEG. The diffusion of the salt within the gelled matrix was faster because the resistance to mass transfer offered by the pores was smaller. Proteinase K crystallization in 6 cm long capillaries was completed after 24 hours, compared to the 3/4 days necessary to complete the pattern of catalase in gels less than 1 cm high. As $(NH_4)_2SO_4$ entered very fast in the system, nucleation was achieved at the same time all along the capillary. The nucleation step was believed to occur when the profile of salt concentration along the capillary reached stationary conditions, i.e., it was flat. The system was equivalent to a batch, thus leading to a homogeneous crystallization pattern.

Thanks to the homogeneous nucleation densities obtained, it was possible to quantify the impact of agarose on nucleation. As demonstrated in § 11.5.2, the nucleation density was directly correlated to the crystal size. The evaluation of the latter is therefore enough to obtain information on the nucleation step. The crystal size vs. agarose content is reported in Fig. 95. A quasi-linear decrease in crystal size was obtained when the agarose increased. The average crystal size ranged between 40 and 500 µm. The crystals populations were increasingly uniform for higher gel contents, similarly to batch crystallization. Interestingly, the decrease in crystal size followed a different trend from the one previously discussed. The discrepancy was attributed to the overlapping of two actions. From the one side, the inducing action of the network was effective in increasing the real supersaturation conditions. On the other side, the presence of ammonium sulfate could compete with this phenomenon. It was hypothesized that the salt could promote the release of entrapped water molecules from the agarose fibers. As a consequence, the salt could have exerted an opposite action on supersaturation. The overall supersaturation would result from these two conflicting processes. Such a premise could explain the deviation from the exponential decay law and the absence of the plateau for agarose > 1.0%. It was therefore concluded

that the real supersaturation was higher than it would be without the gel, but lower than the maximum achievable because of the counteraction of ammonium sulfate.

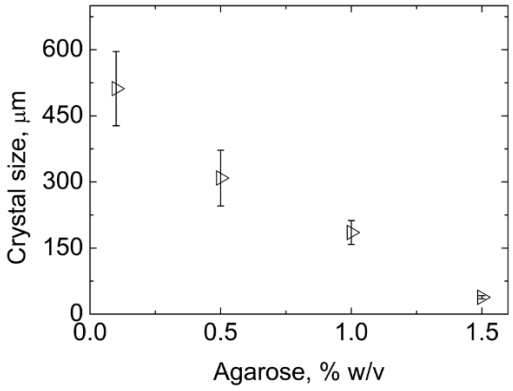

Figure 95 The crystal size as a function of the agarose content for CD crystallization of proteinase K. Error bars refer to SD.

.

The implementation of agarose gradients in capillaries demonstrated that designing the crystallization process was still feasible even in dynamic conditions. Despite the introduction of the precipitant inside the gel by diffusion, the action of the agarose network effectively induced nucleation in a controllable way. Also, the crystallization in capillaries allowed for employing ammonium sulfate as precipitant. The new experimental set-up overcame the limitations encountered when performing CD in vials. The deleterious action of $(NH_4)_2SO_4$ on the gel fibers was mitigated and crystallization in presence of the salt was successfully carried out. The presented configuration could also manage highly concentrated salt solutions, i.e., 3 M, without being compromised.

As a final remark, proteinase K represented a bridge case-study between the batch and the diffusive techniques. The same protein was crystallized with nitrate in vials and with sulfate in capillaries. Considering the same agarose content, e.g., 0.5%, the average crystal size obtained in capillaries was almost six-fold larger than in vials. It was therefore concluded that the gel network did not exert any limiting action over the crystal growth. The pore size of the gel did not represent a constraint on the maximum size achievable by a crystal, excluding any kind of correlation between the two variables.

12.7 Final remarks

The chapter aimed to develop a set-up for the controlled growth of protein crystals in gels even under diffusive conditions. The precipitant and the protein were confined to two separate phases in order to establish a counter-diffusion environment. The protein was immobilized into the gel phase to avoid the deleterious effect of PEGs and ammonium sulfate on agarose gelification. The maximum amounts of PEGs and sulfate that could be employed for batch crystallization in gels were identified. Thanks to the CD approach, catalase and trypsin were successfully crystallized in convection-free environments, and the tuning of crystal size was achieved. A pattern of crystal size was observed along the vials, mirroring the precipitant diffusion. Lastly, the use of ammonium sulfate as a precipitant required a more robust set-up, and the tuning of CD crystallization of proteinase

K was carried out in capillaries. In addition, thanks to the control over the protein mass transport imposed by the network, a previously unknown crystal form of proteinase K was identified.

In conclusion, protein crystallization in gels was successfully implemented and controlled even under dynamic conditions, confirming the robustness of this tool for the design of crystals attributes.

References

Artusio, F., Castellví, A., Sacristán, A., Pisano, R., & Gavira, J. A. (2020b). Agarose gel as a medium for growing and tailoring protein crystals. *Crystal Growth & Design*, **20**(8), 5564-5571.

Charlionet, R., Levasseur, L., & Malandain, J. J. (1996). Eliciting macroporosity in polyacrylamide and agarose gels with polyethylene glycol. *Electrophoresis*, **17**(1), 58–66.

Crowley, P. B., Brett, K., & Muldoon, J. (2008). NMR spectroscopy reveals cytochrome c-poly(ethylene glycol) interactions. *ChemBioChem*, **9**(5), 685–688.

González-Rámirez, L. A., Caballero, A. G., & García-Ruiz, J. M. (2008). Investigation of the compatibility of gels with precipitating agents and detergents in protein crystallization experiment. *Crystal Growth and Design*, **8**(12), 4291–4296.

Letherby, M. R., & Young, D. A. (1981). The gelation of agarose. *Journal of the Chemical Society, Faraday Transactions 1: Physical Chemistry in Condensed Phases*, **77**(8), 1953–1966.

Piculell, L., & Nilsson, S. (1989). Anion-specific salt effects in aqueous agarose systems. 1. Effects on the coil-helix transition and gelation of agarose. *Journal of Physical Chemistry*, **93**(14), 5596–5601.

Ries-Kautt, M. M., & Ducruix, A. F. (1989). Relative effectiveness of various ions on the solubility and crystal growth of lysozyme. *The Journal of Biological Chemistry*, **264**(2), 745–748.

Chapter 13

Conclusions and future developments

The analysis of the crystallization process of pharmaceuticals and biomolecules with engineered systems was the result of a research journey started from the early design and synthesis of heteronucleants. Different research goals were set according to the type of solute to be crystallized, which in turn dictated specific choices in terms of surface design of heteronucleants. Overall, the research work was motivated by a series of questions which were presented at the end of Chapter 1 and that are here reported to try to give them an answer on the basis of the collected experimental evidence.

- *Is it possible to physically isolate the effect of surface chemistry from surface morphology when performing heterogeneous nucleation?*
  In this perspective, a modular concept was applied for the design of the superficial properties of bidimensional heteronucleants. Self-assembled monolayers (SAMs) carrying different exposed groups as the only variable were synthesized. At the same time, the topographic features were constant for all the supports. In this way, the impact of surface chemistry on crystallization was physically deconvoluted from that of surface morphology. The investigation pointed out that a fundamental role was played by the synthesis method for preparing the heteronucleants. Therefore, the first part of this study was devoted to the identification, optimization, and validation of a simple and versatile protocol for the synthesis of SAMs. A picture of SAMs physico-chemical attributes was obtained thanks to the thorough characterization of samples with a variety of techniques, ranging from contact angle, AFM and SEM, to more sophisticated surface analyses techniques such as ToF-SIMS and XPS. To the best of our knowledge, this is the first study presenting a general and reproducible SAM synthesis protocol for four alkoxysilanes having the same hydrocarbon chain length but exposing different chemical groups. High-quality SAMs were obtained in terms of degree of packing, absence of localized deposits of polymerized silanes, uniform thickness, and intra-batch uniformity, thus ensuring a robust platform for studying nucleation.

- *Are smooth surfaces sufficiently nucleation-active?*
  A fundamental role is played by surface roughness when heterogeneous nucleation in batch pharmaceutical crystallization is involved. The prepared SAMs displayed sub-nm roughness to let the action of surface chemistry prevail. The price to pay was a slower nucleation kinetics, leading to longer nucleation induction time, compared to the literature, where nucleants coupling chemistry and rough topography had been studied. Nevertheless, a strong effect of surface chemistry on nucleation kinetics was observed, and nucleation was successfully enhanced or repressed by simply tuning the exposed groups on the substrate. A good temporal separation was obtained since, taking as a reference about 450 h as the nucleation time on untreated supports, nucleation time increased up to more than 1500 h or decreased to less than 90 h when surface chemistry was modified. Accordingly, also the probability of finding crystals was tuned from 30 to 100% on different substrates.

- *What is the main mechanism of interaction governing surface-induced nucleation? How can it be identified?*
  In the present study, aspirin was selected as a small molecule model. As a first step, batch crystallization was studied, and a correlation between the nucleation induction time and the acid surface energy component of SAMs was observed. To confirm such a hypothesis, a method for studying the specific interaction between surface and API was developed. Oriented thin films of aspirin were crystallized on SAMs by spin coating, enabling the direct evaluation of affinity between SAM end groups and specific API crystal planes. Different SAMs promoted the preferential nucleation of different crystal facets, being either (100) or (011), which resulted in modified peak intensity ratios in their corresponding diffractograms and in modified thin-film morphologies. A correlation was identified between the oriented growth and the acid surface energy component of SAMs, pointing out that the matching between acid and base features of solute and surface was the main mechanism of interaction governing both nucleation kinetics and oriented growth.

- *How do surfaces affect small molecule drug and protein crystallization?*
  Surfaces affect several aspects of crystallization, depending on the nature of the target molecule to be crystallized. As regards small-molecule drugs, the main action of SAMs was observed on the tuning of the nucleation kinetics, without affecting the crystalline form. In addition, in thin-film crystallization, surfaces successfully tuned the morphology of the crystals, promoting different orientations and relative growth of the crystal faces. For proteins, the picture was more complex. The tuning of nucleation kinetics was achieved both with SAMs and gels, but other aspects came into play. SAMs were employed to modify the nucleation behavior of target proteins exposed to the same environmental conditions. Gels were employed to tune the nucleation density and the final crystal size and distribution, but also to promote the diffusive mass transport of the protein during crystallization, thus favoring the controlled growth, the appearance of new crystal forms, the stability of the crystals, and the control of the crystal habit.

- *Is the action of networks on protein crystallization mainly physical or chemical?*
  Tridimensional systems were studied to enhance the crystallization of proteins, and agarose gels were employed as a medium to promote nucleation and tailor the crystal size and density of lysozyme, proteinase K, and insulin. The three proteins all displayed different charges and were crystallized at different pH. Nevertheless, the normalized trends of crystal size and nucleation density as a function of the agarose concentration were all overlapping. All the evidence pointed out a marked physical action of agarose gels on nucleation, being it independent of the specific protein nature. A mechanism based on the retention of water by the gel fibers, thus increasing the supersaturation level in the systems, was proposed. Other types of gels, such as the silica gels, led to strong chemical interactions with lysozyme, which eventually hindered the crystallization.

- *Is it possible to fine-tune nucleation to get reproducible and defined crystal populations?*
  This is perhaps the core-question of the present study, which inspired the work at all its stages. Reproducible and defined crystal populations in terms of size, habit, and form could be obtained, if fine-tuning of nucleation were achieved. In this study, the nucleation step was affected by surfaces, as SAMs, or networks, as agarose or silica gels, to force it towards specific directions, involving kinetics or thermodynamics aspects. For example, populations of protein crystals with precise dimensional features were successfully prepared with the help of gels. A method for predicting and tuning the size and density of the crystals grown in gels as a function of the agarose content was developed. Overall, the fine-tuning of nucleation still remains a challenge, but new tools for its study have been proposed and investigated.

Bidimensional and tridimensional supports were demonstrated to effectively alter the nucleation step of target molecules and serve as tools to increase the understanding of pharmaceutical and biopharmaceutical crystallization. Future developments may focus on the controlled and progressive alteration of surface topography, keeping the same SAM chemistry, to introduce and quantify the effect of superficial roughness on nucleation kinetics of small-molecule drugs and proteins. Also, it might be interesting to localize the nucleation active sites on restricted areas of the surface and induce area-selective crystallization to develop chips for bioseparation and purification, as an alternative to expensive chromatographic techniques. In this perspective, nano-structured surfaces could be applied as heteronucleants for APIs and proteins. The use of nanotechnology would support the synthesis of nano-patterned surfaces. Preliminary studies have been carried out to prepare substrates carrying specific patterns of adsorbed gold nanoparticles with the help of focused ion beam (FIB) techniques. Gold nanoparticles can easily be functionalized with selected chemical groups, thus allowing for the study of the effects of controlled superficial morphology coupled to controlled surface chemistry on the heterogeneous nucleation of pharmaceuticals.

Another aspect that is of interest, and which is currently under investigation, regards the role of modified gel chemistries on the crystallization of proteins, with particular attention to the controlled insertion of hydrophobic moieties inside silica gels to grow cross-linked enzyme crystals. In this way, the strong chemical interaction between proteins

and silica gels might be mitigated, thus overcoming the inhibiting action of silica toward protein nucleation and achieving higher nucleation densities. In this way, modified silica gels could be proposed as a novel material for macromolecular crystallography, and the applicability of silica gels to protein crystallization could be expanded.

The present study has the potential to impact not only on the scientific, but also on the economic and social sphere of pharmaceutical technologies. As regards the former aspect, this investigation supports the complex process of early drug discovery, where information on drug stability, nucleation kinetics and all the possible crystalline forms must be collected. The development of new methods for the investigation of surface-solute interactions can support and facilitate this stage, providing new insight into the discovery of new active pharmaceutical ingredients and in the structural determination of therapeutic proteins. The implications of a faster and more robust R&D process are less expensive and safer finished products. Ensuring the medicine safety and guaranteeing a more accessible product for the patients are two key issues of the pharmaceutical industry, which require a lot of effort, especially when the discovery and the manufacturing processes are long and complex.

The results of this research might also support the development of an emerging area of the pharmaceutical manufacturing regarding the coupling of heterogeneous nucleation to continuous crystallization, under controlled conditions. The clarification of the surface chemistry effects on the heterogeneous nucleation of drugs can support the design of novel particles to be used as heteronucleants, as an alternative to crystalline seeds. Future work may focus on the development of functionalized particles containing FDA-approved excipients to regulate the continuous crystallization of pharmaceuticals and limit the downstream processing actions, such as milling and blending. This novel approach to pharmaceutical crystallization lies in the framework of process intensification technologies (PIT) applied to integrated continuous manufacturing (ICM), which has the potential to avoid intra-batch variability, limit expensive downstream processing, facilitate process scale-up, and reduce production costs.

List of symbols

A, A_c, A_{c1}, A_{c2}, A_N	Pre-exponential fitting factors
AR	Aspect ratio
B, B_c, B_{c1}, B_{c2}, B_N	Decay ratio fitting factors
C	Concentration
C_s	Solubility
d	Adlayer thickness
E	Electrical field
f_{mol}	Packing factor
F_{ad}	Adhesion force
ΔG	Nucleation free energy
ΔG_s	Nucleation surface free energy
ΔG_v	Nucleation volume free energy
h, k, l	Miller's indexes
I_{Si}	Si2p signal of functionalized glass
I_{Si0}	Si2p signal of activated glass
J_{sup}	Supersaturation rate
k_e	Elastic constant
K	Scherrer's shape factor
l_c	Crystal size
$\widehat{l_c}$	Normalized crystal size
l_{max}	Maximum extension of HEWL (110) crystal face
l_{min}	Minimum extension of HEWL (110) crystal face
L	Crystallite size
n	Exact number of events
n_{air}	Refractive index of air
n_{mol}	Refractive index of silane molecule
n_{SAM}	Refractive index of SAM
N	Nucleation density
$\widehat{N}$	Normalized nucleation density
P	Probability of not observing nucleation events
q	Protein net charge
R_h	Radius of gyration
R_q	Surface roughness
s	Superficial area of the cluster
S	Supersaturation
t	Time
t_{lag}	Lag time
t_{nuc}	Total nucleation induction time
T_c	Crystallization temperature
T_{sp}	Set-point temperature
v	Volume of the cluster
V_{ASA}	Volume of dispensed solution

x_0, x_1, x_2	Fitting parameters of solubility curves
ZP_{tracer}	Zeta potential of the tracer

Greek letters

γ	Surface tension
γ^+	Acid component of surface tension
γ^-	Basic component of surface tension
γ^{AB}	Polar component of surface tension
γ^{LW}	Lifshitz-van der Waals component of surface tension
γ_l	Surface tension of liquid
γ_s	Surface tension of solid
γ_{sl}	Surface tension between the solid and the liquid
δ	AFM cantilever deflection
θ	Bragg's angle
λ	X-Rays wavelength
ν	Expected number of events
τ	Average nucleation induction time
φ	Contact angle
ω	Rotational speed
$\dot{\omega}$	Rotational acceleration

List of abbreviations

3L	3 Layers
AFM	Atomic Force Microscopy
API	Active Pharmaceutical Ingredient
AMINO	3-aminopropyltrimethoxysilane
AR	Angle Resolved
ASA	Aspirin
ATR	Attenuated Reflectance Mode
CD	Counter-Diffusion
CNT	Classical Nucleation Theory
CPG	Controlled Porous Glass
CPS	Counts Per Second
DLS	Dynamic Light Scattering
EAL	Electronic Attenuation Length
EO	Electro-osmosis
EP	Electrophoresis
EtOH	Ethanol
FE	Field Emission
FPP	Finished Pharmaceutical Product
FTIR	Fourier Transform InfraRed
FWHM	Full Width at Half Maximum
GAME	Gel Acupuncture Method
GCB	Granada Crystallization Box
GPTES	3-glycidyloxyopropyltriethoxysilane
GLY	3-glycidyloxypropyltrimethoxysilane
HB	Hydrogen Bond
HD	Hanging Drop
HEPES	2-[4-(2-hydroxyethyl)piperazin-1-yl]ethanesulfonic acid
HEWL	Hen Egg White Lysozyme
HPLC	High Performance Liquid Chromatography
HR	High Resolution
ICM	Integrated Continuous Manufacturing
ID	Internal Diameter
KE	Kinetic Energy
LMIG	Liquid Metal Ion Gun
LMP	Low Melting Point
MIP	Molecularly Imprinted Polymer
MFC	Mass Flow Controller
THIOL	3-mercaptopropyltrimethoxysilane
MSE	Mean Square Error
MW	Molecular Weight
NMF	Non-negative Matrix Factorialization
PCA	Principal Component Analysis
PCR	Polymerase Chain Reaction

PEG	Polyethylene glycol
PEGDA	Poly(ethylene glycol) diacrylate
PIT	Process Intensification Technology
PVA	Poly(vinyl alcohol)
RSF	Relative Sensitivity Factors
SAD	Selected Area Difference
SAM	Self-Assembled Monolayer
SD	Standard Deviation
SE	Standard Error
SEM	Scanning Electron Microscopy
SFX	Serial Femtosecond Crystallography
SMX	Serial Millisecond Crystallography
SZP	Surface Zeta Potential
TC	Temperature Controller
TI	Temperature Indicator
TLD	Through-Lens Detector
ToA	Take-off Angle
TT	Temperature Transducer
ToF-SIMS	Time-of-Flight Secondary Ion Mass Spectrometry
ACR	3-(trimethoxysilyl)propyl methacrylate
USP	United States Pharmacopoeia
V	Manual Valve
VD	Vapor Diffusion
VOCG	van Oss-Chaudhury-Good
XFEL	X-Ray Free Electron Laser
XPS	X-Ray Photoelectron Spectroscopy
XRD	X-Ray Diffractometry

Appendix A

Additional data on surface analysis of SAMs

Table A1 Atomic composition of the samples referring to the studies of surface activation and surface functionalization with THIOL silane. XPS survey spectra were collected on three different spots per sample. Average at% and standard deviations are reported. Measurements were carried out at ToA = 0°.

Sample	O%	Si%	C%	S%	N%	Rest.% (K, Al, Na, Zn, Ti)
Untreated glass	55.94 (1.37)	22.04 (0.56)	19.21 (1.77)	-	-	< 3
Activated glass	64.47 (0.37)	25.08 (0.23)	8.13 (0.71)	-	-	< 3
T1	60.62 (0.86)	22.27 (0.12)	13.15 (1.54)	< 1	-	< 3
T2	61.33 (1.75)	21.90 (0.29)	12.71 (1.84)	1.30 (0.61)	-	< 3
T3	55.73 (0.63)	21.43 (0.19)	17.65 (0.79)	2.98 (0.14)	-	< 3
T4	46.49 (1.61)	19.64 (0.37)	28.82 (2.45)	3.00 (0.44)	-	< 3
T5	37.66 (1.85)	17.08 (0.63)	37.21 (2.21)	5.84 (0.71)	-	< 3
T6	64.51 (1.00)	21.82 (1.25)	9.95 (0.84)	0.34 (0.40)	-	< 3
T7	60.82 (1.67)	20.59 (0.13)	13.98 (1.24)	1.28 (0.18)	-	< 3
T8	57.27 (1.33)	20.01 (0.24)	17.60 (0.29)	2.33 (0.49)	-	< 3
T9	61.86 (3.10)	20.54 (0.89)	13.17 (3.84)	< 1	-	< 3

Table A2 Atomic composition of the samples referring to the studies of surface functionalization with AMINO, ACR, and GLY silanes. XPS survey spectra were collected on three different spots per sample. Average at% and standard deviations are reported. Measurements were carried out at ToA = 0°.

Sample	O%	Si%	C%	S%	N%	Rest.% (K, Al, Na, Zn, Ti)
A1	23.14 (0.10)	10.91 (0.19)	53.57 (0.18)	-	11.85 (0.07)	< 1
A2	24.63 (1.00)	10.82 (0.68)	52.13 (0.30)	-	11.89 (0.68)	< 1
A3	26.44 (0.52)	14.08 (0.03)	48.56 (0.21)	-	10.37 (0.73)	< 1
A4	58.92 (2.02)	19.45 (0.76)	18.05 (2.01)	-	3.58 (0.5)	< 1
A5	55.02 (0.37)	19.40 (1.00)	21.32 (1.20)	-	4.11 (0.06)	< 1
A6	33.68 (4.96)	13.40 (1.07)	43.66 (5.31)	-	9.06 (0.81)	< 1
A7	29.40 (3.43)	12.33 (0.08)	49.07 (2.11)	-	9.14 (1.44)	< 1
A8	23.26 (0.15)	11.80 (0.12)	53.18 (0.11)	-	11.60 (0.05)	< 1
M1	59.83 (0.51)	20.76 (0.17)	16.09 (0.56)	-	-	< 3
G1	53.85 (0.10)	18.68 (0.37)	25.43 (0.21)	-	-	< 3

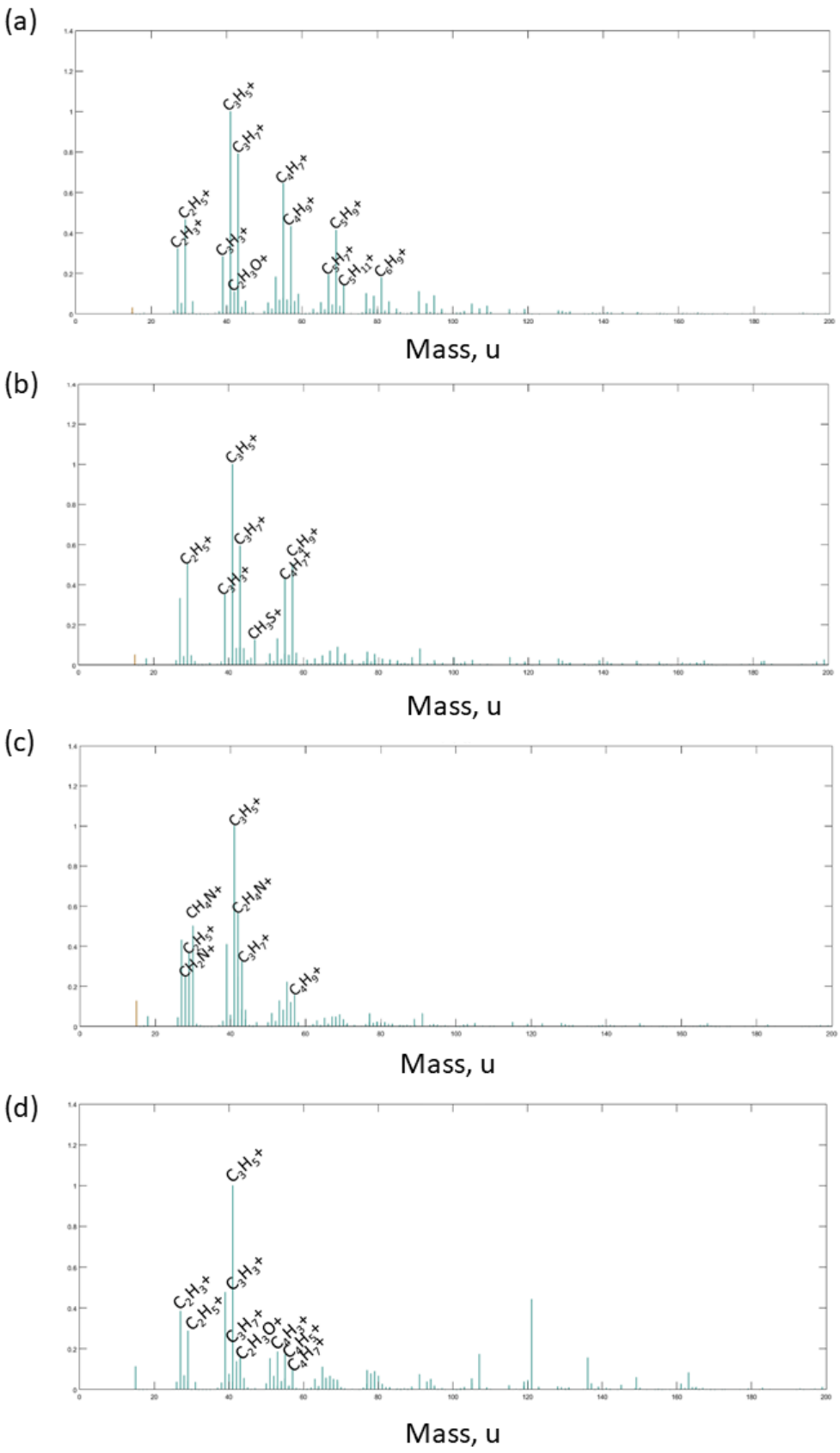

Figure A1 Representative ToF-SIMS spectra of the reference samples for (a) untreated glass, and samples (b) T3, (c) A1 and (d) M1.

Table A3 The values of surface tension γ_l, and dispersive γ_l^{LW}, acid γ_l^+, and base γ_l^- components of the three probing liquids used to determine the surface tension and related components of SAMs according to the VOCG model.

Probing liquid	$\boldsymbol{\gamma_l}$**, mJ/m²**	$\boldsymbol{\gamma_l^{LW}}$**, mJ/m²**	$\boldsymbol{\gamma_l^+}$**, , mJ/m²**	$\boldsymbol{\gamma_l^-}$**, mJ/m²**
Water	72.8	21.8	25.5	25.5
Glycerol	64.0	34.0	3.92	57.4
Diiodomethane	50.8	50.8	0.0	0.0

Appendix B

Conditions for protein crystallization

Table B1 List of the preliminary crystallization experiments carried out for HEWL, catalase C30, and catalase C40 (Chap. 7). Each set of conditions, involving protein and precipitant concentration in the stock solution, the ratio between the volumes of protein and precipitant solution in the drop, and the crystallization set-up, is given a unique reference code.

Reference	Protein, mg/mL	Precipitant	Protein:precipitant	Crystallization set-up
HEWL				
L1	50	1.5% NaCl	1:1	Linbro plate
L2	50	3% NaCl	1:1	Linbro plate
L3	50	4% NaCl	1:1	Linbro plate
L4	50	6% NaCl	1:1	Linbro plate / Mushroom
L5	50	8% NaCl	1:1	Linbro plate
L6	50	12% NaCl	1:1	Linbro plate
L7	50	15% NaCl	1:1	Linbro plate
L8	50	17% NaCl	1:1	Linbro plate
L9	25	6% NaCl	1:1	Mushroom
L10	75	6% NaCl	1:1	Mushroom
Catalase C30				
C301	1.0	10% PEG4000	1:1	Linbro plate
C302	1.0	15% PEG4000	1:1	Linbro plate
C303	1.8	10% PEG4000	1:1	Linbro plate
C304	3.7	20% PEG4000	1:1	Linbro plate
C305	3.7	20% PEG4000	2:1	Linbro plate
C306	3.7	30% PEG4000	1:1	Linbro plate
C307	3.7	30% PEG4000	2:1	Linbro plate
Catalase C40				
C401	1.8	20% PEG4000	1:1	Linbro plate
C402	3.5	20% PEG4000	1:1	Linbro plate
C403	7.0	20% PEG4000	1:1	Linbro plate
C404	14.5	20% PEG4000	1:1	Linbro plate

Table B2 List of the preliminary crystallization experiments carried out for proteinase K (Chap. 7). Each set of conditions, involving protein and precipitant concentration in the stock solution, the ratio between the volumes of protein and precipitant solution in the drop, and the crystallization set-up, is given a unique reference code.

Reference	Protein, mg/mL	Precipitant	Protein:precipitant	Crystallization set-up
Proteinase K				
P1	2.5	1M $NaNO_3$ 50 mM Na citrate pH 6.5	1:1	Linbro plate
P2	5	1M $NaNO_3$ 50 mM Na citrate pH 6.5	1:1	Linbro plate
P3	10	1M $NaNO_3$ 50 mM Na citrate pH 6.5	1:1	Linbro plate
P4	15	1M $NaNO_3$ 50 mM Na citrate pH 6.5	1:1	Linbro plate
P5	10	2M $(NH_4)_2SO_4$, 0.1M Tris-HCl pH 8	1:1	Linbro plate
P6	20	1.2M $(NH_4)_2SO_4$, 0.1M Tris-HCl pH 8	1:1	Linbro plate
P7	20	2M $(NH_4)_2SO_4$, 0.1M Tris-HCl pH 8	1:1	Linbro plate
P8	10	2M $(NH_4)_2SO_4$	1:1	Linbro plate
P9	20	2M $(NH_4)_2SO_4$	1:1	Linbro plate
P10	10	2M $(NH_4)_2SO_4$, 0.1M HEPES pH 7	1:1	Linbro plate
P11	20	2M $(NH_4)_2SO_4$, 0.1M HEPES pH 8	1:1	Linbro plate
P12	10	2M $(NH_4)_2SO_4$ 0.1M K phosphate pH 7	1:1	Linbro plate
P13	20	2M $(NH_4)_2SO_4$ 0.1M K phosphate pH 7	1:1	Linbro plate

Table B3 List of the preliminary crystallization experiments carried out inside *mushroom* crystallizers for HEWL, catalase C30, and proteinase K (Chap. 8). Each set of conditions involving protein and precipitant concentrations, and protein on precipitant ratio in the drop is given a unique reference code.

Reference	Protein, mg/mL	Precipitant	Protein:precipitant
HEWL			
LS1	60	4% NaCl	1:1
LS2	60	7% NaCl	1:1
LS3	60	11% NaCl	1:1
LS4	60	15% NaCl	1:1
LS5	45	4% NaCl	1:1
Catalase C30			
CS1	3.7	15% PEG4000	1 : 1
CS2	1.8	15% PEG4000	1 : 1
CS3	2.4	15% PEG4000	1 : 1
CS4	3.7	20% PEG4000	1 : 1
Proteinase K			
PS1	30	0.25 M $NaNO_3$ 25 mM Na citrate	1:1
PS2	20	0.25 M $NaNO_3$ 25 mM Na citrate	1:1
PS3	15	0.25 M $NaNO_3$ 25 mM Na citrate	1:1
PS4	10	0.25 M $NaNO_3$ 25 mM Na citrate	1:1
PS5	30	1.7 M $(NH_4)_2SO_4$	1:1
PS6	20	1.7 M $(NH_4)_2SO_4$	1:1
PS7	15	1.7 M $(NH_4)_2SO_4$	1:1
PS8	10	1.7 M $(NH_4)_2SO_4$	1:1
PS9	17	0.25 M $NaNO_3$ 25 mM Na citrate	1:1
PS10	19	0.25 M $NaNO_3$ 25 mM Na citrate	1:1
PS11	17	1.7 M $(NH_4)_2SO_4$	1:1
PS12	19	1.7 M $(NH_4)_2SO_4$	1:1

Published works

Works published during PhD period regarding PhD topics:

Artusio, F. & Pisano, R. (2018). Surface-induced crystallization of pharmaceuticals and biopharmaceuticals: A review. *International journal of pharmaceutics*, **547**(1-2), 190-208.

Artusio, F., Fumagalli, F., Bañuls-Ciscar, J., Ceccone, G., & Pisano, R. (2020). General and adaptive synthesis protocol for high-quality organosilane self-assembled monolayers as tunable surface chemistry platforms for biochemical applications. *Biointerphases*, **15**(4), 041005.

Artusio, F., Castellví, A., Sacristán, A., Pisano, R., & Gavira, J. A. (2020). Agarose gel as a medium for growing and tailoring protein crystals. *Crystal Growth & Design*, **20**(8), 5564-5571.

Artusio, F., Fumagalli, F., Valsesia, A., Ceccone, G., & Pisano, R. (2021). Role of self-assembled surface functionalization on nucleation kinetics and oriented crystallization of a small-molecule drug: Batch and thin-film growth of aspirin as a case study. Accepted for publication in *ACS Applied Materials & Interfaces*.

Works published during PhD period on other topics:

Artusio, F., Bazzano, M., Pisano, R., Coulon, P. E., Rizza, G., Schiller, T., & Sangermano, M. (2018). Polymeric nanocapsules via interfacial cationic photopolymerization in miniemulsion. *Polymer*, **139** (1), 155-162.

Artusio, F., Ferri, A., Gigante, V., Massella, D., Mazzarino, I., Sangermano, M., Barresi, A., & Pisano, R. (2019). Synthesis of high payload nanohydrogels for the encapsulation of hydrophilic molecules via inverse miniemulsion polymerization: caffeine as a case study. *Drug Development and Industrial Pharmacy*, **45**(12), 1862-1870.

Proceedings & conference acts:

Artusio, F., Bañuls-Ciscar, J., Ceccone, G., & Pisano, R. (2019, 16-20 June). Probing self-assembly of silane molecules in monolayers at active solid-liquid interfaces. 5th NanoToday Conference, Lisbon.

Artusio, F., Borgogno, A., Cabri, W., Ricci, A., Udrescu, C., Viola, A., & Pisano, R. (2019, 10-12 July). Development of freeze-drying cycle for a peptide-based drug in trays. In Proceedings of 7th European Drying Conference, Torino.

Artusio, F., Pisano, R., Bañuls-Ciscar, J., Valsesia, A., Fumagalli, F., & Ceccone, G. (2019, 15-20 September). Surface analysis of functionalized substrates for the nucleation and crystallization of pharmaceutical molecules. 18th European conference on Applications of Surface and Interface Analysis, Dresden.

Artusio, F., Ceccone, G., & Pisano, R. (2019, 11-15 November). Surface-induced nucleation strategies: seeking symmetries between self-assembly of heteronucleants and crystals. In Proceedings of the Annual Meeting of American Chemical Engineers, Orlando (FL), ISBN: 978-0-8169-1112-7

Artusio, F., Castellví, A., Sacristán, A., Pisano, R., & Gavira, J. A. (2021, 19-21 January). Agarose, the gel to tailor your protein crystals. XXIX Simposio del Grupo Especializado en Cristalografía y Crecimiento Cristalino, Vigo, Spain.